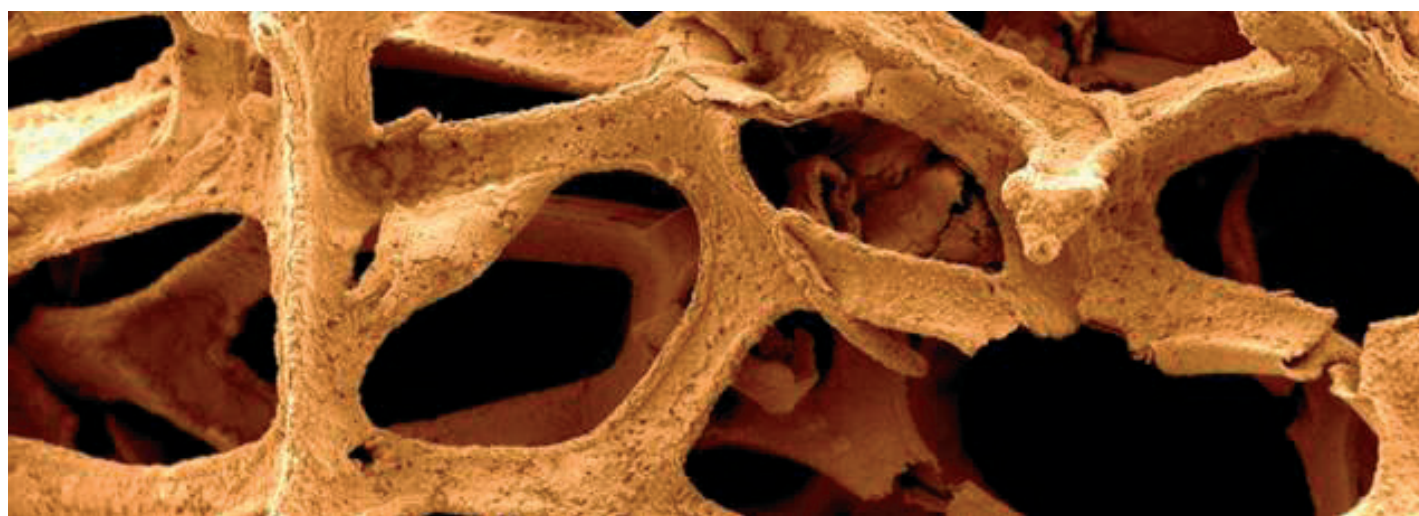


PAUL SCHERRER INSTITUT



Annual Report 2013

Electrochemistry Laboratory

Cover

Nickel foam covered by Sb particles
used for negative electrode in Li-ion
batteries.

© Paul Scherrer Institut

DOI: 10.3929/ethz-a-007047464

PAUL SCHERRER INSTITUT



Annual Report 2013

Electrochemistry Laboratory

Paul Scherrer Institut
Electrochemistry Laboratory
5232 Villigen PSI
Switzerland

Secretary
Phone +41 56 310 29 19
Fax +41 56 310 44 15

**Hardcopies of this report
are available from**

Cordelia Gloor
cordelia.gloor@psi.ch
Paul Scherrer Institut
5232 Villigen PSI
Switzerland



A full version of this report is also available on the web
<http://www.psi.ch/lec>

Publisher

Electrochemistry Laboratory
Paul Scherrer Institut
5232 Villigen PSI

Editorial Team

Cordelia Gloor
Lorenz Gubler
Thomas J. Schmidt

Printing

Paul Scherrer Institut

ISSN 1661-5379

DOI: 10.3929/ethz-a-007047464

PSI Electrochemistry Laboratory :: Annual Report 2013

© Paul Scherrer Institut

CONTENTS

- 1 EDITORIAL**
T.J. Schmidt
- 2 THE ELECTROCHEMISTRY LABORATORY AT A GLANCE**
- 5 SCIENTIFIC ACHIEVEMENTS 2013**
- FUEL CELLS - SYSTEMS & DIAGNOSTICS**
- 7** Hydrogen fuel cell based range extender for electric passenger car
- 8** On the durability of H₂/O₂ polymer electrolyte fuel cells
- 10** Reproducibility of performance and water distribution of small scale differential fuel cells
- 12** Accuracy of water quantification in fuel cells by neutron imaging
- 13** Determination of phosphoric acid concentrations in HT-PEFC components by X-ray tomographic microscopy
- 15** X-ray tomographic imaging of GDLs during pressure driven water imbibitions/drainages
- 17** Limiting current phenomena in PEFC investigated with *in situ* XTM
- 19 FUEL CELLS & ELECTROLYSIS - MATERIALS**
- 21** Radiation grafted polymer electrolyte membranes for water electrolysis cells – characterization of key membrane properties
- 23** Automotive H₂/Air operation of the PSI Gen2 radiation grafted membrane
- 25** Effect of different antioxidants on performance and durability of styrene based radiation grafted membranes (ETFE-*g*-PSSA)
- 27** A degradation study of radiation grafted membranes in PEFCs by exhaust water analysis
- 29** Quantification of the gas barrier properties of radiation grafted membranes using mass spectrometry
- 31** Towards gas diffusion layers with patterned wettability
- 33 BATTERIES & SUPERCAPACITORS - MATERIALS**
- 35** Increasing the specific charge of graphite by the addition of silicon
- 37** Effect of different separators on the performance of Li-S cells
- 39** Grafting of 4-styrenesulfonic acid sodium salt hydrate (SSNa) onto porous PP separator and effects of post-grafting treatment
- 41** New intermetallic compounds as negative electrodes for Lithium-ion batteries
- 42** Investigation of the dilatation behaviour of 0 to 3-dimensional carbons upon charge
- 44** Facile low temperatures synthesis of lithiated manganese oxides, high potential insertion materials
- 46** Influence of electrolyte on the performance and lifetime of NCM family materials
- 48** One-pot synthesis by anhydrous sol-gel chemistry of mixtures of magnetite and greigite, and their use for positive electrode in Li-ion batteries
- 50** Toluene-assisted sulphur impregnation of carbons as a method for preparing positive electrodes for Li-S batteries
- 52** Characterization of Porocarb-Si composite material for negative Li-ion battery electrodes
- 54** Role of the binder in Na-ion batteries
- 55 BATTERIES & SUPERCAPACITORS - DIAGNOSTICS**
- 57** Gas evolution from phosphorous based negative Li-ion battery electrodes
- 58** New insight in the reaction mechanism of Cu_{0.5}TiOPO₄: an *ex situ* ³¹P MAS NMR study
- 59** Electrochemical cell for *operando* studies on lithium-ion batteries using laboratory X-rays apparatus
- 61** Cycling rate effects on half and full cells: 5V-NMC vs. graphite

CONTENTS

- 63** Electrochemical impedance spectroscopy characterization of lithium-ion battery electrodes – technical improvements
- 65** Reactions occurring at HE-NCM electrode/electrolyte interface
- 67** Gas evolution followed by DEMS of HE-NCM electrodes using different electrolytes
- 69** Understanding the SEI properties on conversion-reacting Sn electrodes for Na-ion batteries
- 72** Ionic liquid-based electrolyte for 5V Li-ion batteries and *in situ* XPS studies
- 75** XPS study of the evolution of the interfaces of porous graphite electrodes for Li-O₂ batteries upon cycling
- 77** On the Li(Ni_{0.80}Co_{0.15}Al_{0.05})O₂ system upon (de)lithiation: electrochemical and *in situ* XRD studies
- 79 ELECTROCATALYSIS & INTERFACES**
- 81** Hydrogen underpotential deposition and CO stripping voltammetry on metal-oxide supported platinum catalyst
- 83** Advanced CV studies on high-temperature polymer electrolyte fuel cells
- 85** Positive effect of CO during start/stop on high-temperature PEFCs
- 87** Composite catalysts made by Ba_{0.5}Sr_{0.5}Co_{0.8}Fe_{0.2}O_{3-δ} perovskite and acetylene black carbon for the oxygen reduction reaction in alkaline media
- 89** Structural investigation on Pt₄₀Pd₆₀ aerogel by using multi-edge extended X-ray absorption fine structure (EXAFS) fit analysis
- 91** Fabrication of membrane electrode assemblies with oxide based catalyst by spray coating
- 92** Structural and electrochemical investigation of Pt films produced by PLD
- 94** Extreme ultraviolet lithography for the fabrication of nanoscale Pt model catalysts
- 97 THE ELECTROCHEMISTRY LABORATORY - FACTS & NUMBERS**
- 98** Structure 2013
- 99** ECL-Personnel 2013
- 100** Dissertations 2013
- 101** Exchange students, diploma theses, summer students, guest scientists
- 103** Seminar, invited speakers
- 104** Awards
- 105** Conferences – Symposia
- 106** Review activities of the laboratory
- 107** Industrial partners
- 109** Documentation



2013 was a very successful but also challenging year for PSI's Electrochemistry Laboratory. Last year significant efforts have been centered around setting up large scale proposals within energy research in Switzerland. In the Electrochemistry Laboratory we have coordinated the activities of more than 20 academic research partners

within the application for a Swiss Competence Center of Energy Research (SCCER) in the field of energy storage. The proposal was finally granted in fall 2013. Since the beginning of 2014, PSI's General Energy Department and its Electrochemistry Laboratory are proudly hosting and heading the new *SCCER Heat & Electricity Storage: Materials, Systems and Modeling*, a three-year multi-disciplinary and inter-institutional nationwide virtual competence center working on innovative pathways for the grand challenge of energy storage in an energy landscape dominated by renewable energies. In addition to this, researchers from the Electrochemistry Laboratory are leading a work package within another newly established center, SCCER Mobility, working on innovative, novel designs for polymer electrolyte fuel cells for automotive applications. This big success in acquisition of large scale projects, however, also brings responsibilities and challenges for the Laboratory with respect to integration of many new employees.

In retrospective, 2013 was also specifically successful for five of our PhD students with the final exam of their dissertation to acquire the doctoral degree. Here, we want to congratulate again and wish all the best for their future life after PSI. These PhD students together with all other researchers in the Electrochemistry Laboratory contributed continually and successfully to the 46 peer reviewed publications and book chapters published in 2013 demonstrating our strong contribution to the field of electrochemical energy conversion and storage. Highlights from our work are summarized in 43 contributions to this report displaying the wide spectrum of scientific work from fundamental electrochemistry and materials science, electrocatalysis, development and application of advanced *in situ* diagnostic tools, up to the successful engineering on the system level.

Our PSI Electrochemistry Symposium, held on April 24, 2013, has established itself as an international event and was attended by more than 120 registered participants. In 2013, the Symposium was entitled *Insights from the inside: Imaging Electrochemical Systems* and focused on different imaging techniques in order to obtain *in situ* information on electrochemical systems. We again have been able to invite highly recognized scientists talking about their specialities:

W. Schuhmann (University of Bochum), O. Magnussen (University of Kiel), R. Kostecki (Lawrence Berkeley National Laboratory), P. Boillat (Paul Scherrer Institut), K. Mayrhofer (Max-Planck-Institut für Eisenforschung Düsseldorf), and F.N. Büchi (Paul Scherrer Institut) all shared their insights on length scales from atomic to millimeter resolutions providing fascinating images of electrodes, catalysts and cells. In 2014 we will celebrate already the 30th Electrochemistry Symposium (originally implemented in 1987 by O. Haas) to be held on May 7 entitled *Oxygen: Airborne Energy Conversion and Storage*.

In summary, PSI's Electrochemistry Laboratory and all its members created a very successful year 2013 and demonstrated to be at the pulse of impacting research and development within electrochemical energy storage and conversion, a field whose importance is still about to grow within the next years.

Thomas J. Schmidt

THE ELECTROCHEMISTRY LABORATORY AT A GLANCE

Our Mission

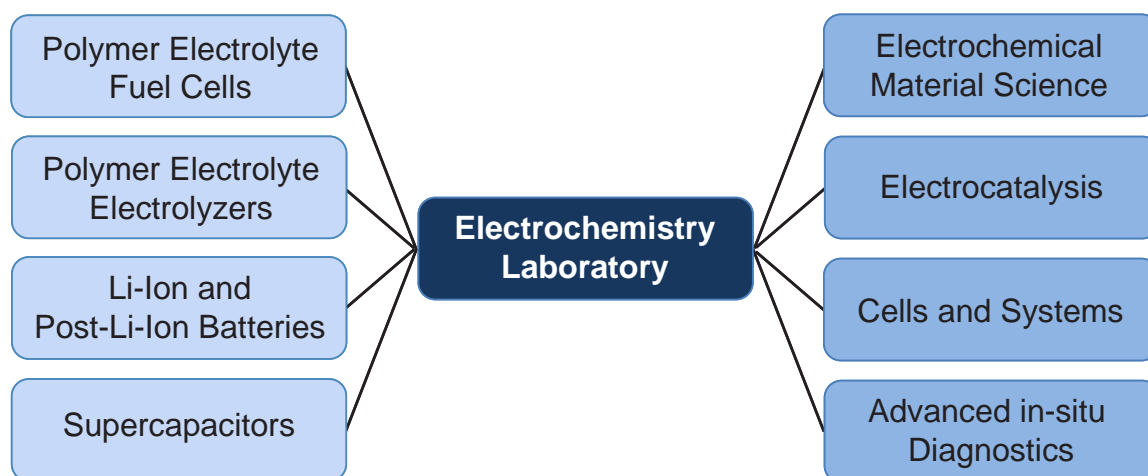
Advancement of electrochemical energy storage and conversion by

- **developing novel electrochemical materials, cells and devices**
- **providing insights into electrochemical materials, cells and device properties**

PSI's Electrochemistry Laboratory is Switzerland's largest Center for Electrochemical Research with around 60 employees. Our mission is to advance the scientific and technological understanding of electrochemical energy storage and conversion specifically in the context of a sustainable energy system, in which renewable energy is required to be stored in batteries or chemicals as e.g., hydrogen and (re-)converted into electricity. Our applied fundamental R & D, hence, is focused on devices like batteries - specifically Li- and Na-based systems -, supercapacitors, polymer electrolyte fuel cells and electrolyzers, respectively.

As a research institute's laboratory we are bridging the gap between fundamental science and applied engineering by answering both academically as well as industrially relevant questions. For all outlined devices we not only develop fundamental understanding of materials on atomic and molecular level (electrochemical materials sciences and electrocatalysis), but also on the applied development of technical cells and devices, e.g., fuel cell systems.

On all technical complexity levels, we are developing and utilizing advanced *in situ* diagnostic tools to gain insights on properties and processes from the nanometer to the centimeter scale, respectively, often making use of PSI's unique large scale facilities.



Electrochemical Energy Storage

The vision of the Electrochemical Energy Storage Section is the development of the best energy storage system.

We work on rechargeable batteries, mainly lithium and sodium based. The scientific goal is a profound understanding of electrochemical processes in complex nonaqueous systems. In particular, of utmost scientific interest are the numerous interactions of all components of electrochemical energy storage systems (batteries, supercapacitors, and hybrids) determining the safety and life time of such systems.



Multi-channel battery testing facilities.

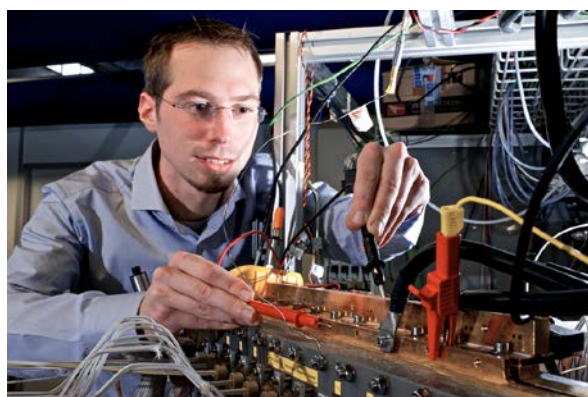
The work equally considers the synthesis of novel materials for electrochemical energy storage and the modification of known materials (e.g., carbon), and material characterization, keeping in mind the entire span from basic science to industrial applications. To answer the scientific questions, we develop various sophisticated *in situ* methods for use in the field of nonaqueous solid-state electrochemistry and investigate the physical and electrochemical properties of insertion materials and electrochemical interfaces *in situ*. Also, we do electrochemical engineering work on three-dimensional electrodes and characterize industrial batteries and battery systems.

Electrochemical Energy Conversion

The Electrochemical Energy Conversion Section is focused on the development and in-depth understanding of materials, processes and devices for the conversion of renewable energy into electricity or chemical energy carriers. Especially in the context of a sustainable energy system utilizing hydrogen as an energy carrier and its electrochemical energy conversion is of particular importance.

In this topical context our goal is the in-depth understanding of technologies like Polymer Electrolyte Fuel Cells (PEFC), Polymer Electrolyte Electrolyzer Cells (PEEC) for water electrolysis and processes like the co-electrolysis of CO₂ and water, respectively. In addition, materials are being developed for small-scale redox flow cells.

The R&D strategy involves activities on four pathways: *i*) system, stack and cell engineering; *ii*) membrane development based on PSI's own radiation-grafting technology and the development of cell components; *iii*) research in electrocatalysis and the reaction kinetics of the important reactions (e.g., the oxygen electrode reactions) for improved understanding of intrinsically limiting factors; and *iv*) the development and application of advanced *in situ* diagnostic tools on stack, cell and component levels including analyses of the electrode-electrolyte interface.



Characterization of a Polymer Electrolyte Fuel Cell with locally resolved analytical tools.

SCIENTIFIC ACHIEVEMENTS 2013

FUEL CELLS

SYSTEMS & DIAGNOSTICS

Hydrogen fuel cell based range extender for electric passenger car

J. Bernard¹, U. Hannesen¹, D. Corson¹, R. Gashi¹, M. Hofer, C. Peter, S. Reinauer¹, E. Saade¹, D. Schmid¹, T.J. Schmidt, A. Closset¹, F.N. Büchi

phone: +41 56 310 2541, e-mail: felix.buechi@psi.ch

A short driving range and long charging times are the main drawbacks of today's battery electric vehicles. The limited driving range is a consequence of the state of the art energy density of the battery technology.

A solution for extending the range is the addition of a second energy storage based on the high energy density of a chemical fuel. In commercial vehicles, this additional energy storage is based on gasoline (Chevrolet Volt, BMW i3) where a combustion engine drives a generator. Also hydrogen is a chemical fuel with high energy density. When hydrogen is converted to electricity with a fuel cell, then the range of battery electric cars can be extended in purely electric driving mode.

Vehicle

A Fiat 500 converted to a battery electric vehicle by Kamoo (Kamoo AG, Switzerland) has been used as platform and a hydrogen tank and fuel cell range extender (in front motor compartment, see Figure 1) were integrated. Table 1 lists the relevant properties of the vehicle with and without hydrogen fuel cell range extender.



Figure 1. Top: Fiat 500 electric; bottom: integration of fuel cell system in front motor compartment.

Driving Data

Data from public road driving is shown in Figure 2. Data was recorded during a 5.8 h drive over 425 km. The average speed was 72.7 km/h and the top speed 110 km/h. At the end of this drive test the battery and the hydrogen tank were emptied.

Fiat 500 electric	
Weight (incl. battery)	1150 kg
Battery type	Li Ion
Battery capacity	31 kWh
Range with battery	ca. 200 km
Weight (incl. battery & range extender)	1300 kg
Fuel cell system type	PEFC
Fuel cell system power	10 kW
Capacity hydrogen tank	1.7 kg
Range with range extender	350 - 400 km

Table 1. Properties of Fiat 500 battery electric vehicle with and without hydrogen fuel cell range extender.

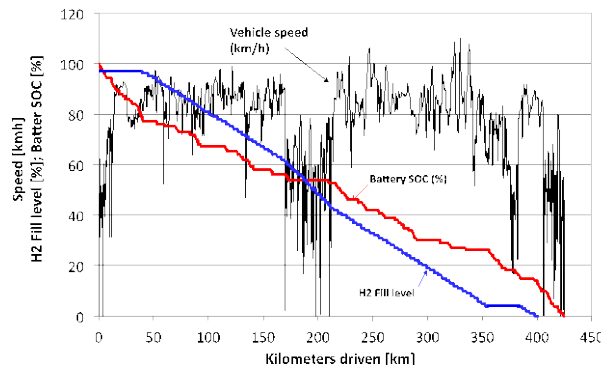


Figure 2. Driving data: speed, state of charge of battery and hydrogen tank pressure as function of distance.

Conclusion

The addition of a hydrogen fuel cell range extender has increased the range of the battery electric vehicle by about a factor of 2. Further more the hydrogen tank can be refilled in few minutes, eliminating long battery charging if required for extending the driving range.

Acknowledgment

The vehicle has been engineered by Belenos Clean Power (BCP), the hydrogen fuel cell development is a joint project between PSI and BCP.

¹ Belenos Clean Power Holding AG, Biel/Bienne

On the durability of H₂/O₂ polymer electrolyte fuel cells

F.N. Büchi, M. Hofer, C. Peter, U. Hannesen¹, J. Bernard¹, A. Closset¹, T.J. Schmidt

phone: +41 56 310 2541, e-mail: felix.buechi@psi.ch

Longevity is one of the major shortcomings of polymer electrolyte fuel cell technology (PEFC) for the use in many targeted applications, though durability goals vary significantly for the different utilizations. From few hundred hours for uninterruptible power supplies (UPS), around 5000 h for passenger cars to more than 40'000 hours in combined heat and power applications are required.

Durability is strongly dependent on the conditions in the application, i.e. dynamics of operation and frequency of start/stop events. If voltage degradation, and not catastrophic events such as membrane failure determine the durability of the fuel cell system, then the service life can be estimated from the voltage degradation rate. So when i.e. a cell voltage loss of 100 mV defines the end of life a durability of 5000 hours requires a voltage degradation rate in the order of 20 $\mu\text{V/h}$ or less.

When PEFC are operated with pure oxygen much less data is available than for the operation with air at the cathode. While the use of oxygen avoids degradation mechanism related to contamination, the high oxygen

partial pressure is of concern for the durability of the membrane ionomer and the catalyst support.

Therefore long-term experiments have been carried out to determine the degradation rates achieved with commercial membrane/electrode components.

Experimental

All experiments were carried out with H₂/O₂ in cells with approx. 200 cm² active area and were obtained in sub-stacks of 3 to 6 cells at a stack temperature of 75 °C and gas pressures of 2.5 bar(abs). In flow through experiments, where the off-gas is lost, the gases were humidified to a dew point of 60 °C. In the experiments with system configuration, the gas utilization was close to 100% and the humidification was relying on the humidity of the recirculated gases that are mixed with the fresh dry gasses.

Two similar cyclic current protocols with 3 current density levels (0.17 – 0.34 – 0.84 and 0.34 – 0.68 – 1.68 A/cm²) and a duration of 70 s for one cycle were used.

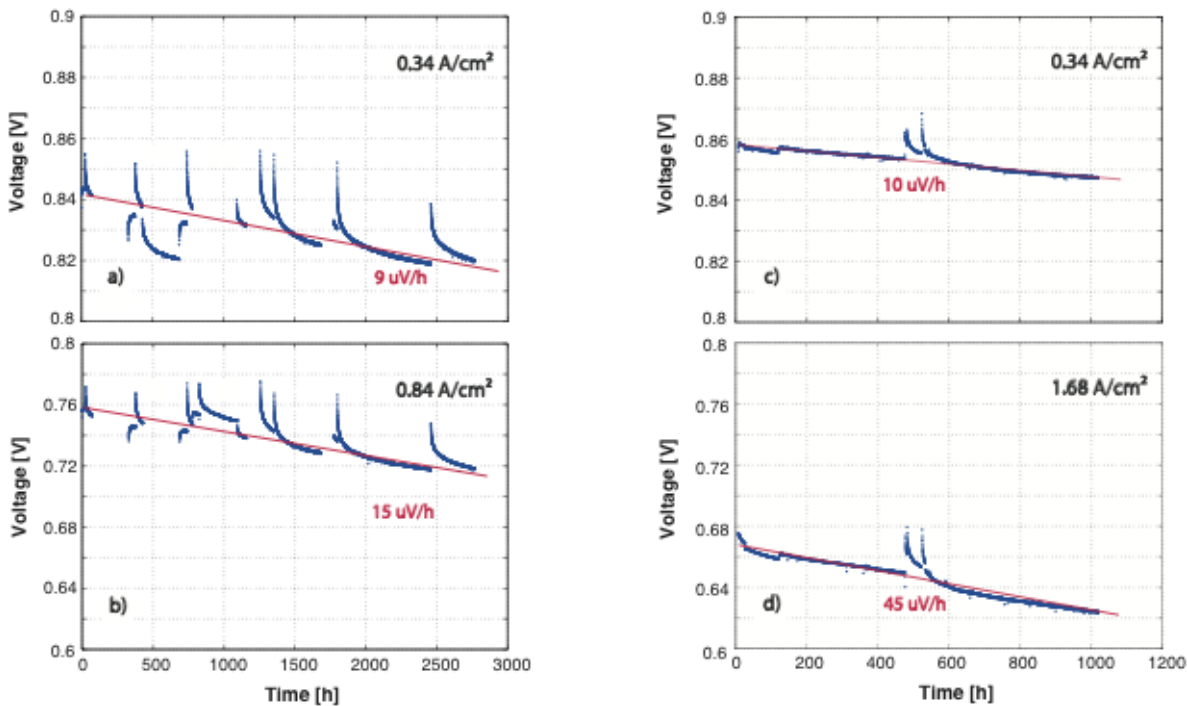


Figure 1. Cell voltage degradation rates (average voltage from 3-cell sub-stacks) measured in flow through experiments at 75 °C, gas pressures of 2.5 bar, stoichiometries of 1.3/1.5 and dew points of 60°C; a,b) for 0.17-0.34-0.84 A/cm² cycle; c,d) for 0.34-0.68-1.68 A/cm² cycle.

¹ Belenos Clean Power Holding AG, Biel/Bienne

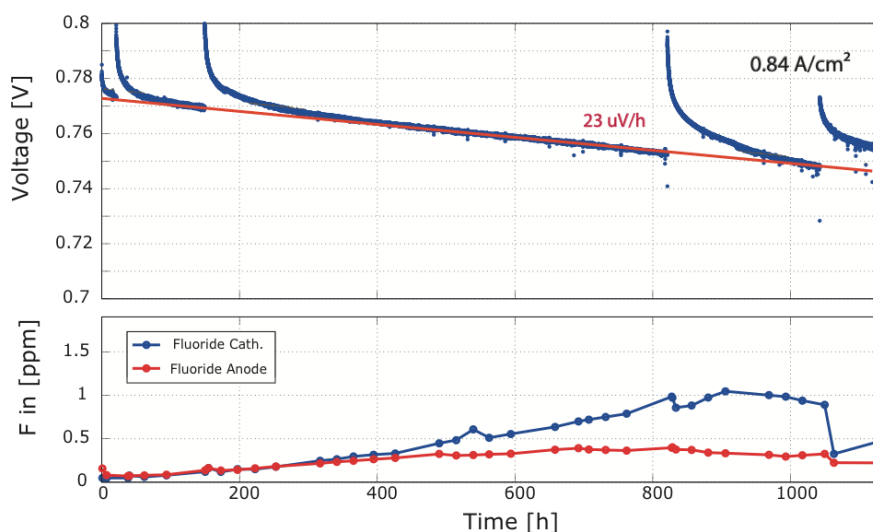


Figure 2. Top: cell voltage degradation (average voltage from 6-cell sub-stacks) at 0.84 A/cm^2 measured in system set-up (recirculated gases) at $75 \text{ }^\circ\text{C}$, gas pressures of 2.5 bar; dew points uncontrolled (measurement shows $56\text{-}58 \text{ }^\circ\text{C}$); bottom: fluoride concentrations in product water at anode and cathode side.

Results

The degradation rate for testing of sub-stacks with a 3-level dynamic current profile (70s per cycle) in flow-through configuration is shown in Figure 1. The cell voltage at the indicated current density at the end of each cycle is plotted as function of operating time. The operation was interrupted at certain intervals, the voltage response can therefore be separated into two distinct phases. At the beginning of a phase of operation with a duration of few hundreds of hours, a steep descent of the voltage is observed during the first 10 to 20 hours, the voltage loss then levels out to much lower degradation rates.

The steep initial degradation is reversible, this cell voltage increase and steep decrease is observed at each restart after a shut down. The slow degradation, observed however is irreversible. For the protocol with the low current levels (between 0.17 and 0.84 A/cm^2 , see Fig. 1 a&b) irreversible degradation rates between 9 and $15 \text{ } \mu\text{V/h}$ are observed between lowest (not shown) and highest current density.

If the degradation would be purely ohmic, then the degradation rate should be proportional to the current density. If, on the other hand degradation is purely electro-catalytic it should be independent of current density. The observed degradation is less than proportional with respect to current density, but higher than unity so the degradation rate is a mix of effects which cannot be unravelled from the voltage data at a single current density.

When the current cycling protocol with higher current densities (all levels are twice the low current protocol) then the degradation rates observed in Figure 1 c&d are observed. The data at 0.34 A/cm^2 indicates that the overall degradation is similar with both protocols, as a similar rate of about $10 \text{ } \mu\text{V/h}$ is observed at the same current density. However the rate at 1.68 A/cm^2 is

significantly higher, indicating that ohmic degradation becomes more important at high current densities.

Figure 2 shows data from a 6-cell stack, operated in system mode. In this case system mode means that the reactant gases are recirculated and the excess flow is fed back to the stack. The resulting gas utilization is about 99 % for hydrogen and 95% for oxygen. This mode of operation is more critical for accumulation of impurities and contaminants in the stack due to recirculation of gases and humidity.

The observed average, irreversible degradation rate at for the first 1000 hours at 0.84 A/cm^2 is $23 \text{ } \mu\text{V/h}$, about 30% higher than in flow-through mode.

The lower plot in Figure 2 shows the fluoride emission from the stack. A steady increase from about 0.1 to 1 ppm at the cathode and 0.3 ppm at the anode is observed. After 1000h ca. 2 % of the fluorine inventory of the cells is lost.

Conclusions

The durability investigation shows that when using H_2/O_2 and a dynamic current protocol, similar degradation rates are observed in flow-through and system set-up. Current densities of up to 1.7 A/cm^2 have no significant influence on the durability. The voltage degradation in the order of $20 \text{ } \mu\text{V/h}$ allows for an estimation of a maximum durability of about 5000 h. However fluoride emission rate indicates that service life may be terminated earlier due to membrane failure because a substantial part of the fluorine inventory (and thus membrane mass) is lost.

Acknowledgement

Technical support by T. Gloor and M. Ammann is gratefully acknowledged.

Reproducibility of performance and water distribution of small scale differential fuel cells

J. Biesdorf, P. Oberholzer, T.J. Schmidt, P. Boillat

phone: +41 56 310 5727, e-mail: johannes.biesdorf@psi.ch

In the last decade, considerable improvements have been achieved regarding the cost and durability of Polymer electrolyte fuel cells (PEFC). However, before their commercialization, reliable methods have to be developed to fully understand the ongoing processes. In order to understand these effects at a local scale, studies have to be performed either with a segmented cell or by emulating a portion of the whole area by a small scale cell, feeding the reactant gases with the same velocities as in the full-size cell (differential fuel cell). With strongly reduced active areas (e.g. 1 cm^2), irreproducibilities resulting from material manufacturing and cell assembly procedures might translate into substantial variations of its performance. Using our recently developed multicell setup, up to six differential PEFCs can be operated simultaneously at identical operating conditions [1]. Hence, uncertainties resulting from operating parameters or cell operation history can be neglected and irreproducibilities are mainly ascribed to cell-to-cell differences. To analyse the source of these differences, advanced methods including pulsed gas analysis [2], membrane conductivity measurement and high-resolution neutron radiography [3] were applied to compare the performance differences of 3 cells of identical design.

Experimental

Cell design - All experiments were performed with an in-house built multicell setup, allowing the simultaneous operation of up to six differential fuel cells [1]. The fuel cells used for this experiment had an active area of 1 cm^2 . The flow fields were built of 5 parallel channels (0.55mm depth and 1mm width), machined into an aluminium block coated with a thin layer of gold. A catalyst coated membrane (CCM) of type Primea 5710 (Gore Ltd., USA) was used. Pt-loadings were 0.1 mgPt/cm^2 on the anode side and 0.4 mgPt/cm^2 on the cathode side. A carbon paper gas diffusion layer (GDL) including a micro porous layer (MPL) of type Sigracet 24BC (SGL Carbon Group, Germany) having 5% wt. of PTFE was used on both anode and cathode sides. The compression rate was fixed to 20%.

Pulsed gas method – The pulsed gas method described in [2] was applied in our experiments. It consists in replacing the cathode gas with helox (21% Helium, 79% N_2) or pure oxygen. Based on the higher diffusivity of helium in N_2 (approx. factor 2-3) bulk mass transport losses can be suppressed. Consequently, the voltage difference between operation with air and helox is an indicator of the bulk mass transport losses. If the PEFC is operated under pure oxygen, the increased partial pressure of oxygen leads additionally to a suppression of the non-bulk diffusion (Knudsen and thin film diffusion) losses. Hence the difference between the voltage with oxygen and helox gives estimation about non-bulk diffusion losses, after correction of a 45 mV difference due to the increased Nernst voltage and kinetics under pure oxygen. In order to avoid artefacts resulting from dry out effects or changes of the catalyst coverage by oxygen-

ated species, the gases are supplied with short pulses (1s) during the continuous operation with air. Further details about the methodology can be found elsewhere [2]. An indicator of conductivity losses of the membrane is obtained by multiplying the high frequency resistance measured at 5 kHz with the total current of the PEFC.

Imaging setup – All experiments presented hereafter were performed at the ICON *beamline* of the SINQ at the Paul Scherrer Institute in order to obtain spatial information about the water distribution inside the PEFC. Further details about the imaging setup are published in ref [4].

Experimental protocol – The results hereafter are based on a so called RH-Map [5]. A RH-Map consists of asymmetric variations of the anode and cathode humidification (see humidification profiles in Figure 1). Every operation point was held 15min, as the equilibrium of the water distribution is obtained after 3 minutes. The PEFCs were operated at a constant current density of 1 A/cm^2 . The cell temperature was set to 70°C at a pressure of $2 \text{ bar}_{\text{abs}}$ on both sides. The cell flows were 0.4 NI/min on the anode and 1 NI/min on the cathode side, translating into stoichiometries of approximately 60 on both sides. The measurement protocol is shown in the humidification profiles in Figure 1.

Results

Figure 1 shows the performance of three identical PEFC at various humidifications of the anode and cathode gas stream. The uncorrected raw voltage of the fuel cells is illustrated in fig. 1d. It can be seen, that the absolute voltage difference between the three different cells accounts for less than 20mV at all operation points. Only a small portion (less than 10mV) can be attributed to differences of catalyst activity, which are reflected in the voltage during oxygen operation corrected for ohmic losses. At low humidifications of the anode gas stream, the raw voltage is highly reduced. This can be attributed to a reduced hydration state of the membrane, leading to highly increased ohmic losses (Figure 1e). As the operating conditions (humidification, temperature, pressure) are identical for all three cells inside our experimental setup, the indicator of ohmic losses (see fig. 1c) shows negligible deviations. However, at anode humidifications below 40%RH, unstable operation conditions lead to small deviations of the ohmic loss indicator between the three cells. Non-bulk diffusion losses (fig. 1c) have been identified to occur mostly inside the ionomer of the electrode on the cathode side [6]. As the CCMs have been cut-off a single foil, high reproducibility is gained.

In contrast to non-bulk losses, the indicator of bulk diffusion shows moderate variations between the three cells. A possible reason could be an inhomogeneous distribution of the porous structure, even if all three cells have been build out of a single sheet of GDL. Another reason for the differences could be slightly inhomogeneous compression rates of the PEFC assembly. Even if the

cell design provides a precise compression of the entire cell, incorrect positioning of the GDL inside the PTFE sealing lead to locations without GDL and locations with crushed GDL. Hence, for highly reproducible results, a precise interface between sealing and GDL is highly demanded.

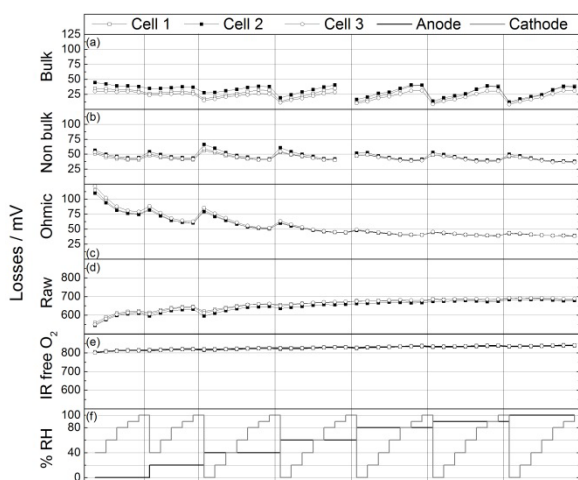


Figure 1. Indicators of the different loss mechanisms obtained with the pulsed gas analysis for three identical PEFC under various humidifications.

Fig. 2 shows the water distribution inside the different layers of the cell during the same experiment. The water content in the membrane region (fig. 2a) is strongly dependent on the humidification of the anode gas stream. As expected, a good correlation is obtained with the trend of the ohmic losses presented in fig. 1a. Inside the gas diffusion layers (Figure 2a & 2b), the amount of water is highly dependent on the humidification level of the fed gases. As a dynamic equilibrium between humidification and product water is reached after approx. 3 min, repeatable water distributions are obtained among the three cells. A good agreement is obtained with the indicator of bulk diffusion losses (fig. 1a): higher water content in the cathode GDL results in increased diffusion losses. Figures 2d and 2e depict the water accumulation inside the anode and cathode flow field. The water accumulated inside the flow channels is established as an equilibrium between water production, drag-out mechanisms of droplets by the gas stream in liquid phase and water uptake of undersaturated gas in the gas phase. Although the water transport includes stochastic processes, the amount of water is almost reproducible from cell to cell.

In summary, highly reproducible results in the measurement of performance and water distribution in differential fuel cells have been obtained. Using the pulsed gas method combined with neutron radiography, remaining deviations could be attributed to differences in bulk mass transport losses. Possible reasons for these differences are variations in the local characteristics of gas diffusion layer, as well as the increased importance of border effects in such small scale cells.

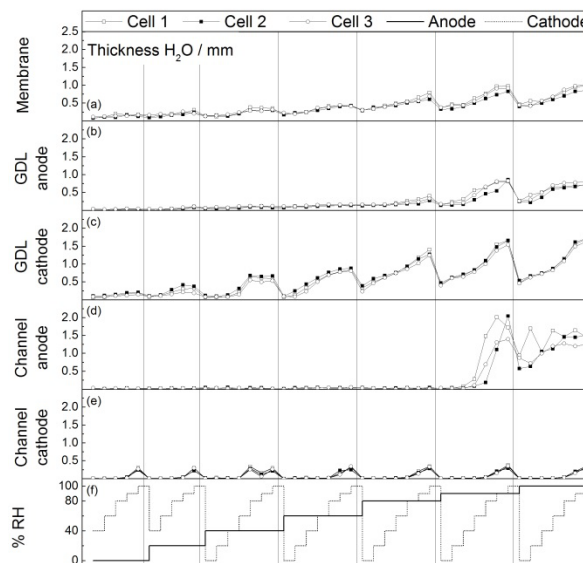


Figure 2. Water distribution inside the different layers of three identical PEFC under various humidifications.

References

- [1] P. Oberholzer, P. Boillat, R. Siegrist, A. Kastner, E.H. Lehmann, G.G. Scherer, A. Wokaun, *Electrochem. Commun.* **20**, 67-70 (2012).
- [2] P. Boillat, P. Oberholzer, A. Kaestner, R. Siegrist, E.H. Lehmann, G.G. Scherer, A. Wokaun, *J. Electrochem. Soc.* **159**, F210-F218 (2012).
- [3] P. Boillat, D. Kramer, B.C. Seyfang, G. Frei, E. Lehmann, G.G. Scherrer, A. Wokaun, Y. Ichikawa, Y. Tasaki, K. Shinohara, *Electrochem. Commun.* **10**, 546-550 (2008).
- [4] P. Oberholzer, P. Boillat, A. Kaestner, E.H. Lehmann, G.G. Scherer, T.J. Schmidt, A. Wokaun, *J. Electrochem. Soc.* **160**, F659-F669 (2013).
- [5] P. Oberholzer, P. Boillat, *J. Electrochem. Soc.* **161**, F192-F198 (2014).
- [6] P. Oberholzer, P. Boillat, *J. Phys. Chem. C* **117**, F139-F152 (2013).

Accuracy of water quantification in fuel cells by neutron imaging

P. Boillat, J. Biesdorf, P. Oberholzer

phone: +41 56 310 2743, e-mail: pierre.boillat@psi.ch

Neutron imaging has been extensively used within the last 10 years to analyse the water distribution in operating polymer electrolyte fuel cells (PEFCs). Quantitative results are often reported, using the Lambert-Beer equation relating the neutron attenuation with the water thickness. For certain applications such as the use of neutron imaging data for the validation of modelling studies, a precise knowledge of the quantification accuracy is required, to know whether observed deviations originate from measurement uncertainties. In this work, we propose a new method for the assessment of quantification accuracy based on the production of a defined amount of water.

Experimental

In usual fuel cell operation, the amount of water accumulating in the cell is the result of a complex equilibrium between water production and removal, the latter including removal by evaporation and in the form of droplets removed by the gas flow. Using a special mode of operation called *double dead-end* (Figure 1), water is neither brought to nor removed from the cell. The water accumulating inside the cell is thus easily calculated assuming a nearly 100% faradaic efficiency of the electrochemical reaction.

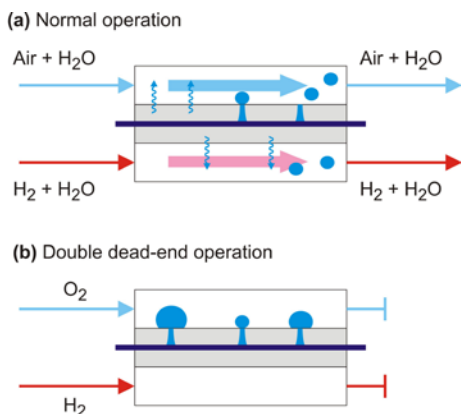


Figure 1. Illustration of normal and double dead-end operation.

The measurement protocol for each point was the following. First, remaining water from previous experiments was removed by flowing dry gases. Then, slightly humidified gases (50% RH) were circulated to humidify the membrane. Finally, the cell was placed in double dead end mode by closing the outlets and keeping a constant inlet pressure, and the current corresponding to the desired water quantity (1, 2, 4 or 8 mg per cell) was drawn during 1 minute. The produced water was measured by neutron imaging by comparing the imaging corresponding to the five minutes before and after the generation steps. All measurements were realized simultaneously on 5 small scale cells mounted in the recently developed multi-cell setup [1]. Each of the 4 quantities defined previously was measured twice. Two different imaging configurations were used: the *in plane* configuration (beam axis parallel to the membrane) which allows the distinction of the different cell layers, and the *through plane* configuration (beam axis perpendicular to

the membrane) allowing the observation of the water distribution over the surface of the membrane. For each setup, the background contribution was carefully corrected, and the attenuation coefficient of neutron was calibrated using two cylindrical water scales (diameters of 0.7 mm and 1.5 mm). All measurements were performed at the ICON beam line [2] at PSI.

Results

The comparison of the known water quantity (the water which is produced by the electrochemical reaction) with the water quantity measured using neutron imaging is presented in Figure 2.

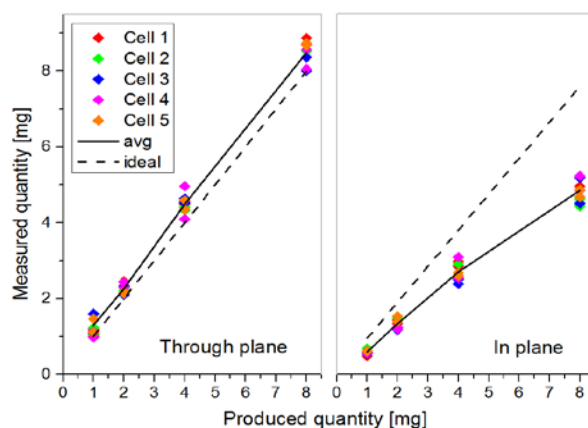


Figure 2. Comparison of produced and measured quantity for the through plane (left) and the in plane (right) setups.

As can be observed, measurements with the through plane setup match well the produced water quantity. With the in plane setup, we observe that the water quantity is systematically underestimated. The reason for this discrepancy is yet to be investigated. Nevertheless, the repeatability including cell-to-cell variations and experiment-to-experiment variations is reasonably good. In consequence, the technique proposed here can be used to calibrate an imaging setup. The proposed *double dead end calibration* method does not require any specific fuel cell hardware, and the fuel cell test station requires minimal adaptations. It is estimated that, after optimization of the test procedure, the calibration can be realized within 1-2 hours. Thus, it is possible to include it as a part of each measurement campaign.

Acknowledgement

This work was carried out with the support of the European Community (European Research Infrastructure H2FC, funded under the FP7 specific programme Capacities, Grant Agreement Number 284522).

References

- [1] P. Oberholzer, P. Boillat, R. Siegrist, A. Kaestner, E.H. Lehmann, G.G. Scherer, A. Wokaun, *Electrochem. Commun.* **20**, 67-70 (2012).
- [2] A.P. Kaestner, S. Hartmann, G. Kühne, G. Frei, C. Grünzweig, L. Josic, F. Schmid, E.H. Lehmann, *Nucl. Instr. Meth. A* **659**, 387-393 (2011).

Determination of phosphoric acid concentrations in HT-PEFC components by X-ray tomographic microscopy

S.H. Eberhardt, F.N. Büchi, T.J. Schmidt

phone: +41 56 310 2541, e-mail: sebastian.eberhardt@psi.ch

High-temperature polymer electrolyte fuel cells (HT-PEFC) use phosphoric acid (PA) doped polybenzimidazole membranes as the proton conducting electrolyte which allows for the increased operating temperature of 160 – 190°C. This renders HT-PEFC especially suitable for combined heat and power applications where reformat based anode feed gases can be used without expensive gas clean-up due to the increased CO oxidation kinetics at the elevated temperatures. Among other degradation modes, e.g. carbon corrosion and pinhole formation, the loss of phosphoric acid plays a vital role in the durability of HT-PEFCs [1]. Up to now, no clear understanding of the degradation mechanisms associated with a loss of phosphoric acid electrolyte has been accomplished. Although first *in situ* studies by X-ray radiography on HT-PEFCs have been performed [2], the simultaneous influence of volume and concentration change of PA on the X-ray attenuation makes the analysis of the results challenging. By using X-ray tomographic microscopy (XTM) the additional 3D information is expected to help in the localization and quantification of the acid electrolyte within the gas diffusion layer (GDL) and catalyst layer. Due to the formation of complex phase compositions of fuel cell components and PA, e.g. micro- and macropores of the GDL, a calibration method to correlate grey scale value in the images with PA concentration and mass has been developed and is presented here.

Method and Experimental

For all experiments BASF Celtec® membrane electrode assemblies (MEA) were used. The MEA consists of a PBI membrane doped with approximately 20 mg/cm² of phosphoric acid and a carbon paper (SGL) gas diffusion electrode (Pt/Vulcan XC-72, 1mg_{Pt}cm⁻² on anode and cathode side respectively). In order to record a calibration curve, the MEAs were doped with 40, 60 and 85 wt% H₃PO₄ and assembled in a specially designed fuel cell with an active area of 0.2 cm² [3]. Calibration data is evaluated for the membrane, GDL and catalyst layer independently due to the formation of single (PA), binary (PA+C) and ternary phases (PA+C+Pt).

XTM scans were recorded at the TOMCAT beamline at the Swiss Light Source (SLS) in phase contrast mode [4] at a beam energy of 20 keV. All tomograms were recorded on non-operated fuel cells at ambient temperature. The combination of a 3 fold magnification objective and a pco.edge camera system resulted in a pixel edge length of 2.14 µm. Image acquisition was performed with 2001 projections at a sample rotation of 180°. Exposure time per projection was 15 ms, leading to a total synchrotron radiation exposure of 30 s for each tomogram. The distance to the detector was adjusted to 25 mm for phase retrieval.

A PA free data set was obtained by flushing the cell with 15 ml of deionized water, heating to 100°C and purging with dry nitrogen for 5 minutes. Absorption contrast was subsequently used for reconstruction. In this way, the macro-porosity of the GDL is retrieved including high

frequency components of the images, which results in higher segmentation accuracy.

Results

A vertical slice of the MEA is shown in Figure 1. Upon initial compression of the MEA during the hot pressing process, the acid gets pushed out of the membrane through the microporous layer (MPL) and the GDL. Cracks within the catalyst layer and MPL form the main paths for PA from the membrane to the adjoining components (MPL, GDL and flow field). This observation becomes clearly visible in the top part of Figure 1, where the absence of highly attenuating Platinum in the catalyst layer makes the cracks in the MPL clearly visible.

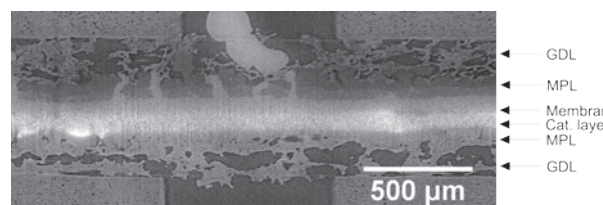


Figure 1. Vertical slice of the MEA. The top “catalyst layer” is Pt free and consist of Vulcan XC-72 only. White and light grey shaded phase is PA or a binary mixture of PA and carbon.

In Figure 2, a PA free GDL is depicted, highlighting the presence of large amounts of microporous binder within the macroporous carbon fiber structure of the GDL.

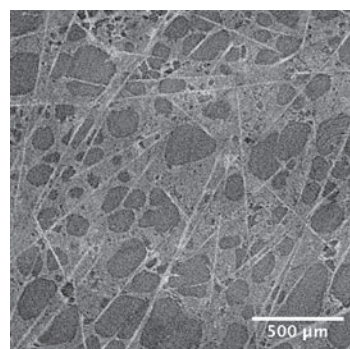


Figure 2. Horizontal slice of the dry GDL structure with carbon fibers (white), microporous polymeric binder (grey) and void (black).

The possibility for PA to accumulate within the macropores as well as the micropores is further emphasised when comparing Figure 2 with Figure 3. It can be clearly seen that the macropores are partially filled with PA droplets. Additionally, in the dry sample binder and fibres have a significant difference in the greyscale value, while there is almost no difference visible in the PA wetted GDL between the two components. It is important to note, that the micropores of the binder cannot be segmented due to the geometric resolution limit of 2.14 µm. Therefore, the binder has to be considered a binary mixture of PA+C, where the resulting greyscale value is a function of PA pore saturation.

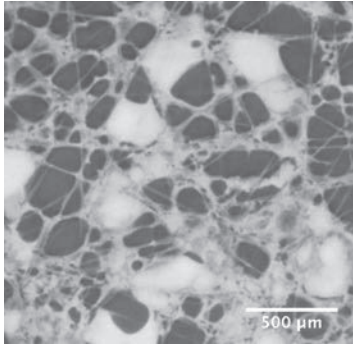


Figure 3. Horizontal slice of the PA wetted GDL structure with PA filled macropores (white), PA filled microporous binder (grey) and void (black).

The porosity of the PA free and PA wetted GDL is plotted in Figure 4 as function of the GDL thickness. Both datasets were segmented using a constant threshold after applying a 2D Gaussian blur to reduce noise. Due to insufficient contrast between carbon and phosphoric acid, the carbon and PA phase were separated from the void as a single phase. The porosity is a strong function of the thickness, due to varying fraction of binder with a maximum amount at 25 μm leading to a minimum porosity of 63 % for the dry sample. The average porosity was calculated to be 72%, not accounting for the pores in the binder. For the PA wetted sample the average porosity dropped to 52% (see Figure 4).

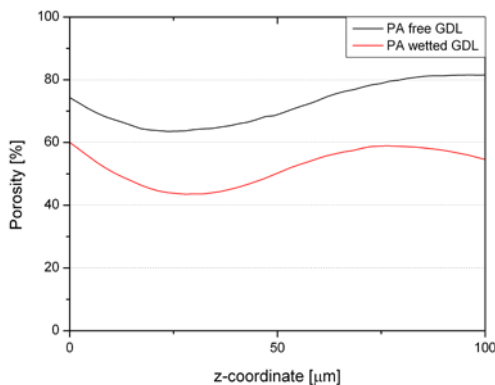


Figure 4. Porosity of the PA free and PA wetted GDL as a function of the z-coordinate (0 μm : flow field, 100 μm : GDL/MPL interface).

The calibration results (grey scale value vs. PA concentration) for the GDL, catalyst layer and membrane are depicted in Figure 5. The GDL results are plotted for the pure PA phase in the macropores and the PA+C phase of binder and acid separately. A linear relation for the single phase and a polynomial relation for the binary mixture were found. Using the calibration and porosity data, concentration and mass of PA in the GDL of a pristine MEA can be obtained.

A 0.2 cm^2 MEA sample was analyzed and the PA concentration was found to be 52 wt% with a mass of 0.24 mg within the first 77 μm of the GDL. These values were then compared to results where PA was leached from the GDL and analysed chemically. With 52 \pm 2.6 wt% these results are in good agreement with XTM. A mass of 0.79 \pm 0.04 mg was measured within a thickness of 261 μm . Assuming a constant relation of $\text{mg}_{\text{PA}}/\mu\text{m}$, a mass of 0.23 \pm 0.01 mg can be calculated

for the equivalent thickness of 77 μm , which is also in good agreement with the 0.24 mg measured by XTM

The catalyst layer is a ternary mixture of PA, carbon black and platinum. In case of a concentration change, the volume of PA will change, resulting in a varying PA loading of the catalyst layer, and hence a shift in the greyscale value. Consequently the determined concentration might not represent the actual concentration present within the catalyst layer. However, it is expected that a concentration increase or decrease can be visualized by a change in average pixel greyscale value independent of the volume change as long as the majority of voxels is completely filled with PA. Therefore, a location with high acid loading of the electrode should be chosen for evaluation, e.g. close to the membrane.

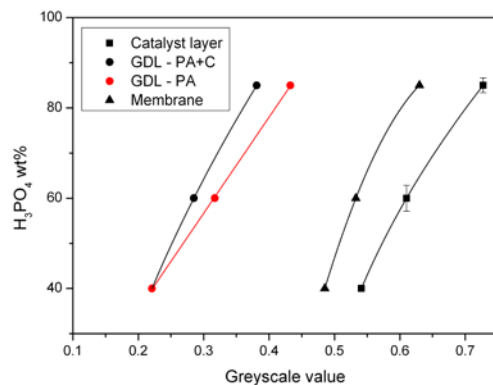


Figure 5. Calibration results for the GDL (macropores filled with PA (PA) and microporous binder filled with PA (PA+C)), catalyst layer and membrane. The straight lines indicate the parameter fitting with red for a linear fit and black for a polynomial fit.

Conclusion and outlook

The formation of mixtures of phosphoric acid and the fuel cell components makes the localization and quantification of PA within a HT-PEFC challenging. Therefore, it is necessary to establish a reference to compare greyscale values of the tomogram with greyscale values of known PA concentrations. A first successful calibration set for GDL, catalyst layer and membrane is presented and can further be used to evaluate PA mass and concentrations under different operating conditions in cells in operando.

Acknowledgment

Financial support by BASF is gratefully acknowledged.

References

- [1] T.J. Schmidt, "High-Temperature Polymer Electrolyte Fuel Cells: Durability Insights," F.N. Büchi, M. Inaba, and T.J. Schmidt (Eds.), Springer, NY, 199-221, (2009).
- [2] W. Maier, T. Arlt, K. Wippermann, C. Wannek, I. Manke, W. Lehnert, D. Stolten, J. Electrochem. Soc., **159**, F398-F404, (2012).
- [3] J. Roth, M. Zurbrugg, F.N. Büchi, PSI Electrochemistry Laboratory Annual Report 2012, 27-28, (2013).
- [4] D. Paganin, S.C. Mayo, T.E. Gureyev, P.R. Miller, S.W. Wilkins, J. Microsc., **206**, 33-40, (2002).

X-ray tomographic imaging of GDLs during pressure driven water imbibitions/drainages

A. Lamibrac, J. Roth, F. Marone, F.N. Büchi

phone: +41 56 310 5768, e-mail: adrien.lamibrac@psi.ch

Polymer electrolyte fuel cells convert hydrogen to electric power with potential high efficiency while releasing only water and heat. Although water is necessary for a good proton conductivity of the membrane, it can also accumulate as liquid in the gas diffusion layers (GDL) and limit the gas transport to the reaction sites. Efficient liquid water removal from the GDL is crucial to achieve high power densities. A balanced water management is therefore a key for high performance, durability and low cost.

To visualize the behavior of liquid water, X-ray tomographic microscopy (XTM) is used during pressure driven GDL imbibition/drainage experiments. XTM provides the advantage that water distribution can be resolved on the scale of the pores [1]. Thus, the link between local liquid saturation of the GDL, the capillary pressure and the material structure can be obtained [2, 3]. This will eventually provide the necessary structure dependent parameterizations required for model based material design.

As a first step towards this goal qualitative results of local saturation during imbibition and drainage are presented.

Experimental

X-ray imaging has been carried out at the TOMCAT beamline of the Swiss Light Source. The beam energy was set to 13.5 keV, exposure time to 15 ms (2001 projections) and the 2-4x microscope was used (pixel size of 2.2 μm). The GDL is imaged in a sample holder, clamped between a hydrophilic (bottom) and a hydrophobic (top) membrane (see insert in Figure 1) to ensure that water always remains confined between these two layers. The top of the sample holder is open to the atmosphere, while the water is fed from the bottom by a remotely controlled syringe pump (Figure 1). The liquid pressure is measured with a relative pressure sensor (accuracy ± 1 mbar). All experiments were made at ambient temperature with a GDL compression of about 20% (compression is applied using a high precision adjustment screw on top of the sample holder).

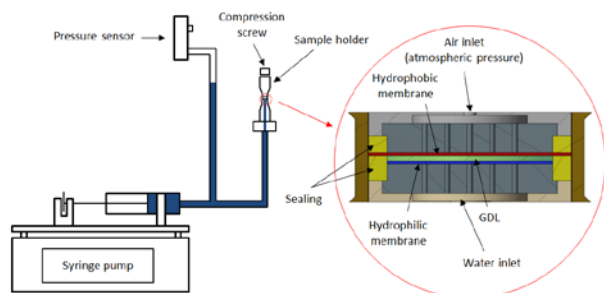


Figure 1. Experimental setup used for the GDL imbibition/drainage imaging.

Results

Figure 2 shows a comparison between two GDL materials (Toray TGP 060, 10wt.% PTFE and SGL 24 BA) taken at similar height (at 20% height of the total GDL thickness) in the GDLs at the same capillary pressures. The dry images on top emphasize the structural difference between the two materials. The void is shown in dark grey and fibres appear in light grey. Influence of the GDL structure on water transport is visible during imbibition (water in light grey), the saturation in the SGL sample increases more rapidly than in the Toray GDL. Similarly, decrease of the saturation during drainage does not occur at similar capillary pressures.

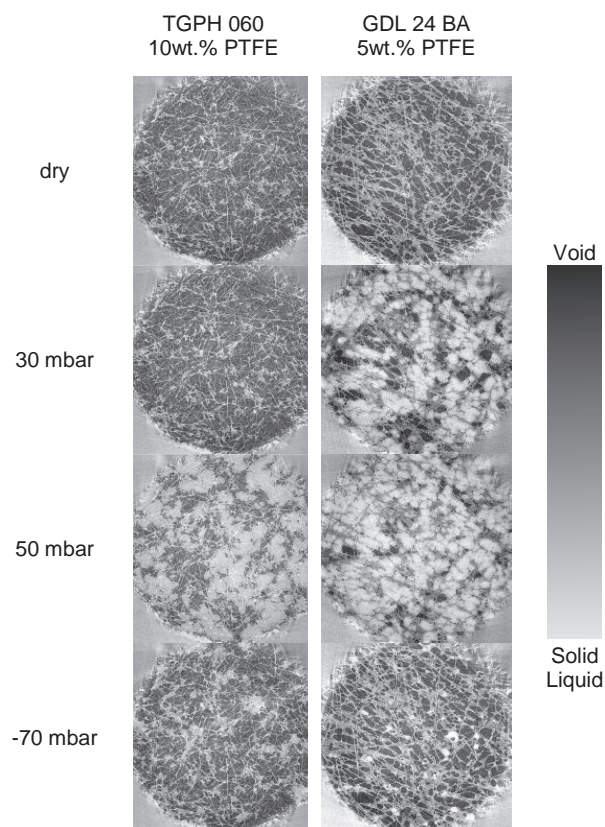


Figure 2. Left: Reconstructed in-plane slices of Toray TGP-H-060 with 10% PTFE. Right: SGL 24 BA (5% PTFE) during imbibition/drainage experiments. Top images: dry conditions. From top to bottom, capillary pressure set to 30 mbar, 50 mbar (imbibition) and -70 mbar (drainage).

The local saturation in the SGL 24 BA material at different heights and at constant capillary pressure is depicted in Figure 3. Qualitatively, the SGL 24 BC shows a significant through plane saturation gradient with high saturation close to the bottom (hydrophilic membrane) and lower saturation near the top (hydrophobic membrane).

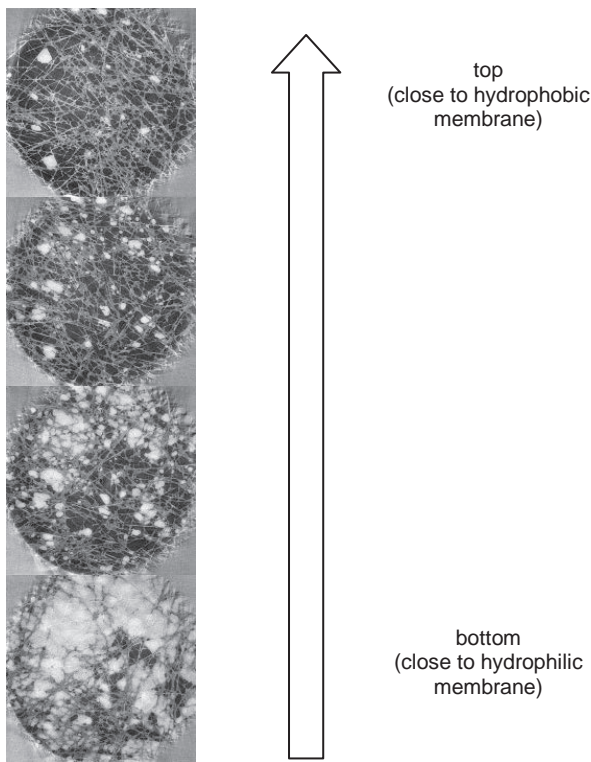


Figure 3. Reconstructed in-plane slices of SGL 24 BA represented through plane from a location close to the hydrophilic membrane (bottom) to a location close to the hydrophobic membrane (top). Capillary pressure: 22 mbar.

In Figure 4, reconstructed images taken at the same location and for two different capillary pressures are shown for three successive imbibition cycles of the same SGL 24 BA sample. Despite some differences, very similar paths seem to be used by liquid water to fill the sample. Part of the differences (yellow circles in Figure 4) observed between the first and the last imbibition could be attributed to hysteresis effects but also an irradiation effect cannot be completely excluded [4] since the sample was exposed to X-ray radiation for a total of 270s after the third imbibition cycle.

Conclusions

The qualitative analysis of the liquid saturation reveals that the structural difference between the Toray and SGL materials has a significant influence on the imbibition and drainage behaviour. In the GDL a saturation gradient is observed and only minor deviation in the liquid pattern is noticed upon repeated imbibition and drainage. This observation is in agreement with the state of the art understanding of the GDL materials and validates the experimental approach.

In future work segmentation of the images into carbon fibres, water and void will enable the quantification of the local liquid saturation as a function of the capillary pressure and the hysteresis effects. The link between structural properties and the capillary pressure relationship can be established by combining the quantitative results with structure based imbibition modelling.

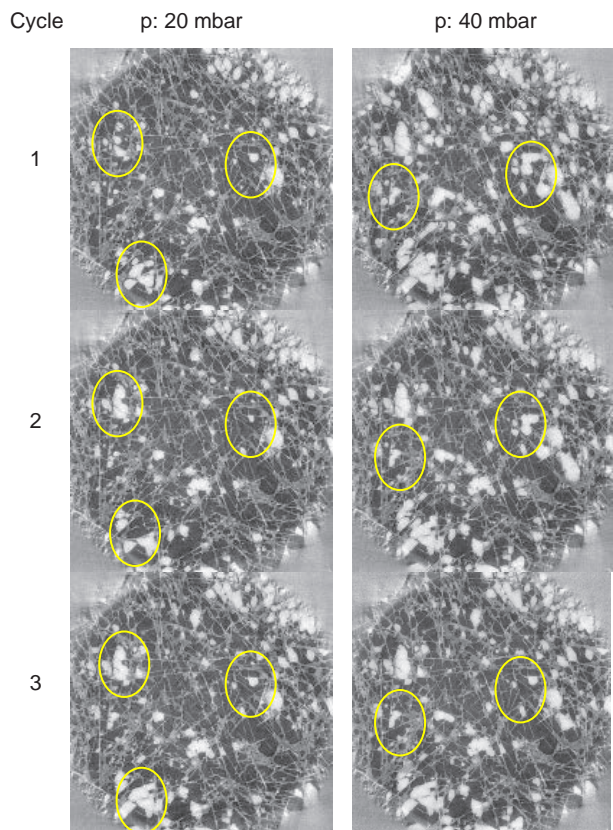


Figure 4. Reconstructed in-plane slices of SGL 24 BA located in the middle of the sample. Capillary pressure set to 20 mbar (right column) and 40 mbar (left column). From top to bottom: 1st, 2nd and 3rd imbibition. Yellow circles indicate qualitative differences.

Acknowledgement

Funding from the European JU-FCH project IMPALA and materials obtained from SGL are gratefully acknowledged.

References

- [1] J. Eller, T. Rosen, F. Marone, M. Stampanoni, A. Wokaun, F.N. Büchi, J. Electrochem. Soc. **158** (8), B963-B970 (2011).
- [2] F.N. Büchi, R. Flückiger, D. Tehlar, F. Marone, M. Stampanoni, ECS Trans. **16** (2), 587-592 (2008).
- [3] J.T. Gostick, H.P. Gunterman, B.W. Kienitz, J.S. Newman, A.A. MacDowell, A.Z. Weber, ECS Trans. **33** (1), 1407-1412 (2010).
- [4] J. Roth, J. Eller, F.N Büchi, J. Electrochem. Soc. **159** (8), F449-F455 (2012).

Limiting current phenomena in PEFC investigated with *in situ* XTM

J. Roth, A. Lamibrac, F. Marone, F.N.Büchi

phone: +41 56 310 5396, e-mail: joerg.roth@psi.ch

Two-phase mass transport phenomena in gas diffusion layers (GDL) for polymer electrolyte fuel cells are still not completely understood, but belong to the parameters with high potential for optimizing cell performance, cost and durability. The large number of boundary conditions present in operating fuel cell makes it difficult to study permeability and diffusivity of GDL under realistic two-phase conditions outside the operating cell.

Baker et al. [1-5] suggested and used limiting current experiments to access the diffusive properties directly under fuel cell operation. The limiting current, measured under different oxygen partial pressures enables to assess the parameters relevant for water induced transport losses. The conceptual idea of this experiment is to consume all oxygen available at the catalyst and derive the oxygen diffusion coefficient based on the electrical current produced at the smallest possible cell voltage. With increasing oxygen partial pressure, the limiting current increases, as well as the product water activity. Beyond a certain oxygen partial pressure, the water starts to condense and inflicts transport losses in the GDL.

In this work, the transport resistance determined by the limiting current method according to Baker et al. [1] is compared to the diffusive transport resistance numerically determined based on water distribution obtained by the in-situ X-ray tomographic microscopy (XTM).

Experimental

The limiting current experiment was done with a specialized fuel cell comprising a serpentine flow field and an active area of 0.18 cm², developed for XTM-imaging. As GDL Toray TGPB 060 carbon paper impregnated with 10wt.% PTFE (no MPL) was used in combination with a H200 Solvicore MEA. The cathode side was fed with different O₂ concentrations, while the anode side was supplied with 100% H₂ (based on dry gas). The feed gases were humidified with customized membrane humidifiers [6]. All the experimental conditions are summarized in Table 1.

Cell temperature	70 °C
Gas velocity (dry)	4.3 m/s
Gas relative humidity	70 %
Gas pressure	150 kPa
Cell voltage used U _{min}	30 – 50 mV
O ₂ fractions used	2, 10, 20, 50, 100 %

Table 1. Conditions for the limiting current experiment.

During the experiment, the cell was polarized with an electronic load (Croma) in galvanostatic mode. The requested current exceeded the maximum current supply of the cell. A cell voltage between 30 – 50 mV established itself at the maximum current. This condition has been maintained for 30 min at each oxygen concentration before the cell was imaged. For a tomographic scan, 2001 radiographies were recorded at 13.5 keV with an

exposure time of 17 ms and a voxel size of (2.2 μm)³. In order to ensure the significance of the experiment, the cell was conditioned and tested under similar conditions prior to the imaging series.

Results

The electrochemically determined transport resistance R_T is calculated from the oxygen concentration x_{O₂} and the limiting current I_{Lim} according to equation (1), which is derived from the combination of Ficks law and the Faraday equation [1].

$$R_T = \frac{h}{D_{eff}} = \frac{4F p_0 x_{O_2}}{RT I_{Lim}} \quad 1)$$

h denotes the GDL thickness, D_{eff} the effective oxygen diffusion constant, F the Faraday constant, p₀ the gas pressure, R the gas constant and T the operating temperature.

In the experiment, the maximum current as well as the transport resistance increased with increasing oxygen concentration. Figure 1 shows the resistance versus limiting current prior to and during XTM imaging, which are in good agreement.

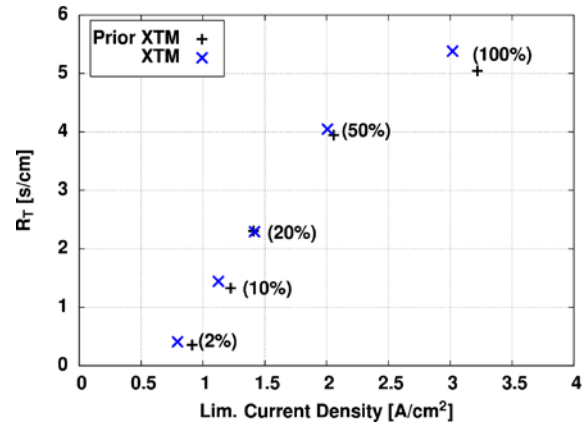


Figure 1. Transport resistance and limiting current for different oxygen concentrations at 70% RH (T cell: 70°C).

Based on the hypothesis of Baker et al., the current at 2% O₂ concentration is limited by the gas transport in the dry structure. At 10% O₂ and beyond, the product water further limits the performance, caused by water accumulation either in the channel, the GDL or the catalyst layer. XTM imaging allows answering this question in a quantitative manner.

To obtain the transport resistance in the GDL based on the XTM experiments, it is necessary to reconstruct the 3D representation from the radiographs taken under operation and segment the resulting stack of images into void and condensed phases. A threshold based algorithm was used for the latter. The required processing steps are described in ref. [7].

It was found that the anode side (channel and GDL) holds no, and the cathode channel only very little water even at 100% O₂ concentration and 3 A/cm², thus the

focus is set on the cathode GDL. The local water distribution and the related diffusion resistance are analyzed to localize and quantify the transport limitation in the GDL. Two regions of interest (ROI) under the rib and two domains under the channel with a length (y) of 3.52 mm, a width (x) of 0.44 mm and a height (z) of 0.13 mm (0.35 mm^3) were selected and averaged for each domain. The cross section trough the cell is shown in Figure 2a, the flow field layout and the regions of interest (ROI) are shown in Figure 2b.

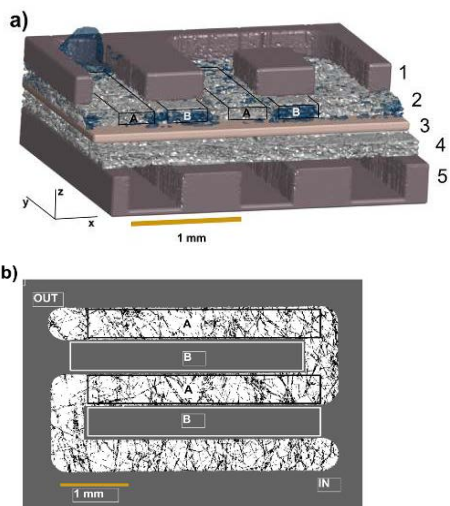


Figure 2 a) Cell cross section. 1 cathode (Ca) flow field (FF), 2 Ca GDL with water, 3 membrane and catalyst layer, 4 anode (An) GDL, 5 An FF; A and B denote the region of interest (ROI) for GDL under channel and rib domain, respectively;. b) FF layout and ROI for GDL.

The GDL saturation profile from the membrane (Pos. 3 in Figure 2a) to the cathode flow field (Pos. 1) in the rib region (Figure 3a) and a higher saturation in the rib region (Figure 3b).

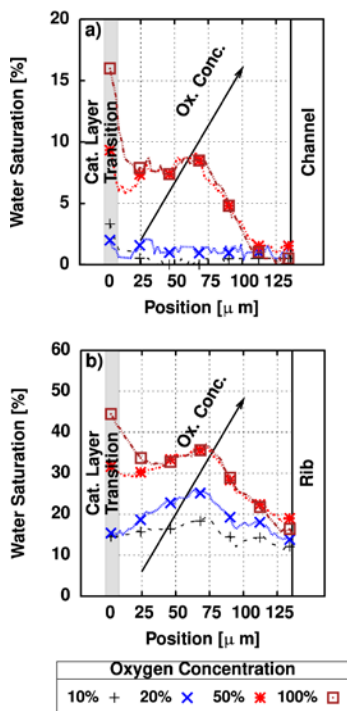


Figure 3 Saturation profile in the GDL channel domain a) and rib domain b) for different oxygen concentrations at 70°C and 70% RH.

Due to the strong X-ray absorption of the Pt catalyst, the interface and the GDL close to the interface are not resolved (labeled “Transition” in Figures 4a and 4b).

From the profiles it becomes clear that the major blockage by water is located below the ribs and near the catalyst layer. It can also be seen that in the rib domain the saturation in case of the 50% and the 100% O_2 concentration is similar but deviates near the catalyst layer.

The diffusion resistance, expressed as the ratio of the free gas diffusion coefficient D and the effective diffusion coefficient D_{eff} is computed for the rib domain using the Geodict software package [8] for the x , y and z -directions and compared to R_T , excluding the transition region near the catalyst (ROI: y : 3.52 mm, x : 0.44 mm, z : 0.11 mm). A correlation between R_T and the ratio D/D_{eff} is found for $R_T < 4$ (50% O_2), beyond this point the D/D_{eff} is only increasing in z direction (see Figure 4).

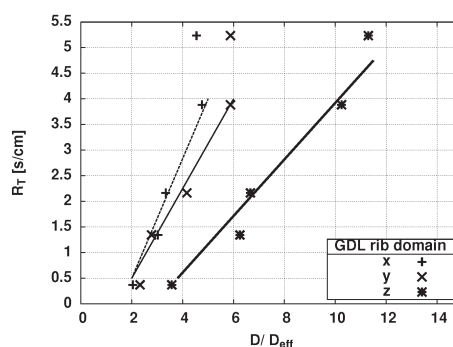


Figure 4 Comparison of electrochemically determined transport resistance (R_T) with calculated D/D_{eff} for the GDL rib domain. The lines help to guide the eye.

This indicates that the transport limitation under the given operating condition rather dominated by the transport in the z -direction under the rib. The saturation profile suggests that water accumulation at the catalyst layer or the interface limits the mass transport.

Conclusions

The electrochemically observed increase of mass transport resistance is found to be related to the bulk saturation in the GDL up to a current density of 2 A/cm^2 at 70°C Cell and 70% RH. Under the most extreme condition of 100% O_2 and 3 A/cm^2 , the transport loss can be attributed to the diffusion limitation in the z -direction.

References

- [1] D.R. Baker, C. Wieser, K.C. Neyerlin, M.W. Murphy, ECS Trans. **3**, 989-999 (2006).
- [2] D.R. Baker, D.A. Caulk, K.C. Neyerlin, M.W. Murphy, J. Electrochem. Soc. **156**, B991-B1003 (2009).
- [3] D.A. Caulk, D.R. Baker, J. Electrochem. Soc. **157**, B1237-B1244 (2010).
- [4] D.A. Caulk, D.R. Baker, J. Electrochem. Soc. **158**, B384-B393 (2011).
- [5] D.R. Baker, D.A. Caulk, ECS Trans. **50**, 35-45 (2012).
- [6] J. Roth, M. Citerne, R. Gaudenzi, J. Eller, F.N. Büchi, PSI Electrochemistry Laboratory Annual Report 2011, 28-29 (2012).
- [7] J. Roth, J. Eller, F. Marone, F.N. Büchi, J. Phys. Chem. C **117**, 25991-25999 (2013).
- [8] <http://www.geodict.com>

SCIENTIFIC ACHIEVEMENTS 2013

FUEL CELLS & ELECTROLYSIS

MATERIALS

Radiation grafted polymer electrolyte membranes for water electrolysis cells – characterization of key membrane properties

A. Albert, T.J. Schmidt, L. Gubler

phone: +41 56 310 4539, e-mail: albert.albert@psi.ch

The usage of electricity from renewable energy makes water electrolysis an environmentally friendly method to store excess electricity in the form of hydrogen. The polymer electrolyte electrolysis cell (PEEC) is one of the common types of water electrolyser. It is commercially available, but due to its high cost it is not yet suitable for large-scale applications [1].

The proton conducting membrane as the electrolyte in a PEEC plays an important role for the efficiency and durability of the system. Nafion N115 and N117 are commonly used in PEECs. However, since these perfluorinated materials are expensive, many alternative membranes are investigated [2]. Radiation grafted membranes are one of these alternatives, since their cost is potentially lower and their properties can be readily modified by varying the composition and architecture of the graft copolymer [3]. An adequate monomer/comonomer combination is necessary for obtaining a membrane with desired properties.

In this study, radiation grafted membranes with a combination of S/AN and S/AN/DiPB as grafting monomers (Figure 1) were investigated and compared to Nafion membranes and AMS/MAN co-grafted membranes, which is based on 25 μm ETFE films and obtained from the previous work in our group [4].

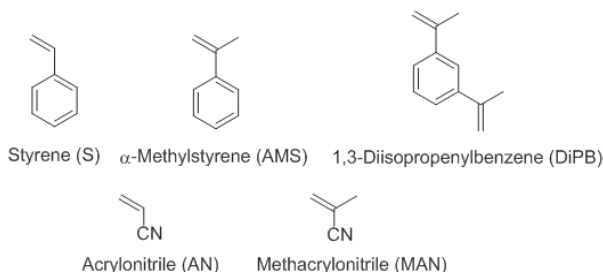


Figure 1. Monomers for radiation grafted membranes.

The PEEC and polymer electrolyte fuel cell (PEFC) exhibit the same mechanism of proton conduction in the membrane. Therefore, it is feasible to investigate the performance and properties of a membrane for the PEEC in a PEFC. PEFC experiments under full humidification were used in this study for evaluating the performance of the membrane and its properties in terms of area resistance and hydrogen crossover.

The 100% relative humidity is chosen to simulate the fully hydrated membrane condition in the PEEC. Area resistance and hydrogen crossover are two key membrane properties highlighted in this study. Area resistance relates to the proton conductivity of a membrane. Hydrogen crossover is a crucial property related to the purity of product gas. In addition, the formation of an explosive mixture of H_2 and O_2 needs to be avoided at any cost.

Experimental

Nafion NR-211, N XL-100, NR-212, N1035, N1135, N105, N115, N117 and N120 were pretreated before the

experiments in order to obtain their fully hydrated forms. After removing the coversheets from the NR-211, N XL-100 and NR-212, the membranes were immersed in a water bath at 90 $^{\circ}\text{C}$ for one hour. The Nafion membranes without coversheets were pretreated with a 32.5 V% nitric acid (HNO_3) solution at 90 $^{\circ}\text{C}$ for one hour to remove impurities and re-protonate the sulfonic acid groups. Afterwards, they were washed twice with 600 mL Millipore water and immersed consecutively in three water baths at 90 $^{\circ}\text{C}$ for 1 hour. The pH of the water bath should be 7 at the end. Finally, all the membranes were stored in boxes filled with Millipore water.

For the in-situ measurement, the fully hydrated membrane was hot pressed with two gas diffusion electrodes (JM ELE0162, 0.4 mg Pt/ cm^2) at 120 $^{\circ}\text{C}$ and 58 bar for 3 minutes. The area resistance and hydrogen crossover of the membrane were electrochemically measured in a fuel cell with 29.16 cm^2 active area at 80 $^{\circ}\text{C}$ and 2.5 bar absolute reactant gas pressure. The feed gases were pure hydrogen and oxygen with 1.5/1.5 stoichiometry, flow limit of 200 mln/min, and 100% relative humidity.

The area resistance was obtained by taking the value at a current density of 0.2 A/ cm^2 in the polarization plot. The plot was made by recording the potential and area resistance during the increase of current. The area resistance at low current density was chosen as reference point, since the influence of the electro-osmotic drag of water becomes significant at higher current densities, especially for the thicker membranes N117 and N120.

The hydrogen crossover was determined by changing the oxygen feed to nitrogen. The measurement started after all the oxygen was removed (at least 2 hours waiting). The hydrogen crossover current density was measured at different potentials. Extrapolation of the current density versus the potential gives the crossover current density at zero potential, which is the hydrogen crossover value of the membrane in the unit mA/ cm^2 .

Radiation grafted membranes were prepared by immersing pre-irradiated (electron beam, 1.5 kGy, air) 50 μm ethylene tetrafluoroethylene (ETFE) film from DuPont or Saint-Gobain in a reaction mixture containing water (10 V%), isopropanol (70 V%) and monomer (20 V%) solution. The detailed membrane synthesis is described elsewhere [3]. The combinations of S/AN and S/AN/DiPB were investigated. In both cases, S/AN was used at a volumetric ratio of 40/60. The DiPB amount in the latter combination is 5 V% of the total monomer. The total monomer content for each combination was kept at 20 V% of the total solution.

Results

The Nafion NR-211, N XL-100, NR-212, N1035, N1135, N105, N115, N117 and N120 were tested in the PEFC as benchmark for the radiation grafted membranes. The property map of area resistance versus hydrogen crossover of Nafion is established and is used as an indicator to evaluate radiation grafted membranes (Figure 2).

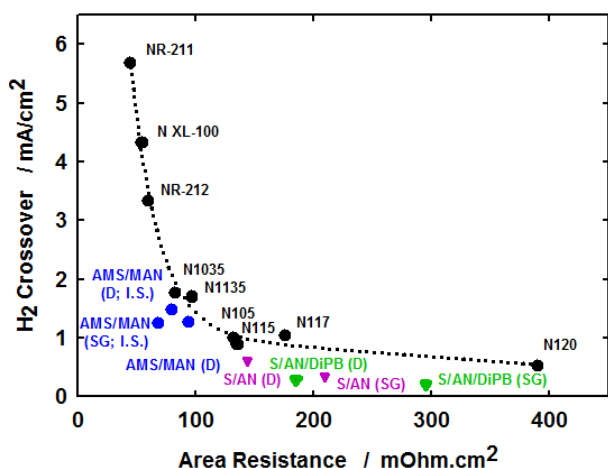


Figure 2. Property map of Nafion and radiation grafted membranes (D=DuPont; SG=Saint-Gobain; I.S.=improved surface).

It appears that the Nafion membranes follow a general trend, indicated by the dotted line in the property map. Their properties are governed by the respective membrane thickness. The preliminary test shows that the radiation grafted membranes have better properties than Nafion in terms of area resistance and hydrogen crossover, especially the AMS/MAN co-grafted membrane (optimized for fuel cell application). S/AN and S/AN/DiPB co-grafted membranes offer excellent gas barrier properties, which is important for the PEEC. However, the area resistances of the S/AN and S/AN/DiPB membranes offer some room for improvement.

The S/AN and S/AN/DiPB co-grafted membranes using DuPont base film showed better properties than the membranes using Saint-Gobain base film. This could be caused by different processing parameters between DuPont and Saint-Gobain, which influence the microstructure of ETFE and eventually the grafting reaction. The effect of DiPB crosslinker is also shown in the S/AN and S/AN/DiPB membranes. As expected, membranes with crosslinker exhibit a lower gas crossover but higher area resistance.

From these results, a figure of merit M can be calculated (Figure 3), which is defined as:

$$M = \frac{1}{R_{\Omega} \cdot i_x}$$

Where R_{Ω} is the area resistance of the membrane (in $\Omega \cdot \text{cm}^2$) and i_x is the hydrogen crossover current density (in A/cm^2). The figure of merit therefore has the unit $1/\text{V}$.

The figure of merit represents the compromise between area resistance and hydrogen crossover. Normally, a membrane with a low gas crossover (thicker membrane) has a higher area resistance and vice versa. With the figure of merit, the optimal combination of these two properties in a membrane can be determined.

AMS/MAN and S/AN co-grafted membranes show a similar or higher figure of merit than Nafion. S/AN/DiPB membranes display the highest figures of merit. These results indicate that the radiation grafted membranes are promising alternatives to Nafion. Unfortunately, the AMS/MAN co-grafted membrane, which is based on 25 μm film, is too thin for the PEEC application. The S/AN and S/AN/DiPB membranes are more suitable for the electrolysis cells, since they are based on a thicker basefilm and therefore offer better gas barrier properties.

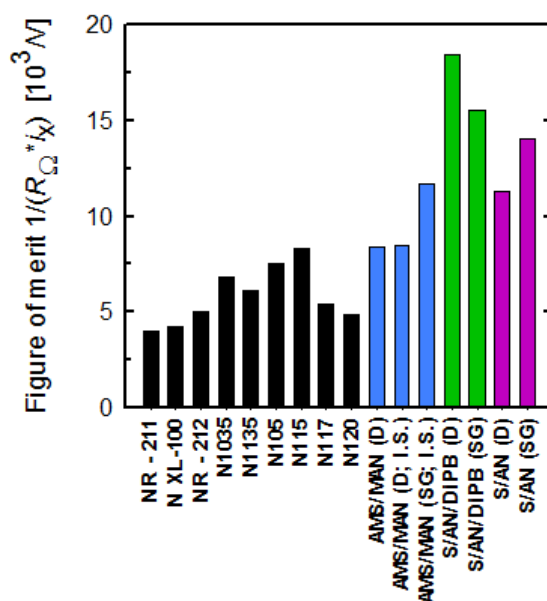


Figure 3. Figure of merit of Nafion and radiation grafted membranes (D=DuPont; SG=Saint-Gobain; I.S.=improved surface).

It should be noted that the property map and figure of merit only consider area resistance and hydrogen crossover properties. The S/AN and S/AN/DiPB membranes excel in the hydrogen crossover, but in terms of performance and area resistance, they are between N117 and N120. Fortunately, radiation grafted membrane can be tailored in order to obtain desired properties. Moreover, it is possible to optimize the interface between membrane and electrode during the hot-pressing of the membrane electrode assembly (MEA) by changing the temperature or pressure.

Conclusion

The property map and figure of merit introduced here can be used for evaluating alternative membranes for electrolyser applications. Preliminary tests show that radiation grafted membranes offer a favorable combination of gas barrier properties and area resistance compared to Nafion membranes, which is promising for PEEC application. There is room for improvement of the membrane electrode interface properties via optimizing membrane synthesis and the conditions for the hot-pressing of the membrane electrode assembly (MEA).

Acknowledgement

The research leading to these results has received funding from the European Union's Seventh Framework Programme (FP7/2007-2013) for the Fuel Cells and Hydrogen Joint Technology Initiative under grant agreement n°303484.

References

- [1] A. Ursua, L.M. Gandia, P.B. Sanchis, Proc. IEEE **100**, 410-426 (2012).
- [2] M. Carmo, D.L. Fritz, J. Merge, D. Stolten, Int. J. Hydrogen Energy **38**, 4901-4934 (2013).
- [3] L. Gubler, G.G. Scherer, in: Handbook of Fuel Cells **5**, W. Vielstich, H.A. Gasteiger, H. Yokokawa (Editors), John Wiley and Sons, Chichester (UK), 313-321 (2009).
- [4] L. Gubler, L. Bonorand, ECS Trans. **58**, 149 (2013).

Automotive H₂ / air operation of the PSI Gen2 radiation grafted membrane

L. Bonorand, J. Thut, L. Gubler

phone: +41 56 310 2132, e-mail: lukas.bonorand@psi.ch

Fuel cell technologies offer a pathway to enable the use of clean energy systems to reduce emission, enhance energy security and stimulate global economy. For the economic viability of polymer electrolyte fuel cell (PEFC) technology, all of its components, such as the proton exchange membrane (PEM), need to meet cost targets, and fulfil technical, as well as application related operational requirements [1]. The current PSI Generation 2 (Gen2) radiation grafted membrane has demonstrated competitive performance and durability [2], in addition to a highly favorable cost potential compared to current state of the art commercial benchmark materials that are widely used in today's global fuel cell industry [3].

However, these competitive membrane characteristics were obtained under H₂/O₂ fuel cell operating conditions. In many environments, such as automotive applications, fuel cells are operated using H₂ and air, and therefore, performance and durability targets need to be met and demonstrated using air as an oxidant. While doing so, none of the other fuel cell components, such as the gas diffusion layers (GDL), electrodes, flow field design of bipolar plates, or the entire cell design used, should become a limitation for characterizing membranes under H₂/air operating conditions and need to be selected appropriately.

Within the widening scope of the PSI radiation grafted membrane development to automotive application in the framework of the Belenos Project, appropriate MEA and cell designs are required to reliably evaluate membranes under relevant H₂/air operating conditions. In this context, we have investigated limitations of the current H₂/O₂ MEA and cell designs and identified strategies to optimize application specific membrane characterization.

Experimental

The membranes used were commercial Nafion[®] NR212 and the PSI Gen2 radiation grafted membrane. MEA assembly was carried out by hot-pressing them with commercially available gas diffusion electrodes (GDE's) supplied by Johnson Matthey Fuel Cells comprising HiSPEC 9100 Pt/C catalyst with a platinum loading of 0.4 mg_{Pt} /cm². Fuel cell characterizations were initially performed in a 30 cm² single cell having a serpentine flow field design with channel / land widths of both 1 mm and a channel depth of 0.5 mm.

Results

An initial performance assessment of Nafion[®] NR212 and the PSI Gen2 membrane at 80°C cell temperature, 70% relative humidity (RH), 2.5 bar_a and stoichiometries of 1.5/2.0 for H₂/air, respectively, indicated mass transport losses at the cathode side, with was reflected in low and unstable performance at higher current densities. An increase in flow rates on the cathode side improved the cell voltage and the voltage stability significantly, which is shown in Figure 1. Both types of membrane display very comparable performance characteristics, irrespective of the operating conditions used. This is

indicative of the observed polarisation behavior more likely being related to potential flooding at the cathode.

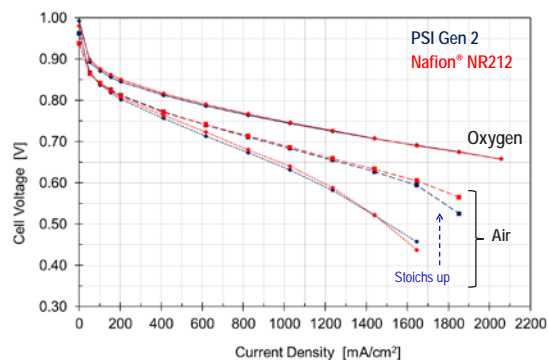


Figure 1. Performance of Nafion[®] NR212 and the PSI Gen2 membrane under H₂/O₂ and H₂/air operating conditions.

Cathode flooding is a common phenomenon during fuel cell operation, when the water production rate is greater than the water removal rate. The water removal rate can be governed by the operating conditions of the cell, as well as by the MEA or unit cell design. However, it is important to find a balance between liquid water removal and membrane drying. In this context, we performed sensitivity analysis on various operating parameters to assess the degree of flooding, but also to identify optimal operating conditions using the current cell design. In a second step, adjustments in MEA and cell design were made as necessary to implement a more suitable test platform for H₂/air operation.

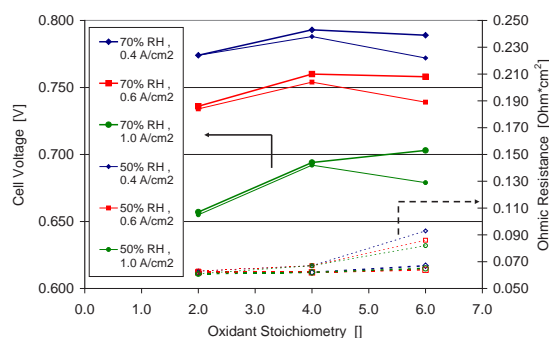


Figure 2. Cell voltage and ohmic resistance as a function of air stoichiometry at different relative humidity and current density.

Figure 2 shows a sensitivity analysis with the current single cell design using Nafion[®] NR212, where the air stoichiometries were varied between 2.0 and 6.0 at relative humidities of 50% and 70% at the oxidant inlet. Cell voltages and ohmic resistances were recorded at a current density of 0.4, 0.6 and 1.0 A/cm². The increase in cell voltage with increasing air stoichiometry is more pronounced at the higher current density, which is in support of cathode flooding, since more water is generated at higher current densities. On the other hand, cell performances at 50% relative humidity (RH) are dropping off at higher stoichiometries, compared to 70% RH.

This is predominantly due to the increase in ohmic resistance at higher flow rates, indicating membrane drying. The iR -corrected cell voltages of both humidification levels show identical values. Lowering relative humidity levels of the inlet gases to 50% did not show an effect on the removal of excess water. On the contrary, the associated membrane drying had an adverse effect on the overall cell voltage.

Operating the cell at stoichiometries of 6.0 at 70% RH for the oxidant side would provide acceptable, as well as stable cell performance for qualifying membranes under H_2 /air operating conditions. However, the pressure drop on the cathode side was found to be excessively high during the polarization curves, reaching up to 500 mbar at a current density of $1.2 A/cm^2$. This may be due to the restrictive nature of the narrow serpentine flow field channels, as well as excess liquid water blocking the pores of the gas diffusion layers (GDL's) or the flow field channels of the bipolar plates. To elucidate the potential contribution of these factors, separate pressure drop measurements were performed using dry inert gases. In this way the contribution of water of the electrochemical reaction due to the operating of the cell can be excluded.

$$\Delta p_{\text{total}} = \Delta p_{\text{dry}} + \Delta p_{\text{ECO}} \quad \Delta p_{\text{ECO}} : \text{Electrochemical Operation (ECO)}$$

The values obtained with dry gases subtracted from those of the operating cell result in the contribution from the electrochemical reaction. As displayed in Figure 3, a significant pressure drop remains from the operation of the cell, which is likely a result of water blockage.

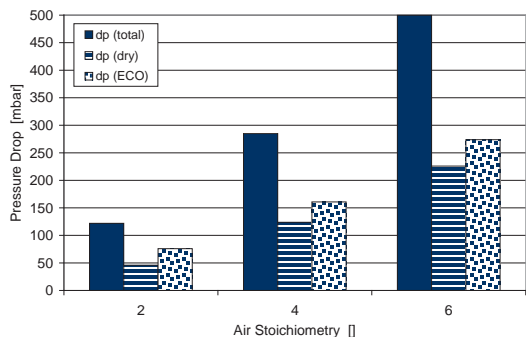


Figure 3. Pressure drop distributions at $1.2 A/cm^2$ at various air stoichiometries ($T=80^\circ C$, $RH=70\%$, $p=2.5bar_a$).

However, the pressure drops observed with dry gases were also considered to be high and were associated to the narrow cross section of the flow field channels. Therefore, bipolar plates with 1.0 mm channel depth instead of 0.5 mm were investigated, which resulted in an expected 4x decrease in pressure drop using dry gases only. Although the reduced pressure drop was in a more suitable range, the corresponding polarization curves suggest that flooding had become worse. Figure 4 demonstrates that mass transport limitations at higher current density are significantly higher, irrespective of the air flows being used. In support of this, stoichiometry sensitivity analysis performed at different pressures indicated noticeably more flooding with deeper channels. This is likely due to the deeper channels facilitating the flow of gases in the channels and therefore reducing the ability to force the gases through the pores of the GDL.

This suggests that flooding occurs more likely in the pores of the GDL, rather than in the flow field channels.

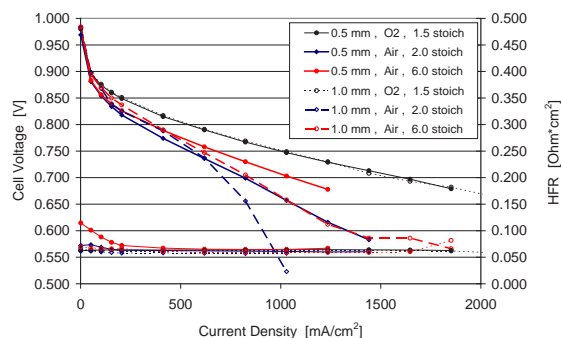


Figure 4. Effect of flow field channel depth on the polarization at different air stoichiometries ($T=80^\circ C$, $RH=70\%$, $p=2.5bar_a$).

Considering that the cathode is prone to flooding, an alternative electrode, having a less hydrophilic GDL, provided significantly enhanced performance, as well as improved voltage stability at higher current density. In addition, the obtained lower stoichiometry sensitivity supports an improved water management. However, as can be seen in Figure 5, cell voltages are lower at lower current densities, as well as when operated with oxygen. This is likely a result if the new electrodes being 50 μm thicker and softer and therefore being over compressed during cell assembly. Seal and cell designs are currently adjusted to fully leverage the potential of the new GDE.

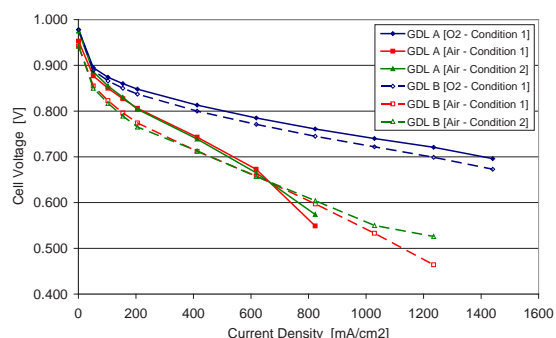


Figure 5. Effect of GDL type on fuel cell performance using Nafion® NR212.

Conclusion

Cathode flooding has been identified as primary source of mass transport limitations when our H_2/O_2 system is used for H_2 /air operation. A new electrode, in combination with an optimized cell design allows to more reliably evaluating our membranes under H_2 /air operation.

Acknowledgement

Financial support by Belenos Clean Power AG (Biel) and the Swiss National Science Foundation (Nano-Tera initiative) is gratefully acknowledged.

References

- [1] U.S. Department of Energy (EERE), Fuel Cell Technologies Office – Pathways to Commercial Success - 2013.
- [2] L. Gubler, L. Bonorand, ECS Trans. **58**, 149 (2013).
- [3] L. Bonorand, G.G. Scherer, L. Gubler, PSI Electrochemistry Annual Report, PSI Electrochemistry - Annual Report 2011, 5-6, DOI: 10.3929/ethz-a-007047464 (2012).

Effect of different antioxidants on performance and durability of styrene based radiation grafted membranes (ETFE-g-PSSA)

Y. Buchmüller, A. Wokaun, L. Gubler

phone: +41 56 310 5450, e-mail: yves.buchmueller@psi.ch

Radiation grafting is a versatile technique to introduce desired properties into polymers [1, 2]. Advantages are the wide range of commercially available monomers and the relatively easy control of the graft component by the appropriate choice of the irradiation dose, monomer concentration in the grafting solution, solvent and additives, the reaction time and temperature. Radiation grafting can be performed to obtain ion-exchange membranes for a number of applications: proton conductive membranes for fuel cells [1], separation membranes for water purification [3], or membranes for the removal of heavy metal ions [4].

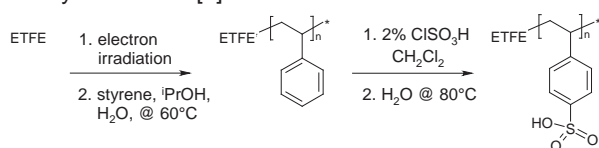


Figure 1. Schematic representation of grafting styrene onto ETFE with subsequent sulfonation to obtain a proton conductive membrane.

Polymer electrolyte membranes for fuel cell application are used under chemically and electrochemically harsh conditions and need to exhibit long term chemical stability and mechanical integrity. State of the art are perfluoroalkylsulfonic acid (PFSA) membranes, e.g. Nafion®, Flemion®. These are aliphatic polymers with promising durability in the fuel cell environment. In contrast, ETFE grafted with polystyrene sulfonic acid (ETFE-g-PSSA), a model system for radiation grafted membranes, exhibits low durability, owing to the weak α -hydrogen of the styrene groups. Roduner et al. and Dockheer et al. showed on model compounds that radical attack leads to the benzylic radical, which can result in chain scission of the styrene grafts [5, 6].

Mitigation strategies against degradation of this kind of membrane can generally be divided into three approaches: the first would be to make the grafted monomer intrinsically more stable by protecting the weak α -position. Another approach is to make the environment less aggressive by lowering the rate of formation of radicals by reducing the gas crossover through the membrane. These two approaches were investigated in detail at PSI during the last decade [7].

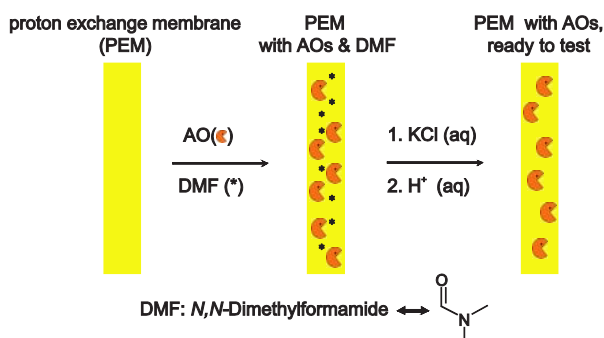


Figure 2. Schematic representation of introduction of antioxidants (AOs) into ETFE-g-PSSA type membranes.

A third approach is to introduce antioxidant functionalities into the membrane. The radicals are envisioned to be scavenged by these antioxidants (AOs) instead of reacting with the membrane polymer. For PFSA type materials it is known that introduction of cerium or manganese ions slows down degradation. This approach could also be applied in the case of organic antioxidants (e.g. phenol type AOs). This work presents a *in situ* degradation study of ETFE-g-PSSA type membranes containing non-covalently attached phenol type AOs (Figure 2).

Experimental

Styrene was grafted onto ETFE film of 25 μm thickness. The graft level (GL) is an important parameter to characterize graft copolymers:

$$GL = \frac{m_{\text{grafted}} - m_{\text{basefilm}}}{m_{\text{basefilm}}} \cdot 100\% \quad (1)$$

where m is the mass. The ETFE base films were electron beam irradiated (Studer Leoni, Däniken) with a dose of 1.5 kGy, the stabilizing agent in GMA was extracted using an inhibitor remover column, and the grafting solution consisted of 2-propanol, water and styrene at a volumetric ratio of 7/1/2. The grafting reaction was performed at 60°C.

Sulfonation of the styrene grafts was performed using a solution consisting of 2% chlorosulfonic acid in dichloromethane (v/v). The reaction was carried out at room temperature for 5 h.

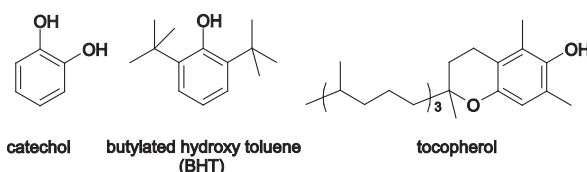


Figure 3. Phenol type antioxidants used within this study.

Membranes of a GL of 23% (ion exchange capacity, IEC of 1.5 mmol/g) were swollen in antioxidant solution (0.25 M in DMF), potassium exchanged and reprotonated to remove residual DMF (Figure 2). In the case of cerium, the membranes were immersed in a 1 mol% solution of cerium(III) carbonate in concentrated sulfuric acid overnight. The treated membranes were hotpressed (110°C, 2.5 MPa, 180s) together with gas diffusion electrodes (JM ELE 162, 4mg Pt/cm²), assembled into a fuel cell and tested under accelerated aging conditions (4h open circuit potential at 2.5bar_a backpressure, H₂ and O₂ gas flows of 600ml/min). After the test, the membranes were backtitrated to determine IEC loss.

Results

The membranes showed a dependency of the performance on the introduced organic AO (Figure 4). For membranes containing tocopherol and BHT, the performance was enhanced while the area resistance de-

creased compared to the pristine ETFE-g-PSSA membrane. A possible explanation for this effect could be the plasticizing effect of the small aromatic BHT, which could lead to better mobility of the grafted chains and, consequently, to better proton transport through the membrane. For tocopherol a kind of van der Waals force could lead to opening of the structure of ETFE-g-PSSA by interpenetration of the lipophilic tail of tocopherol in the lipophilic backbone polymer of the membrane. This opening of the polymer structure of ETFE-g-PSSA would lead to increased mobility of the protogenic groups and hence to higher proton conductivity.

The introduction of cerium and catechol lowers the proton conductivity of ETFE-g-PSSA. The lower proton conductivity for cerium containing membranes can be explained by the blocking of exchange sites by cerium cations, replacing 3 protons per ion, leading to lower proton concentration in the membrane. For catechol, the loss in proton conductivity cannot be explained by replacements of protons. Apparently, the aromatic alcohol does not improve the mobility of the grafted chains.

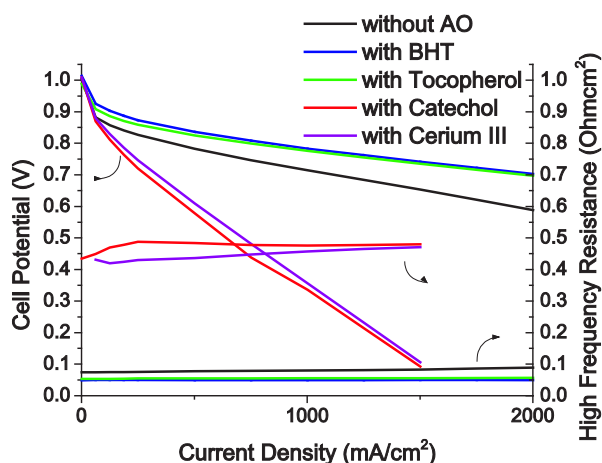


Figure 4. Polarization curves of ETFE-g-PSSA (IEC = 1.5 mmol/g) membranes containing different AOs. The black line shows the polarization curve of ETFE-g-PSSA without AOs.

Representative polarization curves for PSSA type membranes including antioxidants (i.e. BHT) before and after the accelerated stress test (AST) are shown in Figure 5. The membranes containing BHT outperform Nafion® NR212. After the AST the membranes perform still better than untreated pristine PSSA type membranes. The HFR does not change during the AST, indicating a similar conductivity and, consequently, no apparent degradation of the treated membrane during 4h OCV hold.

The IEC determination after test gave no conclusive results, thus, more work needs to be done for application of this methodology to fully assess the effectivity of antioxidants for use in fuel cells.

Conclusion

Styrene based radiation grafted membranes (ETFE-g-PSSA) were doped with different phenol type antioxidants and cerium(III) ions and tested *in situ* under accelerated aging conditions (OCV hold). After the test the membranes were titrated to determine the loss of grafted chains. The different AOs changed the performance of the membranes significantly: BHT and tocopherol enhanced the performance and slowed down degradation,

whereas cerium and catechol had no stabilizing effect and lowered the performance of ETFE-g-PSSA significantly.

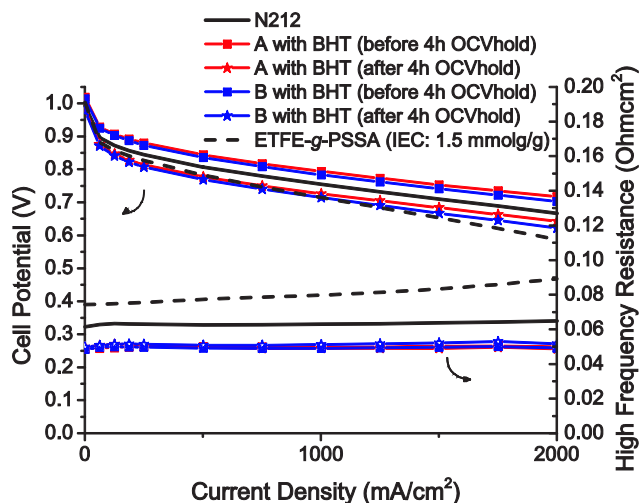


Figure 5. Polarization curves of ETFE-g-PSSA (IEC = 1.5 mmol/g) membranes containing BHT. The curves with the squares were recorded before and the curves with stars after 4h OCVhold. For comparison initial polarization curves of Nafion® NR212 and ETFE-g-PSSA of the same IEC are shown.

Acknowledgement

Funding by the Swiss National Science Foundation is gratefully acknowledged (project 200021_132382).

References

- [1] S. Alkan-Gürsel, L. Gubler, B. Gupta, G.G. Scherer, *Adv. Polym. Sci.* **216**, 157-217 (2008).
- [2] A. Bhattacharya, B.N. Misra, *Progr. Polym. Sci.* **29** (8), 767-814 (2004).
- [3] M.M. Nasef, O. Güven, *Progr. Polym. Sci.* **37** (12), 1597-1656 (2012).
- [4] R. Ishihara, K. Fujiwara, T. Harayama, Y. Okamura, S. Uchiyama, M. Sugiyama, T. Someya, W. Amakai, S. Umino, T. Ono, A. Nide, Y. Hirayama, T. Baba, T. Kojima, D. Umeno, K. Saito, S. Asai, T. Sugo, *J. Nucl. Sci. Technol.* **48**, 1281-1284 (2011).
- [5] G. Hübner, E. Roduner, *J. Mater. Chem.* **9** (2), 409-418 (1999).
- [6] S.M. Dockheer, L. Gubler, P.L. Bounds, A.S. Domazou, G.G. Scherer, A. Wokaun, W.H. Koppenol, *Phys. Chem. Chem. Phys.* **12**, 11609-11616 (2010).
- [7] L. Gubler, L. Bonorand, *ECS Transactions* **58**, 149-162 (2013).

A degradation study of radiation grafted membranes in PEFCs by exhaust water analysis

Z. Zhang, Y. Buchmüller, A. Wokaun, L. Gubler

phone: +41 56 310 4188, e-mail: zhuoxiang.zhang@psi.ch

As an indicator of the 'state-of-health' of the membrane during fuel cell tests, high frequency resistance (HFR) is used to monitor the degradation of polystyrenesulfonic acid (PSSA) based membranes prepared by radiation grafting [1]. Due to intrinsic limitations, HFR is not a precise measure for membrane degradation [2]. A study using the exhaust water analysis to measure membrane degradation is presented in this report.

Experimental

An ETFE-*g*-PSSA membrane with a graft level of ~23% was tested at 80 °C under open circuit voltage (OCV) conditions for 24 h. H₂ and O₂, both fully humidified, were fed to the anode and cathode, respectively, at 300 mL min⁻¹ each and at 2.5 bar_a. The measurements of cell voltage and HFR at 1 KHz were performed at a given interval during the test. Meanwhile, the exhaust water discharged from both sides was collected and analyzed by means of conductivity, ultraviolet (UV) spectroscopy and ion chromatography (IC). The first samples at cathode and anode, respectively, were collected during the first 8 h (samples represented by OCV-1), which was followed by sampling over the remaining time (16 h) of the test at each side (samples represented by OCV-2). Prior to the test, the test bench including the cell was purged with fully humidified nitrogen at 2'000 mL min⁻¹ for over 24h in order to remove residual fragments created in the previous tests as much as possible and obtain a baseline of exhaust water of this system. After the test, the exhaust water from both sides was continuously collected for 7h (samples from N-1 to N-5 collected chronologically) while feeding fully humidified nitrogen at 2'000 mL min⁻¹ to both cathode and anode.

The conductivity was measured at room temperature using a conductivity meter (WTW Cond 3310). UV absorption spectra were obtained on a Varian Cary 4000 UV-Vis spectrophotometer, which can typically measure absorbances beyond 8. The IC measurement was performed using the instrument (Metrohm 882 Compact IC plus – Anion) already calibrated for sulfate quantification.

Results and discussion

Figure 1 shows the results of the measurements of cell voltage decay and HFR development during the OCV hold test. A rapid drop of the cell voltage is observed at the beginning of the test owing to the formation of platinum oxide on the surface of the cathode catalyst. Then, the cell voltage gradually decreases with time as a result of membrane degradation. Initially, a slight decrease in HFR is seen, following which the HFR value increases significantly towards the end of the OCV test, indicating that the membrane has lost a significant fraction of the grafted SSA units and, consequently, proton conductivity. After the test was stopped by feeding N₂ to both sides, a continuous increase in HFR is still observed, as shown by the red dots in Figure 1. This implies that the membrane was still losing the grafted SSA units in the nitrogen environment after the OCV test.

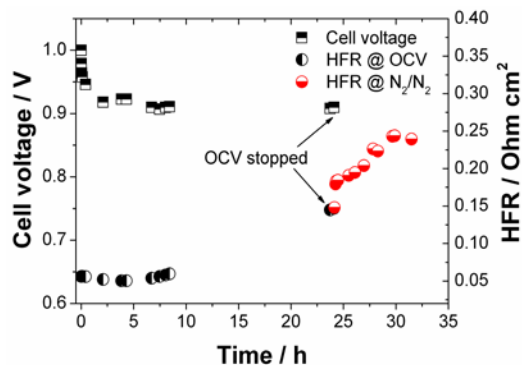


Figure 1. Evolution of cell voltage and membrane resistance (measured by HFR) vs. time of operation of a H₂/O₂ fuel cell at 80 °C for the membrane tested for 24 hours.

The conductivity of the collected exhaust water samples is presented in Figure 2. The conductivity of the samples collected at the anode side is higher than that of the baseline, whereas the samples collected at the cathode show very similar conductivity as the baseline, which is close to the conductivity of deionised water. This suggests that the decomposed fragments from the membrane are mostly leached out at the anode. With the highest conductivity (24.2 μS cm⁻¹) of the sample collected during the first 8h of the OCV hold test, the exhaust water samples from the anode exhibit decreasing conductivities with time, which represents the time dependence for the elution of ionic fragments.

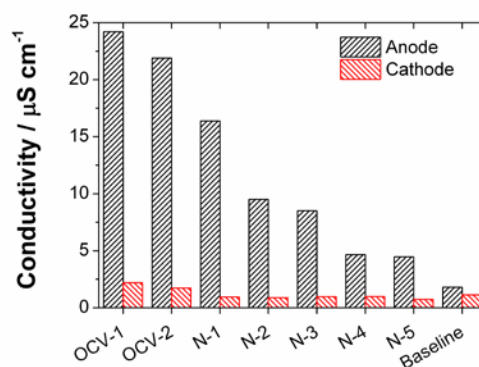


Figure 2. The conductivity of the exhaust water sampled at the cathode and the anode, respectively, at different times of the test. The baseline obtained before the OCV test is plotted for comparison.

The results of UV spectroscopy for the exhaust water samples collected during the 24 h OCV hold test and the subsequent purging period are displayed in Figure 3. At the anode side, in comparison with the spectrum of the baseline, all samples show the absorption bands at the wavelength of maximum absorption (λ_{\max} =225 nm) as the signature of aromatic units, which is exactly the same as the UV profiles of the decomposed extracts from the grafted ETFE films during the thermal stability test and the aqueous solution of commercial poly(sodium 4-styrenesulfonate) that have the aromatic

ring structure in common [3]. In contrast, however, the samples collected at the cathode do not show any remarkable difference from the baseline, which supports the conductivity results, indicating that the decomposed fragments from the grafted SSA polymer chains are mostly eluted with water from the anode side.

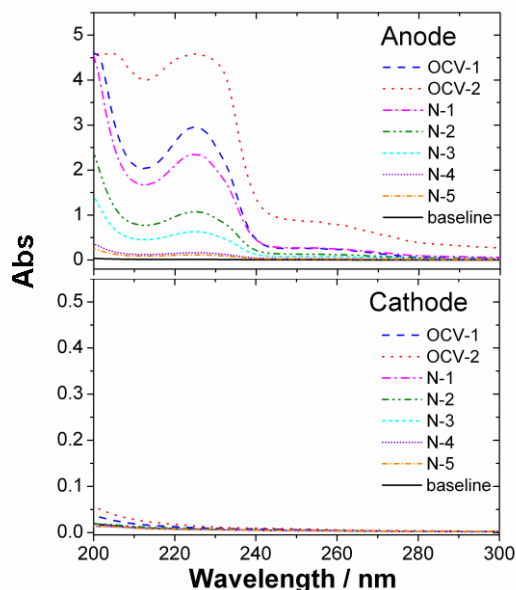


Figure 3. UV spectra of the exhaust water samples collected during the OCV hold test and the subsequent purging period with humidified nitrogen. The baseline obtained before the OCV test is plotted for comparison.

The samples from the anode collected during the nitrogen purging period display decreasing intensities at λ_{\max} with time, indicating the reduced concentrations of the eluted aryl compounds, which is in agreement with the results of conductivity measurements. However, the sample which was collected during the last 16 h (OCV-2) of the OCV hold test shows higher intensity at λ_{\max} than the sample from the first 8 h (OCV-1), while the conductivity of the OCV-2 is lower than that of the OCV-1 sample, as depicted in Figure 2. Hence, there is a discrepancy between the results of conductivity and UV spectroscopy, which measure the concentrations of the eluted fragments during the OCV hold test as a function of time.

To explore the origin of this discrepancy, the exhaust water samples were analyzed by means of IC. Much higher concentrations of sulfate in the samples than the baseline are observed, which indicates that the membrane underwent desulfonation during the test. Generally, it can be found that the concentration of sulfate decreases with time, showing the highest value at the beginning (OCV-1). This can account for the higher conductivity of the OCV-1 vs. OCV-2, which yet shows higher absorption intensity at aryl characteristic wavelenths compared to OCV-1. Again, compared to the baseline, the sulfate concentration at the cathode does not show any qualitative changes, which is consistent with the findings from Figure 2 and 3. So far, yet, we cannot conclude that the degradation of the membrane merely takes place at the anode, because the possibility of mass transport through water flow from cathode to anode cannot be excluded. The characterization of the tested membrane by means of ATR and SEM-EDX, which can distinguish the areas close to the anode from the cathode, may provide further insights in to this issue.

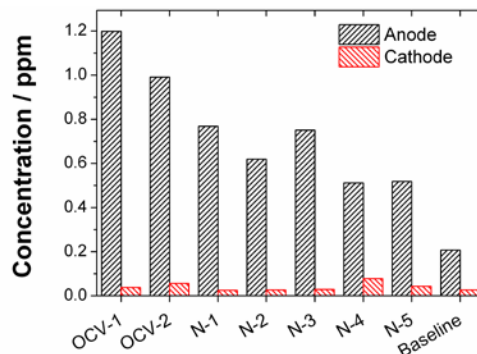


Figure 4. The concentration of sulfate in the exhaust water from the cathode and the anode, respectively, as a function of time. The baseline obtained before the OCV test is plotted for comparison.

Combining the information obtained above, it can be speculated that, at the early stage of the OCV hold test, the grafted PSSA polymers are attacked by radicals and typically detached from the base polymer backbone without fragmentation or scission of the polymer chains, and meanwhile the desulfonation process is initiated. Due to their large size, the detached polymers could not be washed out of the MEA with water immediately, in contrast to the sulfate. Nevertheless, the detached and trapped PSSA fragments can move to some extent, which improves the homogeneity of proton transport through the membrane and thus causes the decrease in HFR at the beginning of the test. With time, the PSSA polymer undergoes chain scission, creating the small fragments that are eluted with water. Therefore, during the N_2 purging period, the HFR still increases and the fragments can be detected in the exhaust water as a consequence of decomposition of those detached and trapped PSSA polymers.

Conclusion

A styrene grafted and sulfonated membrane was tested under OCV conditions in the fuel cell and the degradation was investigated through analyzing the exhaust water by means of conductivity, UV spectroscopy and ion chromatography (IC). The results of conductivity and sulfate concentration of the exhaust water at the anode both show a decreasing trend with time during the OCV hold test and subsequent N_2 purging period. However, the UV spectroscopy result at the anode shows that the concentration of aryl fragments in the exhaust water is higher for the sample collected at the later stage of the OCV hold test. Decomposed compounds from the membrane were hardly detected in the cathode exhaust.

Acknowledgement

Funding by the Swiss Federal Office of Energy (project no. 102245) is gratefully acknowledged.

References

- [1] Z. Zhang, Y. Buchmüller, A. Wokaun, L. Gubler, *ECS Electrochem. Lett.* **2**, F69-F72 (2013).
- [2] Z. Zhang, K. Jetsrisuparb, A. Wokaun, L. Gubler, *J. Power Sources* **243**, 306-316 (2013).
- [3] K. Enomoto, S. Takahashi, T. Iwase, T. Yamashita, Y. Maekawa, *J. Mater. Chem.* **21**, 9343-9349 (2011).

Quantification of the gas barrier properties of radiation grafted membranes using mass spectrometry

Z. Zhang, R. Chattot, A. Wokaun, L. Gubler

phone: +41 56 310 4188, e-mail: zhuoxiang.zhang@psi.ch

Although radiation grafted membranes have achieved remarkable progress in terms of performance and durability [1], the permeability of reactant gases in this class of ionomer used in polymer electrolyte fuel cells has not been studied yet. This report provides a method employing mass spectrometry (MS) to quantify the gas barrier properties of different classes of ionomer and the base film used in radiation grafted membranes.

Methodology

The measurement of gas permeability in the membrane is performed by supplying the target gas (H₂ or O₂, respectively) together with helium (10 vol%) to the anode compartment of the fuel cell. The molar fraction of the permeant target gas and helium is measured in the cathode exhaust stream using a quadrupole mass spectrometer (Pfeiffer Prisma 200M1). Since we cannot measure the crossover rates of H₂ and O₂ at the same time, through comparing the permeant concentrations of helium from two individual measurements, we can examine if the permeant concentrations of the two kinds of target gas measured together with helium were obtained under identical humidification conditions. Basically, the cathode compartment is fed with pure nitrogen as a carrier gas during the measurement.

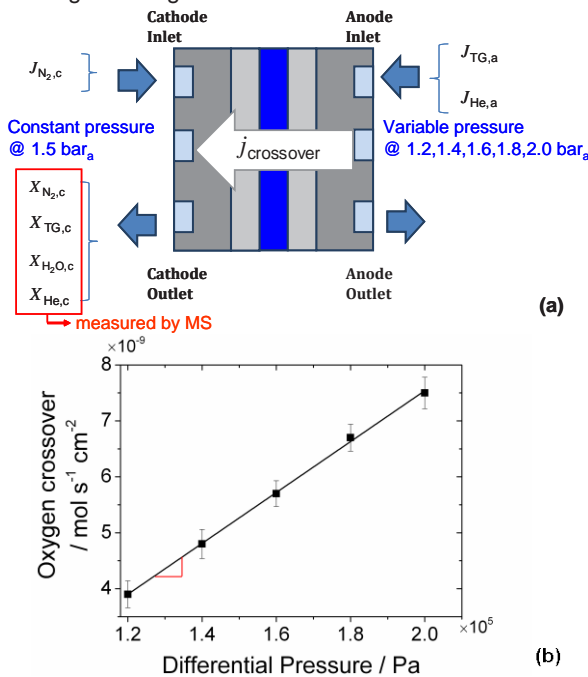


Figure 1. (a) Schematic of gas flow in the cell and notation of various quantities involved in the permeability measurement; (b) An example of the permeability obtained by linear regression analysis of the measured crossover rates at a range of differential pressure values.

Figure 1 outlines the used methodology for obtaining the permeability of the target gas (TG) and helium. The target gas concentration is measured at the outlet of the cathode at a given pressure difference between anode and cathode, such as 1.5 bar_a at the cathode and 2.0 bar_a at the anode. Note that the gas crossover in this

configuration is merely driven by gas diffusion as a result of the difference in the partial pressure of the target gas between anode and cathode, since a pristine membrane without defects, which would cause convective gas transport, is employed.

Firstly, by applying the ideal gas law and considering the calibration conditions of the mass flow controller (i.e. 0°C, 1.01325 bar), the known fluxes (in ml min⁻¹) are converted to a mole based unit (mol s⁻¹). The total flux of all gases (J_{t,c} in mol s⁻¹) at the cathode exhaust can be obtained from the measured N₂ concentration (X_{N₂,c} in mol%) at the cathode and the known N₂ flow rate (J_{N₂,c} in mol s⁻¹), as shown in Equation 1. Then, combining the total flux with the concentration of the permeant target gas (X_{TG,c} in mol%) measured by the MS yields the flux of the permeant target gas (J_{TG,c} in mol s⁻¹), as shown in Equation 2. Under different measuring conditions, the molar fraction of the target gas at the anode (X_{TG,a} in mol%) varies with RH and can be determined using Equation 3, assuming that the water concentration at the cathode (X_{H₂O,c}), which can also be measured by the MS, is equal to the water concentration at the anode (X_{H₂O,a}). Note that the permeation of gas through the membrane is driven by the partial pressure gradient and thus related to the molar fraction of the target gas at the anode. The gas crossover rate (j_{crossover} in mol s⁻¹ cm⁻²) can be obtained by normalizing the flux of the permeant target gas to the molar fraction of the target gas at the anode and the geometry of the membrane (c.f. Equation 4). By systematically changing the pressure difference between anode and cathode, accomplished by maintaining a constant pressure (1.5 bar_a) at the cathode and varying the pressure at the anode (Figure 1a), a linear regression analysis of the gas crossover rate vs. pressure difference (Δp) yields the permeance (mol s⁻¹ cm⁻² kPa⁻¹) of the permeant target gas as the slope, as the example in Figure 1b demonstrates. The permeance multiplied by the thickness of a membrane yields the permeability of the membrane (mol cm s⁻¹ cm⁻² kPa⁻¹).

$$J_{t,c} = \frac{J_{N_2,c}}{X_{N_2,c}} \quad (1)$$

$$J_{TG,c} = J_{t,c} \cdot X_{TG,c} \quad (2)$$

$$X_{TG,a} = (1 - X_{H_2O,c}) \cdot \frac{J_{TG,a}}{J_{TG,a} + J_{He,a}} \quad (3)$$

$$j_{crossover} = \frac{J_{TG,c}}{X_{TG,a} \cdot A} \quad (4)$$

Experimental

In the permeability measurement, the cell temperature was set to 80°C. During the permeability measurement, nitrogen and a mixture of target gas and helium were supplied in a co-flow configuration to the cathode and the anode, respectively. At the cathode side, nitrogen was supplied with a flow rate of 50 ml min⁻¹, while at the anode side, the mixture of target gas and helium was supplied with a total flow rate of 200 ml min⁻¹, in which

the target gas accounts for 90%. Using the back pressure regulator, the pressure at the cathode was maintained at 1.5 bar_a, whereas the pressure at the anode was set to different values, as shown in Figure 1a. Gas humidification was carried out by using bubble type humidifiers connected to the gas source and the inlets of the cell. For the measurement under completely dry conditions, this connection was closed and the gases were directly fed to the cell via a bypass.

The mass spectrometer was connected to the outlet of the cathode to measure the concentrations of the target gas, helium and water vapor. Calibration of the mass spectrometer was conducted before starting a new individual measurement for a membrane. Prior to supplying the target gas and helium to the anode side, both sides were fed with pure nitrogen humidified to a certain RH that was used in the following measurement of gas permeability, and the “background concentration” of each gas of interest was measured. During the following permeability measurement, the “background concentration” was subtracted to obtain the actual concentration of the permeant molecules of interest.

The membranes were prepared by grafting styrene onto pre-irradiated ETFE film (25 μm thickness) followed by sulfonation (ETFE-*g*-PSSA). Some relevant *ex situ* properties of the investigated membrane are shown in Table 1. The obtained membrane was dried in air before it was laminated with gas diffusion electrodes to form a membrane-electrode assembly (MEA) in a hot-press (110°C/2.5 MPa/180 s). Subsequently, the MEAs were assembled into a graphite single cell, which comprised a straight flow field machined into graphite plates. The cell with an active area of 16 cm² was employed for gas permeability measurement. For the cell assembly, a gasket (100 μm PTFE) and sub-gasket (25 μm PEN) were used.

Sample	Graft level (wt-%)	IEC (mmol/g)	Thick- ness (μm)	Water uptake (%)
ETFE- <i>g</i> -PSSA	23%	1.67±0.06	40±1	32.3±2.6
ETFE	n.a.	n.a.	25	n.a.
Nafion [®] 212	n.a.	1.10±0.02	56±1	33.7±1.6

Table 1. *Ex situ* properties of the membranes and film used in this study. Thickness in wet state is shown except for ETFE. IEC is the ion exchange capacity.

Results

Hydrogen and oxygen permeability as a function of RH of Nafion[®] 212 (N212), the pure styrene grafted and sulfonated membrane with a graft level of 23% (S 23), and ETFE base film is presented in Figure 3. The styrene based membrane shows lower permeability values for both hydrogen and oxygen than the ETFE base film under dry condition (i.e. ~0% RH). However, a gradual increase of gas permeability with increasing RH is seen in the styrene based membrane, in which the permeability is around two times higher than that in the ETFE base film at the highest RH (i.e. ~100% RH). In contrast, there is no change in gas barrier properties for the ETFE base film at different RH. With increasing RH, the permeability of hydrogen and oxygen in Nafion[®] 212 shows a more pronounced increase than in the styrene based membrane, although both of them share low permeability values at the dry condition. At the highest RH, the permeability values of hydrogen and oxygen in Nafion[®] 212

are more than 2.5 times and 3.5 times higher, respectively, than in the styrene based radiation grafted membrane. The difference in gas barrier properties between PFSA membranes and radiation grafted membranes has been observed before using an electrochemical method to measure hydrogen crossover current density at 100% RH [2], with which the results from this study are in good agreement. It again shows that radiation grafted membranes can offer superior gas barrier properties compared to PFSA based materials. The permeability of oxygen in Nafion[®] 212 is on the same order of magnitude as the results reported earlier in the literature, which were obtained using an electrochemical method, for example, $1.8 \cdot 10^{-13} \text{ mol cm s}^{-1} \text{ cm}^{-2} \text{ kPa}^{-1}$ at ~100% RH and $1.2 \cdot 10^{-13} \text{ mol cm s}^{-1} \text{ cm}^{-2} \text{ kPa}^{-1}$ at ~50% RH, respectively [3].

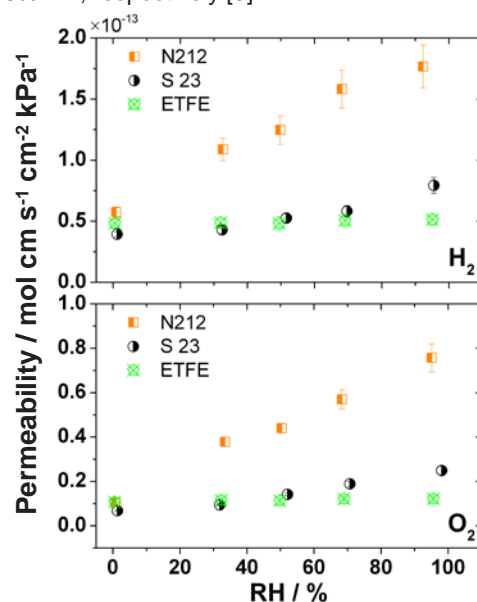


Figure 2. Gas permeability in the ionomer membranes and ETFE base film measured at 80°C.

Conclusion

A method that uses a mass spectrometer to quantify the gas barrier properties of polymer electrolyte membranes in the fuel cell is developed. The permeability of hydrogen and oxygen in a styrene grafted membrane, ETFE base film and Nafion[®] 212 is measured as a function of RH. The results show that the radiation grafted membranes and Nafion[®] 212 share the same trend of increasing gas permeability with RH, while the ETFE base film does not show RH dependency. The difference in gas barrier properties between the styrene grafted membrane and Nafion[®] 212 becomes more pronounced with RH, showing much lower permeability in the former than in the latter at high RH.

Acknowledgement

Funding by the Swiss Federal Office of Energy (project no. 102245) is gratefully acknowledged.

References

- [1] L. Gubler, L. Bonorand, ECS Trans. **58**, 149-162 (2013).
- [2] Z. Zhang, K. Jetsrisuparb, A. Wokaun, L. Gubler, J. Power Sources **243**, 306-316 (2013).
- [3] J. Zhang, H.A. Gasteiger, W. Gu, J. Electrochem. Soc. **160**, F616-F622 (2013).

Towards gas diffusion layers with patterned wettability

A. Forner Cuenca, L. Gubler, T.J. Schmidt, P. Boillat

phone: +41 56 310 5125, e-mail: antoni.forner@psi.ch

The gas diffusion layer (GDL) plays an important role in the water management in PEFCs. Mass transport performance losses are related with the partial filling of porous media by water, limiting the gas reactant access to the catalyst layer. Advanced water management strategies are required to address this issue. The general idea is to define hydrophilic pathways to force the water to flow by them and vacate the rest of the area for the transport of gases, decreasing the tortuosity.

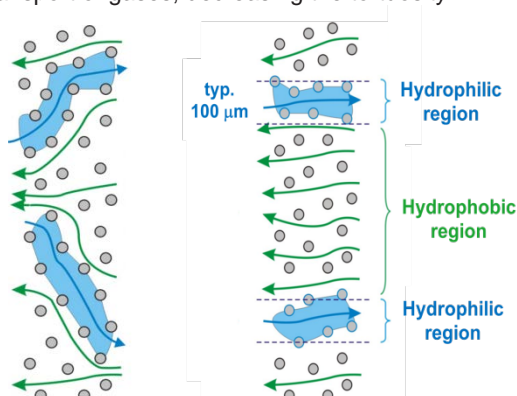


Figure 1. Illustration of the relation between the pathways for liquid water (blue) and for reactant gases (green) in porous materials. Left: in standard hydrophobic GDL. Right: in the new proposed material.

GDLs are carbon fiber based porous materials arranged in different configurations: felt, paper or cloth with a thickness of 150-300 μm . A polymeric coating (PTFE mainly) is usually applied in order to increase the hydrophobicity. The left side of Figure 1 shows the standard commercially available material, where the coating is equally distributed and the capillary pressure gradient will define the water pathway. On the right side, our proposed material has hydrophilic regions created via surface functionalization of the coating. A similar approach consisting of laser perforation of the GDL [1] to create cylindrical passages as water removal channels was reported. The advantage of our approach is a full flexibility in the pattern design, without compromising the mechanical integrity of the GDL. In this report, we present first steps towards the realization of the proposed material.

The functionalization of the coating is performed via radiation grafting (Figure 2), targeting to achieve a surface modification of the coating (not a bulk process). Surface activation sources like plasma seems suitable for this application. Nevertheless, the porous structure skeleton is expected to entail notable shadow effects. For that reason, penetrating radiation (e- beam) is chosen. Patterned masks are used to selectively stop the electrons, and allow the definition of rectangular activated stripes (in the range of 200-1000 μm width). Therefore, the verification of an acceptable resolution and the effectiveness of the blocking-mask are two fundamental points. The electrically conductive carbon fibers composing the GDLs are expected to cause scattering (as

schematized in Figure 3) and this effect was further investigated.

Acrylic acid is an attractive candidate due to its low price and favorable reaction kinetics. By controlling the conditions [2,3] (irradiation dose, reaction time, monomer concentration, temperature, presence of additives...), a surface grafting is targeted. The choice of the grafted monomer will define the minimum surface contact angle (CA) which can be reached. For the poly(acrylic acid), values of 55° have been reported. Other candidates, such as poly(vinylamine) can lower the CA to values as low as 10° [4], resulting in differences of 40% in the capillary pressure.

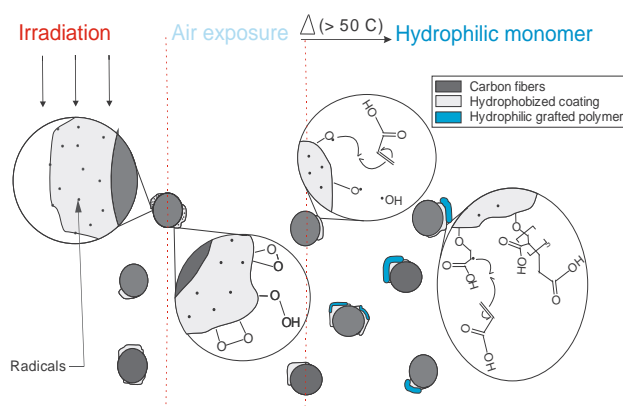


Figure 2. Illustration of the grafting mechanism on the hydrophobized coating of the carbon fibres. Acrylic acid in the hydrophilic monomer in the example.

Experimental

Samples were electron activated (Studer Leoni, Däniken) with doses of 0.5 kGy (1 MeV). The configurations shown in Figure 3 were used to study the resolution. On the left side setup, a GDL is sandwiched between mask and FEP film. On the right side, the FEP film is placed directly behind the mask. In both cases, FEP films were grafted and characterized. The signal behind the GDL contains information about the effect of scattering. Differences between both signals are expected to allow identifying the impact of scattering within the GDL on the achievable resolution. The mask is made out of stainless steel (10x10cm) and has a thickness of 2 mm. Rectangular slits having a width of 1, 0.5 and 0.2 mm, respectively, were cut using water jet (Microwaterjet AG). FEP (Gauge 100) of 25 μm thickness was obtained from DuPont and cleaned with ethanol. 24BA (5% PTFE) GDLs were obtained from SGL Sigracet.

Acrylic acid was used as grafted monomer, dissolved in water (15% weight). The solution was introduced together with the films into a 600 mL stainless steel reactor. Deoxygenation of the reaction medium was done by bubbling argon during 60 min. The reactor was then placed in a water thermal bath at 60°C during 90 min. A

previous systematic study was carried out to find out suitable conditions for the grafting process. A very low polymerization may not allow identifying the acrylic acid, and a very aggressive one would hinder the results due to diffusion and further reaction all over the area (not only in the initially activated regions). After the reaction time ended, the samples were rinsed with ethanol and soaked in water overnight.

Circular samples of 8 mm diameter were punched for the replacement of the protons with sodium. Each sample was ion exchanged in 50 mL 0.025M NaOH overnight. Due to the weak acidity of the acrylic acid, the use of a strong base was required to force the detachment of the protons and allow the sodium to take its place. Afterwards, samples were sputtered with chromium (Leica EM SCD 500) to a thickness of around 8 nm. Energy dispersive X-ray analysis (EDX) mapping (512 pixel and 64 frames -51.5 min-) of the samples was performed for the following elements: C, O, F and Na. The edge energies of oxygen (0.537 keV) and fluorine (0.686 keV) are very close and superposition of the peaks does not allow a clear identification of the carboxylic acid group based on oxygen concentration. The replacement of the proton by sodium with a distant energy (1.067 keV) allows a clear identification of the carboxylic group.

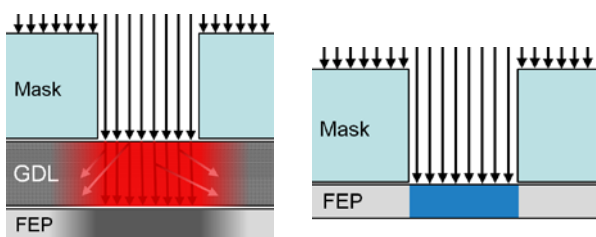


Figure 3. Illustration of the setup used in the resolution experiment. Left: combination of mask-GDL-FEP to study the activation behind the GDL. Right: combination of mask-FEP to study the activation when no GDL is present.

Results and Discussion

Figure 4 shows the resulting grafting profile of the FEP films irradiated using both configurations. The grafting is quantified as the sodium to carbon ratio calculated from the EDX maps. The results show a significant increase of the sodium concentration in the region corresponding to the mask aperture for both cases. The obtained resolution is promising, although some improvements are necessary to reach our target (lines/spacings of 100 μm). We observed no clear differences between the samples irradiated with and without a GDL, indicating a negligible impact of scattering.

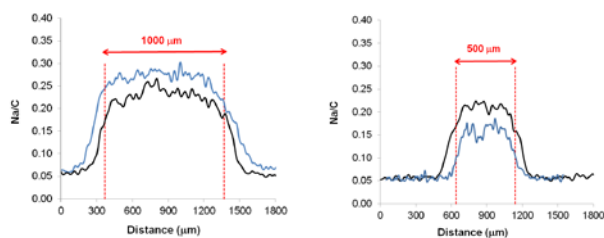


Figure 4. Results of the resolution checkout experiment. Left: 1000 μm mask thickness. Right: 500 μm mask thickness. The black line represents configuration with GDL and the blue line without GDL.

A base value of around 0.05 Na/C is observed in the area adjacent to the exposed region. This effect has been further investigated by applying the sodium replacement step on non-irradiated samples. The signal obtained in that case was nearly zero, indicating that the measured background is not an artefact of the EDX system. The backscattering of the electrons coming from the transporting trays may be one possibility for the activation of the surroundings. The nature of the grafting process (diffusion) could also explain the presence of acrylic acid groups in the periphery. However, the measured background extends far away from the grafted line, which is not consistent with this explanation. Finally, a possibility is that the mask is not entirely blocking the radiation, and increasing its thickness could decrease the amount of grafting in the non-targeted regions.

In summary, we could validate the adequacy of the electron beam radiation for the activation step, at least for the resolution currently achievable with our grafting process.

Acknowledgement

Funding by the Swiss National Science Foundation (project no 143432) is gratefully acknowledged.

References

- [1] D. Gerteisen, T. Heilmann, C. Ziegler, J. Power Sources **177**, 438-354 (2008).
- [2] S. Alkan-Gürsel, L. Gubler, B. Gupta, G.G. Scherer, Adv. Polym. Sci. **215**, 157-217 (2008).
- [3] A. Chapiro, G. Derai, Eur. Polym. J. **7**, 1595-1613 (1971).
- [4] S. Neuhaus, C. Padeste, N.D. Spencer, Langmuir **27**, 6855-6861 (2011).

SCIENTIFIC ACHIEVEMENTS 2013

BATTERIES & SUPERCAPACITORS

MATERIALS

Increasing the specific charge of graphite by the addition of silicon

C. Bünzli, D. Cericola¹, T. Hucke¹, M.E. Spahr¹, P. Novák, J.L. Gómez-Cámer

phone: +41 56 310 5770, e-mail: juan-luis.gomez@psi.ch

Negative electrodes in nowadays Li-ion batteries for portable electronics or electric vehicles consist mainly of graphite or other carbonaceous materials [1]. Graphite based negative electrodes provide very good cycling stability, but the maximum specific charge that can be reached with these materials is 372 mAh/g.

On the other hand, alloying materials such as Si [2], Sn [3], Al [4] and related intermetallics [5] are claimed to be the materials of choice for the negative electrodes for next generation Li-ion batteries due to their high specific charge. Despite that Si can deliver a theoretical specific charge of 3579 mAh/g – corresponding to an alloy with composition $\text{Li}_{3.75}\text{Si}$ – electrodes based on Si are far inferior in cycling stability compared to graphite electrodes. Nevertheless, recent advances in the field of electrode engineering have successfully increased the reversibility of Si electrodes via better management of the large volume changes taking place upon lithiation.

A compromise solution between cycling stability and higher specific charge can be found in the combination of graphite and Si. Many efforts have been put in the last two decades in the synthesis of Si/C composites, typically with less than 50 wt% Si, including simple methods such as plain mixtures or milling. Here we investigate different compositions and cycling conditions of low Si loading Si/C electrodes, targeting stable cycling conditions at a specific charge larger than 450 mAh/g.

Experimental

Silicon nanoparticles (30 – 50 nm, Nanostructured & Amorphous Materials, Inc., USA) were added to two graphite powder samples, KS6 and SLP30, and to PC6 coke powder (TIMCAL, SA). The electrode coatings were prepared with three different compositions:

- 95 wt% graphite/coke, 1 wt% SC65 conductive additive, 4 wt% binder
- 4.75 wt% Si (30 – 50 nm), 90.25 wt% graphite/coke, 1 wt% SC65 conductive additive, 4 wt% binder
- 9.25 wt% Si (30 – 50 nm), 85.75 wt% graphite, 1 wt% SC65, 4 wt% binder

Two binders were tested, polyvinylidene fluoride (PVDF KF polymer, W#9100, Kureha) and a mixture of carboxymethyl cellulose (CMC, Alfa Aesar) with polyacrylic acid (PAA, 25 wt% sol. in H_2O , Average M.W. 240.000, Alfa Aesar) in 1:1 weight ratio, from now on called CMC/PAA. Both, N-methyl pyrrolidone (NMP) and water based slurries, were prepared from a simple mixture of the active materials, graphite and Si, in the weight percentages indicated above. First, the binder was dissolved, PVDF in NMP or CMC/PAA in water, and carbon black pre-mixed with the binder, then Si nanoparticles were mixed in, previous to the addition of graphite or coke powders. The slurries were cast onto copper foil at the necessary wet thickness to prepare electrodes with the desired mass loading of 7 – 8 mg. Then the casted electrodes were dried under vacuum at 80 °C overnight, in the case of PVDF containing electrodes. The electrodes with CMC/PAA mixture as a binder were heated at

150 °C under vacuum in order to favour the cross-linking reaction between CMC and PAA via condensation of hydroxyl groups (R–OH) and carboxylic acid groups (R–COOH) to form ester type bonds (R–CO–O–R') [6].

Prior to electrochemical tests, 13 mm diameter electrodes were heated at 120 °C under vacuum and inserted into an Argon filled glovebox (<1 ppm O_2) where coin type test cells, described elsewhere [7], were assembled. Standard electrochemical cells were used to perform the galvanostatic cycling of the cells. Glass fibre separator soaked in LP30 electrolyte (ethylene carbonate: diethyl carbonate (EC:DEC=1:1), 1M in LiPF_6) and Li foil as counter electrode were used in the half-cells. Fluoroethylene carbonate (FEC) additive was added to the electrolyte for some of the electrochemical tests in the amount of 2 wt%.

Results

Electrodes prepared with PVDF as the binder are presented in Figure 1. Both graphites, KS6 and SLP30, exhibited good cycling behaviour with similar specific charges, whereas the coke sample, PC6, delivered lower specific charges, as expected. In all cases, when silicon nanoparticles are included in the electrode formulation, the specific charge fades in the first 10 – 15 cycles to values corresponding to graphite or coke contribution. In the case of SLP30 graphite, the specific charges dropped even below this level, indicating that SLP30 electrodes with Si failed according to a different mechanism. Coulombic efficiencies were found to be lower at the initial cycles for the samples containing Si, increasing afterwards to similar values – in the range of 98-100% – when the specific charge dropped to that of the graphite or coke contribution.

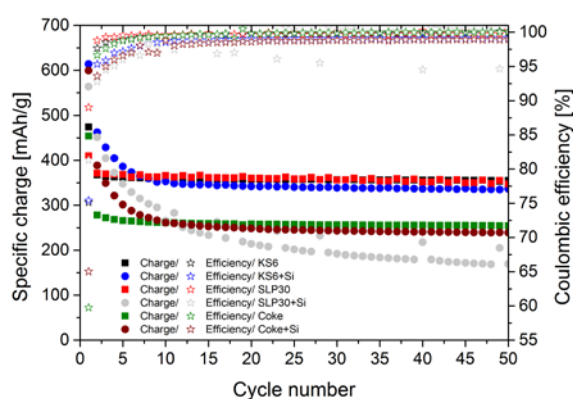


Figure 1. Comparison of the specific charge and coulombic efficiency with cycle number of KS6 and SLP30 graphites, and PC6 coke, with and without silicon using PVDF binder.

Due to its higher initial specific charge in combination with Si, KS6 graphite was chosen for further investigations regarding electrode formulations.

Figure 2 shows the specific charges of the electrodes prepared with KS6 graphite, alone or with Si, and the crosslinked CMC/PAA binder. The electrode containing only KS6 performed similarly to that prepared with PVDF

¹ TIMCAL S.A., Bodio

binder (see Figure 1), on the contrary, KS6 electrode prepared with 4.75 wt% Si particles and the crosslinked binder exhibited much better charge retention than its PVDF counterpart. The KS6/Si electrode with 4.75 wt% Si and CMC/PAA maintained a specific charge superior to 500 mAh/g for at least 20 cycles, fading rapidly afterwards to charge values close to the graphite's. When the amount of Si in the electrode is doubled, to 9.5 wt%, the specific charge increases from 500 to almost 700 mAh/g. The cycling stability exhibited by these electrodes is similar to that of the electrodes containing 4.75 wt% Si in the initial cycles, however, the coulombic efficiency is lower and the fading is more pronounced for the higher Si content.

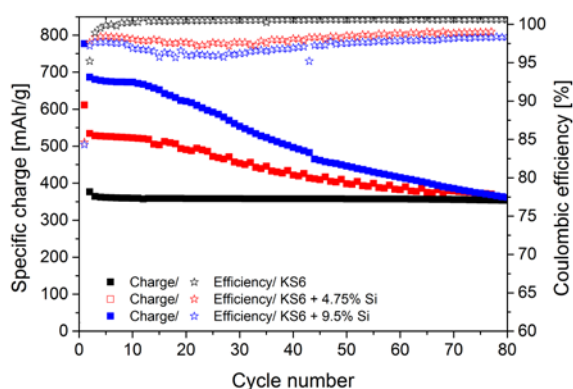


Figure 2. Comparison of the specific charge and coulombic efficiency with cycle number of KS6 graphite alone and with 4.75 and 9.5 wt% silicon using CMC/PAA binder.

A possible failure mechanism for Si containing electrodes is the electrical isolation of Si particles due to an excessive growth of the electrolyte decomposition film (SEI) upon cycling. Electrolyte additives, e.g. FEC [8], are known to mitigate this effect by creating a stable SEI film at the earlier stages of cycling. Figure 3 shows the electrochemical behaviour of KS6 graphite electrodes containing Si particles, prepared with the crosslinked CMC/PAA binder and cycled against Li counter electrode in standard and FEC containing LP30 electrolyte.

As can be observed in Figure 3, electrodes cycled in the presence of FEC additive exhibit much better charge retention with similar or slightly better coulombic efficiency, maintaining over 500 mAh/g in charge during at least

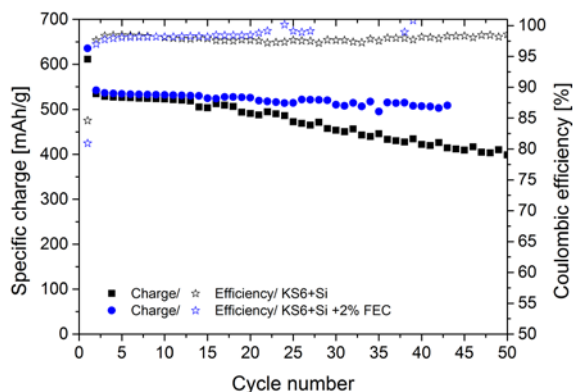


Figure 3. Comparison of the specific charge and coulombic efficiency with cycle number of KS6 graphite with and without silicon using CMC/PAA binder and 2% fluoroethylene carbonate (FEC) additive to the electrolyte.

40 cycles, vs. the 400 mAh/g exhibited in the standard electrolyte.

Conclusions

Graphite based electrodes containing Si particles have been prepared by simple mixture method and successfully cycled against lithium. A crosslinked binder composed of carboxymethyl cellulose and polyacrylic acid has been found to enhance the cycling properties of these electrodes. Furthermore, improved cycling stability has been reached using fluoroethylene carbonate as electrolyte additive. A specific charge superior to 500 mAh/g per composite mass has been achieved during 40 cycles before further electrode optimization.

Acknowledgement

Financial support from TIMCAL S.A. is gratefully acknowledged.

References

- [1] M.R. Palacín, *Chem. Soc. Rev.* **38**, 2565 (2009).
- [2] J.L. Gómez-Cámer, J. Morales, L. Sánchez, *J. Mater. Chem.* **21**, 811 (2011).
- [3] A. Caballero, J. Morales, L. Sánchez, *Electrochem. Solid State Lett.* **8**, A464 (2005).
- [4] Y. Hamon, T. Brousse, F. Jousse, P. Topart, P. Buvat, D.M. Schleich, *J. Power Sources* **97-98**, 185 (2001).
- [5] C.Y. Wang, Y.S. Meng, G. Ceder, Y. Li, *J. Electrochem. Soc.* **155** (9), A615 (2008).
- [6] B. Koo, H. Kim, Y. Cho, K.T. Lee, N.S. Choi, J. Cho, *Angew. Chem. Int. Ed.* **51**, 11836 (2012).
- [7] P. Novák, W. Scheifele, F. Joho, O. Haas, *J. Electrochem. Soc.* **142**, 2540-2544 (1995).
- [8] R. McMillan, H. Slegel, Z.X. Shu, W. Wang, *J. Power Sources* **81-82**, 20 (1999).

Effect of different separators on the performance of Li-S cells

J.M. Conder, S. Urbonaite, L. Gubler, P. Novák

phone: +41 56 310 2120, e-mail: joanna.conder@psi.ch

The lithium sulfur battery (Li-S) is a promising electrochemical system for large-scale energy storage applications. The sulfur electrode has a theoretical specific charge of 1672 mAh g^{-1} , which results in energy density of ca. 2600 Wh kg^{-1} , much higher than the values for commercial Li-ion batteries based on intercalation materials (i.e. LiFePO_4 or LiMn_2O_4) [1]. Although being safe, environmentally friendly, and cost effective, the Li-S battery faces a number of challenges that need to be overcome. These include short cycle life, low charging efficiency, and high self-discharge rate – problems arising from the highly soluble polysulfides (Li_2S_n , $2 < n < 8$) forming during the cycling of a Li-S battery [2]. One approach to tackle these limitations is to design a single Li-ion conducting polymer separator in the form of a cation-exchange membrane. It is believed that this kind of membrane with a thin cation-exchange barrier layer (polymer skin) will allow selective Li-ion transport. Moreover, it is expected to suppress polysulfides crossover to the anode and their deposition on lithium, forming an insulating layer and leading to specific charge loss. The chemical modification and functionalization to obtain a composite porous membrane can be carried out by grafting monomers comprising cation-exchange constituents into surface-near regions of commercial porous separators.

In this work, different porous substrates were tested as separators in order to select a suitable support to be subsequently modified and functionalized by graft copolymerization. Following polyolefins were chosen for preliminary tests: Celgard 2400 (single layer polypropylene separator), polypropylene (PP TreoPore), and ultra-high molecular weight polyethylene (UPE SureVent).

Experimental

Standard Li-S composite electrodes were prepared by mixing 60% of sulfur and 30% of carbon black, and using 10% of PEO binder in a solution of acetonitrile. Slurries were mixed by turbostrirring, and then doctor-bladed onto carbon-pre-coated aluminum foil. After at least 24 h of drying in air at room temperature, electrode discs were punched out and transferred to a glove box for assembly. Li-S cells were assembled in Ar atmosphere into coin-type cells by placing the separator onto the composite electrode, introducing $50 \mu\text{l}$ of 1 M LiTFSI in DME:Diox (2:1) standard electrolyte or $50 \mu\text{l}$ 1 M LiTFSI in DME:Diox (2:1) electrolyte with 0.5 M LiNO_3 additive. LiTFSI stands for lithium bis(trifluoromethane sulfonyl)imide, DME is dimethoxyethane and Diox is 1,3-dioxolane [3].

Cells with lithium counter electrode were galvanostatically cycled at room temperature between 1.8 and 2.7 V vs. Li^+/Li at C/5 rate (the C-rate is defined as $I=1672 \text{ mA g}^{-1}$ of S). The performance of different porous substrates in the role of separator was tested and their properties were compared. Selected features of chosen materials are listed in Table 1.

Material	Thickness [μm]	Porosity [%]	Pore size [μm]	Shrinkage MD [%]	Shrinkage TD [%]
Celgard 2400	25	41	0.04	0.0 ^a	>7.0 ^a
PP TreoPore	30	~60	<0.05	4.0 ^b	0.03 ^b
UPE SureVent	67	- ^c	0.05	- ^c	- ^c

Table 1. Properties of the separators tested in the Li-S cells; ^a @ $90^\circ\text{C} / 1 \text{ hour}$, ^b @ $100^\circ\text{C} / 1 \text{ hour}$, ^c not specified. Data taken from base films specifications.

All separators used in this study were dried under vacuum for 12 h at 60°C prior to assembly. Celgard 2400, a standard separator for Li-S cells, was used in order to create a benchmark for further experiments.

The morphology of pristine porous substrates was investigated using a scanning electron microscope (SEM) Ultra 55, Zeiss (Germany), at an acceleration voltage 5 kV.

Results

Figures 1 and 2 show the SEM micrographs of pristine polyolefins. It can be seen that the surface morphology varies from the anisotropic structure of Celgard 2400 (Figure 1 top) with parallel arrays of pores [3], the isotropic, flowerlike structure of UPE (Figure 2) to the more disordered, branchlike PP structure (Figure 1 bottom).

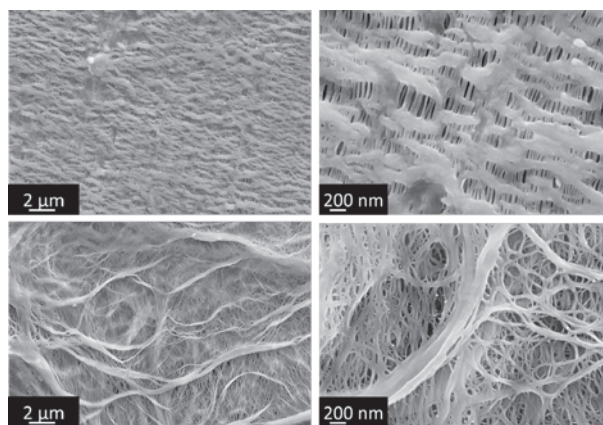


Figure 1. SEM micrographs of unmodified separators: Celgard 2400 (top) and PP TreoPore (bottom) at low (left) and high (right) magnifications.

In addition, the UPE material, widely used as a separation membrane in microfiltration, has a slightly different morphology on one side (Figure 2, top) than on the other one (Figure 2, bottom). It is also almost three times thicker than Celgard 2400 and PP TreoPore film. Based on these observations, one could expect that the individual morphological features of each porous material will find their reflection in the electrochemical performance of Li-S batteries. Thus, all three selected separators were tested by galvanostatic cycling in Li-S cells.

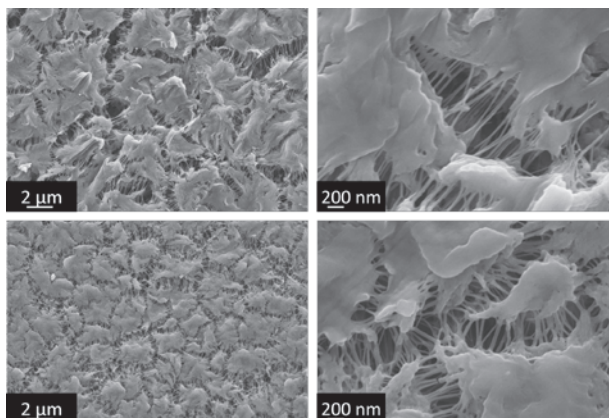


Figure 2. SEM micrographs of unmodified UPE SureVent material: one side (top) and the reverse side (bottom) at low (left) and high (right) magnifications.

Figures 3 and 4 show the specific charge as well as the coulombic efficiency as a function of the number of cycles. As can be seen, both selected polymeric materials show cycling behavior similar to that of Celgard 2400 (used here as a reference separator) regardless of the type of electrolyte introduced. In all cases after 20 cycles, upon cycling at a C/5 rate using the electrolyte without additive, a specific charge of ca. 660–695 mAh g⁻¹ is retained. It decreases slightly after 30 cycles to ca. 625–638 mAh g⁻¹.

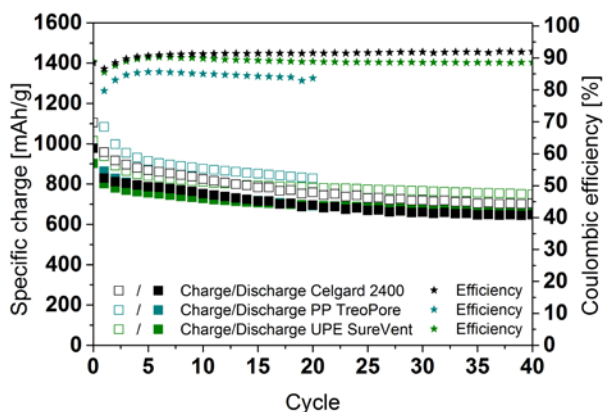


Figure 3. Cycling performance of Li-S cells with different, unmodified separators at a rate C/5 in 50 μl of 1M LiTFSI in DME:Diox (2:1) at RT.

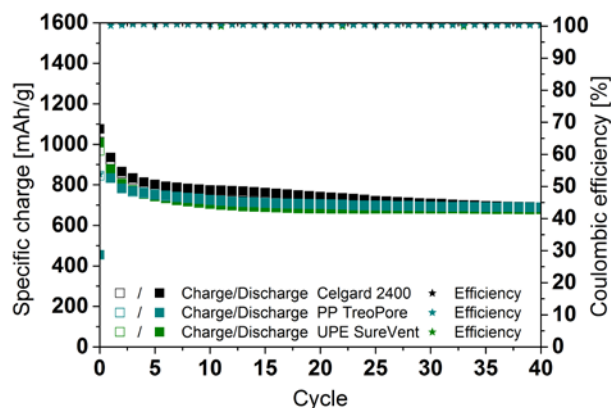


Figure 4. Cycling performance of Li-S cells with different, unmodified separators at a rate C/5 in 50 μl of 1M LiTFSI with 0.5 M LiNO₃ in DME:Diox (2:1) at RT.

When LiNO₃ is used as an additive (Figure 4) the coulombic efficiency is improved reaching almost 100%, whereas in case of the electrolyte without an additive the efficiency is about 80 to 90 %.

Conclusions

Three different polymeric materials have been galvanostatically tested as separators in Li-S cells. Despite significant differences in physical and morphological properties, the cycling performance of all three separators was surprisingly similar. This finding suggests that the selection of the optimal porous support, which will be further modified, is not critical and can be therefore, based on polymer susceptibility to swelling in the electrolyte and its ability to graft copolymerization.

Acknowledgement

The authors thank the Swiss National Science Foundation (project no 200021_144292) for financial support.

References

- [1] S. Evers, L.F. Nazar, *Acc. Chem. Res.* **45**, 1135-1143 (2013).
- [2] S.S. Zhang, *J. Power Sources* **231**, 153-162 (2013).
- [3] S. Urbonaite, P. Novak, *J. Power Sources* **249**, 497-502 (2014).
- [4] L.C. Sawyer, D.T. Grubb, G.F. Meyers, *Polymer Microscopy*, Springer (2008).

Grafting of 4-styrenesulfonic acid sodium salt hydrate (SSNa) onto porous PP separator and effects of post-grafting treatment

J.M. Conder, S. Urbonaite, P. Novák, L. Gubler

phone: +41 56 310 2120, e-mail: joanna.conder@psi.ch

The constantly growing demand of cation-exchange polymer membranes for separation, electrochemical, and biological applications, as well as the high cost of commercially available perfluorinated ionomeric membranes have driven research to develop alternative synthetic membranes [1]. These membranes can be classified in two groups: symmetric and asymmetric polymeric composites. The latter consists of two layers, each with different structure and permeabilities (Figure 1). The top, very thin, so-called dense skin layer ensures the selective permeation properties. The bottom porous support layer provides mechanical strength to the polymeric composite [2].

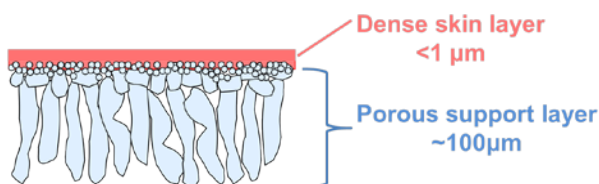


Figure 1. Schematic cross-sectional view of a composite asymmetric membrane, adapted from [2].

The main advantage of this type of membranes is that the dense skin layer as well as the following sublayer can be separately designed and functionalized leading thus to customizable membranes dedicated to different applications. One of the possible methods to prepare the membrane with tailored properties is graft copolymerization of cation-exchange groups (e.g. sulfonate) onto surface-near regions.

In this work, grafting of 4-styrenesulfonic acid sodium salt hydrate (SSNa) onto plasma activated porous polypropylene (PP, TreoPore) base polymer as well as two different post-grafting treatment pathways are presented and discussed.

Experimental

The preparation of ion exchange membranes based on porous PP was carried out by adapting a one-step procedure reported for grafting acrylic acid and sodium styrene sulfonate onto high-density polyethylene (HDPE) film [3]. The porous PP was exposed to an Ar plasma (30 W, gas flow rate of 72 ml/min) for 5 min from one side. The lag time after plasma treatment during which the activated film was exposed to ambient conditions before starting the copolymerization was 30 min. The grafting reaction mixture consisted of 4-styrenesulfonic acid sodium salt hydrate (SSNa, 10 v-%), water (40 v-%), and isopropanol (50 v-%). The reaction was carried out in a temperature-controlled bath at 60°C. After a predefined time, the grafted membranes (PP-g-PSSNa) were removed from the reactor, washed in 60 °C distilled water overnight, and vacuum-dried (60 °C).

In some experiments, instead of washing the PP-g-PSSNa membranes with water, a multi-stage solvent exchange and evaporation method was applied [4]. After

24 h grafting at 60 °C, the membranes were first immersed in EtOH. Then, a second volatile solvent, here n-pentane replaced the EtOH. In a final step, the films were dried at 60 °C under vacuum. All grafted films were characterized with Fourier transform infrared spectroscopy (FTIR) and gravimetrically. The morphology of the pristine porous substrate as well as of the PP-g-PSSNa membranes was investigated using a scanning electron microscope (SEM) Ultra 55 (Zeiss Germany) at an acceleration voltage of 5 kV.

Results

The kinetics for the grafting of SSNa monomer onto porous PP base film is presented in Figure 2. It can be seen that the graft level increases gradually with the increase of grafting time within the limits of the durations studied (2-24 h).

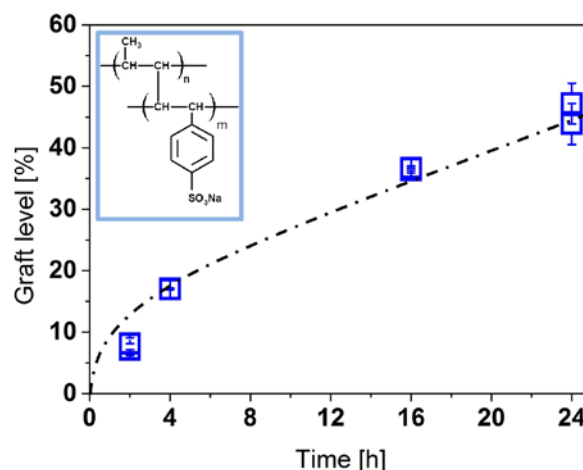


Figure 2. Grafting kinetics of SSNa onto porous PP base film.

In order to confirm that SSNa was successfully grafted onto PP porous films, FTIR spectroscopy was used. The enlarged view of FTIR spectra of PP pristine film and ion-exchange membrane modified with sodium sulfonate ($-\text{SO}_3\text{Na}$) groups are shown in Figure 3. Polypropylene used as a base film has strong bands near 2950 cm^{-1} (not displayed here), 1460 cm^{-1} , and 1380 cm^{-1} . Additionally, bands of medium intensity are observed near 1155 and 970 cm^{-1} . [5]. The main difference between the base film and the membrane grafted with bulky sulfonate groups is the sequence of peaks in the region $1200\text{--}1000\text{ cm}^{-1}$. Thus, the bands present in the spectrum of the PP-g-PSSNa membrane at 1182 , 1130 , 1044 , and 1011 cm^{-1} are due to the presence of $-\text{SO}_3\text{Na}$ groups [6].

Grafting of SSNa and the subsequent treatment has been found to induce not only structural changes but also geometrical changes of obtained membranes, compared to the pristine PP substrate. Grafting was found to have a greater influence on the length (MD = machine direction) and the thickness of the PP membrane than on its width (TD = transverse direction) (Figure 4).

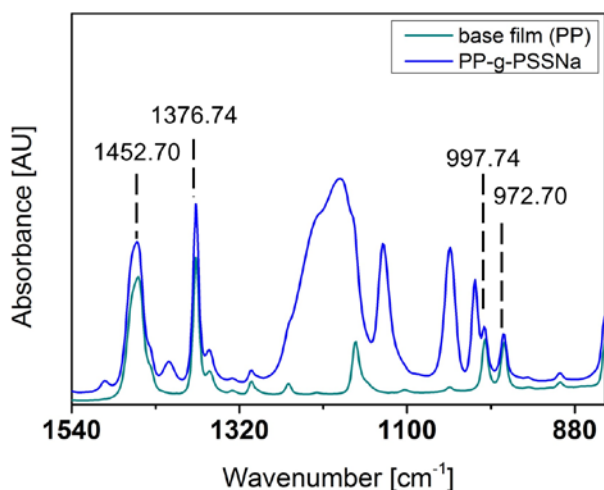


Figure 3. Enlarged FTIR spectra of PP pristine film and PP-g-PSSNa film in the range of 1540-840 cm^{-1} .

The observed shrinkage as well as the different appearance of the grafted membranes (white/translucent random regions) was correlated to the drying step of the PP-g-PSSNa. Therefore, to reduce and/or suppress inhomogeneity of the grafted membranes, post-grafting treatment was further investigated.

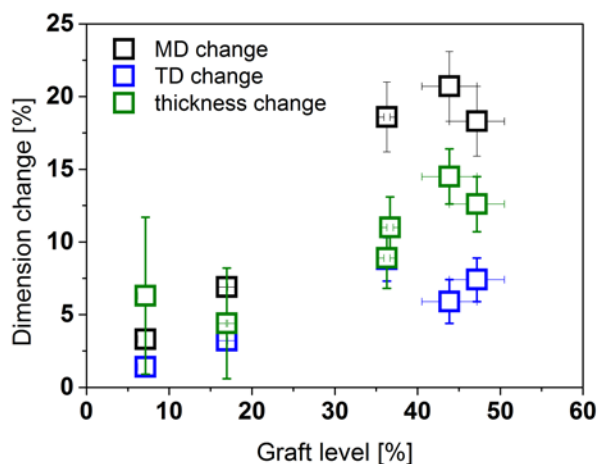


Figure 4. The relationship between graft level and the subsequent dimensional changes of the PP grafted polymers.

According to Davis et al. [4] a way to preserve the asymmetric structure of the membrane is to not dry the membrane directly in air. Hence, a multi-stage solvent exchange and evaporation method is introduced. In this method, a water-miscible solvent, e.g. EtOH, first replaces the water in the membrane. Afterwards, the EtOH is replaced by a second, volatile solvent such as hexane or n-pentane, which is air-evaporated in the final step. The latter step is made to reduce the capillary force inside the pores and, consequently, to preserve the asymmetric structure. As this drying procedure seemed to be reasonable, it has been adapted for our studied grafting system. As a result, after 24 h of grafting similar graft level equal to 46% was found when compared to the PP-g-PSSNa membranes washed only with water (Figure 2). Moreover, the inhomogeneity was no longer observed and the shrinkage was only weakly pronounced.

The potential structural differences between those two types of membranes were analyzed by SEM. According

to the micrographs shown in Figure 5 after 24 h of grafting, in both cases (middle and bottom micrograph) the pores of the PP film are gradually being closed. However, on the surface of the membrane treated only with water, some precipitates are present. Presumably, it is remaining unreacted monomer or PSSNa homopolymer which was not entirely washed out.

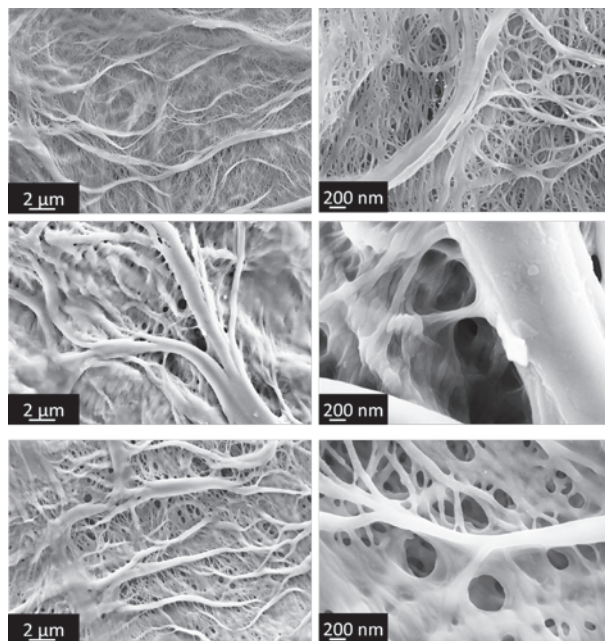


Figure 5. SEM micrographs of PP base film (top), PP-g-PSSNa membrane washed with H_2O after grafting (middle) and the membrane in which the multi-stage solvent exchange and evaporation method was applied (bottom) at low (left) and high (right) magnifications.

Conclusions

SSNa monomer was successfully grafted onto plasma-activated porous PP substrate. The graft level of PP-g-PSSNa membranes varied with the grafting time from ca. 8 % after 2 h up to ca. 50 % after 24 h. Results of the two different post-grafting treatments suggest that this step plays an important role. With a suitable procedure (multi-stage solvent exchange) inhomogeneities in the grafted membranes can be minimized.

Acknowledgement

The authors thank the Swiss National Science Foundation (project no 200021_144292) for financial support.

References

- [1] M.M. Nasef, E.-S.A. Hegazy, *Prog. Polym. Sci.* **29**, 499-561 (2004).
- [2] T. Matsuura, *Synthetic Membranes and Membrane Separation Processing*, CRS Press., Boca Raton, USA (1994).
- [3] J. Zu, M. Wu, J. Zhang, C. Yu, X. Liu, L. Tong, *J Appl Polym Sci* **99**, 3401-3405 (2006).
- [4] Davis et al., US Patent No 4,430,807 (1984).
- [5] G. Socrates, *Infrared and Raman Characteristic Group Frequencies: Tables and Charts*, John Wiley and Sons, Ltd, Chichester, Third Edition (2001).
- [6] The HITRAN 2008 molecular spectroscopic database <http://cfa-www.harvard.edu/hitran//>

New intermetallic compounds as negative electrodes for lithium-ion batteries

J.L. Gómez-Cámer, C. Villevieille, P. Novák

phone: +41 56 310 5770, e-mail: juan-luis.gomez@psi.ch

Lithium ion batteries are the main energy source for many small devices such as laptops or mobile phones and larger devices as e-bikes or electric cars. The current choice of anode materials for lithium ion batteries is graphite, due to its long cycle life, abundance and low cost. However, graphite delivers low specific charge values (372 mAh/g) and several alternatives have been investigated in the recent years [1].

The group of elements capable of react directly with lithium is limited to a group of metals and semimetals among which Si, Sn and Sb are the most important in terms of gravimetric and volumetric energy density (3590 mAh/g and 8365 mAh/cm³ and 372 mAh/g and 975 mAh/cm³ for silicon and graphite respectively).

The main challenge when using the alloy materials in lithium batteries is the enormous volume change associated to the (de)alloying processes. In the case of Si, the volume change can go up to 300% leading to electrical disconnection of active material particles, cracks in the particles (active materials) and in the electrodes (binder and conductive agent) and, at the end, electrode failure. Several strategies to overcome this problem have been proposed in the last years. The most popular are the preparation of Si/C composites and Si-based alloys, either with active or inactive matrices [2].

In this report two Si-based compounds have been synthesized and tested in lithium half cells. The two materials have been synthesized by ball milling with a 3d metal and a matrix of Si and P. Both elements are expected to react with lithium, giving large specific charge values.

Results

Preliminary electrochemical tests were performed using standard electrodes with the ratio active material/carbon black/PVDF of 80/10/10. The specific charge delivered by the MSiP-1 compound cycled between 1.5 V and 5 mV is shown in Figure 1.

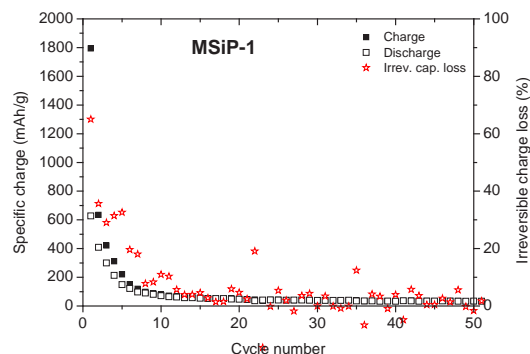


Figure 1. Specific charge and irreversible charge loss for the compound MSiP-1.

The specific charge in the first cycle (ca. 1800 mAh/g) is lower than the expected theoretical one, but still 5 times higher than the specific charge of graphite. The irreversible charge loss is very high and at this stage of

research, electrode engineering is needed to improve the cycle life of the material.

Figure 2 shows the specific charges delivered by the compound MSiP-2. The initial charge (ca. 470 mAh/g) is, lower than the theoretical value and close to the values of graphite; however this material is able to maintain over 200 mAh/g for 30 cycles without any engineering. The irreversible charge loss is also significantly lower than for MSiP-1. The main difference between both electrodes is the amount of inactive matrix, higher in the MSiP-2, buffering more effectively the volume changes and resulting in less pronounced fading.

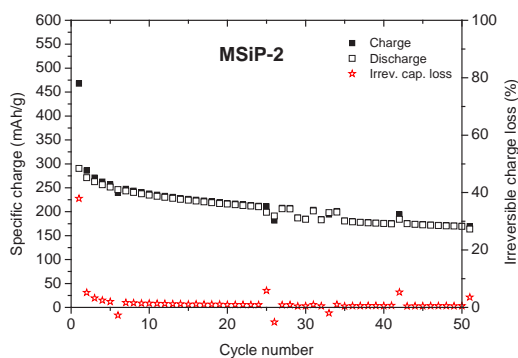


Figure 2. Specific charge and irreversible charge loss for the compound MSiP-2.

Conclusions

New materials based on the MSiP system have been synthesized and their electrochemical properties have been explored. The composition with higher inactive matrix ratio is able to maintain higher charge values with low charge loss during cycling.

Acknowledgment

Financial support from BASF SE is gratefully acknowledged.

References

- [1] W.J. Zhang, *J. Power Sources* **196**, 13-24 (2011).
- [2] U. Kasavajjula, C. Wang, A.J. Appleby, *J. Power Sources* **163**, 1003-1039 (2007).

Investigation of the dilatation behaviour of 0 to 3-dimensional carbons upon charge

M.M. Hantel¹, R. Kötz

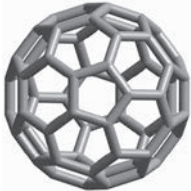
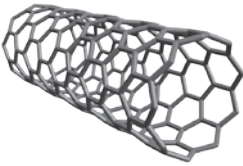
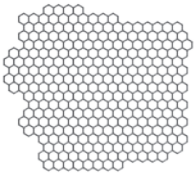
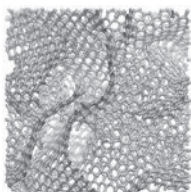
phone: +41 56 310 4189, e-mail: moritz.hantel@psi.ch

Today's energy storage systems, such as batteries and electrochemical double layer capacitors, utilize a variety of carbon materials as both active storage material and conductive additive [1]. Several studies have shown that the employed carbon composite electrodes exhibit dilatation due to electrochemical polarization [2, 3]. This charge induced expansion is expected to be a source for electrode degradation and, hence, the induced mechanical stress might lead to a reduction of the overall lifetime.

Recent investigations [3-7] on the carbon dilatation behaviour were always conducted on a specific carbon allotrope and, hence, the observed effects were only discussed within the morphology boundaries of the employed carbon-electrolyte-combination. As a result, the proposed mechanisms were limited to a specific carbon geometry. In order to extend the scope of these observations a more comprehensive comparison is necessary including different carbon morphologies. The commonly employed carbon allotropes can be classified into [1]: 0-dimensional fullerene-like, 1-dimensional nanotube-like, 2-dimensional graphene based and 3-dimensional activated carbon-like (compare Table 1).

The scope of this work is to review dilatation studies to identify expansion mechanisms which are related to the dimension of the employed carbon.

Table 1. Summary of 0 to 3 dimensional carbon allotropes.

	0 – dimensional carbon Onion like carbon [6] Specific surface area: 400 m ² /g Specific capacitance: ~23 F/g Expansion up to: 0.2%
	1 – dimensional carbon Single walled carbon nanotube [4] Specific surface area: 820 m ² /g Specific capacitance: ~50 F/g Expansion up to: 3.5 %
	2 – dimensional carbon Graphite (graphene based) [3, 7] Specific surface area: 10-20 m ² /g Specific capacitance: N/A Expansion up to: 3.7 %
	3 – dimensional carbon Carbide derived carbon [5, 8] Specific surface area: 1980 m ² /g Specific capacitance: ~ 130 F/g Expansion up to: 1.7 %

Experimental

The expansion behaviour during charge and discharge was investigated using a custom designed dilatometer as described in reference [3]. The dilatometer cell is based on a three electrode design using PTFE bound active carbon for the counter and quasi-reference electrode. In order to have a fixed reference level for the expansion measurements a glass frit (porosity P2: 40-100 µm) is used as the separator. The investigated electrodes were compressed between the glass frit and a movable Ti plunger with an additional weight load of 10 N. Any expansion during the electrochemical experiments was recorded by a displacement transducer DP1S (Solartron Metrology, UK) with an accuracy of 0.06 µm. The electrochemical characterization was done by cyclic voltammetry (IM6e potentiostat, Zahner-Elektrik GmbH&Co. KG, Germany) using a sweep rate of 1 mV/s and the organic electrolyte tetraethylammonium tetrafluoroborate in acetonitrile (1M TEABF₄ / AN).

Results and discussion

Comparing the available dilatation studies reveals a first anomaly related to an irreversible expansion which can be observed upon first polarization. This effect is only reported for carbon nanotubes [4] and partially reduced graphite oxide (GOpr) [7] and exhibits a magnitude between 5 and 40% electrode expansion (Figure 1). In case of single walled carbon nanotubes this effect was correlated with the debundling of tube bundles upon first polarization. For GOpr the observed irreversible expansion is the result of the electrochemical activation of the material which allows ion access to the individual graphene-like layers. In both cases the irreversible dilatation is the separation of graphene-like surfaces and hence the weakening of a van der Waals interaction. Since this kind of interaction depends on extended graphene-like surface areas this dilatation effect can only be observed for 1 and 2 dimensional carbon allotropes.

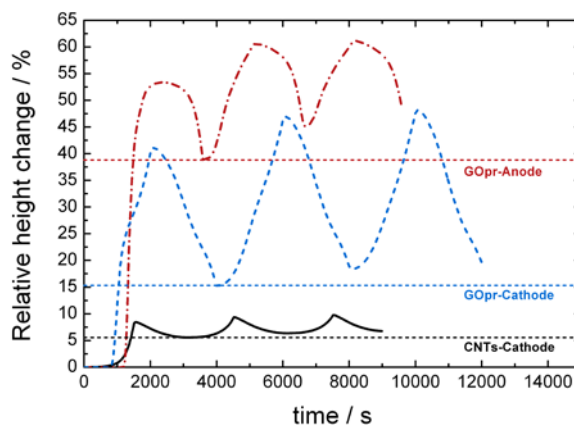


Figure 1. Expansion of partially reduced graphite oxide (2D) and carbon nano tubes (1D) due to polarization as a function of time using 1M TEABF₄ / AN.

¹ Laboratory of Inorganic Chemistry, ETH Zürich

Beside nonrecurring dilatation effects which are limited to 1 and 2 dimensional carbons also the reversible expansion behaviour is compared. Figure 2 summarizes the electrode expansion as a function of charge. The shown data is based on the investigation of 0D onion like carbons [6], 1D single walled carbon nanotubes [4], 2D graphite [3] and 3D carbide derived carbon [5].

Even though the scale of the applied charge is limited the comparison reveals two different dilatation behaviours. On the one hand side both 0D and 3D carbons exhibit almost no expansion in the investigated charge range. On the other hand 1D as well as 2D carbon encounter increased electrode expansions already when applying a small charge.

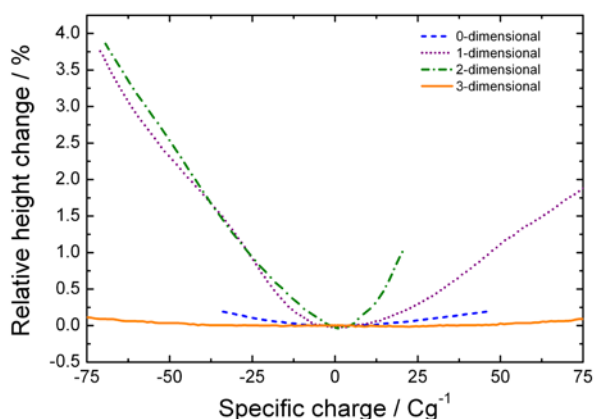


Figure 2. Dilatation of 0 to 3 dimensional carbons as a function of charge using 1M TEABF₄ / AN.

For a more detailed comparison Figure 3 summarizes the anodic as well as the cathodic expansion of the different carbons at a fixed charge value of 20 C/g. The plot emphasizes on the difference between 0D and 3D carbons in contrast to 1D and 2D carbons.

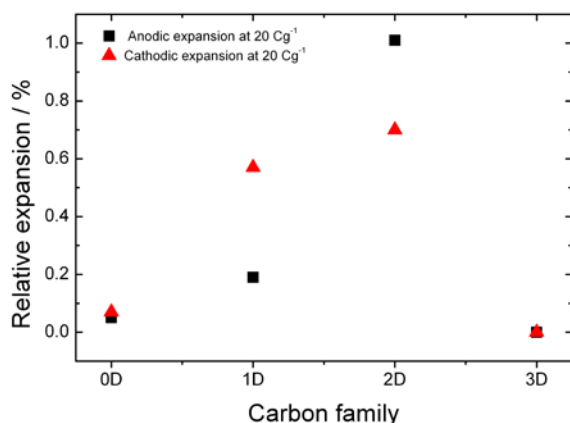


Figure 3. Comparing the relative expansion of 0 to 3 dimensional carbons at a fixed charge value of 20 C/g for both anodic and cathodic polarization in 1M TEABF₄ / AN.

The fact that both 0D and 3D carbons do not show any expansion at a charge of 20 C/g might originate from the inflexible carbon network formed by either the OLC aggregates or the activated carbon. In contrast both the carbon nanotubes as well as the graphite have a more flexible carbon framework with the individual nanotubes as well as the graphene layers only bound by weak van der Waals forces.

Conclusions

The dilatation comparison of 0 to 3 dimensional carbons revealed a strong dependence on the macroscopic carbon frame work. In case of an inflexible carbon frame-work (0D / 3D) there is no expansion observable upon applying a small charge. Hence, neither the accumulated number of ions nor the potential has any influence on the existing carbon network in the electrode.

For carbon electrodes based on bound carbon entities like graphene and nanotubes, however, already the accumulation of a small amount of ions has a measurable effect on the overall electrode height. Therefore, carbon entities bound by van der Waals forces are influenced in their interaction distance upon charging which results in an increased electrode dilatation.

Acknowledgment

The authors would like to thank Swiss National Science Foundation (SNSF) for financial support (project # 200021_126855/1). In addition the authors like to thank Volker Presser from the Leibniz Institute for New Materials (INM) and Jake McDonough as well as Yury Gogotsi from the Drexel Nanotechnology Institute (DNI).

References

- [1] P. Simon, Y. Gogotsi, *Acc. Chem. Res.* **46** (5), 1094-1103 (2013).
- [2] M. Hahn, O. Barbieri, R. Gallay, R. Kötz, *Carbon* **44** (12), 2523–2533 (2006).
- [3] M. Hahn, O. Barbieri, F.P. Campana, R. Kötz, R. Gallay, *Appl. Phys. A-Mater.* **82** (4), 633–638 (2006).
- [4] P.W. Ruch, R. Kötz, A. Wokaun, *Electrochim. Acta* **54** (19), 4451–4458 (2009).
- [5] M.M. Hantel, V. Presser, R. Kötz, Y. Gogotsi, *Electrochem. Commun.* **13** (11), 1221–1224 (2011).
- [6] M.M. Hantel, V. Presser, J. K. McDonough, G. Feng, P.T. Cummings, Y. Gogotsi, R. Kötz, *J. Electrochem. Soc.* **159** (11), A1897–A1903 (2012).
- [7] M.M. Hantel, T. Kaspar, R.d Nesper, A. Wokaun, R. Kötz, *Electrochem. Commun.* **34**, 189–191 (2013).
- [8] J.C. Palmer, A. Llobet, S.-H. Yeon, J.E. Fischer, Y. Shi, Y. Gogotsi, K.E. Gubbins, *Carbon* **48** (4), 1116–1123 (2010).

Facile low temperatures synthesis of lithiated manganese oxides, high potential insertion materials

L. Lutz, S.Sallard, P. Novák

phone: +41 56 310 5746, e-mail: sebastien.sallard@psi.ch

Over two decades, manganese oxide spinels based on LiMn_2O_4 and derivatives have been considered as one of the candidates to replace LiCoO_2 (cobalt is expensive, rare and toxic) in commercial Li-ion batteries. LiMn_2O_4 is a cheap, safe and abundant material providing up to 4V operating potential. Our project focuses on the development of derivatives of LiMn_2O_4 to improve its energy storage capacity, to enhance the potential and/or the specific charge. The first step was to investigate the most interesting method to produce LiMn_2O_4 as reference material, before to extend it to derivatives. In the last two decades different strategies have been developed in the soft chemistry to synthesize LiMn_2O_4 : (i) oxidation of manganese (II) precursor [1], or (ii) reduction of potassium permanganate [2]. We have focused, based on our own experience, on the first option (i) because it offers the highest flexibility and combination possibilities in the further development of derivatives of the LiMn_2O_4 .

Barboux *et al.* [1] showed at the beginning of the 90's that the LiMn_2O_4 can be synthesized from Mn(II) acetate *via* formation of a Mn(II) complex followed by oxidation at high temperatures either under oxidative or neutral atmosphere. Similarly MnCO_3 and Li_2CO_3 can form LiMn_2O_4 at high temperatures [3]. Our goal is to develop syntheses of LiMn_2O_4 by annealing lithiated manganese oxides produced previously from molecular precursors by sol-gel chemistry. We expect from the sol-gel route to form more homogeneous dispersions of the different elements in the raw material than a simple mixture of powders, to finally obtain LiMn_2O_4 and derivatives with improved electrochemical properties (specific charge, stability).

Experimental

Mn (II) acetate tetrahydrate is dissolved in benzyl alcohol in presence of lithium carbonate under argon bubbling and magnetic stirring at ambient temperature. After 10 min the bubbling is stopped and the solution is heated to up 175°C under argon atmosphere. After 40 h the solution is cooled down to ambient temperature. The solution is poured with acetone, centrifuged and the precipitate is washed two times with acetone before to be dried in a furnace at 60°C and then completely desiccated in a vacuum-oven at 90°C over night. In a second step the material is annealed in a muffle oven with ambient atmosphere at different temperatures (300, 600 or 800°C). The synthesis was performed similarly using dried Mn (II) acetate, Mn (III) acetylacetonate, and dry lithium acetate as well.

The synthesized powders were characterized by X-ray diffraction (XRD) and then used to prepare tests by a standard procedure. Slurries were done by mixing the Mn-based material powder with black carbon Super-P and Kynar Flex in a 80/10/10 weight ratio in n-methyl-2-pyrrolidone. The slurries were doctor-bladed on an aluminum foil and dried. Coin-like test cells were build with lithium metal as counter electrode, glass fiber as separator and LiPF_6 1M in ethylene carbonate/dimethylcarbonate (1:1 in weight ratio) as electrolyte solution.

The galvanostatic measurements were performed between 3 to 5 V vs. Li^+/Li with a specific current of 14.8 mA/g (C/10 for a theoretical capacity of 1 Li^+ extraction/insertion per formula unit of LiMn_2O_4), starting with the charge step, *i.e.* oxidation of the Mn-based material.

Sample	From sol-gel synthesis	Annealed at 300°C	Annealed at 600°C	Annealed at 800°C
Mn (II) acetate + Li_2CO_3	(A.1) Li_2CO_3 ~70% + Mn_3O_4 ~30%	(A.2) Li_2CO_3 ~70% + Mn_3O_4 ~30%	(A.3) Li_2MnO_3 ~55% + Li_2CO_3 ~45% 50 Ah/kg	(A.4) Li_2MnO_3 ~75% + LiMn_2O_4 ~25% 80 Ah/kg
Mn (II) acetate 4 H_2O + Li_2CO_3	(B.1) Li_2CO_3 ~65% + Mn_3O_4 ~35%	(B.2) LiMn_2O_4 ~35% + Li_2CO_3 ~35% + Mn_3O_4 ~30% 60-75 Ah/kg	(B.3) LiMn_2O_4 ~90% + Mn_2O_3 ~10% 80-100 Ah/kg high fading	(B.4) LiMn_2O_4 ~90% + Mn_2O_3 ~10% 80-85 Ah/kg
Mn (III) acetylacetonate + Li_2CO_3	(C.1) Li_2CO_3 ~80% + MnCO_3 ~20%	(C.2) LiMn_2O_4 ~30% + Li_2CO_3 ~50% + Mn_3O_4 ~20% 70-80 Ah/kg	(C.3) LiMn_2O_4 ~35% + Li_2MnO_3 ~65% 85-95 Ah/kg	(C.4) LiMn_2O_4 ~45% + Li_2MnO_3 ~55% 80 Ah/kg
Mn (III) acetylacetonate + Li acetate	(D.1) Unidentified mixture maybe Mn_3O_4 in ??	(D.2) Mn_3O_4 95-100 Ah/kg	(D.3) LiMn_2O_4 70-80 Ah/kg	(D.4) LiMn_2O_4 ~55% + Li_2MnO_3 ~45% 70-75 Ah/kg
Mn_3O_4 commercial + Li acetate	-	(E.2) Mn_3O_4 ~95% + LiMn_2O_4 ~5% 75-85 Ah/kg	(E.3) Mn_3O_4 ~30% + LiMn_2O_4 ~70%	(E.4) Mn_3O_4 ~55% + LiMn_2O_4 ~45%
Mn(II) CO_3 commercial + Li_2CO_3	-	(F.2) Li_2CO_3 ~65% + Mn_3O_4 ~35%	(F.3) Li_2CO_3 ~25% + LiMn_2O_3 ~60% + LiMn_2O_4 ~15%	(F.4) Li_2CO_3 ~40% + LiMn_2O_3 ~60%

Table 1. Synthesis parameters, materials produced and their specific charge in electrodes in half-cells.

Results

The different synthesized materials are summarized in Table 1. As expected, the materials syntheses depend of many parameters, especially the temperature and the chemicals used (Mn, Li and the counter ions). A successful result is that monophasic LiMn_2O_4 (D.3) can be obtained from the sol-gel synthesis of Mn(III) acetylacetonate with lithium acetate and annealing at 600°C *via* the conversion of *in situ* formed Mn_3O_4 . Mn_3O_4 annealing in presence of a Li^+ precursor is known to be a synthetic route to produce LiMn_2O_4 [4]. One can notice that the specific charge of our LiMn_2O_4 , even if it is

a monophasic material, shows a rather low specific charge of 70-80 Ah/kg, but at the present point the annealing procedure (temperature and duration) has not been optimized. Our goal with these preliminary results was to validate the possibility to synthesize LiMn_2O_4 by a facile route, before to focus on more promising derivatives. Another improvement would be to optimize the engineering of the electrodes, especially to use the particle aggregates at sub-micrometric size while it is presently up to micrometric (Figure 1).

The synthesis C.1 could be seen as a simple reduction of Mn(III) to Mn(II) with ligand exchange in benzyl alcohol to form a Mn(II)CO_3 and Li_2CO_3 mixture. But when a similar mixture from commercial Mn(II)CO_3 and Li_2CO_3 is prepared, results are different with mainly formation of LiMn_2O_3 .

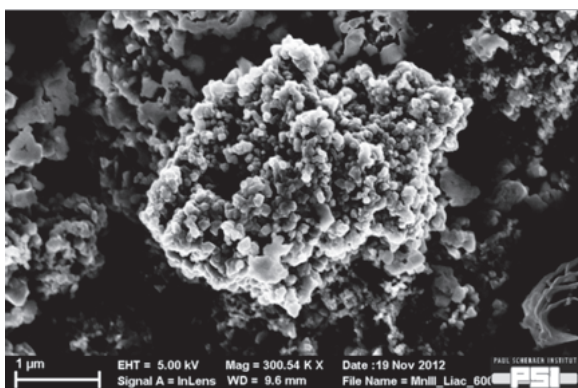


Figure 1. SEM image of the electrode prepared with LiMn_2O_4 (D.3)/super P/Kynar flex, 80/10/10 weight ratio.

Mn_3O_4 is usually described as a material of high specific charge but also for potentials below 3V vs. Li^+/Li when it is lithiated [5-6]. The Mn_3O_4 (D.2) can be cycled at high potentials between 3 to 5 V vs. Li^+/Li with specific charge between 95-100 Ah/kg (Figure 2). It is even the best material we have obtained with these preliminary experiments. No presence of lithium is detected by XRD but a lithium precursor is necessarily present as annealing at higher temperatures leads to the formation of lithiated materials (Table 1, syntheses D.3 and D.4). Supposing a modification of the Mn_3O_4 (D.2) during the first oxidation step appears reasonable, as the materials shows a high irreversibility and different shape of the cycling curves between 4.2-4.7 V, than the following 2nd-5th cycles. The cycling shows also a good reversibility (Figure 2). Another point is that the cycling of Mn_3O_4 (D.2) reveals an evolution of the shape of 10th cycle in comparison to the 2nd and 5th cycles both for the charge and discharge steps. At this point a second material modification may be possible but further investigations are necessary to clarify by *in situ* and *post-mortem* XRD analyses.

In order to investigate this phenomenon and to point out the possible importance of the first step of the synthesis performed in benzyl alcohol with molecular precursors, we have annealed a commercial Mn_3O_4 powder mixed with lithium acetate by a similar annealing procedure. The Mn_3O_4 phase is quite unchanged at 300 °C (E.2), no formation of LiMn_2O_4 , and the material is also cycling at high potentials between 3-5V vs. Li^+/Li (Figure 2). But the galvanostatic cycling reveals clear differences: (i) No

activation or material transformation seems to occur during the first oxidation. (ii) The material Mn_3O_4 (E.2) delivers a specific charge lower and less stable than for the Mn_3O_4 (D.2). A possible explanation could be a reaction between the Mn_3O_4 (D.2) with the amorphous part containing the Li^+ , attributed to high interface area between the different compounds (due to the sol-gel synthesis in benzyl alcohol) while the mixture of commercial powders does not allow to form such homogeneous and highly dispersed material with Mn_3O_4 (E.2).

In conclusion, manganese oxide based materials for high voltage electrodes to Li-ion batteries have been obtained. The most promising route appears to be the one using Mn(III) acetylacetonate and lithium acetate in benzyl alcohol in a first step followed by annealing.

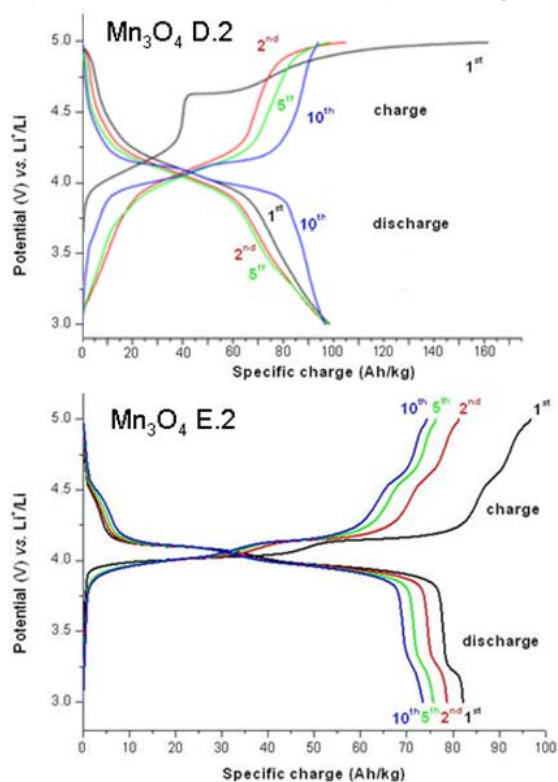


Figure 2. Galvanostatic curves of Mn_3O_4 (D.2) and Mn_3O_4 (E.2).

References

- [1] P. Barboux, J.M. Tarascon, F.K. Shokoohi, J. Solid Stat. Chem. **94**, 185-196 (1991).
- [2] X. Hao, O. Gourdon, B.J. Liddle, B.M. Bartlett, J. Mater. Chem. **22**, 1578-1591 (2012).
- [3] M.M. Thackeray, M.H. Rossouw, J. Solid Stat. Chem. **113**, 441-443 (1994).
- [4] H. Krampitz, G. Wohner, Process for preparing lithium manganese oxides, U.S. Patent 6706443 (2004).
- [5] M.M Thackeray, W.I.F. David, P.G. Bruce, J.B. Goodenough, Mat. Re. Bull. **18**, 461-472 (1983).
- [6] H. Wang, L.-F. Cui, Y. Yang, H.S. Casalongue, J. T. Robinson, Y. Liang, Y. Cui, H. Dai, JACS **113**, 13978-13980 (2010).

Influence of electrolyte on the performance and lifetime of NCM family materials

H.-J. Peng, C. Villevieille, S. Urbonaite, H. Wolf¹, K. Leitner¹, P. Novák

phone: +41 56 310 5737, e-mail: hai-jung.peng@psi.ch

There have been many attempts to search for alternative layered lithium transition metal oxides by substituting Co by other transition metals due to the low practical specific charge and limited thermal stability of LiCoO_2 , as well as the toxicity and high cost of Co. Particularly, the family of $\text{LiNi}_{1-x-y}\text{Co}_x\text{Mn}_y\text{O}_2$ (NCM) materials has shown promising electrochemical properties which can be fine-tuned and optimized by changing the ratio of different transition metals. Among them, NCM111 and NCM523 ($\text{LiNi}_{0.33}\text{Co}_{0.33}\text{Mn}_{0.33}\text{O}_2$ and $\text{LiNi}_{0.5}\text{Co}_{0.2}\text{Mn}_{0.3}\text{O}_2$, respectively) are especially important for industrial applications. NCM111 is one of the most studied materials in NCM family. Ohzuku and Makimura have reported a specific charge of 150 mAh/g for NCM111 within the potential window of 2.5-4.2 V vs. Li^+/Li , which is comparable or better than that of LiCoO_2 , and with improved safety [1]. However, by increasing cut-off voltage, cation disorder, which deteriorates the performance, occurs and shortens the lifetime of cells based on NCM111 material [2]. Recently, NCM523 has attracted much attention because it delivers higher specific charge within the same potential window as NCM111 and is more cost-efficient. However, it suffers from a more pronounced decay of specific charge during cycling.

Experimental

Aiming to understand the failure mechanism of NCMs, the cycling behaviour of NCM111 and NCM523 was investigated in two different electrolytes in half-cell setup: 1 M LiPF_6 in ethylene carbonate (EC)/dimethyl carbonate (DMC) electrolyte (LP30) and 1 M LiPF_6 in ethylene carbonate (EC)/ethyl methyl carbonate (EMC) (LP57). The cycling protocol was as follows: 2 cycles at C/10 rate followed by prolonged cycling at C/2 rate within the potential window of 2.5-4.3 V vs. Li^+/Li .

The variation of the electrolyte composition was analysed by gas chromatography after 0 (the cell stays at OCV for 2 days), 1, 3, and 10 cycles. The electrolyte in the cycled cells was leached with 1 ml EMC or DMC (for cells cycled with LP30 and LP57, respectively). The measurements were carried out with Agilent 7890A gas chromatograph with DB-1 capillary (60 m x 0.32 mm i.d., 5 μm) and built-in flame ionization detector from Agilent Technologies. A constant flow of N_2 at 1 ml/min was used as carrier gas. 1 μl of the sample solution were transferred from the injector which was maintained at 240 °C to the capillary column. The temperature of the column was ramped from 80 °C to 260 °C with a rate of 6 °C/min and held for 25 minutes at 260 °C. The duration of each measurement was 47.5 min.

Results

Figure 1 compares the cycling performance of NCM111 and NCM523 in LP30 (Figure 1a) and LP57 (Figure 1b). It can be seen that NCM523 shows a higher specific charge than NCM111 within 250 cycles in both LP30 and LP57 electrolyte. However, while the specific charge of NCM111 decreases at the rate of around 0.06 % per cycle (with respect to the nominal specific charge of 141

mAh/g), it is at around 0.09 % per cycle (with respect to the nominal specific charge of 162 mAh/g) for NCM523 in LP30. It is worth noting that with LP57 apparent faster decay can be seen approximately after 150 cycles and 100 cycles for NCM111 and NCM523, respectively. Before the accelerated decay, the decline of specific charge is at around 0.09 % for NCM111 and 0.11 % for NCM523 in LP57.

The influence of the different electrolytes on the performance of NCM111 and NCM523 is compared in Figure 2a and Figure 2b, respectively. The decay of specific charge is clearly more pronounced for the cells cycled with LP57. It is reported in the literature that graphite and lithium metal are more stable in EMC than in DMC due to the better passivation of the surface [3,4]. This is consistent with observed trend that the cells cycled with LP30 are more prone to inefficient charging after 200 cycles (possibly due to dendrite formation). However, by considering 80 % of the nominal specific charge as the end of the lifetime of a lithium-ion cell, cells cycled with LP57 reach the end of life around 40 (for NCM111) and 100 (for NCM523) cycles earlier than the ones with LP30.

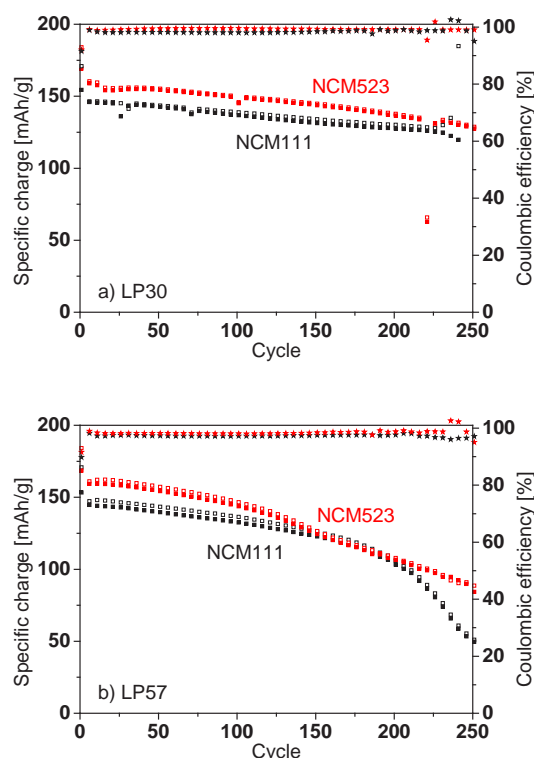


Figure 1. Cycling behaviour of NCM111 and NCM523 at C/2 rate between 2.5 - 4.3 V vs. Li^+/Li with a) LP30 and b) LP57 electrolytes (\square : specific charge, \blacksquare : specific discharge, $*$: coulombic efficiency).

Figure 3 shows the results for the composition evolution of the electrolyte during cycling in NCM111 cells. Although for the cells cycled with different electrolytes, the

¹ BASF SE, Ludwigshafen, Germany

specific discharge is almost identical within 10 cycles, the variation of electrolyte composition during cycling depends on the binary solvent used. It seems that for the cells assembled with LP30, just by keeping the cell at OCV, it results in the build-up of decomposed constituents at the primary expense of DMC. Then, the composition stays roughly unchanged till the 10th cycle. On the contrary, for the cell cycled with LP57, continuous variation of electrolyte composition is observed. During 10 cycles, a clear decrease of the EMC percentage can be observed. This could be correlated to the fact that coulombic efficiency of the LP57 cells is generally lower than the one of LP30 cells due to the more pronounced side reactions. However, the faster decrease of the linear carbonate than cyclic carbonate is not expected because EC is generally considered to be less stable and more easily reacting through ring-opening mechanism. In addition, while EC contributes with its good dielectric properties to the binary solvent, the low viscosity of DMC and EMC realises the good conductivity of the electrolyte. The continuous decomposition of EMC in the LP57 cells would result in increased viscosity of the electrolyte and decreased conductivity, and in turn decreased practical specific charge due to higher overpotentials. Although no apparent differences in terms of specific charge are noticeable between the two electrolytes within the studied 10 cycles, increase in viscosity may play a role in the faster performance decay for the cells cycled with LP57 in the long term.

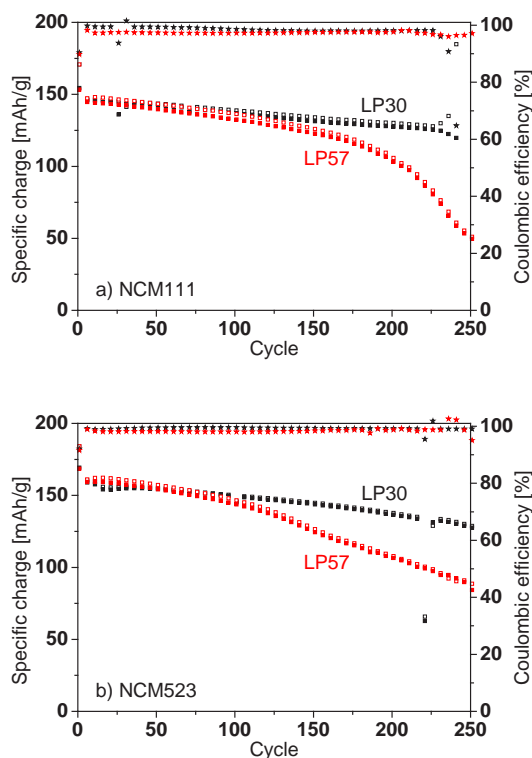


Figure 2. Cycling behaviour of a) NCM111 and b) NCM523 at C/2 rate 2.5 - 4.3 V vs. Li⁺/Li with LP30 and LP57 electrolytes (□: specific charge, ■: specific discharge, *: coulombic efficiency).

Conclusion

Although NCM523 delivers higher specific charge, the decay of specific charge during cycling is more pronounced. In addition, different electrolytes affect the performance and lifetime of the cells to a large extent. In a half-cell system, cells cycled with LP57 tend to have a stronger fading which might be correlated to the faster decomposition of EMC according to the results obtained from gas chromatography.

Acknowledgement

The authors are grateful for financial support from BASF SE as well as Mr. Dietze Robert, Mr. Schmitt Volker, and Ms. Kimmel Michaela for the experimental supports and Ms. Laschak Vibeke for the gas chromatography measurements.

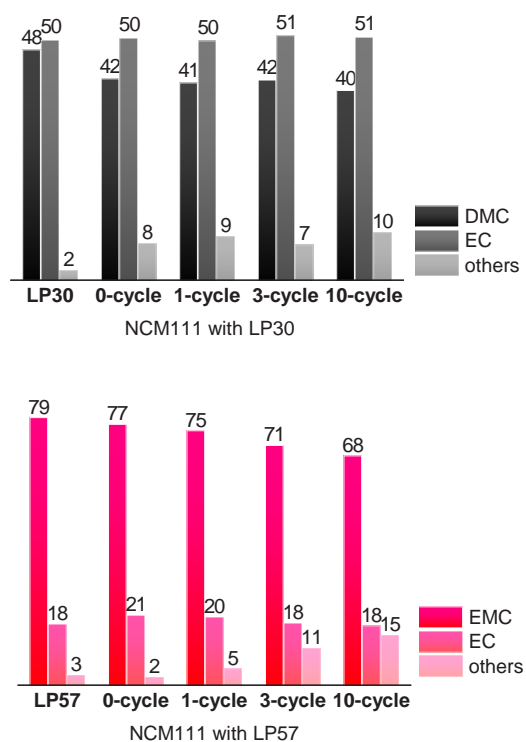


Figure 3. Evolution of electrolyte composition shown in percentage during the first 10 cycles of NCM111 cells with a) LP30 and b) LP57. Pristine electrolyte and the electrolyte from the cells stayed at OCV for 2 days are served as references.

References

- [1] T. Ohzuku, Y. Makimura, Chem. Lett. **30**, 642-643 (2001).
- [2] S.-C. Yin, Y.-H. Rho, I. Swainson, L.F. Nazar, Chem. Mater. **18**, 1901-1910 (2006).
- [3] S.S. Zhang, T.R. Jow, K. Amine, G.L. Henriksen, J. Power Sources **107**, 18-23 (2002).
- [4] Y. Ein-Eli, S.R. Thomas, V. Koch, D. Aurbach, B. Markovsky, A. Schechter, J. Electrochem. Soc. **143**, L273-L277 (1996).

One-pot synthesis by anhydrous sol-gel chemistry of mixtures of magnetite and greigite, and their use for positive electrode in Li-ion batteries

S. Sallard, P. Novák

phone: +41 56 310 5746, e-mail: sebastien.sallard@psi.ch

Both metal oxides and metal sulfides can be both used as active materials to reversibly store electrical energy by a redox process. However their properties are different. Metal oxides present usually stable but low specific charges while metal sulfides present high specific charges for the first cycles but a really fast and strong fading. The main reason of such contrasted electrochemical properties is due to the different mechanisms of the oxidation and reduction metal oxides and metal sulfides. An interesting progress in the battery field would be to obtain a material able to combine the advantages of each material, *i.e.*, the high specific charge of the metal sulfide and the good cycling stability of the metal oxide.

Metal oxysulfide materials are the first target to reach this goal but the standard synthesis is by pulse laser deposition (PLD) [1]. The amount of material produced is too low for further use of the material to build electrodes. A post-synthesis mixture of metal oxide and metal sulfide powder does not provide any advantage and annealing process is not possible due to the low thermal stability of the metal sulfides. A possibility would be to have a fine mixture, where the high dispersion of the metal sulfide in the material limits the total volume change of the active material during the successive oxidations and reductions and consequently prevents the formation of cracks (*i.e.*, lost of electrical contact) in the electrode.

The sol-gel chemistry allows to produce material starting from molecular precursor at relative low temperatures. The anhydrous route was developed by Niederberger and co-workers [2] during the last decade and many different metal oxides can be synthesized using benzyl alcohol as solvent and co-reactant. Recently, this route was extended to produce metal sulfides using benzyl mercaptan [3]. We describe here the different combinations of benzyl alcohol and benzyl mercaptan with an molecular iron source, to produce in one-pot different mixtures of magnetite Fe_3O_4 and greigite Fe_3S_4 . Fine mixture with an optimal ratio between the magnetite and greigite, $\text{Fe}_3\text{O}_4 \sim \text{Fe}_3\text{S}_4$, delivers as active material for Li-ion batteries a specific charge higher than the one of metal oxide and the mixture is reasonably stable, *i.e.*, the specific charge is more stable upon cycling than the one of metal sulfide.

Experimental

Iron (III) acetylacetonate is dissolved in benzyl alcohol in a mixture of benzyl alcohol and benzyl mercaptan under argon bubbling and magnetic stirring at ambient temperature. After 10 min the bubbling is stopped and the solution is heated up at 175°C under argon atmosphere. After 40 h the solution is cooled down to ambient temperature. The solution is poured with acetone, centrifuged, and the precipitate is washed two times with acetone before to be dried in a furnace at 60°C .

The synthesized powders were characterized by Energy-dispersive X-ray spectroscopy (EDX), X-ray

diffraction (XRD) and scanning electron microscopy (SEM) and then used to make electrodes by a standard procedure. Slurries were done by mixing the iron-based material powder with black carbon Super-P and Kynar Flex binder in a 80/10/10 weight ratio in *n*-methyl-2-pyrrolidone. The slurries were doctor-bladed on an aluminum foil and then dried. Coin-like test cells were built with lithium metal as counter electrode, glass fiber as separator and LiPF_6 1M in ethylene carbonate/dimethylenecarbonate (1:1 in weight ratio) as electrolyte solution. The galvanostatic measurements were performed between 1 to 3 V vs. Li^+/Li with a specific current of 34 mA/g starting with the discharge step, *i.e.* reduction of the Fe-based material.

Results

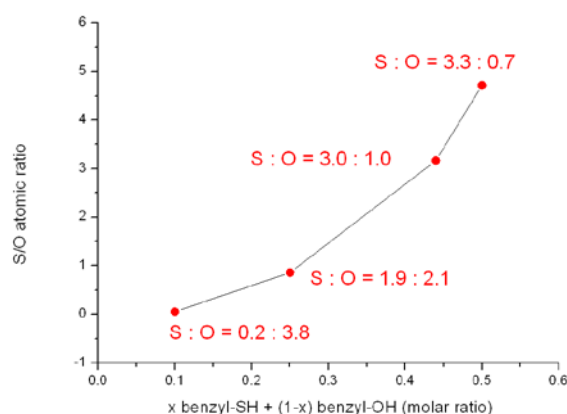


Figure 1. Relation between the sulphur/oxygen (S/O) atomic ratio in the mixture of magnetite and greigite synthesized, and the composition of the benzyl alcohol and benzyl mercaptan mixture used. Data are collected from EDX analysis. S:O values represent the respective number of sulphur and oxygen atom for a total of 4 atoms.

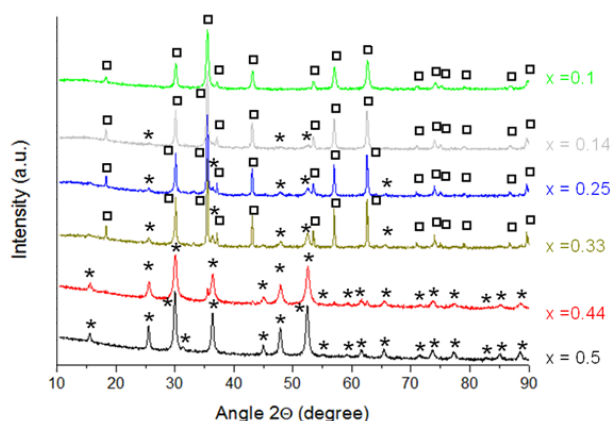


Figure 2. X-ray diffractograms of synthesized materials. "x" is the same molar ratio of benzyl mercaptan as in figure 1. The squares and the stars symbolize the peaks attributed to the magnetite and greigite phases, respectively.

The analysis by EDX is accurate enough to estimate the atomic ratio of oxygen and sulphur present in the collected powder after synthesis, purification, and drying. It is obvious from Figure 1 that the atomic S/O ratio of the product can be controlled by the respective quantity of benzyl alcohol and benzyl mercaptan used for the synthesis even if the correlation is not linear.

The XRD analysis relates directly the chemical composition of the materials, *i.e.* S/O ratio, and the crystal phase present. A material rich in oxygen contains mainly magnetite phase and a material rich in sulphur contains mainly greigite phase. The phase composition of the final material can be then directly controlled by the respective amount of benzyl alcohol and benzyl mercaptan used for the synthesis. The Rietveld refinement of the diffractograms suggests that the greigite does not have any oxygen doping when present in any material produced. The magnetite phase seems to be able to accommodate sulphur in its lattice but the effect is limited to several percent for the best. It can be excluded that any relevant amount of oxysulfide was then produced. The material can be described either as magnetite, greigite, or mixture of both.

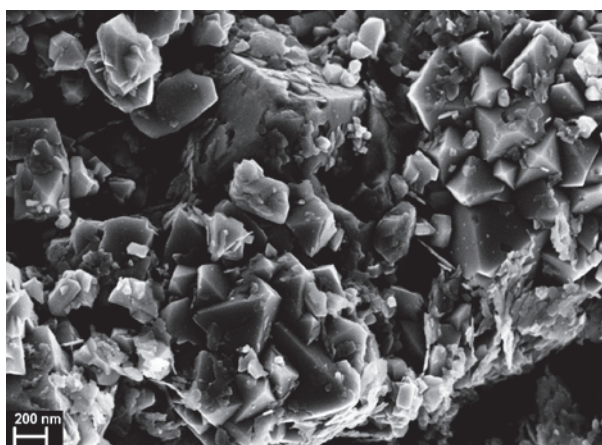


Figure 3. SEM image of the material composed of equivalent amounts of oxygen and sulphur $\text{Fe}_3\text{O}_4 \sim \text{Fe}_3\text{S}_4$, synthesized with $x = 0.25$.

The morphology of the materials is a nanometric granular powder and fine pellets when the chemical composition is mainly Fe_3O_4 and Fe_3S_4 , respectively. When the chemical composition is $\text{Fe}_3\text{O}_4 \sim \text{Fe}_3\text{S}_4$ an octahedral morphology is also observed (Figure 3).

From Figure 4, the specific charge of the materials composed mainly of greigite, S : O = 3.3 : 0.7 and 3 : 1, shows for the first cycle really high specific charges, over 500 mAh/g, but as expected the fading of the specific charge is really rapid. After 10 cycles their specific charge is below 150 mAh/g. The materials composed mainly of magnetite, S : O = 0.2 : 3.8, show the lowest specific charge of the materials studied with a value of 150 mAh/g for the first cycle but it is much more stable than the greigite based materials. The material composed of $\text{Fe}_3\text{O}_4 \sim \text{Fe}_3\text{S}_4$, S : O = 1.9 : 2.1 has an interesting property; its specific charge is for the first cycle close to 250 mAh/g and it shows proportionally the lowest fading for the 10 first cycles (Figure 4).

When we compare the one pot produced S : O = 1.9 : 2.1 material to a post-synthesis equimolar mixture of magnetite and greigite as active material (Figure 4), even if the chemical composition is the same, same respective amount of Fe_3O_4 and Fe_3S_4 in both powders, the electrochemical properties are different. The post-synthesis mixture of magnetite and greigite powder shows an evolution close to the solely greigite material, *i.e.* high specific charge at the beginning but fast fading.

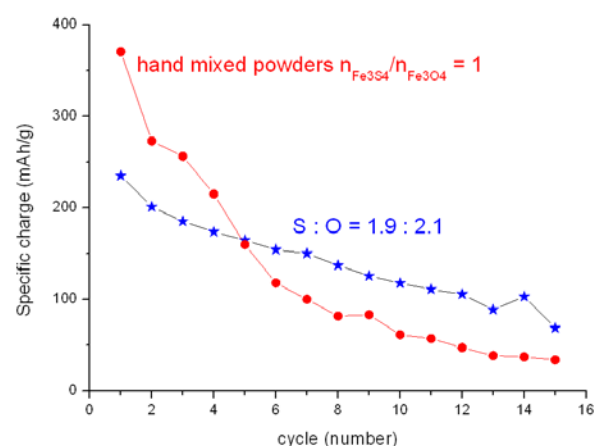
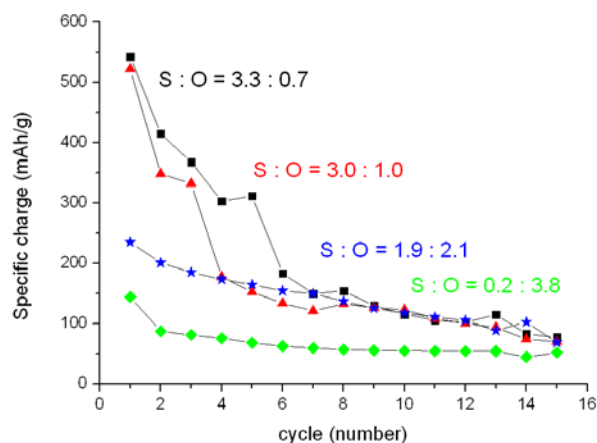


Figure 4. Specific charge evolution upon cycling of the magnetite, greigite, and mixtures of magnetite and greigite powders for the discharge (reduction) step.

In conclusion, a fine mixture of metal oxide and metal sulphide can be obtained by a one-pot synthesis. The electrochemical properties of an equimolar mixture combine a high specific charge and good stability which is not the case when the same metal oxide and metal sulphide are synthesized separately and afterward mixed.

Acknowledgment : BASF Company

References

- [1] S.H. Deuklar, J.-L. Huang, M. Neumann-Spallart, J. Elec. Mater. **39**, 589-594 (2010).
- [2] N. Pinna, M. Niederberger, Angew. Chem. Int. Ed. **47**, 5292-5304 (2008).
- [3] X. Ludi, I. Olliges-Stadler, M.D. Rossell, M. Niederberger, Chem. Commun. **47**, 5280-5282 (2011).

Toluene-assisted sulphur impregnation of carbons as a method for preparing positive electrodes for Li–S batteries

S. Urbonaite, P. Novák

phone: +41 56 310 5775, e-mail: sigita.urbonaite@psi.ch

Li–S batteries have been studied for several decades, motivated by predictions of high specific charge (1672 mAh/g) and high specific energy (2,500 Wh/kg) [1]. However, the development of Li–S batteries faces a number of challenging problems on the way to maximum performance. One of them is the insulating nature of sulphur, necessitating the addition of conductive additives to the electrode. The most widely used conductive additive is carbon, and many different forms have been employed for the positive electrodes of Li–S batteries [2 – 5]. Our recent publication [6] reports a variety of other parameters influencing the performance of Li–S batteries and shows that carbon–sulphur electrodes based on simple mixing are at least as good as most of the electrodes based on the advanced carbons and prepared by advanced composite-preparation methods [4]. Many ways to distribute sulphur in the carbonaceous matrix have been reported, such as melt infiltration and gas infiltration, often resulting in improved cell performance [4, 5], most probably due to homogeneous sulphur distribution.

To explore potential improvements in the specific charge of sulphur electrodes by homogeneously distributing sulphur within the electrode, a method to impregnate carbon with sulphur was developed based on the good solubility of sulphur in toluene above 80 °C. In this work, we present a method of sulphur impregnation into carbonaceous matrixes from sulphur solutions in toluene, as well as cycling performance of the resulting composites.

Experimental

For sulphur impregnation from toluene, 6 g of sulphur were dissolved in ~200 g of toluene at 90 °C under stirring. Then 2 g of Super P (TIMCAL, Switzerland) was added under stirring. The mixture then was stirred until all toluene evaporated. A scanning electron microscopy (SEM) study was performed to confirm that no sulphur agglomerations are present; the SEM was operated at an accelerating voltage of 5 kV.

Electrodes were prepared by mixing sulphur-impregnated carbon, additional carbon black (Super P) and polyethylene oxide (PEO) binder by turbostirring, and then doctor blading the resulting slurry onto a carbon-precoated Al foil. The final composition of electrodes was 60 % sulphur, 30 % carbon and 10 % PEO. After drying at room temperature for at least 24 h, the electrodes were punched into 13-mm-diameter discs and assembled into the cells with Celgard 2400 as a separator, metallic lithium as the counter electrode and 30 µl of electrolyte containing 1 M LiTFSI in DME:Diox (2:1) or with adding an electrolyte additive, 0.5 M LiNO₃. (LiTFSI: lithium bis(trifluoromethane sulfone)imide, DME: dimethoxyethane; Diox: 1,3-dioxolane). Electrodes were galvanostatically cycled at a C/5 rate (1C is defined as I = 1672 mA/g_S) between 1.8 and 2.7 V vs. Li⁺/Li.

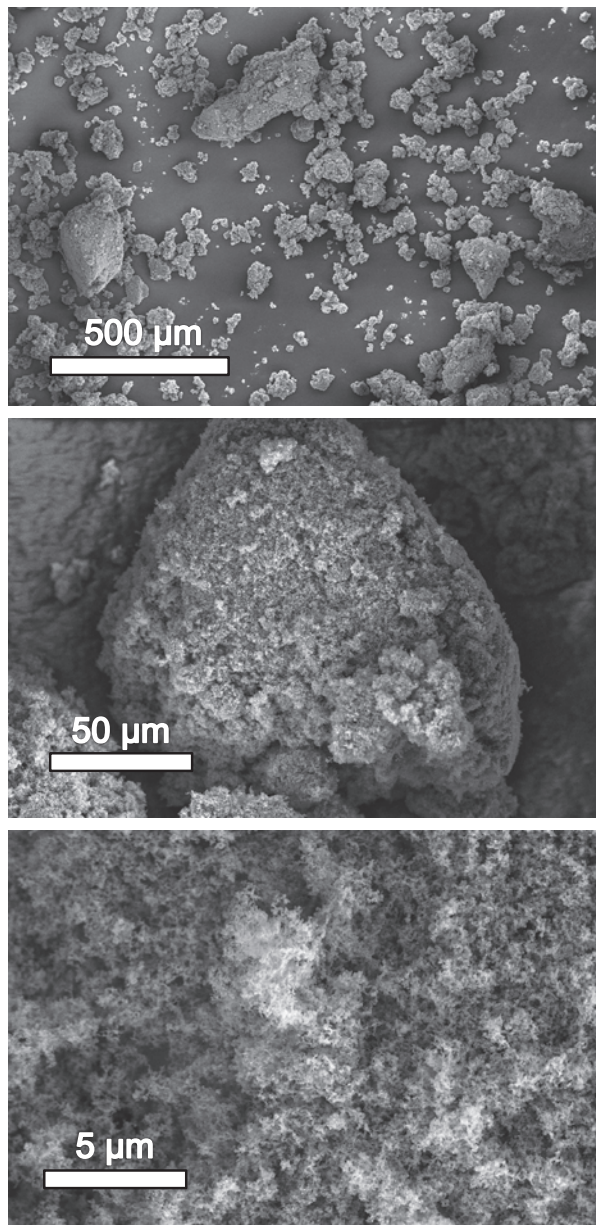


Figure 1. SEM micrographs showing the morphology of Super P impregnated with sulphur from toluene.

Results

Super P carbon after impregnation, despite its relatively low surface area of 62 cm²/g, did not show any visible sulphur agglomerations, as can be seen in the SEM micrographs (Figure 1). The results of galvanostatic cycling of the cells made with S–C composites obtained by sulphur impregnation of carbon from toluene is presented in Figure 2. Cells show long cycling life (500 cycles) with good specific-charge retention.

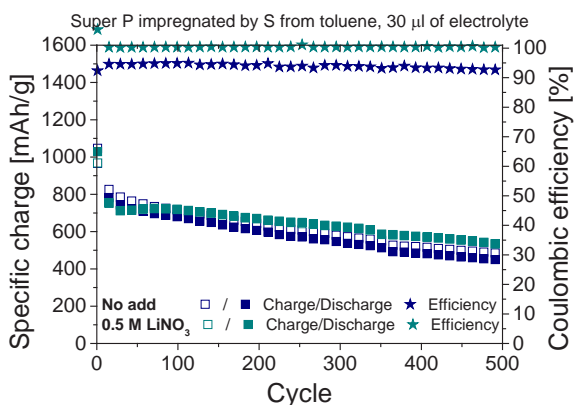


Figure 2. Galvanostatic cycling performance of electrodes made from sulphur-impregnated Super P, with 30 μ l of electrolyte.

The specific charge after 500 cycles was at 530 mAh/g, which is about 250 mAh per gram of sulphur higher than previously reported for mixtures of simple carbon black and S at the same cycling and assembly conditions [6], see Figure 3. This leads to the conclusion that a homogeneous distribution of sulphur is highly advantageous.

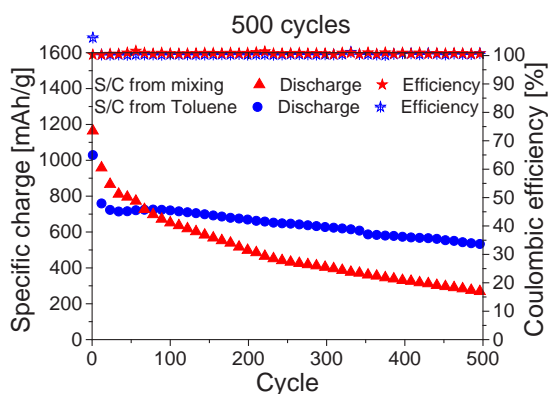


Figure 3. Galvanostatic cycling performance of electrodes made from sulphur-impregnated Super P and from a physical mixture of Super P and sulphur.

Conclusions

An alternative method for impregnating carbon with sulphur was developed, based on the sulphur solubility in toluene at elevated temperatures. It has been shown that carbons with different surface areas and porosities can be impregnated using this method. The resulting sulphur-carbon composites have a homogeneous sulphur distribution in the carbonaceous matrix without S agglomerates.

A clear advantage of homogeneous sulphur distribution in composite, and thus in electrodes, on the cycling performance of Li-S cell has been demonstrated. After 500 cycles, for Li-S cells based on the newly developed composites made by toluene-assisted impregnation a specific charge of 530 mAh/g was achieved, improving the result obtained with standard sulphur electrodes from physical mixture of sulphur and carbon by 250 mAh/g.

Acknowledgement

BASF SE is acknowledged for financial support within the "BASF Scientific Network on Electrochemistry and Batteries".

References

- [1] X. Ji, K.T. Lee, L.F. Nazar, *Nat. Mat.* **8**, 500–506 (2009).
- [2] H. Wang, Y. Yang, Y. Liang, J.T. Robinson, Y. Li, A. Jackson, Y. Cui, H. Dai, *Nano Lett.* **11**, 2644–2647 (2011).
- [3] Y. Yang, G. Yu, J.J. Cha, H. Wu, M. Vosgueritchian, Y. Yao, Z. Bao, Y. Cui, *Nano Lett.* **5**, 9187–9193 (2011).
- [4] Y. Yang, G. Zheng, Y. Cui, *Chem. Soc. Rev.* **42**, 3018–3032 (2013).
- [5] S. Evers, L.F. Nazar, *Acc. Chem. Res.* **46**, 1135–1143 (2013).
- [6] S. Urbonaitė, P. Novák, *J. Power Sources* **249**, 497–502 (2014).

Characterization of Porocarb–Si composite material for negative Li-ion battery electrodes

S. Urbonaite, C. Neumann¹, J. Becker¹, M. Otter¹, S. Pihan¹, P. Novák

phone: +41 56 310 5775, e-mail: sigita.urbonaite@psi.ch

Silicon is an attractive material for lithium-ion battery negative electrodes as it has a high theoretical gravimetric specific charge of 4200 mAh/g at high temperatures and a desirable low working potential of ~ 0.5 V vs. Li^+/Li . This makes it a candidate for replacing graphite negative electrodes, because graphite's theoretical specific charge is much lower, 372 mAh/g. While graphite can deliver specific charge close to the theoretical one, its improvement limits have been reached. However, two main disadvantages of silicon that needs to be addressed are its low intrinsic electronic conductivity and drastic (up to 400%) volume expansion upon lithiation. The first problem can be solved by downscaling silicon particles and incorporating them into a conductive matrix; the second one has been addressed by many different approaches: by nanostructuring of Si (nanowires, nanocables, nanospheres), by using coatings (conductive agents, oxides, metals, conductive polymers), by limiting charge and so not allowing full volume expansion of the material [1], which would result in cracking of particles and — due to this — an ever growing SEI.

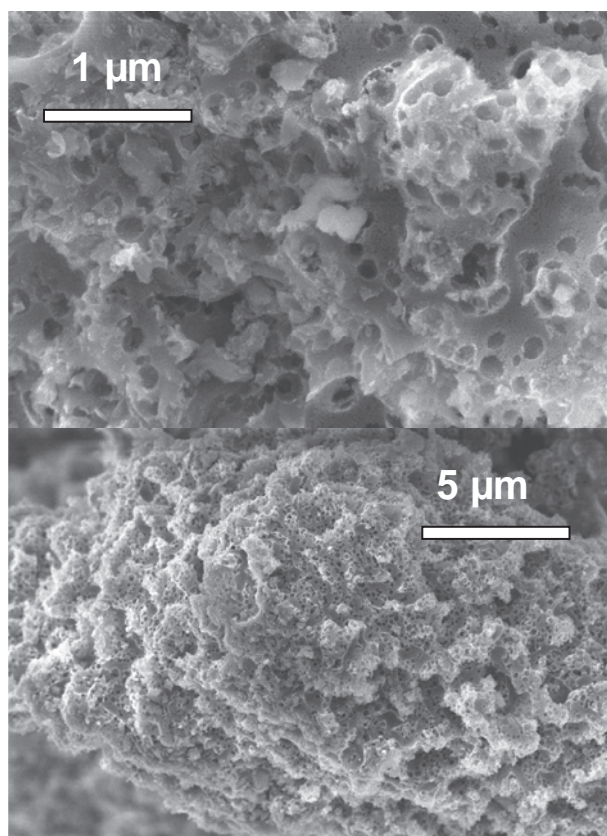


Figure 1. SEM micrographs of Porocarb–Si composite. All these approaches work to some extent, but long-term stable cycling without severely limiting the specific charge of Si is not achievable. The alternative, to obtain negative electrodes with higher specific charge than graphite and at the same time to avoid problems associated with Si, is to incorporate small amounts of nano-

sized Si into the carbonaceous matrix, which is able to accommodate volume changes, in this way avoiding particle cracking and electrode degradation, and thus avoiding the growth of a thick SEI.

Here we report the performance of a new pre-commercial carbon–silicon composite, where nanosilicon (average size 100 nm) is fully embedded into the porous carbon structure, exhibiting a high and stable specific charge for more than 100 cycles. The new pre-commercial carbon–silicon composite, where Si embedded into the porous carbon structure, is expected to deliver higher capacity than graphite, high coulombic efficiency and to have only the carbon surface exposed to the electrolyte, which would enable a stable and well-controlled SEI as opposed to the ever growing, unstable SEI on Si surface.

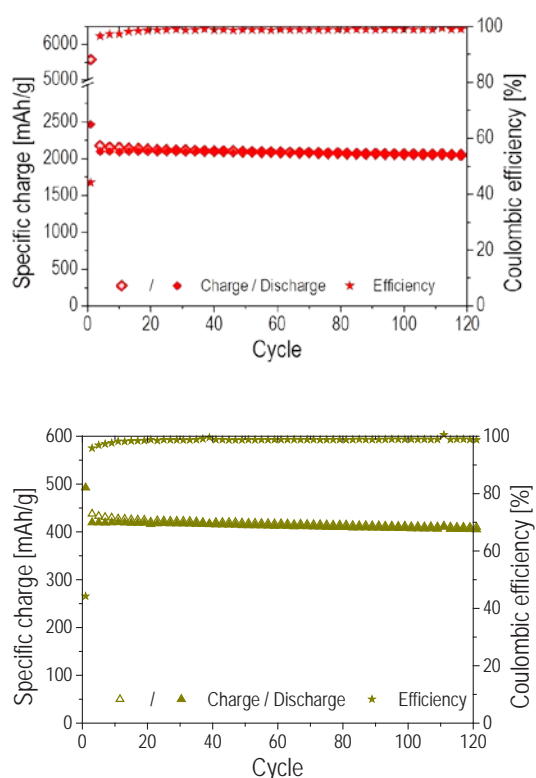


Figure 2. Cycling performance of Porocarb–Si composite at C/10 rate per g-Si (top) and per g-composite (bottom).

Experimental

The silicon–carbon composite has been manufactured in a two-step synthesis procedure developed at Heraeus Quarzglas. First, a carbon precursor was mixed with silicon nanoparticles and homogenized by melting. The obtained composite was infiltrated into an interconnected silica-matrix template and subsequently carbonized. Etching of the template in a HF bath finally exposed the inner porosity of the carbon–Si composite particles. The

¹ Heraeus Quarzglas GmbH & Co. KG, Kleinostheim, Germany

underlying production process is similar to that used for the porous carbon alone: a detailed description of the synthesis and electrochemical performance of Porocarb can be found in B. Jache *et al* [2].

Electrodes were prepared by mixing 80% of Porocarb–Si composite (Heraeus Quarzglas, Germany) with 10% of Super P carbon (TIMCAL, Switzerland) and 10% of PVDF by turbostirring and then doctor-blading onto a Cu foil. Electrode coatings were dried at 80 °C for 18 h, then punched into 13-mm discs, dried again at 120 °C for 12 h and then loaded into an Ar-filled glove box for cell assembly. Half-cells were assembled by placing the Porocarb–Si electrode, a glass-fibre separator and Li-foil into the coin-type cell with 500 μ l of standard LP 30 (1M LiPF₆ in EC/DMC (1:1) electrolyte, where EC is ethylene carbonate and DMC is dimethyl carbonate). Electrodes were cycled at a C/10 rate, where C is defined as I=4200 mA/g of Si, between 5mV and 1V vs. Li⁺/Li.

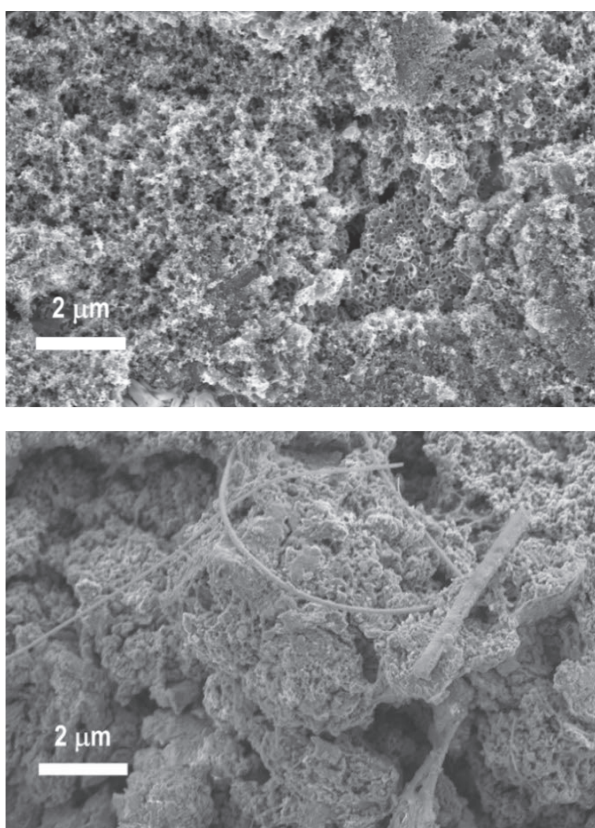


Figure 3. SEM micrographs of pristine electrode (top) and after 120 cycles (bottom).

Results

The morphology of the Porocarb–Si composite material is shown in Figure 1, where the hierarchical porosity of the Porocarb can be seen. The cycling performance of Porocarb–Si is shown in Figure 2 (top graph), where stable cycling over more than 100 cycles is presented, with a specific charge above 2000 m Ah g⁻¹ of Si. This is lower than the theoretical specific charge of Si, which can be explained by silicon oxide present on the surface of nano-Si particles. The presence of silicon oxide is also reflected in low coulombic efficiency during the first cycle. Low coulombic efficiency during the first cycle can also be due to the high surface area of Porocarb materials and reaction with residual functional groups on the carbon surface. However, afterwards cycling is remarkably stable, with the coulombic efficiency higher than 99%.

In the bottom graph of Figure 2, specific charge per gram of Porocarb-Si composite is presented. A specific charge above 400 m Ah g⁻¹ is reached for composite and this result shows that specific charges greater than graphite's can be achieved by making this type of composites. It also shows the importance of silicon purity, because if the silicon oxide's presence would be minimized, the composites specific charge could be significantly improved up to 600-700 m Ah g⁻¹ of composite (if the specific charge per Si would reach values closer to the theoretical one).

Figure 3 presents SEM micrographs of pristine (top) and cycled (bottom) electrodes. It is clearly visible that the SEI layer after more than 100 cycles is quite thin and the morphology of the carbon, including its porosity, is still visible, which is an indication that a SEI is formed on the carbon. This, in combination with high coulombic efficiency, indicates that SEI formation is not affected by Si presence and this means that silicon during cycling is contained within carbon and not exposed to the electrolyte. In turn it means that a Porocarb-type matrix sustains expansion of Si within its inner porosity.

Concluding remarks and outlook

Porocarb–Si R&D materials show excellent cycling performance; however several areas where it can be further improved have been identified: making a carbon host with lower surface area and silicon with minimal oxide surface, as this is crucial to suppress the initial irreversible capacity loss. A comparison of the SEI of only-carbon and carbon–Si composite electrodes will be made by XPS and DEMS to confirm that SEI formation is solely on carbon.

References

- [1] X. Zhou, Y.-X. Yin, A.-M. Cao, L.-J. Wan, Y.-G. Guo, *ACS Appl. Mater. Interfaces* **4**, 2824-2828 (2012).
- [2] B. Jache, C. Neumann, J. Becker, B.M. Smarsly, P. Adelhelm, *J. Mater. Chem.* **22**, 10787-10794 (2012).

Role of the binder in Na-ion batteries

C. Villevieille

phone: +41 56 310 2410, e-mail: claire.villevieille@psi.ch

Na-ion batteries are promising energy storage systems to replace Li-ion batteries due to i) their low cost compared to Li-ion batteries, ii) the fact that sodium is more abundant than lithium, iii) the fact that the number of compounds containing sodium existing in ICSD (inorganic crystallographic structure database) is three times higher than the number of compounds containing lithium. Nevertheless, at the moment, the studies reported in the literature focus on finding new materials for positive and negative electrodes of Na-ion batteries [1] but hardly any researcher is studying the role of the SEI in Na-ion batteries as well as the impact of the binder or conductive agent on the electrochemical properties. In this study, we set out to select a well-known compound of the lithium-ion batteries' technology, FeSb_2 , and investigate its behavior in sodium-ion batteries. FeSb_2 is known to react through a conversion process which leads to Li_3Sb (fcc) and Fe^0 [2] when cycled versus lithium. During delithiation a conversion process takes place yielding mainly Sb. This reaction leads to quite poor cyclability of this material due to the large volume change of the electrode during cycling. In sodium-ion batteries, the reaction mechanism should be the same because Sb is converted into Na_3Sb , and because the volume change between $\text{Sb} \rightarrow \text{Li}_3\text{Sb}$ (248%) and $\text{Sb} \rightarrow \text{Na}_3\text{Sb}$ (243%) is rather similar. Therefore, poor cyclability in Na-ion batteries was expected [3].

Experimental

Electrodes were prepared by two different routes. The first one consists of casting a mixture of 80 wt.% FeSb_2 synthesized by solid state reaction, 10 wt.% PVDF (binder), and 10 wt.% Super-P carbon additive (TIMCAL), all suspended in N-methyl-2-pyrrolidone (Fluka), onto a copper foil used as current collector. The second route consists of casting a mixture of 83 wt.% of FeSb_2 , 7 wt.% Super-P carbon additive (TIMCAL), and 10 wt.% CMC used as a binder, all suspended in water. After drying, the electrodes were punched out and assembled in an argon-filled glove box. The electrolyte used for this study was 1M NaClO_4 dissolved in PC with fluoroethylene carbonate (FEC) used as an additive (5 wt. %). The electrodes were cycled vs. Na metal in a 5 mV-1.5 V vs. Na^+/Na potential window.

Electrochemical properties

Figure 1 shows the cycling stability as well as the coulombic efficiency of FeSb_2 electrodes cycled at different C-rates. As we can see, with a value close to 85%, the coulombic efficiency is rather low for the electrodes with PVDF as a binder. The specific charge also drops drastically from about 1100 mAh/g for the first cycle to reach only 150 mAh/g for the cells cycled at C/2 after 15 cycles and then 0 mAh/g after 20 cycles. The same C-rate was applied to other cells with electrodes containing CMC as a binder instead of PVDF. The results improved significantly with a lower specific charge during the first cycle of around 700 mAh/g and a coulombic efficiency of 93%. The cycling stability is also slightly improved with a specific charge of about 450 mAh/g after more than 30

cycles. Because the results were promising with the CMC binder, we also tested the faster 2C rate. As one can see, the coulombic efficiency is further improved and reached a value close to 95-97% and the specific charge is rather stable during 30 cycles with values higher than 300 mAh/g after 30 cycles.

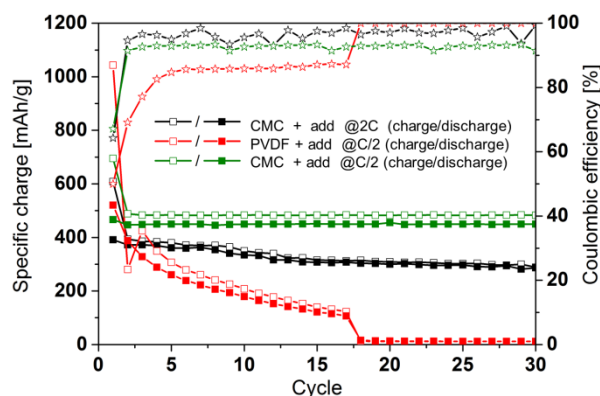


Figure 1. Specific charge of FeSb_2 electrodes cycled vs. Na.

Conclusion

We demonstrated the crucial role of the binder in the FeSb_2 conversion/alloying electrode for sodium-ion batteries with electrode expansion of 200% during cycling. Whereas PVDF, when used as a binder, shows some serious limitations and a specific charge dropping to 0 mAh/g after 20 cycles at C/2, CMC binder shows more impressive results with values above 300 mAh/g at a fast rate (2C), and around 450 mAh/g at a reasonable rate of C/2. Understanding the role of the binder as well as its interactions with the electrolyte will help us to understand why the CMC binder is more appropriate for sodium-ion batteries when using high-volume-change electrodes.

References

- [1] S.W. Kim, D.H. Seo, X.H. Ma, G. Ceder, K. Kang, *Adv. Energy Mater.* **2**, 710-721 (2012).
- [2] C. Villevieille, B. Fraisse, M. Womes, J.C. Jumas, L. Monconduit, *J. Power Sources* **189**, 324-330 (2008).
- [3] A. Darwiche, C. Marino, M.T. Sougrati, B. Fraisse, L. Stievano, L. Monconduit, *J. Am. Chem. Soc.* **135**, 10179-10179 (2013).

SCIENTIFIC ACHIEVEMENTS 2013

BATTERIES & SUPERCAPACITORS

DIAGNOSTICS

Gas evolution from phosphorus based negative Li-ion battery electrodes

E.J. Berg, C. Villevieille, P. Novák

phone: +41 56 310 5736, e-mail: erik.jaemstorp-berg@psi.ch

Much effort is spent into developing novel negative electrode materials for Li-ion batteries with higher energy density aiming to replace the presently mostly used active material, graphite. Elemental phosphorus (P) offers a high theoretical specific charge of 2595 mAhg^{-1} when forming the final Li_3P phase, compared to 372 mAhg^{-1} of graphite with the chemical formula LiC_6 in its lithiated state. However, P suffers from poor electrical conductivity, severe volume expansion and adverse reactions with the electrolyte during cycling [1]. A typical signature of such side-reaction is gas evolution due to decomposition of the organic electrolyte. On the other hand, gas evolution may also reveal important information, e.g., on the solid electrolyte interphase (SEI) formation on graphite [2]. Although the requirements on the SEI of conversion based materials, such as P, differs from graphite, the surface layer at the active material interface is known [1] to critically influence both cycling stability as well as the coulombic efficiency. Differential electrochemical mass spectrometry (DEMS) has previously been successfully developed and applied in our group to study the gas evolution at both positive and negative electrode materials (c.f. [2] and references therein). The aim of the present study is to apply DEMS to compare the gas evolution profile of a typical carbon electrode with a P based electrode during the initial cycles in order to elucidate the reactions at the phosphorus active material interface.

Experimental

Electrodes, denoted SFG44 and P/C, composed of 70% graphite SFG44 (TIMCAL) or phosphorus red (av. part. size $44 \mu\text{m}$, Sigma-Aldrich), 20% PVDF (Solvey) and 10% Super P (TIMCAL) were prepared by directly mixing the respective powders in NMP to form a viscous slurry, which in turn was cast on Ti current collectors of the PSI DEMS cells [2] and then dried (80°C , 12h, dyn. vac.). The dried electrodes were weighed, again dried (120°C , 12h, dyn. vac.), assembled into a half-cell filled with 1M LiPF_6 in 1:1 EC:DMC and potentiodynamically cycled (20 mV/s, 0-1.5V vs. Li^+/Li , 3 cycles) under a constant Ar flow (0.85 mL/min) in the DEMS setup [2]. Mass spectra and relevant ion-current intensities (m/z) were continuously recorded. All potentials are given vs. Li^+/Li .

Results

Figure 1 shows the electrochemical and gas evolution data for electrodes based on (a) graphite and (b) phosphorus. Judging from the current response, graphite displayed an expected stable cycling behaviour with lower coulombic efficiency only in the 1st cycle due to the formation of the SEI layer. The specific charge of the P/C cell is considerably lower than expected, mainly due to the unoptimized formulation of the electrode. H_2 ($m/z=2$) appears for both electrodes at about 1.9V during the 1st cathodic sweep and continues to evolve during whole cycle with maxima more or less coinciding with the reductive current peaks. Interestingly, ion-current intensity ($m/z=34$) most probably corresponding to PH_3 simultaneously increases for the P/C electrode, proving that the active material reaction initiates at this potential.

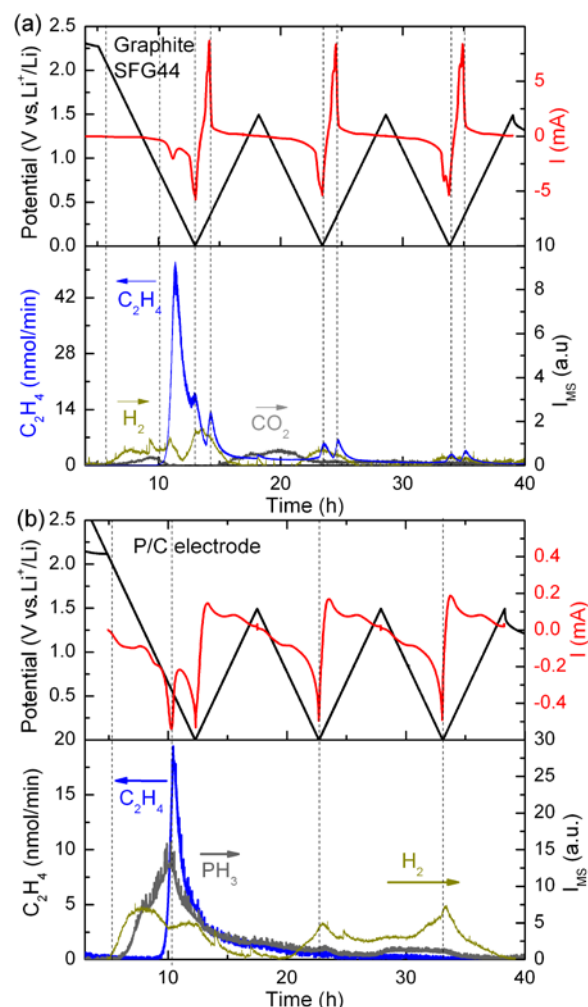


Figure 1. Potential (black), current response (red), and C_2H_4 (blue), H_2 (yellow), CO_2 (dark grey) as well as PH_3 (grey) gas evolution profiles for DEMS cells containing (a) graphite and (b) phosphorus based electrodes during potentiodynamic cycling.

Ethylene is a well known decomposition product of ethylene carbonate (EC) [2] and is observed to evolve at $\sim 0.8\text{V}$ and 0.9V for the SFG44 and the P/C electrode, respectively, thus possibly indicating a slight catalytic enhancement of EC degradation at the interface of P. CO_2 was observed mainly during the 1st cycle for graphite [2], but absent for P. The major part of the gas evolution for both electrodes occurs in the first cycle, coinciding with the build-up of the SEI, although the gassing continues in subsequent cycles, particularly at low potentials and high reductive currents, showing that electrolyte degradation prevails well after the first cycle.

Acknowledgment

BASF SE is gratefully acknowledged for financial support.

References

- [1] C. Marino, L. Boulet, P. Gaveau, B. Fraisse, L. Monconduit, J. Mater. Chem. **44**, 22713-22720 (2012).
- [2] F. La Mantia, PhD Thesis, ETH No. 17848, Zürich (2008).

New insight in the reaction mechanism of $\text{Cu}_{0.5}\text{TiOPO}_4$: an *ex situ* ^{31}P MAS NMR study

P. Bleith, M. Valla¹, P. Novák, C. Villevieille

phone: +41 56 310 2797, e-mail: peter.bleith@psi.ch

In order to increase the specific energy of battery materials, new materials are synthesised and tested as electrode materials in Li-ion batteries. To further improve the materials it is important to elucidate the reaction mechanism of the materials. Quite often one characterization technique alone does not give definite results. So a combination with complementary methods is necessary. In our studies, preliminary results obtained by X-ray absorption spectroscopy (XAS) at the Ti-K α absorption edge of different lithiation states of $\text{Cu}_{0.5}\text{TiOPO}_4$ were now confirmed using ^{31}P MAS NMR measurements.

Experimental

$\text{Cu}_{0.5}\text{TiOPO}_4$ was prepared by a co-precipitation method published recently [1]. The synthesis results in micron-sized particles of both polymorphs, α - and β - $\text{Cu}_{0.5}\text{TiOPO}_4$ with some percent of $\text{Cu}_3(\text{PO}_4)_2$ as impurity. For *ex situ* ^{31}P -MAS-NMR, a viscous slurry of 80 wt% $\text{Cu}_{0.5}\text{TiOPO}_4$, 10 wt% SuperP and 10 wt% Kynarfex[®] 2108 dispersed in NMP was coated on a copper foil and cycled with lithium counter electrode and a 1:1 mixture of EC:DMC with 1 M LiClO_4 as electrolyte. The cells were disassembled in an Ar-filled glove box and the electrodes washed with DMC. All the spectra were acquired on a 400 MHz (9.4 T) ultrashield Bruker spectrometer equipped with a 4 mm HX MAS probe. ^{31}P single excitation with an Rf field of 125 kHz was used on a 85 kHz spectral width to record the spectra.

Results

As mentioned in the annual report 2012, the energy of the absorption edge of titanium decreases in $\text{Cu}_{0.5}\text{TiOPO}_4$ at potentials negative to 0.5 V (figure 1). This can indicate a further reduction of Ti^{3+} . However, using only XAS measurements, the results are not completely clear because the position of the absorption edge can not only shift due to a reduction of an atom but also due to changes in the coordination of the atom. Since at this stage of the cycling the sample turns amorphous, there are certainly major structural changes. These changes can affect the coordination of the titanium. These changes cannot be distinguished by XAS measurements from a change in the oxidation state.

Ex situ ^{31}P MAS NMR measurements can help to elucidate whether phosphate is reduced upon lithiation to 0.01 V vs. Li^+/Li or not. Figure 2 shows the ^{31}P NMR spectrum of $\text{Cu}_{0.5}\text{TiOPO}_4$ as synthesised (OCV) and after cycling to different potentials. As a reference, the spectrum of Li_3PO_4 is given as well. In the starting compound, two peaks can be distinguished one being at 429 ppm with a paramagnetic shift assigned to be $\text{Cu}_{0.5}\text{TiOPO}_4$ and one at -28 ppm assigned to be $\text{Cu}_3(\text{PO}_4)_2$. Upon lithiation to 1.75 V, two peaks are detected at -3 and -9 ppm. This intermediate phase is most likely LiTiOPO_4 in its triclinic phase. Further lithiation leads to a decrease of the intensity of these two peaks and an increase of a peak at 11 ppm. This peak is maintained also upon delithiation to 3.0 V vs. Li^+/Li and can be assigned to Li_3PO_4 .

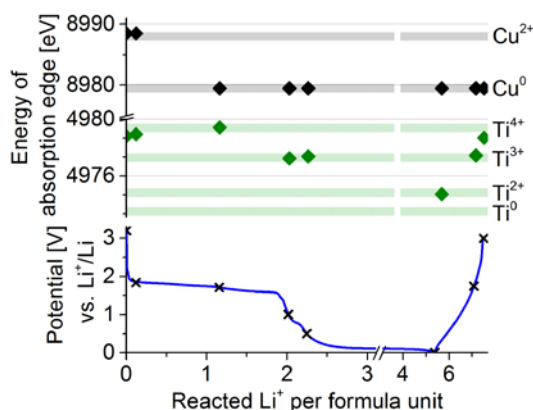


Figure 1: Change of energy of the K_{α} absorption edge of copper and titanium in *ex situ* XAS measurements for $\text{Cu}_{0.5}\text{TiOPO}_4$ upon lithiation and delithiation.

The presence of Li_3PO_4 at 0.01 V excludes the possibility that phosphate is reduced upon lithiation to 0.01 V, leaving only two further components in the system to be the one reduced between 0.5 and 0.01 V: the conductive additive Super-P and Ti^{3+} . The contribution from the Super-P carbon is known from experiments with electrodes that only contain Super-P and its contribution to the specific charge is less than 1/6 of the remaining unexplained specific charge of the material taking into account the 10% content of Super-P. This indicates, together with the results from XAS, that titanium is reduced from Ti^{3+} at these potentials at least to Ti^{2+} , most likely further. The rest of the specific charge could be explained by the reduction of the electrolyte on newly exposed surfaces by the amorphisation reaction forming a kind of SEI.

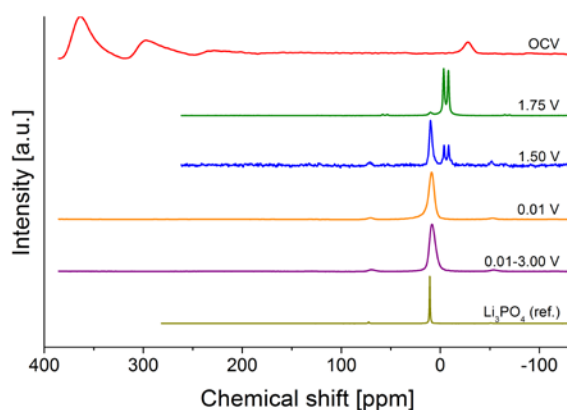


Figure 2: ^{31}P MAS NMR spectra of *ex situ* samples of $\text{Cu}_{0.5}\text{TiOPO}_4$ and pure Li_3PO_4 .

Acknowledgment

Swiss National Science Foundation is thanked for financial support (project no 200021_129508).

References

- [1] P. Bleith, P. Novák, C. Villevieille, J. Electrochem. Soc. **160**, A1534-A1538 (2013).

¹ Laboratory for Inorganic Chemistry, ETH Zürich

Electrochemical cell for *operando* studies on lithium-ion batteries using laboratory X-rays apparatus

P. Bleith, R. Robert, H. Kaiser, P. Novák, C. Villevieille

phone: +41 56 310 2797, e-mail: peter.bleith@psi.ch

During cycling of lithium-ion batteries, structural changes occur in the electrode materials. These changes can be observed using X-ray diffraction (XRD). *Operando* studies give the opportunity to analyse these structural changes at the time and at the potential the processes of lithiation and delithiation are taking place. A full understanding of the reaction mechanism by which the battery operates can help to identify and understand failure mechanisms or reasons for degradation in electrode materials. This knowledge is fundamental for the development of better materials for lithium-ion batteries.

Operando studies at the synchrotron give the possibility to measure test cells in transmission geometry and record a broad angle of the diffractogram in a short time with a good resolution and intensity. However, measurement time at the synchrotron is not always available. Therefore, it is of great interest to develop a cell to measure *operando* XRD in a laboratory X-ray diffractometer.

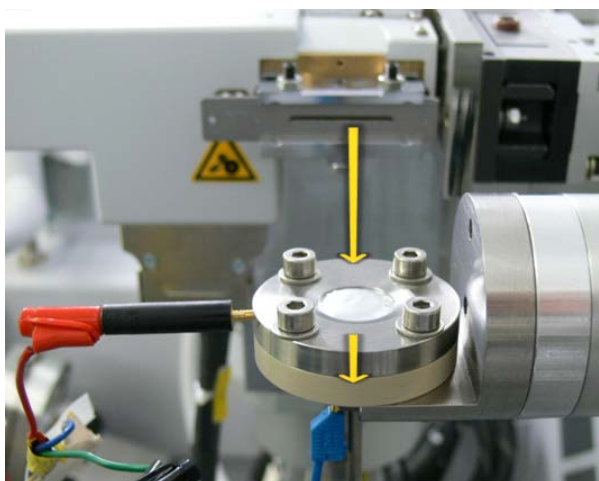


Figure 1: Electrochemical cell mounted in the PANalytical Empyrean X-ray diffractometer.

Results

An electrochemical cell was built for a PANalytical Empyrean diffractometer (Figure 1). Measurements are performed in reflection geometry. The cell is easy to assemble and it can be used in full- and half-cell configuration. Positive or negative electrode materials can be studied by using a suitable material for the X-ray window (Be, Al, Cu, glassy carbon, ...). The lower intensity of the X-ray laboratory source compared to the synchrotron limits the minimum acquisition time necessary to record a pattern. On the one hand, the time required to record an XRD pattern using laboratory X-rays can be a limiting factor if electrochemical reactions are happening fast or a fast cycling rate has to be studied. However, strategies can be chosen in order to reduce total acquisition time, such as: 1) limiting the 2Θ angular range to a reflection of interest, 2) adapting the counting time per point and 3)

increasing the step width. On the other hand, long acquisition time is not a problem if studies on slow cycling rates are planned. If you can limit the measurement to a certain angular domain at slow cycling rates, laboratory X-ray is preferred over synchrotron since the measurement time of the overall experiment is not limited by beam time availability and the reflection geometry is giving you no contributions from cell parts except the window material.

Results obtained at the laboratory diffractometer are comparable to synchrotron measurements concerning the observation of the structural evolution of the studied materials. As an example, a positive electrode material, $\text{LiNi}_{0.80}\text{Co}_{0.15}\text{Al}_{0.05}\text{O}_2$, has been studied using both laboratory X-rays and synchrotron radiation. Figure 2b shows the change of the 003 reflection in the 1st charge of $\text{LiNi}_{0.80}\text{Co}_{0.15}\text{Al}_{0.05}\text{O}_2$ observed using laboratory XRD while figure 3 shows the same using synchrotron XRD. In both measurements, we are able to follow the structural changes happening during the charge and dis-

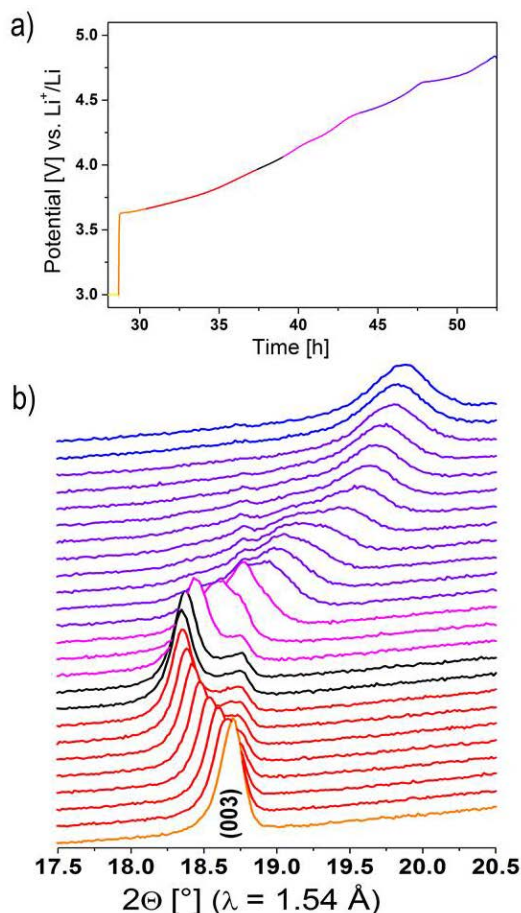


Figure 2: a) First charge curve of a $\text{LiNi}_{0.80}\text{Co}_{0.15}\text{Al}_{0.05}\text{O}_2$ electrode and b) *in situ* XRD pattern of the 003 reflection of $\text{LiNi}_{0.80}\text{Co}_{0.15}\text{Al}_{0.05}\text{O}_2$, as observed using laboratory XRD. The colour code corresponds to the galvanostatic curve (a).

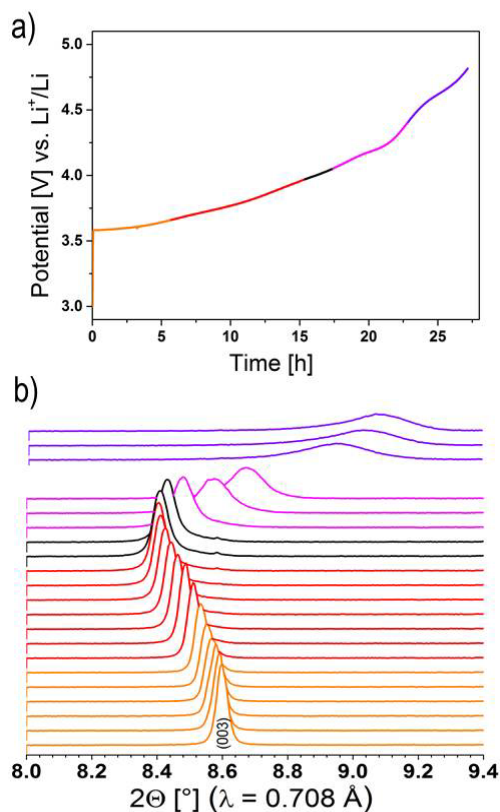


Figure 3: a) First charge curve of a $\text{LiNi}_{0.80}\text{Co}_{0.15}\text{Al}_{0.05}\text{O}_2$ electrode and b) in situ XRD pattern of the 003 reflection of $\text{LiNi}_{0.80}\text{Co}_{0.15}\text{Al}_{0.05}\text{O}_2$, as observed using synchrotron XRD. The colour code corresponds to the galvanostatic curve (a). The XRD acquisition was interrupted for ≈ 3 h (between pink and lilac patterns) due to technical problems.

charge of the $\text{LiNi}_{0.80}\text{Co}_{0.15}\text{Al}_{0.05}\text{O}_2$ electrode. In this case, synchrotron data was recorded during a full charge cycle in approx. 27 hours while laboratory X-ray data requested a whole weekend.

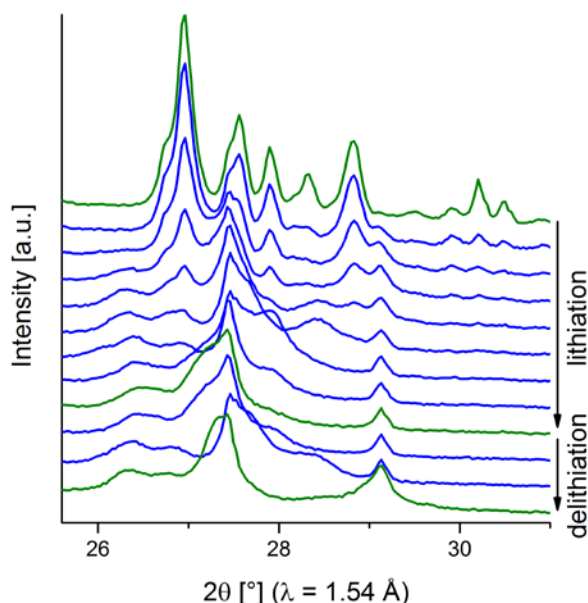


Figure 4: Change of the most intense reflections in the 1st cycle of $\text{Cu}_{0.5}\text{TiOPO}_4$, as observed using laboratory XRD.

As another example, a negative electrode was also studied. Figure 4 shows the region with the most intense reflections of $\text{Cu}_{0.5}\text{TiOPO}_4$ upon lithiation with 2 Li^+ per formula unit and following delithiation in the 1st cycle, as observed using laboratory XRD. Figure 5 shows a similar measurement using synchrotron XRD.

Structural changes of the material can be observed by both methods. Since $\text{Cu}_{0.5}\text{TiOPO}_4$ is less crystalline than $\text{LiNi}_{0.80}\text{Co}_{0.15}\text{Al}_{0.05}\text{O}_2$ a different strategy had to be followed. The step size was increased in order to get better statistics in the same acquisition time. This allowed identifying less intense reflections of the evolving phases that were not detected in the synchrotron measurement where a faster cycling rate and a 10-fold shorter acquisition time for a larger 2θ angular range is used.

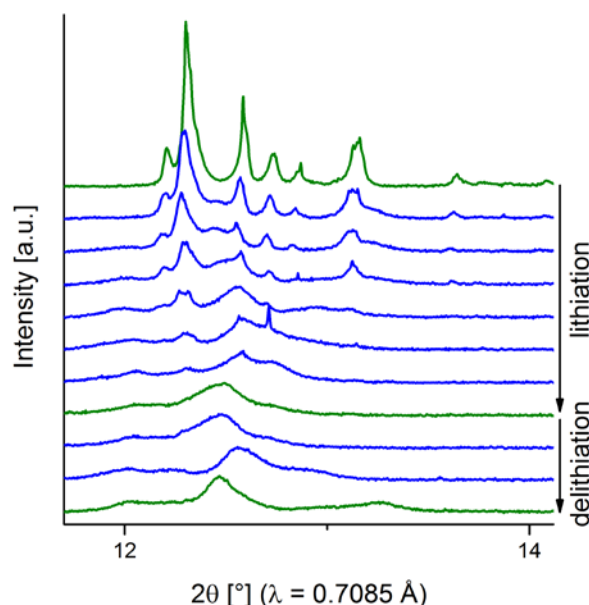


Figure 5: Change of the most intense reflections in the 1st cycle of $\text{Cu}_{0.5}\text{TiOPO}_4$, as observed using synchrotron XRD.

Conclusion

The developed electrochemical cell for *operando* studies of lithium-ion batteries using laboratory X-rays is a great tool to study structural changes of electrode materials. Experiments using laboratory X-rays have to be carefully optimised in order to obtain comparable results to those obtained using synchrotron radiation. The main disadvantage of the laboratory X-ray source is the long acquisition time which restricts the 2θ angular range under observation. Additionally, the exchangeable window material and the reflection geometry (in comparison to transmission geometry at the synchrotron) allow also studying reflections that might otherwise be overlapping with other reflections of the cell.

Acknowledgment

The support of the team of the MS powder beamline at SLS for the synchrotron measurements was appreciated. Swiss National Science Foundation is thanked for financial support (project no 200021_129508).

Cycling rate effects on half and full cells: 5V-NMC vs. graphite

L. Boulet-Roblin, M. El Kazzi, P. Novák, C. Villevieille

phone: +41 56 310 310 2115, e-mail: lucien.boulet@psi.ch

Nowadays, the specific energy of Li-ion batteries is not sufficient to compete with gasoline cars for long range. To improve the specific energy and the safety, many novel electroactive materials have been studied over the two last decades [1]. A new generation of cathodes has been developed and the layered oxide 5V-NMC (layered $\text{Li}(\text{Ni}, \text{Co}, \text{Mn})\text{O}_2$, NMC with Li_2MnO_3 domains) is one of the most promising. This cathode is able to deliver a specific charge of up to 250 mAh/g while cycling until 4.8 V vs. Li^+/Li [2], [3]. At the moment the material is promising in half-cell configuration (vs. Li), however, its behavior in full-cell configuration has not been fully investigated. Thus, the behavior of this material has to be studied in full cell configuration (vs. a real anode, e.g., graphite). The goal of this study is to have a look at the behavior of this promising 5 V cathode in the full-cell configuration and to have a look at the limiting properties of common electrolytes in the 5 V region. Here we present preliminary results of the cycling rate effects for half and full-cell configurations combining 5V-NMC and graphite.

Experimental

5V-NMC was synthesized using a citric acid route with two heat treatment steps. The graphite (SFG44) was provided by TIMCAL. The electrodes were prepared by casting a mixture of 80 wt. % active material (5V-NMC or graphite), 10 wt. % Super-P carbon (TIMCAL), and 10 wt. % Kynar Flex binder (Solvay), suspended in N-methyl-2-pyrrolidinone (Fluka) and by doctor blading onto an aluminium foil for 5V-NMC and onto copper foil for graphite. The casted slurries were dried under vacuum at 80°C. Electrochemical cells were assembled from these electrodes with glass fiber separator soaked with LP30 electrolyte (Novolyte) (ethylene carbonate (EC): dimethyl carbonate (DMC) (1:1 w/w) and 1 M LiPF_6). The electrochemical cycling of the full cells was carried out galvanostatically between 1.0 V and 4.8 V at different C-rates (assuming theoretical specific charges of 280 mAh/g for 5V-NMC and 372 mAh/g for graphite). For the balancing of the electrodes in the full cell configuration an excess of graphite (ca. 10 % based on 372 mAh/g) was added to avoid lithium plating.

Results

Figure 1 presents the specific charge at two different rates (C/10 and 1-C) for the respective half cells (5V-NMC vs. Li^+/Li and graphite vs. Li^+/Li). At slow rate (C/10), around 250 mAh/g are reached with 5V-NMC but significant fading occurs during the first 100 cycles. This fading is less pronounced at fast rate (1-C) but only 175 mAh/g can be practically obtained. The same behavior is observed for the graphite electrode (~380 mAh/g at C/10 without fading and ~200 mAh/g at 1-C with a fading occurring after 20 cycles).

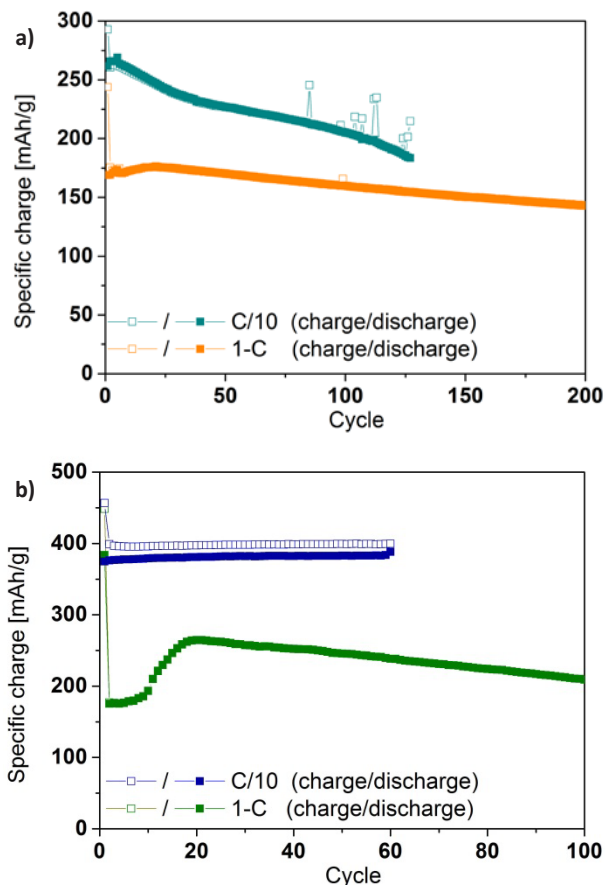


Figure 1. a) Typical specific charge of 5V-NMC electrodes in half cells at 1-C and C/10 rates; b) Specific charge of graphite electrodes in half cells at 1-C and C/10 rates.

Figure 2 shows the specific charge of 5V-NMC vs. graphite cells using different C-rates. We can see two major trends between the fast rates (1-C and C/2) and the lower rates (C/5 and C/10). We measured a specific charge close to 250 mAh/g for the low rates and a specific charge close to 200 mAh/g for the fast rates. During cycling, a better capacity retention with only ~10 % fading after 100 cycles at 1-C rate is observed. However, at the lower rate (C/10), a fading close to 50 % is observed after 100 cycles. One of our hypotheses is that the degradation is more important at lower rates than at faster rates because of the cycling time spent in highly oxidative conditions (positive to 4.5 V). If we compare the results of the half and full cells, we obtain a better specific charge and lifetime at fast rates (1-C) for the full cell than for the half-cell configuration. But at the slow rate (C/10) the performances of the full cells are worse than those of the corresponding half cells. Surface investigation such as *post mortem* SEM analyses and *ex situ* XPS were performed to study the surface and the morphology of the electrodes after cycling.

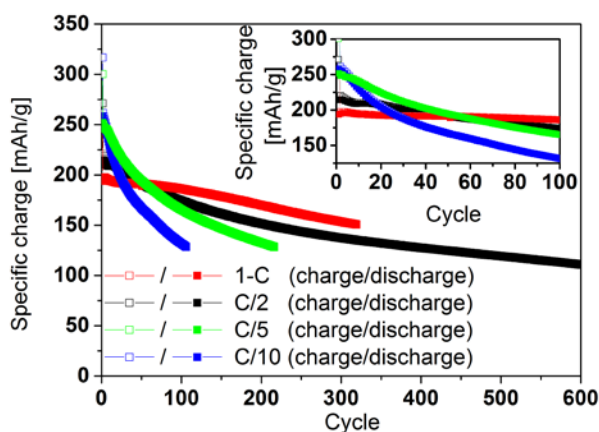


Figure 2. Typical specific charge in respect to the oxide electrode of 5V-NMC/C full cells at different C rates (1-C, C/2, C/5, and C/10); the inset shows the first 100 cycles.

A few cracks are visible at the surface of 5V-NMC particles only in the case of the half-cell configuration (figure 3a). At the moment, we can only speculate on these cracks; they can come from a structural re-organization during cycling and/or from the oxygen release which creates pressure inside the particles. We can see big changes between the graphite surface of the half and full cells after cycling at C/10 rate (figure 3c and 3d). It is obvious from the images that the surface of the graphite is more damaged in the full cell (d) than the one in the half cell (c). As one can see, the graphite particles are covered by a thick “polymer” layer in full cell configuration. The presence of the “polymer” may be responsible of the limited electrochemical properties of graphite.

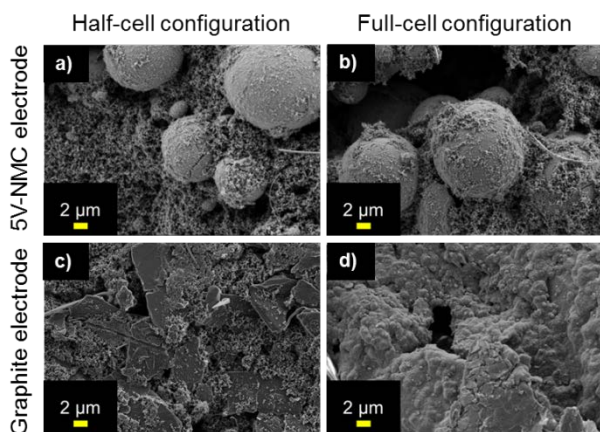


Figure 3. SEM images of cycled 5V-NMC (a, b) and graphite (c, d) electrodes at C/10 rate: a) and c) in half-cell configuration and b) and d) in full-cell configuration.

In order to determine the composition of this “polymer” at the surface of the graphite particles, *ex situ* XPS analyses were performed and only the most relevant spectra are presented in this contribution. Figure 4 shows the spectra of the cobalt and manganese binding energies of 5V-NMC pristine electrodes and the graphite electrode cycled in full-cell configuration at the C/10 rate.

Surprisingly, the signals of transition metals at the 5V-NMC pristine surface are the same as for the graphite electrode. This indicates that the transition metals migrate from the positive electrode to the negative electrode through the electrolyte during cycling. This result shows a strong interaction between the positive and the negative electrode. From the literature, it is already known that the Mn disproportionation leads to destabilization of the SEI on the graphite [4]. Thus, we can hypothesize that the transition metals migrate through the electrolyte and can react with the SEI at the graphite surface and change its cycling properties.

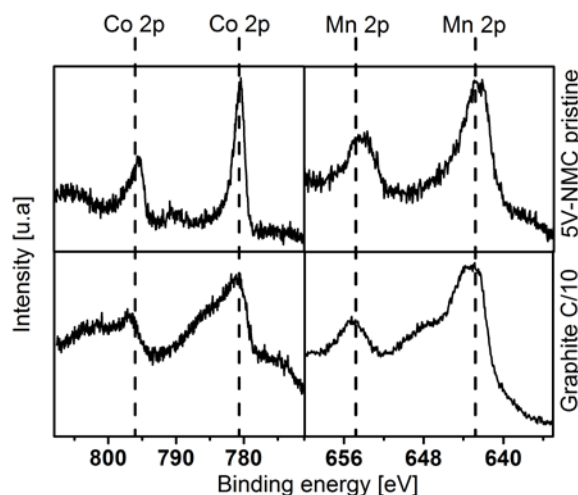


Figure 4. Co 2p and Mn 2p XPS spectra of pristine 5V-NMC and graphite electrode in full cell cycled during 100 cycles at C/10 rate.

Conclusion

We showed that the 5V-NMC cathode is one of the most promising cathodes but its behavior in full-cell configuration vs. graphite needs to be optimized. Using standard electrolyte and standard anode (graphite) material leads to an important destabilization of the system which causes failure of the test cells. Further surface investigations are in progress to overcome these issues.

Acknowledgment

BASF SE is gratefully acknowledged for financial support.

References

- [1] V. Etacheri, R. Marom, R. Elazari, G. Salitra, D. Aurbach, *Energy Environ. Sci.* **4**, 3243 (2011).
- [2] H. Kobayashi, Y. Arachi, S. Emura, H. Kageyama, K. Tatsumi, T. Kamiyama, *J. Power Sources* **146**, 640–644 (2005).
- [3] R. Robert, C. Villevieille, P. Novák, *J. Mater. Chem. A* under press (2014).
- [4] J-H. Kim, N.P.W. Pieczonka, Z. Li, Y. Wu, S. Harris, B.R. Powell, *Elect. Acta* **90**, 556-562 (2013).

Electrochemical impedance spectroscopy characterization of lithium-ion battery electrodes – technical improvements

C. Bünzli, H. Kaiser, P. Novák

phone: +41 56 310 2161, e-mail: christa.buenzli@psi.ch

Electrochemical impedance spectroscopy (EIS) is a powerful tool to characterise Li-ion batteries as it allows in carefully designed experiments the discrimination of the factors limiting the cell performance such as the charge transfer resistance, passivating film formation or ionic resistance. The use of a reference electrode (RE) is thereby crucial to investigate the electrode of interest without the influence from the counter electrode (CE) [1]. With a stable three electrode system, intermittent EIS measurement could be performed at specific stages of electrode cycling. In order to exhibit good cycling performance, battery electrodes have certain cell requirements like the need of applied pressure and air tightness, which complicates the introduction of a RE. In addition, inappropriate placement of the RE can lead to distortions in the EIS response, as was demonstrated by Klink et al., who proposed a modified Swagelok® cell with a coaxially positioned RE in the middle of ring electrodes [2].

Here, two designs of reusable EIS cells for the measurement of practical Li-ion battery electrodes are introduced, characterized and compared. As in reference [2], the RE is placed in the middle of a ring shaped WE as is shown in Figure 1. Current collector parts are made of titanium, while for the outer construction stainless steel was used. Insulating parts were made of PEEK and the cell was made air tight with EPDM rubber O-rings. In both designs, a spring is incorporated to apply mechanical pressure to the electrodes. Design B is a modified version of the coin-type like standard cell commonly employed in our laboratory which exhibits good cycling performance. The cells were tested in a half cell setup using LiCoO₂ (LCO) electrodes as exemplary WEs and

using Li both as CE and RE. The cycling behaviour was compared to the standard electrode and the EIS measurement was tested for consistency and reproducibility.

Experimental

Composite electrodes consisting of 87 wt% battery grade LCO, 3 wt% carbon black (C-ENERGY™ SuperC65, TIMCAL), 3 wt% graphite (C-ENERGY™ KS6L, TIMCAL) and 7 wt% polyvinylidene fluoride (PVDF, KF polymer W#1300, Kureha) as the binder material and *N*-methylpyrrolidone as the solvent were prepared. The slurries were casted by a doctor blade technique onto aluminium foil and the electrodes were dried under vacuum at 80 °C overnight. Similarly, a CE consisting of 80 wt% Li₄Ti₅O₁₂ (LTO, SüdChemie), 10 wt% SC65 and 10 wt% PVDF (Kureha KF Polymer W#9100) was prepared on copper foil. Electrodes of a geometrical area of ~1.3 cm² were punched out; ring electrodes with an outer diameter of 15 mm and a centred hole of 7.5 mm diameter and disks with a diameter of 13 mm for the standard electrodes. The electrodes were dried under vacuum at 120 °C overnight before they were assembled in an argon filled glovebox. A glass fibre fleece was used as a separator and was soaked with 1 M LiPF₆ in ethylene carbonate : dimethyl carbonate = 1 : 1 by weight (Ferro).

Electrochemical measurements were performed in a temperature controlled chamber at 25 °C. Galvanostatic cycling was performed by a computer controlled cell capture system (CCCC, Astrol Electronic AG) between 3.0 and 4.2 V vs. Li⁺/Li, at C/3 (1C = 150 mA/g). Each galvanostatic phase was followed by a potentiostatic step until the specific current dropped to < 5 mA/g. Electrochemical impedance spectra were recorded with a VMP3 potentiostat (BioLogic Science Instruments) after an equilibration time of 2 hours. A sinusoidal potential perturbation was applied around OCV vs. Li⁺/Li with an amplitude of 10 mV in the frequency range 100 kHz – 10 mHz.

Results

The cycling performance of LCO electrodes in the two EIS cells is compared in Figure 2 to the cycling in the standard cell. A specific charge of 140 – 145 mAh/g was achieved and retained over > 50 cycles in the standard cell. The same charges were reached at the beginning in both EIS cell designs and the galvanostatic curves of all cells were overlapping (not shown). However, electrodes cycled in cell design A exhibited a loss in the specific charge with each cycle. In contrast, cell design B allowed comparable cycling as in the standard cell for up to 30 cycles (180 hours), which could be even extended to > 200 cycles with the use of teflon instead of the rubber O-rings. The failure of stable cycling in cell A is not a consequence of leakage, as cycling the cell in the controlled atmosphere of the glovebox also led to strong charge fading. We speculate that the O-ring of the gliding electrode stub is swelling in contact with the electrolyte and gets stuck such that the applied pressure

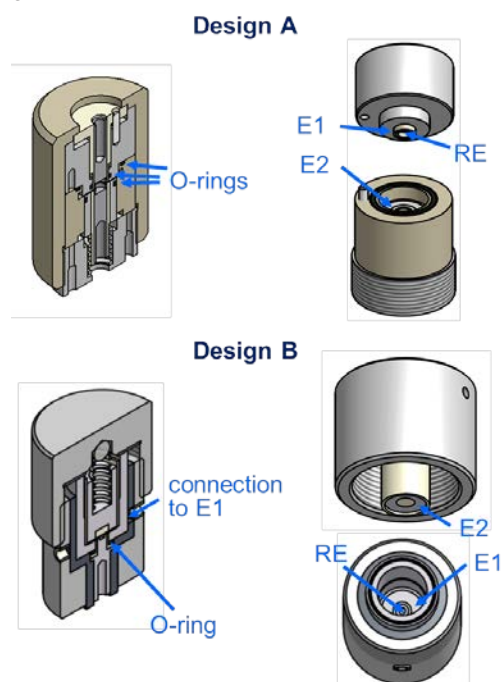


Figure 1. Drawings of the EIS cells employed in this work.

from the spring is altered. In cell design B, such gliding O-rings at critical positions were avoided.

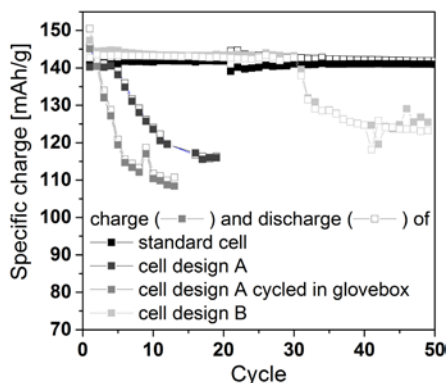


Figure 2. LCO electrodes cycled against lithium.

To test the EIS performance of the cells, a symmetric setup was used where both E1 and E2 were LCO electrodes. By selecting electrodes of the same active mass weight, the same EIS response could be expected from both positions. Figure 3 confirms that this was indeed the case. Due to different applied pressure and configuration of the parts in both cells, the response from the two cell designs exhibited some variances.

Simulations and experiments have shown that the EIS measurement is very sensitive to misalignment of E1 and E2. Relative shifts of < 0.5 mm can already lead to considerable distortions and shifts in the EIS response [2-4]. The practical realisation of the alignment of the two electrodes is more consistent and reliable for cell design A. The reproducibility is demonstrated in Figure 3 by two repeat experiments where the cells were freshly assembled. Obviously, positions E1 and E2 of cell design B are not exactly equivalent, whereas in cell design A they are interchangeable.

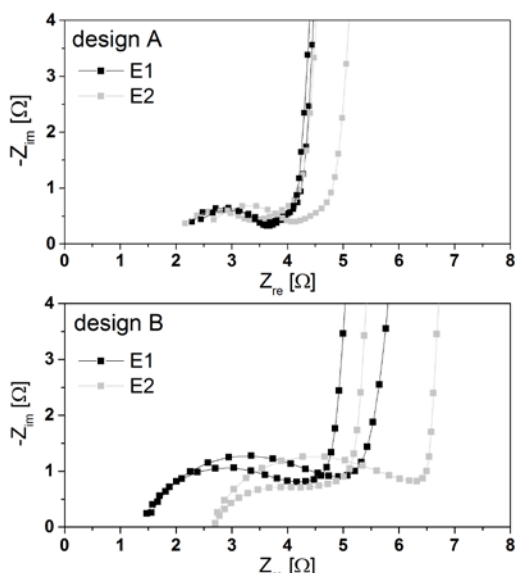


Figure 3. Nyquist plots comparing the EIS response from LCO in positions E1 and E2 of the two cell designs. Two repeated measurements are shown.

Usually, it is desirable to measure EIS at different states of charge or different number of cycles. Therefore, a CE able to deliver/accept electrons and Li^+ is required. For convenience, lithium foil is commonly employed. However, this can considerably affect the response from the

WE (the electrode of interest), as is demonstrated in Figure 4. The LCO WE employed therein was always the same, while the CE was exchanged. A control experiment with intermittent EIS measurement within the same time span caused only small variations. Using Li foil as the CE, an absolute impedance ($|Z|$) of up to 5.5 times higher the one of the symmetric configuration was obtained at frequencies above 2 Hz. In principle, using a reference electrode allows the measurement of the WE independently of the CE – as long as the impedance of the CE is low enough. Since Z is inversely proportional to the electrode's surface area, the relatively smooth surface area of the Li foil results in a Z too big for the EIS measurement of practical Li-ion battery with high effective surface areas. Furthermore, the formation of a passivation film on the reactive Li surface and dendrite formation change the impedance of Li and consequently its limiting effect on the EIS measurement [5]. Therefore, using another Li-ion battery CE with a high surface area can circumvent this problem. For example, using a LTO CE for the measurement of the LCO electrode yielded practically the same response as was obtained with the symmetric setup (Figure 4).

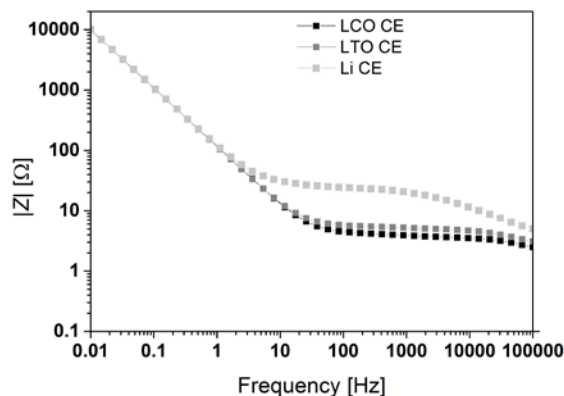


Figure 4. The absolute impedance $|Z|$ of LCO measured in cell design A with different CEs as indicated in the legend.

Conclusion

Both cell designs can provide reliable EIS data, but only cell design B is capable to deliver at the same time stable cycling behaviour. The often used Li foil is not suitable as a CE in EIS measurements of high surface area Li-ion battery electrodes.

Acknowledgement

The authors are grateful for technical assistance and TIMCAL SA (Bodio, Switzerland) for financial support.

References

- [1] M. Dollé, F. Orsini, A.S. Gozdz, J.-M. Tarascon, J. Electrochem. Soc. **148**, A851-A857 (2001).
- [2] S. Klink, E. Madej, E. Ventosa, A. Lindner, W. Schuhmann, F. La Mantia, Electrochem. Commun. **22**, 120-123 (2012).
- [3] S. Klink, D. Höche, F. La Mantia, W. Schuhmann, J. Power Sources **240**, 273-280 (2013).
- [4] M. Ender, A. Weber, E. Ivers-Tiffée, J. Electrochem. Soc. **159**, A128-A136 (2012).
- [5] N. Schweikert, H. Hahn, S. Indris, Phys. Chem. Chem. Phys. **13**, 6235-6240 (2011).

Reactions occurring at HE-NCM electrode/electrolyte interface

E. Castel, E.J. Berg, M. El Kazzi, P. Novák, C. Villevieille

phone: +41 56 310 4542, e-mail : elias.castel@psi.ch

In order to achieve better energy densities, cathode materials with higher specific charges and highly positive potentials must be identified. Nevertheless, high charging potentials accelerate electrolyte oxidation reactions that generate several byproducts. Solid products may form a passivation layer at the electrode/electrolyte interface that will increase the internal resistance of the cell and lower the practical output voltage of the battery. Gaseous products may increase an internal pressure inside the cell and thereby increase the risk of casing degradation, contact losses, venting, or explosion. The understanding of the formation of byproducts at the electrode/electrolyte interface is thus essential to the development of next-generation power sources.

Lithium-rich NCM (HE-NCM), which can also be written as $\text{Li}_2\text{MnO}_3 \bullet \text{Li}(\text{Ni}_x\text{Co}_y\text{Mn}_z)\text{O}_2$, delivers a higher specific charge (~250 Ah/kg) and a higher energy density than other commonly used cathode materials [1]. In a previous study [2], we reported the evolution of the gaseous products being formed during the cycling of HE-NCM electrodes in different electrolytes by employing differential electrochemical mass spectrometry (DEMS). This study showed that oxygen detection was systematically accompanied by a strong CO_2 formation. Therefore, the oxidation of the solvents' carbonates was assumed.

In the present report, we discuss the evolution of the solid products formed during cycling of HE-NCM electrodes. X-ray photoelectron spectroscopy (XPS) was used to investigate the nature and to determine the composition of HE-NCM electrode/electrolyte interfaces formed after two galvanostatic cycles versus metallic lithium counter electrodes when LP30, LP10, and LC30 are used as electrolytes.

Results

Figure 1 shows the C1s, O1s, F1s and the Li1s together with Ni3p, Co3p and Mn3p core levels spectra, respectively, of a pristine electrode and for the electrodes cycled in LP30, LP10, and LC30.

Charge and discharge cycles were performed in galvanostatic mode at C/10 rate with cut-off voltages of 5V and 2 V vs. Li^+/Li without any potentiostatic step. These conditions are here to reproduce the galvanostatic cycling program used for all DEMS experiments. At the end of the second cycle, a final charging process is carried out to reach 3V for 3 HE-NCM electrodes cycling with LP30, LP10 and LC30, or 4V for another 3 HE-NCM electrodes.

For the pristine electrode, the C 1s spectrum shows the signal of Super P carbon at 284.4 eV and PVDF at 286.4 and 290.8 eV. Additional components located at 285.5 eV (C-H components) and 290 eV (CO_3 components) are assigned to hydrocarbons and Li_2CO_3 . Traces of lithium alkoxides (ROLi) can be also considered (C-O components, giving a peak at 286.7 eV). The O1s core level shows mainly the oxygen within the HE-NCM located at 530 eV. Li_2CO_3 is observed at 531.5 eV. Additional peaks between 532.5 and 533.5 eV are also seen

and are potentially related to lithium alkoxides.

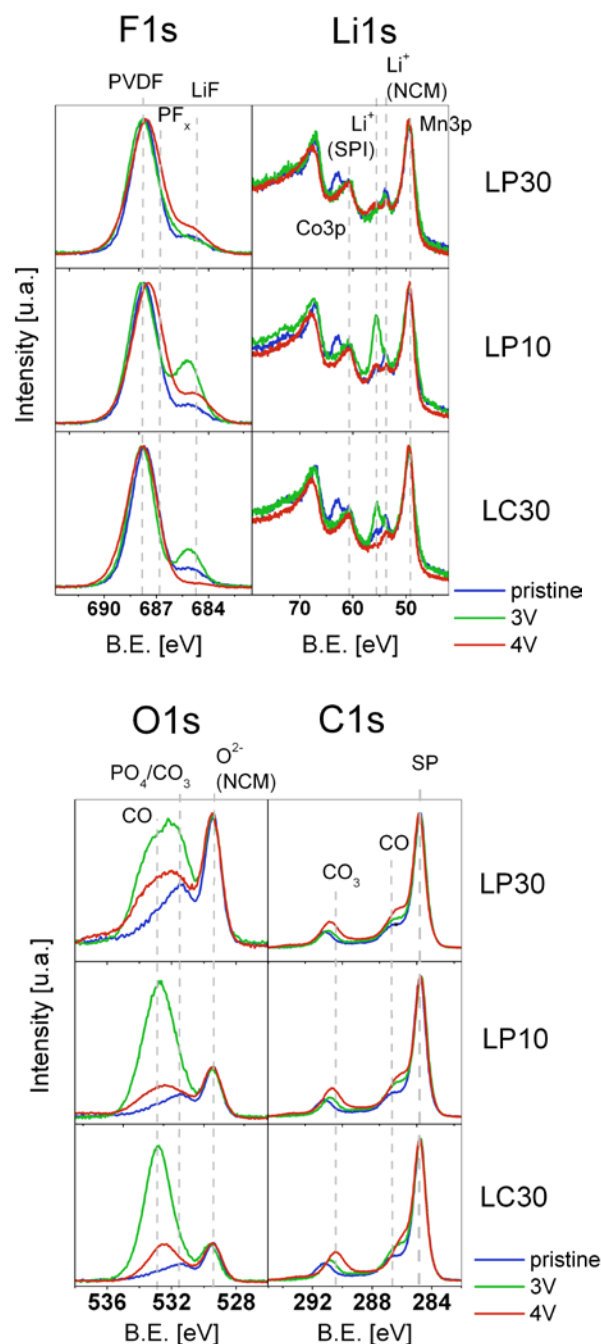


Figure 1. C 1s, O 1s, and F 1s core peak spectra of HE-NCM pristine electrode (80% HE-NCM, 10% Super P, 10% PVDF), HE-NCM electrodes obtained after cycling in LP30, LP10, and LC30 electrolytes to 3V (green curves) and 4V (red curves) after 2 cycles.

In the F1s spectra we observe the signal for PVDF and LiF, at 688eV and 685.4 eV, respectively. The Li1s spectrum displays two contributions, one at 54.3 eV related to the lithium of the HE-NCM electroactive material, and another peak located at 56.2 eV that can be assigned to

LiF (Li1s ~56.5 eV), Li₂CO₃ (Li1s ~55 eV), and other species constituting the native films on the surface of the electrode.

For cycled electrodes stopped at 3V vs. Li⁺/Li, the C1s spectra show that, whatever the electrolyte, the signals located at 285, 286.7, and 290 eV increased, suggesting the formation of some carbonates and species containing C=C, C-H, and C=O. For the O1s XPS spectra, the peak located at 531.5 eV, related to carbonate species, has considerably grown. Moreover, additional contributions between 532.5 and 533.5 eV are observed, suggesting the presence of other carbonates compounds (from Li₂CO₃ to any ROCO₂Li carbonates like R=CH₃ or C₂H₅), lithium alkoxides or polyethylene oxides [3]. The amount of oxygen-rich deposits - most likely carbonates - seems to be very high with LP10 and LC30. When LP30 is used, the amount of deposits seems to be comparatively less. The F1s XPS spectra show that the LiF component is evolving strongly with LP10 and LC30 electrolytes, whereas it changes much less with the LP30 electrolyte. The peak located at 56.2 eV in the Li1s spectra, assigned to species constituting the native film on the surface of the electrode has considerably grown with LP10 and LC30 electrolyte.

For cycled electrodes stopped at 4V vs. Li⁺/Li, the C1s spectra show that the amount of carbonates and species containing C=C, C-H, and C=O has increased. The surface layer covering the Super P and the PVDF components remains very thin as the PVDF binder contribution is still detected. Comparable amounts of deposits are observed with LP30 and LP10. When the LC30 electrolyte is used, more hydrocarbons are present and less Li₂CO₃ is observed. The O1s spectrum shows that the amount of carbonates, C-O-rich, and other oxygen-rich species has decreased, suggesting some decomposition of the products formed below 4V vs. Li⁺/Li (initially covering the HE-NCM particles). The contribution of the LiF component in the F1s spectra increased with LP30. Surprisingly, with LP10, less LiF is observed. No LiF could be detected with LC30. Finally, the Li1s spectra show that the amount of lithium located in the growing film on the surface of the electrode is higher in LiPF₆-based electrolytes. With LC30, almost no lithium is detected in the surface layer.

Conclusion

XPS data demonstrated that a film with nearly the same thickness was formed on the top of HE-NCM electrodes, after 2 galvanostatic cycles in the three investigated electrolytes. The composition of the film layer is slightly different according to the employed electrolyte, but the presence of several carbonate species has been detected, and polyethylene oxide type species (oligomers) are observed on the surface of each electrode after cycling.

At 3V vs. Li⁺/Li, some carbonates grow on the PVDF/Super P surfaces and a significant portion of oxygen-rich species is formed on HE-NCM particles (for the moment we can only confirm Li₂CO₃, but other carbonates and even polyethylene oxide-like components could be taken into account). At 4V vs. Li⁺/Li, the surface layer covering PVDF and Super C seems to grow.

Thus formation/and deformation of surface layer happens most likely on the surface of HE-NCM particles highlighting the chemical activity of the surface of the oxygen source. Nevertheless, some carbonates and

polyethylene oxides seem to be growing as well on the PVDF/Super P part of the electrode. The species covering this part of the electrode may resist at higher potentials. Further products of the decomposition of the electrolyte could be deposited on the remaining surface layers covering PVDF binder and Super P particles at a later stage of the cycling, to form a thicker solid film.

Acknowledgment

Financial support from BASF SE is gratefully acknowledged.

References

- [1] M.M. Thackeray, S.-H. Kang, C.S. Johnson, J.T. Vaughey, R. Benedek, S.A. Hackney, *J. Mater. Chem.* **17**, 3112–3125 (2007).
- [2] E. Castel, E.J. Berg, C. Villevieille, P. Novák, *PSI Electrochemistry Laboratory – Annual Report 2012*, 63-64, DOI: 10.3929/ethz-a-007047464 (2013).
- [3] R. Dedryvère, H. Martinez, S. Leroy, D. Lemordant, F. Bonhomme, P. Biensan, D. Gonbeau, *J. Power Sources* **174**, 462-468 (2007).

Gas evolution followed by DEMS of HE-NCM electrodes using different electrolytes

E. Castel, E.J. Berg, M. El Kazzi, P. Novák, C. Vilevieille

phone: +41 56 310 4542, e-mail : elias.castel@psi.ch

Increasing the battery voltage is imperative to improve the energy density of a lithium-ion cell. Therefore a lot of effort has been paid to develop 5-Volt materials for the positive electrode. While increasing the energy density with 5-Volt cathodes, several challenges remain such as the inherent cycling stability and safety. Among the 5-Volt cathodes reported so far, the lithium-rich layered metal oxide HE-NCM is certainly one of the most promising [1]. Higher specific charge is available after a first charging positive to 4.5V vs. Li⁺/Li. This potential corresponds to the activation of the Li₂MnO₃ domains integrated into the NCM structure: the delithiation is followed by the oxidation of O²⁻ from the crystal structure and subsequent evolution of oxygen gas. After the loss of "Li₂O", manganese is getting activated which helps to maintain the practical specific charge high [2]. From the literature it is well-known that oxygen is known to react with carbonate-based electrolytes [3]. In the present report, we discuss the evolution of the gaseous reaction products formed during cycling of HE-NCM electrodes by using DEMS measurements.

Results

Figure 1 shows the results of DEMS experiments performed during the two first galvanostatic cycling of HE-NCM electrodes, between 2.0V and 5.0V vs. Li⁺/Li at C/10 rate (10 hours for the full delithiation). The evolution of the potential (vs. Li⁺/Li), the evolution rate of carbon dioxide, rCO₂, and oxygen, rO₂, and the respective integrated amounts nCO₂ and nO₂ are given versus the cycling time, while cycling the electrodes with LP30 (1M LiPF₆ in a mixture of EC/DMC, 1:1), LP10 (1M LiPF₆ in mixture of EC/DMC/EMC, 3:3:4) and LC30 (1M LiClO₄ in a mixture of EC/DMC, 1:1) electrolytes, respectively.

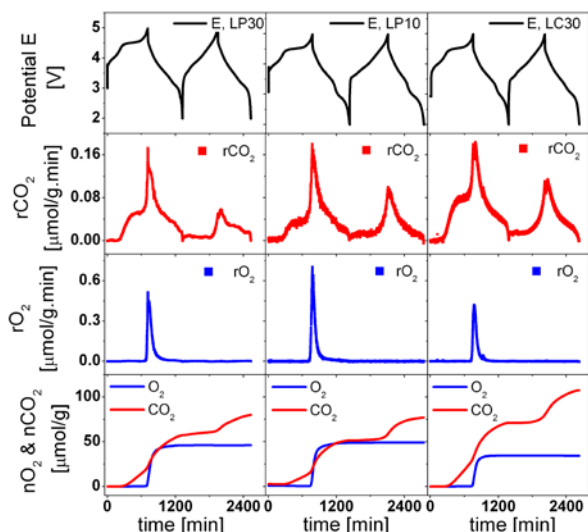


Figure 1. Plot of the CO₂ and O₂ evolution rates and the gas amounts during the galvanostatic cycling of HE-NCM vs. Li. at C/10 rate in LP30, LP10 and LC30 electrolytes respectively.

Whatever the electrolyte, during the first charge, in the potential range between 4.2V (4.5V in the case of LP10)

and 4.7V vs. Li⁺/Li, only CO₂ is evolving, accelerating as a first step, to be then rather constant during the potential plateau. When 5.0V vs. Li⁺/Li is reached, rO₂ and rCO₂ are both maximal. During the discharge, the rO₂ decelerates faster than rCO₂. Indeed, we observe that rO₂ is near zero at ca. 3.5V vs. Li⁺/Li, whereas rCO₂ is still decelerating. At potentials close to 3.0V vs. Li⁺/Li rCO₂ remains a certain time constant before dropping near zero when 2.0V vs. Li⁺/Li is reached.

In the potential range 2.0V-4.4V during the second charge, rCO₂ is evolving slowly. During the second cycle, at the potentials between 4.4V-2.0V vs. Li⁺/Li, rCO₂ is accelerating with the increase of the potential to be maximal at 5.0V. During the discharge, rCO₂ is decelerating continuously.

After two galvanostatic cycles, the amount of detected CO₂ is about 84±4 μmol/g for LP30, 79±6 μmol/g for LP10 and 105±15 μmol/g for LC30 electrolyte. The amount of detected oxygen is about 44±3 μmol/g for LP30, 45±8 μmol/g for LP10 and 38±4 μmol/g for LC30 electrolyte.

Figure 2 shows the results of cyclic voltammetry with LP30, LP10 and LC30 electrolytes. For the first charging process, the selected scan rate was 0.061 mV/sec between 2.8V (OCV) and 5.0V vs. Li⁺/Li for the first charge, and then 0.0833 mV/sec between 5.0V and 2.0V vs. Li⁺/Li for the subsequent discharging/charging process, thus the cycling time corresponds to ca. C/10.

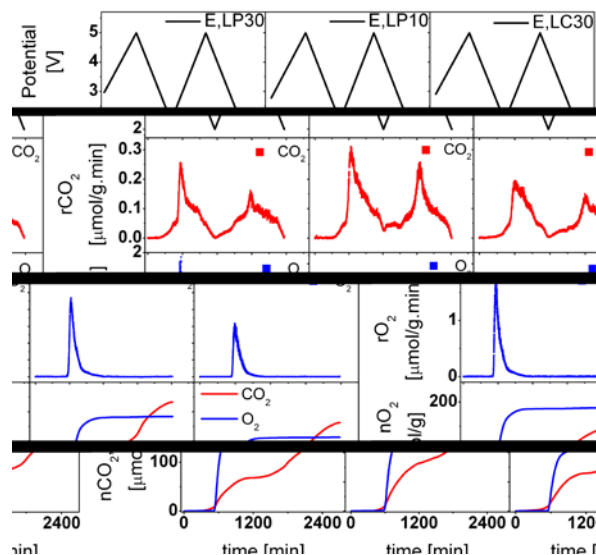


Figure 2. Plot of the CO₂ and O₂ evolution rates and the gas amounts during cyclic voltammetry of HE-NCM vs. Li. in LP30, LP10 and LC30 electrolytes respectively.

As for galvanostatic cyclic experiments, CO₂ only is evolving until 4.7V vs. Li⁺/Li is reached. Nevertheless rCO₂ starts to accelerate at ca. 3.7V vs. Li⁺/Li (3.8V in the case of LP10), which is a detection onset lower than the one found for galvanostatic cycling. Oxygen is evolving in the potential range 4.7V-2.0V vs. Li⁺/Li, which means during the end of the charge and along the entire

first discharge. Once oxygen is detected, $r\text{CO}_2$ is accelerating. At 5.0V vs. Li^+/Li both $r\text{O}_2$ and $r\text{CO}_2$ are maximal. During the discharge, the $r\text{O}_2$ decelerates continuously until ca. 4.0V vs. Li^+/Li . Below 4.0V, the deceleration of $r\text{O}_2$ is less pronounced. During the discharge $r\text{CO}_2$ decelerates stepwise with a first break at ca. 4.4V and a second break at 3.4V and a last one at ca. 3.0V vs. Li^+/Li . When 2V vs. Li^+/Li is reached, both $r\text{CO}_2$ and $r\text{O}_2$ are almost not detectable. In the potential range between 2.0V and 3.45V vs. Li^+/Li during the second charge, $r\text{CO}_2$ is almost constant close to zero and accelerates at potentials more positive than 3.45V vs. Li^+/Li . $r\text{CO}_2$ is then maximum at 5.0V vs. Li^+/Li and decelerates stepwise along the second discharge.

Regarding the amount of detected gases after cycling, the amount of CO_2 is about $140 \pm 15 \mu\text{mol/g}$ for LP30, $200 \pm 15 \mu\text{mol/g}$ for LP10 and $160 \pm 15 \mu\text{mol/g}$ for LC30 electrolytes, respectively. The amount of oxygen was found to be about $180 \pm 15 \mu\text{mol/g}$ for LP30, $170 \pm 15 \mu\text{mol/g}$ for LP10 and $130 \pm 15 \mu\text{mol/g}$ for LC30 electrolyte. As observed for galvanostatic cycling, the oxygen is evolving during the first cycle only. Regarding carbon dioxide $n\text{CO}_2$ is about $70 \pm 15 \mu\text{mol/g}$ for LP30, $100 \pm 15 \mu\text{mol/g}$ for LP10 and $80 \pm 15 \mu\text{mol/g}$ for LC30 electrolytes, respectively, after the first cycle.

Discussion

For both cycling conditions, the oxygen gas evolves only during the first charging process as expected with the activation of Li_2MnO_3 domains occurring during the potential plateau at 4.5V vs. Li^+/Li . For each electrolyte, we observe a “two-step mechanism” for the evolution rate of the carbon dioxide. The CO_2 gas formed at high potential has been experimentally detected and assigned as the primary product of the oxidative decomposition of EC from the electrolyte [4]. The electro-oxidation of the carbonates is detected at ~4.2V vs. Li^+/Li in galvanostatic cyclic, ~3.7V vs. Li^+/Li in CV-mode. When the potential onset of oxygen is reached at 4.7V vs. Li^+/Li , a strong acceleration of $r\text{CO}_2$ is observed. Moreover $r\text{CO}_2$ and $r\text{O}_2$ are simultaneously maximal at ca. 5.0V vs. Li^+/Li at the end of the first charge. The systematic relationship between $r\text{O}_2$ and $r\text{CO}_2$ lets assume that the oxygen released by the active material at the positive electrode is involved in oxidative reactions with the carbonates coming from the electrolyte solvent. Some mechanisms in the literature show that oxygen anions/radicals react with cyclic carbonates via a nucleophilic attack predominantly at the CH_2 group [5]. The nucleophilic attack was confirmed by several mass spectrometric experiments and directly shows that carbonates are unstable against chemical oxidation. Moreover, roughly the same amounts of detected gases suggest common interfacial mechanisms, regardless the electrolyte composition.

It is also interesting to note that the detection onset of carbon dioxide in the first cycle and the second cycle are always different, whatever the cycling mode (CV or galvanostatic cycling). This suggests different electro-oxidation pathways for the carbonates or the oxidation of different chemical species, at the electrode/electrolyte interface.

Nevertheless, ca. 2 times more CO_2 and 4 times more oxygen are detected after 2 cycles in CV mode when we compare with the constant current mode, despite a similar cycling rate. These differences could highlight the fact that any chemical reactions occurring at the

electrode/electrolyte interface, involving oxygen, are kinetically limited, and coupled with the course of the potential during cycling, several oxidation pathways may occur, giving different amounts of CO_2 and O_2 as products.

Conclusion

We showed with DEMS measurements that a part of the oxygen originally leaving HE-NCM materials at 4.5V vs. Li^+/Li is leaving the electrode/electrolyte interface at 4.7V vs. Li^+/Li . The lag between the oxygen release and its detection onset on the mass spectrometer cannot be explained by the DEMS setup only. Thus, we can assume that the oxygen species are accumulated at the electrode/electrolyte interface, most likely on the surface of HE-NCM particles, prior to react with the carbonates at potentials between 4.5-4.7V vs. Li^+/Li . The CO_2 gas evolving at 4.2-4.5V vs. Li^+/Li , mainly comes from the electro-oxidation of the carbonates. Thus an oxidative decomposition reaction of the carbonates is assumed. Another possibility could be that the oxygen, bounded at the surface of HE-NCM particles, reacts with the components of the “native surface layer film” on the top of the electrode.

Acknowledgement

Financial support from BASF SE is gratefully acknowledged.

References

- [1] A. Kraytsberg, Y. Ein-Eli, *Adv. Energy Mater.* **2**, 922-939 (2012).
- [2] Z.H. Lu, J.R. Dahn, *J. Electrochem. Soc.* **149**, A815-A822 (2002).
- [3] B.D. McCloskey, D.S. Bethune, R.M. Shelby, G. Girishkumar, A.C. Luntz, *J. Phys. Chem. Lett.* **2**, 1161-1166 (2011).
- [4] L. Xing, W. Li, C. Wang, F. Gu, M. Xu, C. Tan, J. Yi, *J. Phys. Chem. B* **113**, 16596-16602 (2009).
- [5] V.S. Bryantsev, M. Blanco, *J. Phys. Chem. Lett.* **2**, 379-383 (2011).

Understanding the SEI properties on conversion-reacting Sn electrodes for Na-ion batteries

M. El Kazzi, S. Pérez-Villar¹, C. Villevieille

phone: +41 56 310 2410, e-mail: claire.villevieille@psi.ch

In the field of energy storage, Na-ion batteries are one of the most promising challenges of the decade. The fundamental principles of sodium batteries are by principle identical to the lithium ones, but the number of known materials to be investigated is three times higher than the materials containing lithium, according to the database ICSD (inorganic crystallographic structure database). Therefore, unexplored reaction mechanisms are expected in Na-based systems, which should be investigated and understood to warrant further development.

In the literature, some groups reported impressive specific charges above 400mAh/g and unexpected coulombic efficiencies beyond 95% for materials with more than 200% volume change during lithiation/sodiation such as Sn[1], Sb[2] or intermetallic alloys Cu₂Sb[3], SnSb[4]. Most of these researchers used the same electrolyte, 1M NaClO₄ dissolved in propylene carbonate (PC) with or without fluoroethylene carbonate (FEC) used as additive. The FEC additive is reported to be of great importance to maintain the specific charge above 300 mAh/g and to help to sustain the coulombic efficiency during more than 100 cycles in intermetallic electrodes [2, 4]. Here, we analyze the properties of the interface layer (SEI) on electrodes made from pure commercial element Sn during the first discharge by *post mortem* SEM & XPS, and at the same time the role of the additive is been discussed.

Experimental

Electrodes were prepared by casting a mixture of 80% Sn commercial particles (Sigma Aldrich), 10% PVDF (binder) and 10% Super-P carbon used as a conductive additive (TIMCAL), all suspended in N-methyl-2-pyrrolidone (Fluka) onto a copper foil used as a current collector. After drying, the electrodes were punched out and assembled in an Argon filled glove box. The respective electrolytes used for this study were 1M NaClO₄ dissolved in pure PC or PC with a 5% of FEC as additive. The samples for the *post mortem* analysis (XPS and SEM) were washed with DMC and transferred in Ar controlled atmosphere.

Electrochemical properties

Figure 1 shows the cycling behavior as well as the coulombic efficiency of Sn electrodes cycled at a C/10 rate. The specific charge drops drastically from above 1100 mAh/g for the first cycle to reach only 375 mAh/g for the cells with additive and only 250 mAh/g for the cell without additive after only 10 cycles. The coulombic efficiency is rather low with values close to 85% and 90% for both cells cycled with and without additive, respectively.

In figure 2, we can see the galvanostatic curves of the first and fifth cycle of the cells cycled with and without additive. During the first discharge, a different behavior is observed in the region from 1.5V to 0.25V vs. Na⁺/Na.

The presence of additive seems to modify the electrochemical properties of the Sn electrode.

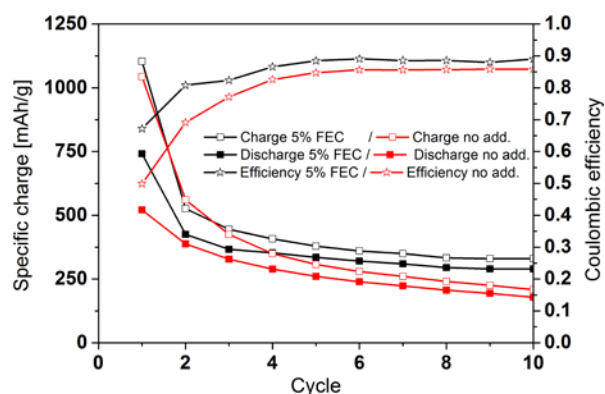


Figure 1. Specific charge of a Sn electrode cycled at C/10 rate against Na with and without FEC additive.

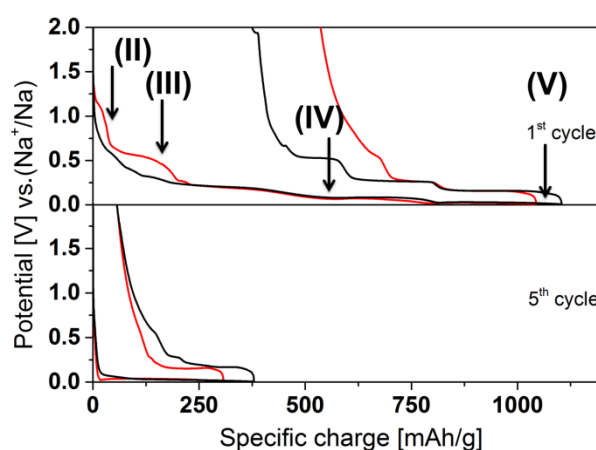


Figure 2. Galvanostatic curves of a Sn electrode cycled with (black) and without FEC additive (red) at C/10 vs. Na⁺/Na. The roman number indicates at which potential the *post mortem* analysis were performed.

Post mortem SEM

An interfacial study was then undertaken in order to understand the impact of the FEC additive on the SEI layer formed on the Sn electrode cycled versus Na. Figure 3 presents the SEM pictures taken during the first discharge/sodiation with and without additive. Apparently, for the electrodes cycled with electrolyte additive, there are two different kinds of behavior, the first one until 550 mV vs Na⁺/Na where some spheres ascribable to the SEI film are visible on the top of the Sn particles and then, the second one until the end of the sodiation, in which the spheres disappear and significant cracks occur. For the cell cycled without additive such behavior is not observed, and a film is visible at the surface of the

¹ CIC Energigune, Vitoria-Gasteiz, Spain

particles. Surprisingly, no cracks appear along the sodiation neither at the end of the full sodiation where the volume change of the electrode is above 200%.

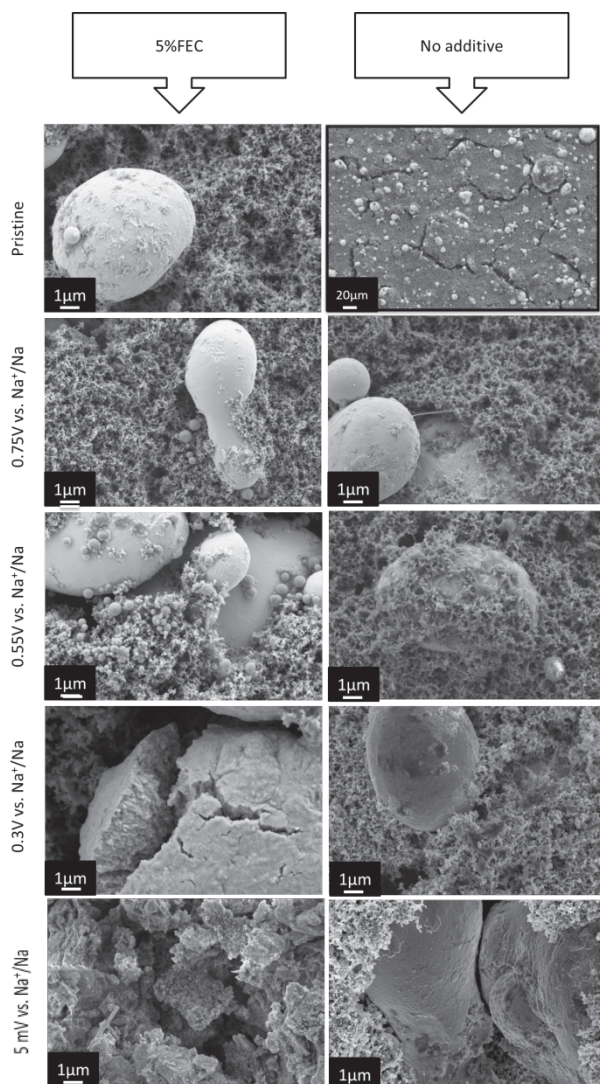


Figure 3. SEM images of pristine Sn electrodes and electrodes cycled against sodium in 1M NaClO₄/PC, (left) with additive (FEC); (right) without additive.

Post mortem XPS

To complete this *post mortem* study, XPS was performed on the same samples and results are presented in figures 4 and 5 for electrodes cycled without electrolyte additive and for the cells cycled with additive, respectively. The measurements of 4 different core levels are presented for C1s, Cl2p_{3/2-1/2}, F1s and Sn3d_{5/2}. For the samples cycled without electrolyte additive (figure 4), we can notice from the Sn3d_{5/2} peak at high binding energy (BE) (red component) that the surface of tin particles is covered by a thin layer of tin oxide (SnO₂) coming most probably from air contamination of the commercial powder. The second contribution is coming from the bulk and is ascribable to pure tin with zero oxidation state (Sn⁰, the green components). During the sodiation till 550 mV, the Sn⁰ contribution is highly increasing leading us to hypothesis that some nano-cracks occur in the Sn particles not visible in the SEM images, allowing the out-going of the Sn photoelectron

from the deep of the Sn particles without any scattering by the SEI layer. Afterward for the following sodiation, the signal of the Sn⁰ is decreasing again indicating that possibly a polymer recover the nano-cracks leading to an attenuation of the signal. Finally, at the end of the full sodiation, the signal of the Sn⁰ is slightly increasing due to the development of new nano-cracks. The F1s core level shows the presence of two components, in blue at low binding energy (BE) associated to NaF species and at high BE to CF_x species. The NaF is the product of a reaction between the Na and the PVDF binder as an only source of fluorine. The analyses of the Cl2p core level shows that the sodium perchlorate NaClO₄ salt is decomposed during the discharge in sodium chlorate NaClO₃, sodium chlorite NaClO₂ and sodium chloride NaCl. Regarding the C1s core level the deconvolution is more difficult due to the large amount of different contributions. The main components come essentially from the carbon super P with C-C bonds and PVDF CH₂ and CF₂ bonds (components are in green). Additional components appear during the discharge, assigned to sodium carbonate Na₂CO₃ in blue, CF_x species with x≥2 (light blue), hydrocarbons (light gray) and C-O, C=O (orange) due to salt, electrolyte, and PVDF degradation. The weak attenuation of the signal from the C-C component of the C1s core level during the entire discharge allows the estimation of the SEI thickness to be below 5nm.

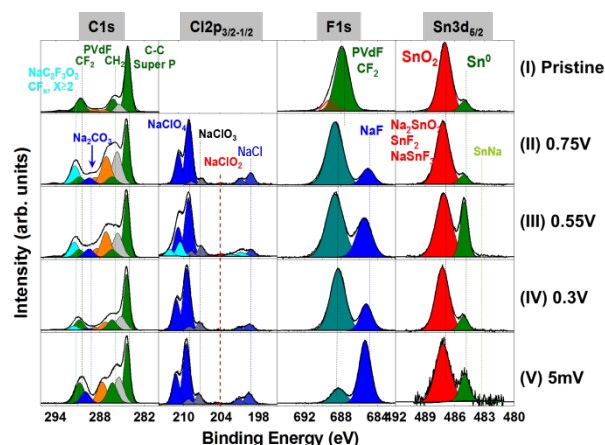


Figure 4. XPS analysis of Sn electrodes at different stage of sodiation, cycled at C/10 without additive.

In Figure 5, the same study was done on the cells cycled versus sodium with 5% FEC additive used as additive. We can still notice from Sn3d_{5/2} core level the presence of SnO₂ at the surface of the Sn particle. However, at 300 mV, no signal is detected due to a thicker SEI layer. At the end of the full sodiation, three components can be detected: Sn⁰, SnO₂ and NaSn. Combining this result with the SEM picture, we can clearly understand that at the end of the full sodiation the electrode “exploded” leading to new “fresh” surface of unreacted Sn, and a small amount of SnO₂. Moreover, the detection of intermediate species such as NaSn points out the low mass transfer rate between the surface of the material and the bulk. This phenomenon indicates a core-shell process, well pronounced for this sodium cell. For the C1s, Cl2p and F1s core levels, we can notice the same decomposition of the PVDF and the electrolyte as described above with the only difference, the complete attenuation of the super P signal in the C1s peak at 5 mV indicating that the SEI layer is thicker than 6nm, the maximum limit

of the escape depth of a photoelectron in our geometry configuration.

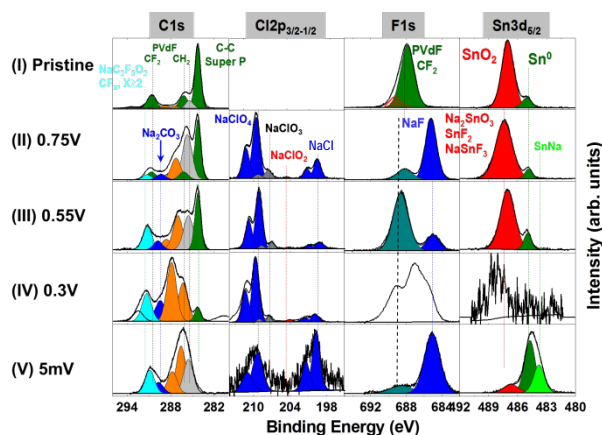


Figure 5. XPS analysis of Sn electrodes at different stage of sodiation, cycled at C/10 with FEC additive.

Conclusion

By combining two different surface techniques such as XPS and SEM, we were able to propose the interfacial mechanism of the first sodiation of commercial tin particle cycled with or without additive in a sodium-ion battery at room temperature (Figure 6). The presence or absence of the electrolyte additive (FEC) has a predominant effect in the first cycles. We demonstrate that with the FEC additive a thicker SEI layer is formed. In addition, the cycling stability (90% of coulombic efficiency) and the capacity retention (375 mAh/g) is improved, even if the SEM pictures show a total destruction of the electrode and Sn particles. Nevertheless, it seems that in both cases the electrolyte as well as the binder are decomposed during the first sodiation. This indicates that another binder and different electrolyte composition have to be considered for the sodium-ion batteries technology.

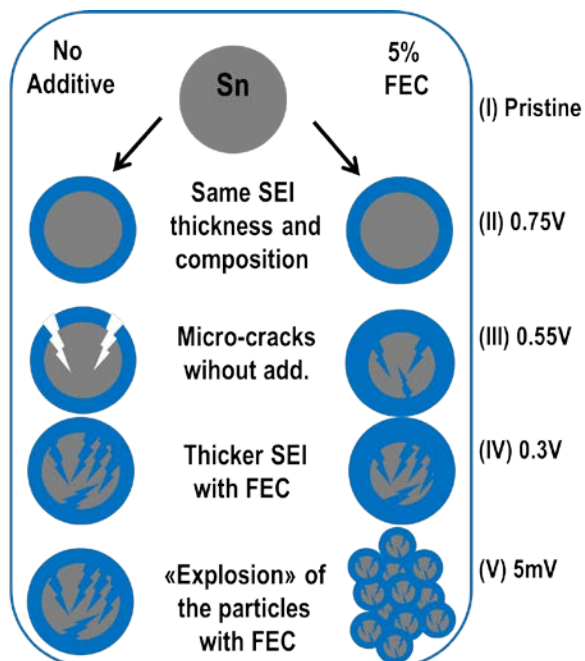


Figure 6. Scheme of the different mechanisms occurring during cycling of Sn electrodes vs. Na at C/10 rate with and without additive.

References

- [1] L. Baggetto, P. Ganesh, R.P. Meisner, R.R. Unocic, J.C. Jumas, C.A. Bridges, G.M. Veith, *J. Power Sources* **234**, 48 (2013).
- [2] A. Darwiche, C. Marino, M.T. Sougrati, B. Fraisse, L. Stievano, L. Monconduit, *J. Am. Chem. Soc.* **134**, 20805 (2012).
- [3] L. Baggetto, E. Allcorn, A. Manthiram, G.M. Veith, *Electrochem. Commun.* **27**, 168 (2013).
- [4] A. Darwiche, M.T. Sougrati, B. Fraisse, L. Stievano, L. Monconduit, *Electrochem. Commun.* **32**, 18 (2013).

Ionic liquid-based electrolyte for 5V Li-ion batteries and *in situ* XPS studies

M. El Kazzi, E. Jämstorp Berg, C. Villevieille, P. Novák

phone: +41 56 310 5149, e-mail : mario.el-kazzi@psi.ch

The instability (electrode/electrolyte interaction) at high temperatures ($> 50^{\circ}\text{C}$) and high potentials ($> 4.3\text{V}$) of the most commonly used carbonate-based electrolytes limits further progress in the development of the next generation of high specific energy Li-ion batteries.[1] Moreover, they are unsuitable for performing *in situ/operando* studies of batteries using ultra high vacuum (UHV) characterization techniques. However, these problems can mainly be overcome by the use of ionic liquids (IL). Their physical properties, such as thermal/electrochemical stability and low vapor pressure, make them promising electrolytes.[2]

In this context, the aim of this work is to first investigate the electrochemical properties of high voltage Li-ion battery interfaces using IL versus a carbonate-based electrolyte and second to check the cycling capability of a homemade *in situ* x ray photoelectron spectroscopy (XPS) cell for performing *operando* measurements on electrode surfaces by probing IL/UHV, electrodes/UHV and IL/electrodes interfaces.[3] Finally post mortem physico-chemical characterization of the cycled electrode surfaces by using XPS in order to determine their composition in respect to the two different electrolytes is performed.

For this purpose, 1-butyl-3-methylimidazolium tetrafluoroborate (BMIBF₄) IL was used as a representative example among the large family of ionic liquids [4] due to its high ionic conductivity, Li salt solubility and ability of reversible Li intercalation in positive electrodes [5]. The full cell used for this study combines spinel lithium titanate Li₄Ti₅O₂ (LTO) (Clariant) and NCM (layered Li(Ni, Co, Mn)O₂ (BASF), called HE-NCM, as appropriate negative and positive electrodes respectively. [6], [7]

Experimental

Negative and positive electrodes were prepared by casting a mixture of 80% active materials HE-NCM or LTO with 10% PVDF (binder) and 10% Super-P carbon used as conductive additive (TIMCAL), all suspended in N-methyl-2-pyrrolidone (Fluka) onto the current collector (aluminum foil). After drying at 120°C , the electrodes were punched out and assembled in an argon-filled glove box. Two electrolytes were employed for this study (I) LP30 carbonate-based (from BASF) which is a mixture of 1M LiPF₆ with ethylene carbonate and dimethyl carbonate (EC:DMC 1:1), and IL-based, which is a mixture of 1M LiBF₄ and BMIBF₄. The evolution of the electrode surfaces composition was analyzed *post mortem* with XPS after cycling under the following conditions: 30 cycles at a rate of C/15 and 2 cycles at a rate of C/30 within the 2.4 V - 5.1 V (recalculated vs. Li/Li⁺) cutoff limits in LP30 and IL, respectively. The measurements were realized on unwashed and washed positive and negative electrodes with dimethyl carbonate (DMC) after transfer from the glove-box to the XPS via an Ar-filled atmosphere chamber.

Electrochemical properties

Figure 1 present the first and second cycle of the CV curves performed on a full cell HE-NCM/LTO at room temperature (RT) by using two different electrolytes (a) LP30 and (b) 1M LiBF₄/BMIBF₄ with a scan rate of $50\mu\text{V/s}$. These CV curves are compared to the one measured by using the home made *in situ* XPS cell [3] in 1M LiBF₄/BMIBF₄. Their behavior is typical of lithium deinsertion/insertion from/to HE-NCM.[7] During the first delithiation in LP30 two main peaks are visible. The first one appears at around 4V and is attributed to the oxidation of Ni²⁺ to Ni³⁺ and Ni³⁺ to Ni⁴⁺ in both metal slabs and interslabs. The second peak at around 4.6 V is associated with Li₂MnO₃ activation with the irreversible removal of Li₂O. Once the material is activated, we can clearly see that this peak disappears during the next cycle. However, four other peaks appear upon the second delithiation between 3.2 V and 4.3 V. The CV measured for the cells with IL shows peaks broadening and a slight shift to higher potentials by 0.1 V for the standard PSI cell and 0.22 V for the homemade XPS cell. The observed overpotential is most likely related to the lower ionic conductivity of the IL with respect to the LP30 as well as to the XPS cell geometry with quite a long distance between the two electrodes (5 cm) compared to the PSI cell (50 μm).

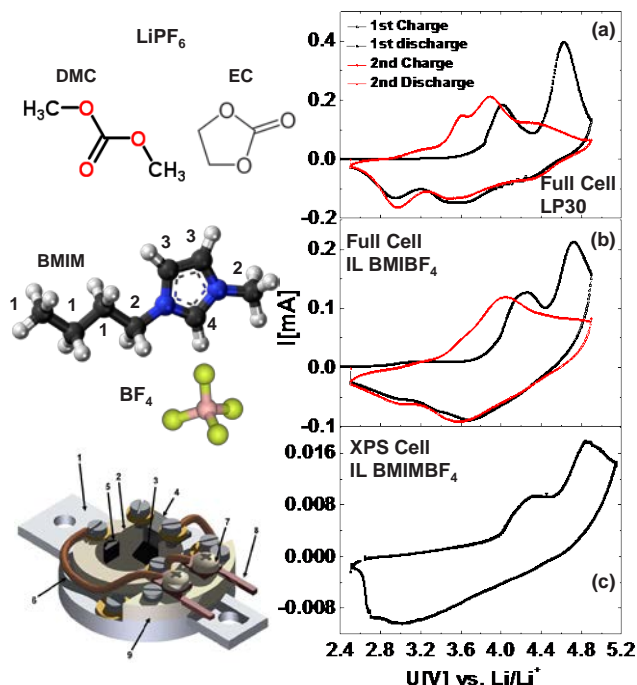


Figure 1: Cyclic voltammetry of full cells HE-NCM/LTO at RT with a scan rate of $50\mu\text{V/s}$ in (a) LP30, (b) 1M LiBF₄/BMIBF₄ as electrolytes and (c) using the *in situ* XPS cell with 1M LiBF₄/BMIBF₄.

Figure 2 presents the evolution of the specific charge from galvanostatic (GS) cycled at C/5 rate for HE-

NCM/LTO cells. Quite different cycling behavior is observed for the two employed electrolytes LP30 and IL at RT. The GS cycling in LP30 exhibits a fairly stable specific charge of 220 mAh/g over 120 cycles. The first delithiation process gives almost 350 mAh/g due to the irreversible activation of Li_2MnO_3 . However, with IL the cells are able to cycle but with quite a low specific charge. During the first delithiation around 200 mAh/g were delivered for C/5 and 263 mAh/g for C/10 (not shown), 43 % to 25 % less than with LP30. The irreversible specific charge is found to be also quite high (85 mAh/g). The continuous fading after the 3rd cycle is obvious until it reaches 100 cycles with a specific charge around 30 mAh/g. The difference in the electrochemical properties could be explained by the difference in conductivity and viscosity of the two electrolytes. Furthermore, we cannot exclude the formation of different surface layers on the electrodes depending on the electrolyte decomposition. In order to determine the composition of the different species at the surface of both electrodes, *post mortem* XPS analyses were undertaken.

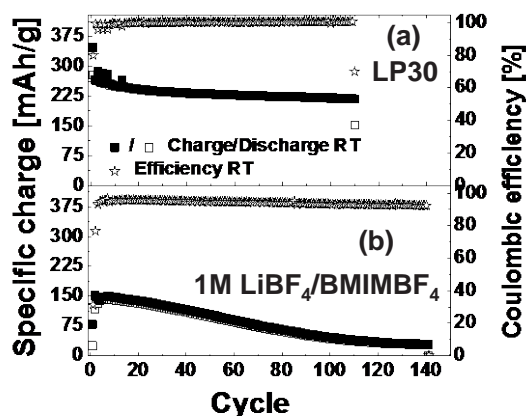


Figure 2: Galvanostatic cycling of HE-NCM/LTO cells cycled at C/5 at RT, with two different electrolytes (a) LP30 and (b) 1M $\text{LiBF}_4/\text{BMIMBF}_4$ within 2.4 V – 5.1 V vs. Li/Li^+ cutoff limits.

Post mortem XPS

(I) LP30

The C1s and $\text{Ti}2p_{3/2-1/2}$ core levels spectra acquired on HE-NCM and LTO electrodes with LP30 are presented in Figure 3. These peaks show an obvious evolution of the surface composition between the two, pristine and the cycled ones as well as between unwashed and washed electrodes. On both pristine HE-NCM and LTO the deconvolution of the C1s peaks show the presence of almost the same components. The main intense component at 284.4 eV binding energy (BE) is associated with C-C bonds of the Super P (in dark green). The two carbons related to $(-\text{CH}_2-)$ and $(-\text{CF}_2-)$ from the PVDF are also detected at 286.4 eV and 290.76 eV, respectively (in dark green). Further components are also observed, linked to hydrocarbon at 285.5 eV (in light gray) and carbon in the environment of C=O and O-C=O at around 286.7 eV (ether C-O), 287.8 eV (carbonyl C=O), 288.9 eV (carboxyl O-C=O) respectively (in orange), and carbonate $\text{Li}_2\text{CO}_3/\text{CO}_3$ at 290.1 eV (in blue). However on the pristine LTO surface an additional component at 292 eV is also detected and associated with CF_x with $X>2$ (light blue). Nevertheless, the $\text{Ti}2p_{3/2-1/2}$ spectrum shows a single narrow peak at 459.7 eV assigned to the Ti^{4+} oxidation state.

(I.a) HE-NCM electrode

After cycling, the C1s peak on the HE-NCM electrode shows attenuation of the super P (C-C) and PVDF peaks due to the formation of a thin surface layer estimated to be < 5nm. Simultaneously, two new components appear at 286.8 eV and 292.1 eV associated with carbon in a C-O and CF_x ($x>2$) environment respectively. Such behavior is explained by the electrolyte decomposition leading to the formation of additional ether, carbonyl, carboxyl and carbonate functional groups. Other species due to the electrolyte decomposition, such as LiF , LiPF_6 , $\text{Li}_x\text{P-F}_y$ and $\text{Li}_x\text{PF}_y\text{O}_z$ measured on the F1s and P2p core levels (not shown) are detected as well. Moreover, a $\text{Ti}2p$ peak at 461 eV was also observed evidencing the presence of titanium tetrafluoride TiF_4 species on the positive electrodes, probably due to the dissolution of the Ti form LTO in the electrolyte and then migration to the positive electrode. After washing with DMC, the C1s peak indicates that the thin surface layer was thinned, mainly due to the dissolution of the hydrocarbon, ether and carboxyl species. Their intensity decreases while, again, the intensity of the super P and PVDF increases. On the other hand, the carbonate intensity remains almost the same. The TiF_4 was also removed during washing, the peak intensity decreased drastically and the presence of additional components to low and high BE was observed.

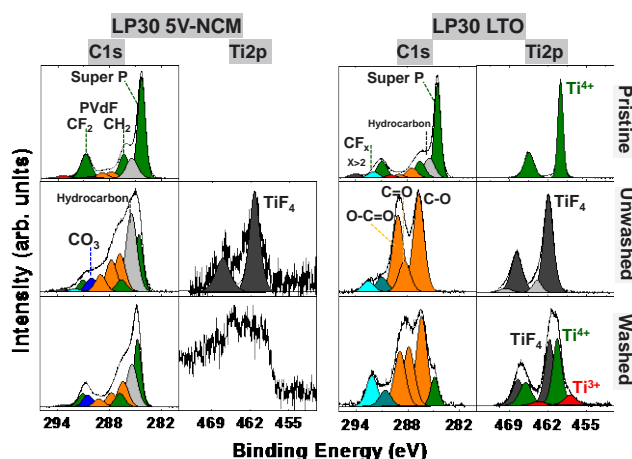


Figure 3: C1s and $\text{Ti}2p_{3/2-1/2}$ XPS core levels acquired on pristine and unwashed/washed HE-NCM and LTO electrodes cycled in LP30.

(I.b) LTO electrode

Regarding the LTO electrode the surface layer formed after cycling is slightly different from the one on the positive electrode. The C1s core level shows that the layer thickness is more than 6 nm since the carbon component of the Super P (C-C) is completely attenuated. It is also obvious that the hydrocarbon component (~285.5 eV) disappears completely. The components related to ether (286.7 eV), carbonyl (288.4 eV) and carboxyl (289.1 eV) groups (in orange) as well as components assigned to CF_x groups with $x=2$ (291 eV) and $x=3$ (292.5 eV) (light blue) are pronounced. Despite the presence of a thick surface layer, we still detect the $\text{Ti}2p$ signal associated with TiF_4 . The presence of the titanium tetrafluoride in or onto the surface layer cannot originate from LTO particles but results from the Ti dissolution and its reaction with the F from the PVDF and/or the salt LiPF_6 . The dissolution of Mn and Co was also ob-

served by detecting signal coming from the Mn2p and Co2p core levels (not shown).

After washing with DMC similar behavior was observed as for NCM, i.e. a thinner surface layer and intensity decrease of the ether and carboxyl groups and increase of the CF₄ component. However a big modification occurs on the Ti2p, a decrease of the TiF₄ component and the appearance of an additional one. Ti⁴⁺ (dark green) originate from the LTO particles at 460 eV and Ti³⁺ at 458 eV either related to the Ti⁴⁺ reduction or LTO decomposition in DMC.

(II) IL BMIMBF₄

The same study was performed with IL and the results are presented in Figure 4. As expected, the deconvolution of the C1s acquired on a droplet of IL displays 4 main peaks associated with 1) aliphatic C, 2) C-N bonds, 3) C-C*-N in imidazolium ring and 4) N-C-N in imidazolium ring (all in light grey, see Figure 1). For B1s and N1s one single peak is observed, assigned to the B in the tetrafluoroborate anion and to the N in the 1-butyl-3-methylimidazolium cation. After cycling, an obvious shift of -1.45 eV to lower and of 1.3 eV to higher BE occurred on the C1s, B1s and N1s components which belong to the IL on top of the HE-NCM and LTO electrodes, respectively.

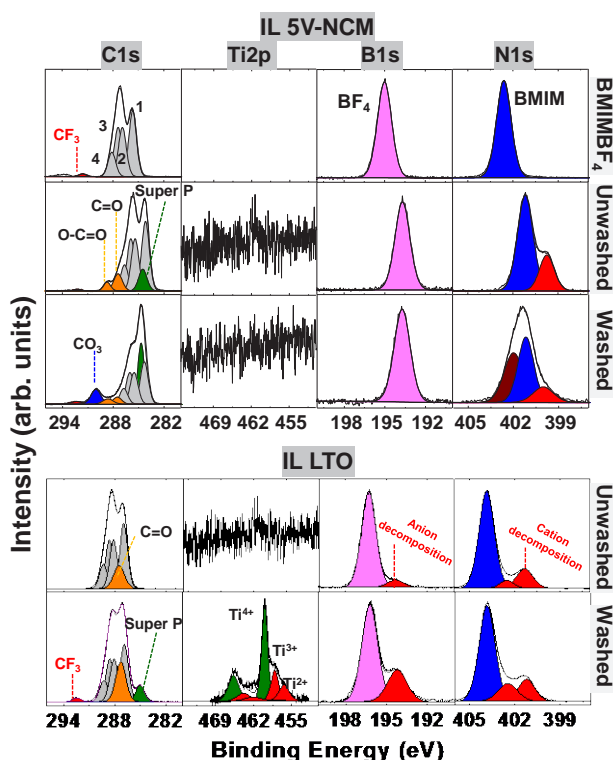


Figure 4: C1s, Ti2p_{3/2-1/2}, B1s and N1s XPS core levels acquired on a droplet of IL (1M LiBF₄/BMIMBF₄) (taken as reference) and unwashed/washed HE-NCM and LTO electrodes cycled in IL.

(II.a) HE-NCM electrode

On unwashed HE-NCM electrodes the C1s peak shows, in addition to the IL components (in grey), four additional ones, related to the carbon super P (in dark green), carbonyl/carboxyl groups (in orange) and CF_x species (in red) with x>2 at 284.5 eV, 287.4 eV, 288.7 eV and 292.2 eV, respectively. No presence of any carbonate or dissolved Ti was detected. No change was observed in

the B1s core level while an additional component shifted to low BE was detected in N1s peak (in red) most probably related to cation decomposition. The absence of any signal related to the LTO particles in the O1s peak (not shown) evidenced that the surface layer thickness formed on the carbon particles is below 5 nm while it is above 6 nm on LTO.

(II.b) LTO electrode

On the unwashed LTO just one additional component was observed in the C1s peak related to carbonyl group at 287.5 eV. Electrolyte decomposition was observed on both B1s and N1s with the presence of shifted components to low BE (in red). The thickness of the SEI layer is estimated to be thicker than 6 nm because signal was detected neither from the Super P nor LTO. No dissolution of any transition metal like Ni, Mn and Co was detected, as was the case with LP30.

After washing with DMC the signal from the Super P and LTO is well pronounced on both electrodes. Additional components were observed on C1s like carbonate at 290 eV (in red) at the positive electrode and CF_x with x>2 on the negative one. Finally the Ti2p on the LTO electrode presented two additional components shifted to lower BE related to Ti³⁺ and Ti²⁺ oxidation state.

Conclusion

We reported in the first part reversible cycling of HE-NCM/LTO cells by using two different electrolytes LP30 and IL (1M LiBF₄/BMIMBF₄). Despite the high potential cutoff 5.1 V vs. Li/Li⁺, good electrochemical cycling was demonstrated with LP30, however with the IL 55% less specific charge was obtained on the 2nd charge with continuous fading up to 30 mAh/g after almost 130 cycles. In the second part we proved that we were able to cycle the HE-NCM/LTO cells in the home made *in situ* XPS cell with the IL as electrolyte. This promising result opens the way to a potential use of the cell in UHV and to perform *operando* XPS measurements on the IL, electrode surface and the IL/electrode interface. Finally, *post mortem* XPS was acquired on both negative and positive electrodes after cycling providing precious information regarding the electrolyte stability and the surface layer formation and composition.

Acknowledgment

The authors are very grateful for the financial support from BASF.

References

- [1] J.B. Goodenough, J. Solid State Electrochem. **16** (6), 2019-2029 (2012).
- [2] M. Buzzeo, R. Evans, R. Compton, Chem. Phys. Chem. **5**, 1106-1120 (2004).
- [3] D. Weingarh, A. Foelske-Schmitz, A. Wokaun, R. Kötz, Electrochem. Commun. **11**, 619-622 (2011).
- [4] A. Lewandowski, A. Swiderska-Mocek, J. Power Sources, **194**, 601-609 (2009).
- [5] E. Markevich, V. Branchugov, D. Aurbach, Electrochem. Commun. **8**, 1331-1334 (2006).
- [6] J. Christensen, V. Srinivasan, J. Newman, J. Electrochem. Soc. **153** (3), A560-A565 (2006).
- [7] H. Yu, H. Kim, Y. Wang, P. He, D. Asakura, Y. Nakamura, H. Zhou, Phys. Chem. Chem. Phys. **14**, 6584-6595 (2012).

XPS study of the evolution of the interfaces of porous graphite electrodes for Li-O₂ batteries upon cycling

A. Guéguen, E. Jämstorp Berg, P. Novák

phone: +41 56 310 2176, e-mail: aurelie.gueguen@psi.ch

In order to decrease our dependency on environmentally unfriendly and non-abundant energy sources, e.g. fossil fuel, alternative technologies need to be developed. For instance, Li-O₂ batteries are one of the most promising candidates to provide power to electric vehicles due to their very high theoretical specific energy [1]. However, several scientific and technical issues (electrolyte stability, charging overpotential, cyclability) have to be overcome to produce viable commercial Li-O₂ batteries.

The Li-O₂ cell consists of a negative electrode (e.g. Li metal) and a positive porous electrode (usually carbon) exposed to gaseous O₂. During discharge, oxygen dissolves in the electrolyte and is reduced at the porous electrode. At the same time, Li metal is oxidized into Li⁺ at the negative electrode and the Li⁺ cations diffuse through the electrolyte and react with the reduced oxygen to form the discharge product Li₂O₂ filling the pores of the electrode. Upon charge, the discharge product is oxidized, thus releasing Li cations and O₂ gas, the initial reactants.

However the reduced oxygen species formed upon discharge are very reactive and side reactions involving the electrolyte and the porous electrode components occur. Nevertheless, ether-based electrolytes have been shown to be less reactive than carbonate-based electrolytes conventionally used in Li-ion batteries. Furthermore, the nature and amount of such side products critically affects the electrochemical behaviour of the cell.

X-ray Photoelectron Spectroscopy (XPS) is a powerful tool to analyze the chemical composition of surfaces. In the case of Li-O₂ batteries, XPS may be used to investigate the nature and amount of the decomposition products resulting from the electrochemical charge/discharge of the cell. The aim of the current work is to understand the reactions taking place upon discharge of porous graphite electrodes. Complementary data collecting upon further cycling give information about the evolution of these species.

Experimental

Porous self-standing electrodes with composition 85wt% graphite / 15wt% PTFE (polytetrafluoroethylene) were prepared by adding the respective amount of PTFE dispersion (Sigma-Aldrich) and subsequently graphite SFG6 (TIMCAL) to a solution of isopropanol and water (1:1). The mixture was sonicated and then kept under stirring at 100 °C until evaporation of the solvents and formation of a "dough-like" paste. The electrode sheets were obtained by working the dough with a spatula and mechanical rolling (thickness 200 µm) and dried at room temperature. Electrodes were subsequently punched (18mm diameter) and dried (120 °C dyn. vac.) before being introduced into the Ar-filled glove-box.

The Li-O₂ cells were assembled in a home-designed electrochemical cell (Annual Report 2012, p.47). The porous carbonaceous electrodes were cycled vs Li metal (i.e. all potentials in the report are given vs. Li⁺/Li) under

constant current (0.3 mA). 0.2 M LiTFSI in diglyme was used as the electrolyte and Celgard 2400 sheets as separators. Before starting the electrochemical measurement, the cells were connected to high purity O₂ gas and were allowed to equilibrate for one hour before the first discharge. After cycling the porous electrodes were washed in diglyme under Ar atmosphere.

XPS analyses were carried out using a focused monochromatized Al Kα radiation (1486.6 eV). The analysed surface area was 500 µm. Core peaks (C 1s, F 1s, O 1s, Li 1s, S 2p) were recorded with a constant 30 eV pass energy. The samples were transferred to the XPS introduction chamber in a hermetically sealed transfer chamber to avoid any air contamination. XPS data were collected for the pristine electrode and electrodes recovered after the 1st discharge, the 1st charge and 10 cycles (for clarity only C 1s and F 1s spectra collected for the side facing the O₂ inlet are presented here).

Results

Figure 1 shows the electrochemical data obtained after one cycle for several Li-O₂ cells. A single potential plateau of ~2.6 V is observed upon the first discharge and two plateaus of ~3.5-3.7 and 4.1-4.2 V upon the first charge. The specific charge of the carbon electrodes (76-96 mAh/g) is similar to previous studies [2] and consistent with the low surface area of the graphite SFG6 (16 m²/g) limiting the area for Li₂O₂ formation.

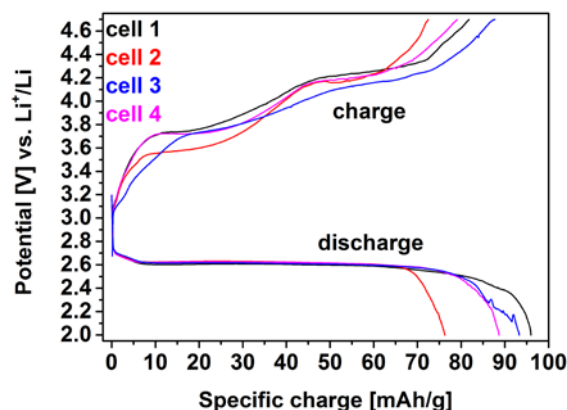


Figure 1. Galvanostatic data obtained for the 1st cycle for Li-O₂ cells containing the porous electrodes (85wt% SFG6 / 15wt% PTFE).

The C 1s spectrum of the pristine electrode (Figure 2a) consists of a main component at 284.6 eV attributed to the graphite SFG6. However, minor components are also observed such as the peak at 292.1 eV which corresponds to -CF₂ groups present in the PTFE binder. Remaining components correspond to oxygenated carbonaceous species adsorbed on the surface. The main peak at 689.7 eV on the F 1s spectrum (Figure 2b) is in good agreement with presence of CF₂ groups in the PTFE binder.

At the end of the 1st discharge, the graphite component still remains the main peak in the C 1s spectrum (Figure

2a). This indicates that the thickness of any layer is less than ca. 5nm with regard to the depth analysis of XPS. An extra component at 293 eV shows presence of species containing $-\text{CF}_3$ environments, probably arising from the LiTFSI salt and its possible degradation products. This is confirmed by the S 2p spectrum (not shown here), for which two components are present, the major component being assigned to the LiTFSI salt. A second component at 685 eV attributed to LiF is observed on the F 1s spectrum of the discharged electrode (Figure 2b). LiF is probably related to the degradation of the LiTFSI salt and/or PTFE binder upon discharge. No LiF was observed for electrodes recovered after blank experiment under Ar or O_2 atmosphere. It is hard to distinguish Li_2O_2 from other lithiated species at the surface of the discharged electrode. Quantification results (Figure 3) show a significant decrease in the contribution of C 1s to the global signal and increase of species containing F and O. More oxygenated and less fluorinated species are present on the side of the electrode facing the separator.

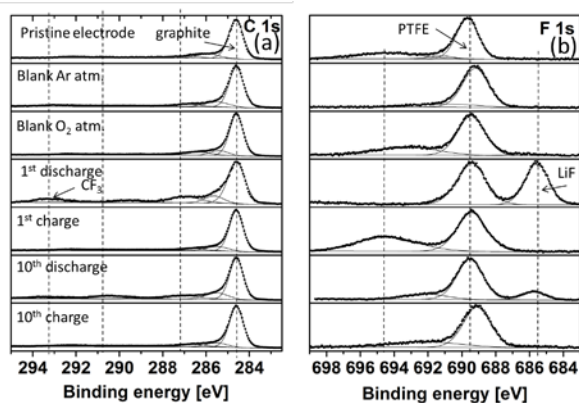


Figure 2. (a) C 1s and (b) F 1s spectra collected for the pristine 85wt% SFG6/15wt% PTFE electrode and electrodes recovered after blank experiments (Ar and O_2 atmosphere) and after the 1st discharge, the 1st charge, the 10th discharge and 10th charge.

At the end of the 1st charge, the C 1s and F 1s spectra are quite similar to those of the pristine electrode (Figure 2). No lithiated species were observed in the Li 1s spectrum (not shown here). Quantification data show also similar ratios for the pristine and charged electrodes. This indicates that the species formed during the 1st discharge are decomposed upon the following charge. This is in good agreement with results reported by Younesi et al. for a Li-air cell containing 1M LiPF₆ in PC electrolyte and amorphous SuperP carbon [3].

Similar characterizations were carried out on electrodes recovered after 10 cycles. Such electrodes exhibit very low specific charge (~ 3 mAh/g). After 10 cycles, the main component of the C 1s spectrum remains that of the graphite (Figure 2a). Thus the thickness of the interfacial layer does not increase significantly after 10 cycles. At the end of the 10th discharge, LiF is still observed at the surface of the side of the porous electrode facing the O_2 inlet but the amount is lower than that observed at the end of the 1st discharge (Figure 2b). Quantification shows higher amount of oxygenated species compared to the 1st discharge (Figure 3).

At the end of the 10th charge, no lithiated species were observed on the F 1s (Figure 2b) and Li 1s spectrum (not shown here). Quantification indicates a lower

amount of oxygenated species compared to the 10th discharge, close to the data obtained for the pristine electrode and for the 1st charge. After 10 cycles, a significant amount of the species formed during the 10th discharge is still decomposed upon the following charge.

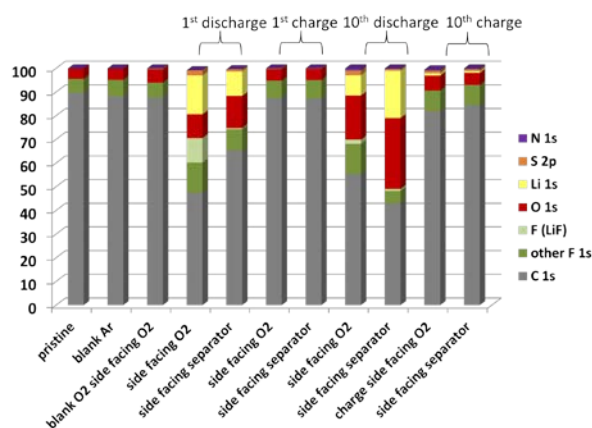


Figure 3. Relative contribution (%) of each element to the global signal for the pristine electrode (85wt% SFG6 / 15wt% PTFE) and cycled electrodes.

The interface layer on the Li electrodes was not analyzed during the study. However a black layer was observed by eye on the surface of the Li electrode when the cells recovered after 10 cycles were opened. Such a black layer was reported by Younesi et al. on Li electrodes recovered after cycling Li- O_2 cells containing 1M LiPF₆ in PC electrolyte [4]. They observed by XPS a constant evolution of the interface layer upon the 1st cycle.

Conclusions

Our XPS study shows the formation of LiF and oxygenated species at the surface of the porous electrode (85wt% SFG6-15wt% PTFE) upon the first discharge. The major part of these species is decomposed upon the following charge. After 10 cycles, the reversibility of these reactions is still observed. However no clear conclusion regarding the presence of Li_2O_2 at the surface of the porous electrode can be drawn. Similar studies will be carried out on porous electrode containing amorphous carbon in order to investigate the influence of the nature of the carbon on the electrochemical properties of the Li- O_2 cell and on the chemical composition of the interface layer.

Acknowledgement

The authors thank BASF SE for financial support.

References

- [1] K. Abraham, Z. Jiang, J. Electrochem. Soc. **143**, 1-5 (1996).
- [2] J. Christensen, P. Albertus, R. Sanchez-Carrera, T. Lohmann, B. Kozinski, R. Liedtke, J. Ahmed, A. Kojic, J. Electrochem. Soc. **159**, R1-530 (2012).
- [3] R. Younesi, S. Urbonaite, K. Edström, M. Hahlin, J. Phys. Chem. C **116**, 20673-20680 (2012).
- [4] R. Younesi, M. Hahlin, M. Roberts, K. Edström, J. Power. Sources **225**, 40-45 (2013).

On the $\text{Li}(\text{Ni}_{0.80}\text{Co}_{0.15}\text{Al}_{0.05})\text{O}_2$ system upon (de)lithiation: electrochemical and *in situ* XRD studies

R. Robert, P. Novák

phone: +41 56 310 5426, e-mail: rosa.robert@psi.ch

High-voltage layered oxides are desirable to increase the energy density of the lithium-ion battery. LiNiO_2 is a promising 4 V cathode material for Li-ion rechargeable batteries due to its low cost and high specific charge. However, it is also known to have bad cycling performance and high thermal instability when fully charged. $\text{Li}(\text{Ni},\text{Co},\text{Al})\text{O}_2$ (NCA) is a good candidate able to de/insert lithium and operate at a high voltage. In this particular system, Co doping helps to maintain the layered structure [1] and Al doping improves thermal stability at high potentials [2].

The reaction pathways that this material undergoes during its electrochemical reaction with lithium are generally known and have been extensively studied by diffraction techniques. However, details of the activation process occurring during the first charge and at high potentials, i.e. 4.6 V, are rarely mentioned in the literature. Our aim is to investigate in detail these unknown processes occurring at the bulk electrode and at the surface level using complementary techniques such as *in situ* and *ex situ* X-ray diffraction (XRD), and electrochemical characterizations.

Experimental

The positive electrode mixture consisted of 80 wt% of the active material (commercial $\text{Li}(\text{Ni},\text{Co},\text{Al})\text{O}_2$ powders), 10 wt% of Super P carbon black, and 10 wt% of polyvinylidene fluoride (PVDF) binder. Slurry of the positive electrode mixture was prepared using N-methyl pyrrolidone (NMP) as solvent. The slurry was tape cast on Al metal foil and dried 80°C in a vacuum oven for a minimum of 12 h. Standard electrochemical cells were assembled in an argon-filled glove box. Each cell typically contained about 5 mg of active material, separated from Li foil as negative electrode by a glass fiber separator. A 1M solution of either LiPF_6 or LiClO_4 in EC:DMC (1:1) has been used as the electrolyte, referred as LP30 and LC30 respectively. Cyclic voltammograms were carried out at different rates, i.e. 5 $\mu\text{V/s}$ and 20 $\mu\text{V/s}$. Operando X-ray powder diffraction studies were performed using a PANalytical Empyrean diffractometer, equipped with a linear detector (X'Celerator) and Cu- K_α radiation, by step scanning (with a step size of 0.017°) over the 2θ range of $15^\circ \leq 2\theta \leq 22^\circ$. Electrochemical cycling using a self-constructed cell was carried out galvanostatically between 3.0 V and 5.0 V at a C/20 rate.

Results

Cyclic voltammetry (CV) is used to characterize the redox potentials of the $\text{LiNi}_{0.8}\text{Co}_{0.15}\text{Al}_{0.05}\text{O}_2$ electrode within the potential range of 3.0 V to 5.1 V vs. Li^+/Li . Figure 1a provides a qualitative analysis of the potentials at which chemical reactions that accompany electron transfer in the $\text{LiNi}_{0.8}\text{Co}_{0.15}\text{Al}_{0.05}\text{O}_2$ electrode occur. In the first cycle there is a prominent anodic reaction (~3.9 V) in the first charge of the CV, which is not seen in the following cycles, and may be attributed to a possible activation of the material, i.e. a surface reaction of the electrode with the electrolyte and/or to an irreversible

phase transition that decreases the potential of the reaction by ~0.2 V compared to the next charge cycle.

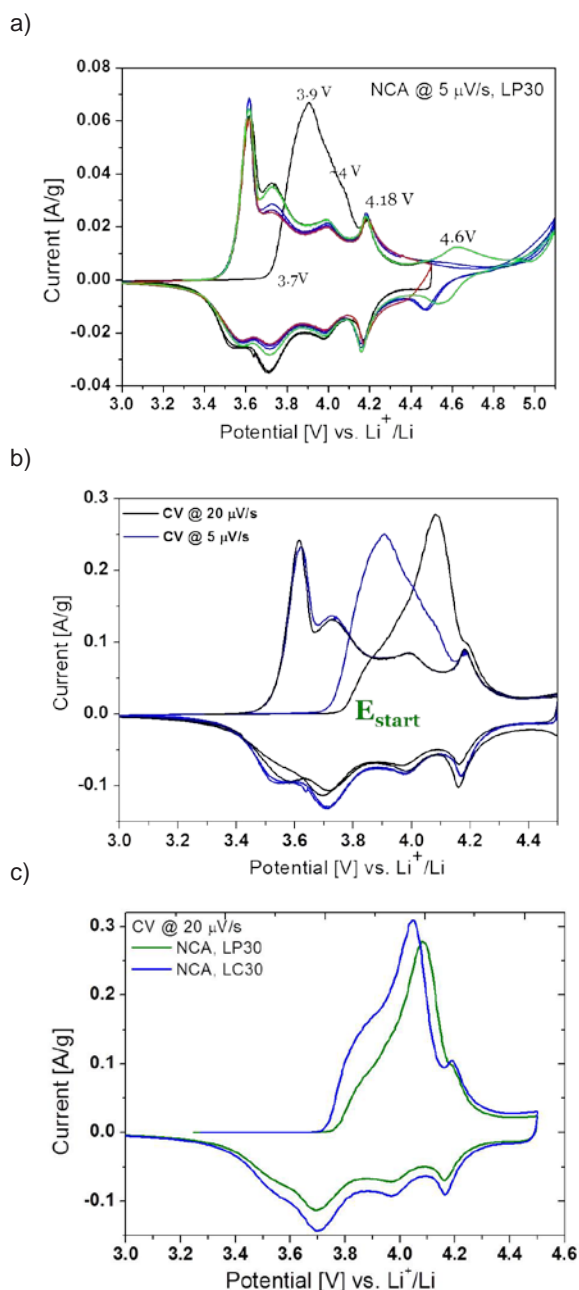


Figure 1. Cyclic voltammogram of $\text{LiNi}_{0.8}\text{Co}_{0.15}\text{Al}_{0.05}\text{O}_2$ in the potential range of 3.0 V to 5.1 V vs. Li^+/Li , a) at 5 $\mu\text{V/s}$ in LP30, b) at two different rates in LP30, and c) in LP30 and LC30.

The activation potential of the NCA electrode is strongly influenced by i) the cycling rate (Figure 1b), i.e. the potential at which the electrode activation starts (E_{start}) is about 50 mV more negative when NCA is cycled at 5 $\mu\text{V/s}$ compared to 20 $\mu\text{V/s}$ - this may be an indication of

a kinetically driven process, and ii) the electrolyte composition (Figure 1c), i.e. the E_{start} of the activation process varies when LP30 or LC30 is used - this may be an indication that a different surface reaction involving the formation of a solid polymer interphase (SPI) may take place. From Figure 1a we can determine that this first activation process is irreversible. After the activation (during the first cycle), the first redox process is reversible and reproducible on the following cycles.

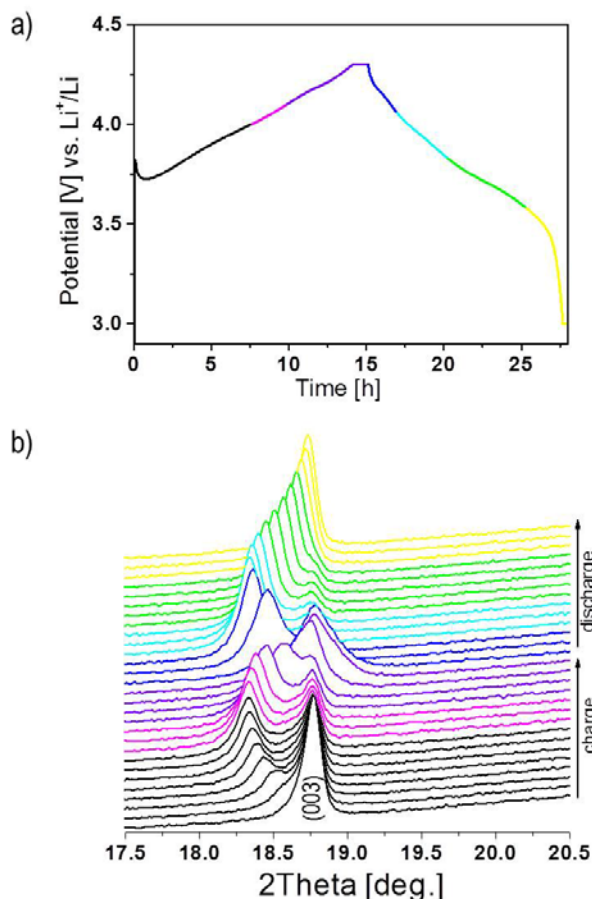


Figure 2. a) First charge/discharge curve at C/20 of an NCA electrode and b) *in situ* XRD pattern in the (003) Bragg peak region for NCA with space group R-3m. The colour code corresponds to the galvanostatic curve (a).

Operando XRD studies during the first galvanostatic cycle (Figure 2 a) show a two-phase de-insertion process with the coexistence of the pristine phase and a second rhombohedral phase with a larger c lattice parameter. At ~ 4.2 V the c lattice parameter of the second phase contracts which seems to be reversible on lithiation, i.e. an expansion of the c lattice parameter is observed (Figure 2 b). Furthermore, during discharge, *in situ* XRD data reveal a lithiation mechanism based on a solid solution process. In the second cycle, this new second phase already appears at 3.6 V, as observed in the XRD data (not shown here) and reflected in the CV curves (Figure 1a).

The CV of NCA shows other interesting features. A reversible redox reaction is observed at around 4.6 V (Figure 1a), which interestingly shifts in potential during the following cycles. At this point, 0.8 mols of Li have been removed from the $\text{LiNi}_{0.8}\text{Co}_{0.15}\text{Al}_{0.05}\text{O}_2$ and it is unclear which, Co or Ni, have an active redox couple in

this range. XRD data (not shown here) reveals the formation of a new phase around this potential.

Figure 3 displays the contour plot of *in situ* XRD patterns for the first (a) and second (b) charge curves. This picture clearly discloses mechanistic differences on the reaction pathways between the 1st and 2nd cycles (Figure 2). While the first charge cycle until 4.3 V consist of a combination of two-phase transition plus a solid solution mechanism, the second charge process is mainly dominated by a solid solution.

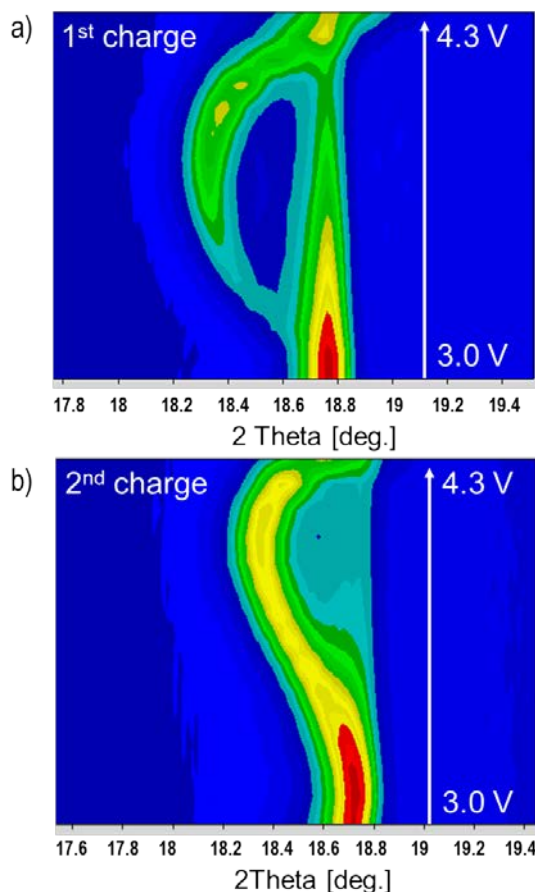


Figure 3. Contour plot of *in situ* XRD patterns for the first (a) and second (b) charge curves, in the (003) Bragg peak region for NCA with space group R-3m.

This study showed that the activation mechanism is affected by several factors. Possibly, a structural irreversible transition combined with a surface reaction is taking place. The potential at which this process occurs is correlated to electrolyte composition and cycling rate. Additional studies, not shown here, also reveal that the initial composition of the sample also affects the E_{start} of this activation process. *In situ* XRD data reveal significant differences in the reaction mechanism between the 1st and 2nd cycles. Moreover, at high potentials a reversible process involves the formation of a new phase. In order to better understand these chemical reactions further impedance and DEMS experiments are currently being carried out.

References

- [1] C. Delmas, I. Saadoune, *Solid State Ionics* **370**, 53 (1992).
- [2] T. Ohzuku, T. Yanagawa, M. Kouguchi, A. Ueda, *J. Power Sources* **68**, 131 (1997).

SCIENTIFIC ACHIEVEMENTS 2013

ELECTROCATALYSIS & INTERFACES

Hydrogen underpotential deposition and CO stripping voltammetry on metal-oxide supported platinum catalyst

T. Binninger, E. Fabbri, R. Kötz, T.J. Schmidt

phone: +41 56 310 5728, e-mail: tobias.binninger@psi.ch

Recent efforts in the development of polymer electrolyte fuel cell (PEFC) cathode catalysts focus on metal-oxide supported platinum nanoparticles. The reason is the potentially superior durability of metal-oxide materials compared with the standard carbon supports, which suffer from severe degradation in the oxidative cathode environment. Furthermore, the metal-oxide support can positively influence the intrinsic activity of the Pt nanoparticles towards the oxygen reduction reaction (ORR) due to so-called strong metal-support interactions (SMSI).

For an experimental analysis of the stability and activity properties of such metal-oxide supported Pt catalysts, the determination of the electrochemically active surface area (ECSA) of the Pt nanoparticles is inevitable. There are two standard methods to measure the ECSA: Hydrogen underpotential deposition (H_{upd}) and carbon monoxide stripping voltammetry (CO stripping). In both methods, the Pt surface area is determined from the charge which is associated with the reductive adsorption / oxidative desorption of one monolayer of an adsorbate species. In the case of H_{upd} , the adsorbate species is atomic hydrogen, whereas for CO stripping carbon monoxide is used as adsorbate.

Both H_{upd} and CO stripping are well established for conventional carbon supported Pt catalysts (Pt / C). In the following, we will present how these methods have to be adjusted for the case of metal-oxide supported Pt catalysts [1].

Experimental

The ECSA measurement methodology was studied for Pt nanoparticles supported on a mixed iridium-titanium oxide [2]. The Pt / $\text{Ir}_{0.8}\text{Ti}_{0.2}\text{O}_2$ catalyst was supplied by Umicore AG & Co KG with a loading of 8.8 wt.-% Pt nanoparticles. Thin-film electrodes were prepared from a suspension made from 5 mg of the catalyst / oxide powder, 1 ml ultrapure Milli-Q water, 4 ml isopropanol, and 20 μl Nafion as a binder. 40 μl of the suspension were dropped and then dried on glassy carbon disks with 5 mm diameter (geometric surface area $A_{\text{geo}} = 0.196 \text{ cm}^2$), resulting in a Pt loading of $18 \mu\text{g}_{\text{Pt}} \text{ cm}^{-2}$. For comparison with a standard Pt / C catalyst, a 47 wt.-% Pt / HSAC (high surface area carbon, TTK) was used for reference thin-film electrodes with a Pt loading of $24 \mu\text{g}_{\text{Pt}} \text{ cm}^{-2}$.

The electrodes were immersed under potential control inside a three electrode glass cell in 0.1 M HClO_4 electrolyte, prepared from Suprapur 70% perchloric acid (Merck KGaA) and ultrapure Milli-Q water. All electrochemical measurements were performed at room temperature. The reference electrode was a saturated Hg / Hg_2SO_4 electrode (ALS Co., Ltd) and a platinum mesh served as counter electrode. The potentiostat used was a Metrohm Autolab PGSTAT 128N.

For the H_{upd} analysis, we performed cyclic voltammetry (CV) with a sweep rate of 50 mV s^{-1} in nitrogen (N_2)

saturated electrolyte. The upper potential limit was 1.0 V vs. RHE, and the lower potential limit was set between 0.0 V and 0.05 V vs. RHE to see the onset of hydrogen evolution in the CV. As discussed below, we performed the same CV also in CO saturated electrolyte with the electrode rotating at 1600 rpm.

CO stripping experiments were done according to the following protocol: First, CO was purged for 10 min in the electrolyte with the electrode potential kept at 0.1 V vs. RHE. Then, the gas was switched to N_2 for 30 min in order to remove the CO from the electrolyte with the electrode potential still kept at 0.1 V vs. RHE. Subsequently, the CO monolayer on the Pt surface was stripped off by performing a CV at 20 mV s^{-1} , starting at 0.1 V vs. RHE to an upper potential limit of 1.0 V vs. RHE. As described below, "CO stripping simulation" experiments were performed according to the same protocol with the only difference that the electrolyte was always purged with N_2 .

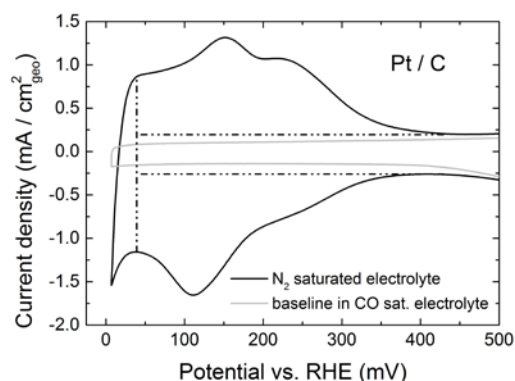


Figure 1. CV of the Pt / C catalyst in N_2 and in CO saturated 0.1 M HClO_4 at 50 mV s^{-1} .

Results

Figure 1 plots the hydrogen adsorption / desorption region of the CV of the Pt / C catalyst obtained in N_2 saturated (deaerated) electrolyte. Also plotted is the CV recorded in CO saturated electrolyte. In the latter case, the current is almost constant and purely capacitive below 0.4 V vs. RHE, which shows that the whole Pt surface is blocked by adsorbed CO. In a commonly used H_{upd} analysis, the capacitive currents in the double layer region are extrapolated into the potential region $< 0.4 \text{ V vs. RHE}$ (horizontal dashed lines in Figure 1) and taken as subtraction baselines for the hydrogen adsorption / desorption peaks. Mayrhofer et al. [3] suggested the use of the CV currents obtained in CO saturated electrolyte as an improved baseline for the H_{upd} analysis. However, due to the flatness of these CO-baseline currents in the H_{upd} region, we found the difference between both baseline methods for the Pt / C catalyst to be negligible in regard of the experimental errors.

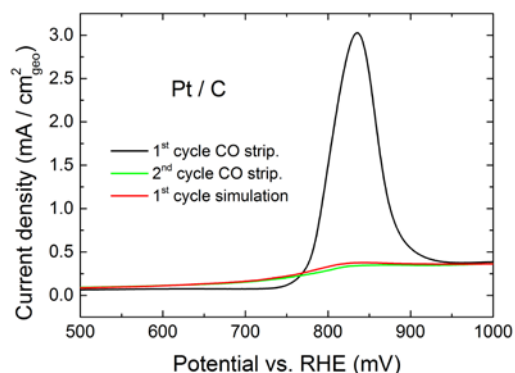


Figure 2. CO stripping CV and CO stripping simulation CV of the Pt / C catalyst in 0.1 M HClO₄ at 20 mV s⁻¹.

A second method frequently used to determine the ECSA is CO stripping voltammetry. Conventionally, the second cycle of the CO stripping CV is used as baseline for the CO stripping peak which occurs in the first cycle. This is shown in Figure 2 for the Pt / C catalyst together with the first cycle of the “CO stripping simulation” experiment [1, 2] described in the Experimental section above. It is obvious that both the second cycle of the true CO stripping experiment and the first cycle of the simulation experiment can be used as baseline for the CO stripping peak in this case of the Pt / C catalyst.

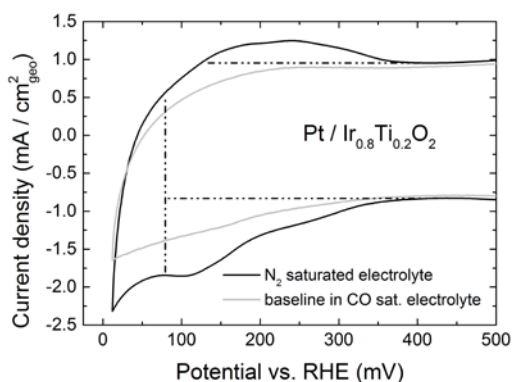


Figure 3. CV of the Pt / Ir_{0.8}Ti_{0.2}O₂ catalyst in N₂ and in CO saturated 0.1 M HClO₄ at 50 mV s⁻¹.

This situation drastically changes for the iridium-titanium oxide supported Pt catalyst. Figure 3 plots the H_{upd} region of the corresponding CVs in N₂ and in CO saturated electrolyte. The shape of the CV in N₂ purged electrolyte differs very much from the conventional “platinum CV” as shown in Figure 1 for the Pt / C catalyst. The reason for this difference is the metal-oxide support, which gives a much larger contribution to the currents than a conventional carbon support. As a consequence, the standard baselines (horizontal dashed lines in Figure 3) for the H_{upd} analysis clearly fail in this case. However, the CV recorded in CO saturated electrolyte can serve as a well suited baseline for the H_{upd} signals. As shown in Figure 4, after subtraction of this CO-baseline the well-known platinum H_{upd} shape can be recovered from the CV in N₂ purged electrolyte.

The first and the second cycle of a true CO stripping experiment on the Pt / Ir_{0.8}Ti_{0.2}O₂ catalyst are plotted in Figure 5, as well as the first cycle of the CO stripping simulation experiment.

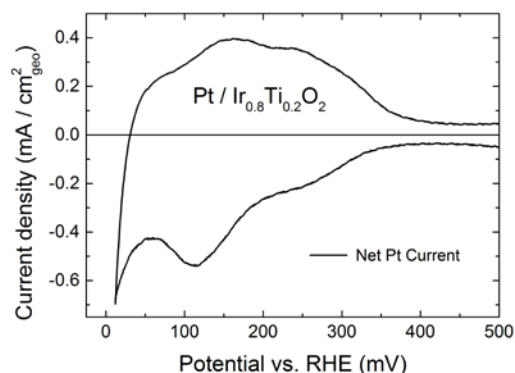


Figure 4. Net H_{upd} currents after subtraction of the CV in CO saturated electrolyte from the CV in N₂ saturated electrolyte, see Figure 3.

The standard baseline (second cycle of the CO stripping CV) clearly fails in this case, because the anodic currents of the first cycle have a positive offset with respect to the second cycle. This can be explained by the partial reduction of the Ir_{0.8}Ti_{0.2}O₂ oxide during potential hold at 0.1 V vs. RHE. This reduction is followed by a reoxidation in the anodic scan of the first cycle, leading to the observed positive offset of the oxidation currents. The reduction / oxidation behaviour of the metal-oxide support can be reproduced in the CO stripping simulation experiment as shown in Figure 5. Thus, the first cycle of this simulation experiment can serve as a reliable baseline for CO stripping voltammetry on the metal-oxide supported Pt catalyst.

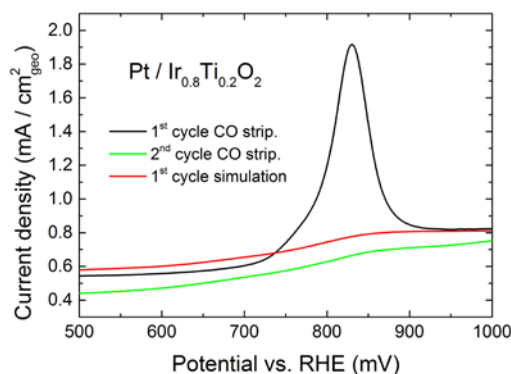


Figure 5. CO stripping CV and CO stripping simulation CV of the Pt / Ir_{0.8}Ti_{0.2}O₂ catalyst in 0.1 M HClO₄ at 20 mV s⁻¹.

Acknowledgement

This work is supported by CCEM Switzerland and Umico AG & Co KG within the project DuraCat.

References

- [1] T. Binninger, E. Fabbri, R. Kötz, T.J. Schmidt, J. Electrochem. Soc. **161** (3), H121-H128 (2014).
- [2] T. Binninger, E. Fabbri, R. Kötz, T.J. Schmidt, ECS Trans. **58** (1), 1835 (2013).
- [3] K.J.J. Mayrhofer, D. Strmcnik, B.B. Blizanac, V. Stamenkovic, M. Arenz, N.M. Markovic, Electrochim. Acta **53**, 3181 (2008).

Advanced CV studies on high-temperature polymer electrolyte fuel cells

T. Engl, J. Käse, L. Gubler, T.J. Schmidt

phone: +41 56 310 5237, e-mail: tom.engl@psi.ch

The high-temperature polymer electrolyte fuel cell (HT-PEFC) based on phosphoric acid doped polybenzimidazole (PBI) membranes as a gel-type proton transport medium show a number of significant differences in comparison to the low temperature PEFC based on a perfluorosulfonic acid membrane. The BASF Celtec® membrane, which has been used exclusively for experiments reported in this study, is synthesized via a sol-gel pathway. The first notable difference between HT- and LT-PEFC, which is a result of the membrane type, is that the HT-PEFC does not require humidified process gases, because water is replaced by phosphoric acid as a proton transport matrix. This results in a much simpler overall system design with fewer balance-of-plant components and hence reduced costs. Secondly, the HT-PEFC working temperature is at around 160°C, which means that effects of CO poisoning of the catalyst are far less pronounced [1,2]. Therefore, the system can be used to generate electricity from hydrogen-rich reformat gases without complex and energy intensive CO cleanup. Furthermore, the HT-PEFC can be combined effectively with heating systems due to the higher working temperature, leading to overall higher system efficiencies in combined heat and power (CHP) applications [3].

Nevertheless, reliable HT-PEFC characterization is rather difficult, in particular the determination of the electrochemically active surface area (ECSA). A novel technique was developed in order to overcome temperature dependency and side reactions during ECSA measurements via CO oxidation [4]. In this manuscript more detailed experiments to improve the understanding of cyclic voltammogram (CV) measurements, which are required for ECSA estimations, are provided. Especially the influence of temperature and the hold potential during the electrode conditioning was investigated.

Experimental

Within the first experimental series, CVs at six different temperatures from 40 to 180°C were recorded. Prior to the CV measurement, the cathode electrode was held at a constant potential of 150 mV vs. the reference hydrogen-platinum anode electrode. This potential is chosen for CO adsorption since it is high enough for only marginal hydrogen evolution to occur and low enough to prevent premature CO oxidation during poisoning and purging. During this conditioning step the flow rate of nitrogen was set to 27 L_nh⁻¹ for 5 minutes. This phase mimics the CO poisoning, whereas the subsequent flow rate of 72 L_nh⁻¹ is used for removing residual CO by purging for 30 minutes. A description of the detailed reference CV measurement procedure can be found elsewhere [4]. A second experiment was carried out in which the temperature was set to 180°C but the hold potential during conditioning was changed to 868 mV. This potential features a local current minimum at CV measurements and is not interfering with the oxidation peak between approx. 0.4 and 0.7 V. The flow rates and all other parameters were kept identical within the second experiment.

Results

The CVs recorded at different temperatures (Figure 1a) differ in various aspects. Besides the vanishing hydrogen underpotential deposition peaks especially the features between 0.4 and 0.7 V become very prominent. In Figure 1b this potential range is shown in detail for 40 and 180°C. One can see that at 40°C no feature can be observed, neither for the first nor for the subsequent potential cycles.

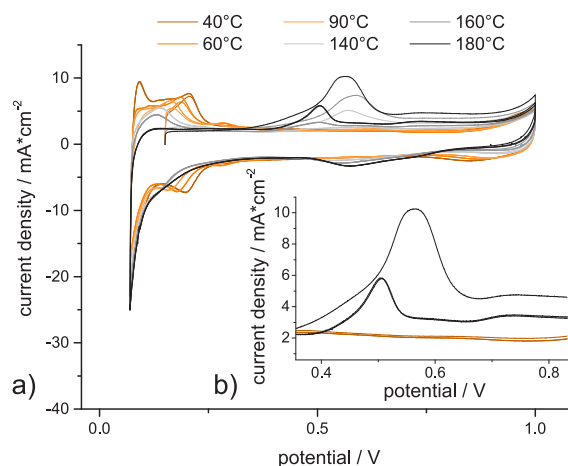


Figure 1. a) CVs recorded at different temperatures. b) Detailed deviation between CVs measured at 40 and 180°C. Measuring conditions: H₂ @ 4.5 L_nh⁻¹ on anode, N₂ @ 10 L_nh⁻¹ on cathode, 10 mV/s scan rate, hold potential 150 mV.

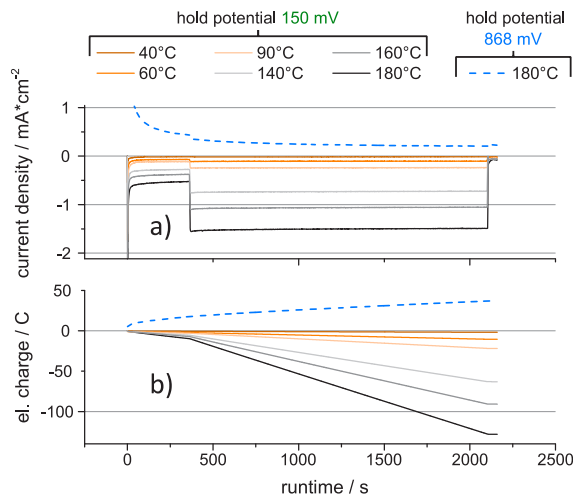


Figure 2. a) Current density at different temperatures and hold potentials. b) Electric charge characteristic during constant potential hold. Measuring conditions: H₂ @ 4.5 L_nh⁻¹ on anode, N₂ @ 27 L_nh⁻¹ → 72 L_nh⁻¹ (from 300 s) → 10 L_nh⁻¹ (from 2100 s) on cathode, applied hold potential 150 mV resp. 868 mV (starting from OCV).

In order to improve the understanding of the peak observed in the first cycle a second experiment was carried out with a hold potential at 868 mV instead of 150 mV. As already mentioned, the value of the higher potential is chosen because of the local minimum current ob-

served at this point in the previous CV. Furthermore, the temperature was set to 180°C because the first cycle oxidation peak increases with temperature (cf. Figure 1). In Figure 2a the current density during the conditioning at different temperatures and two different hold potentials is plotted. The graph indicates an increasing reducing current with increasing temperature. The current also depends on the nitrogen flow rate on the cathode side. Interestingly, the hold potential of 868 mV results in an oxidizing current that is far less pronounced compared to 150 mV at the same temperature. In Figure 2b the increasing charge passed during the entire conditioning phase highlights those findings.

The accumulated charge during the conditioning at the higher hold potential is approximately 70% lower compared to the charge corresponding to the lower hold potential at 180°C (cf. Figure 3).

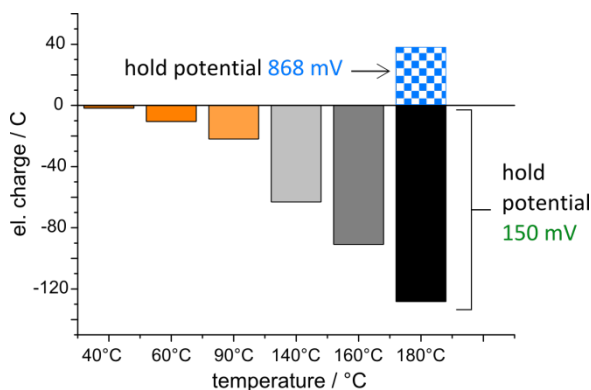


Figure 3. Accumulated charge during potential hold at different temperatures.

Subsequent to the electrode conditioning two CVs at 180°C were recorded (cf. Figure 4). The black solid and blue dashed CV is associated with a hold potential of 150 mV and 868 mV, respectively. The charge under the oxidation peak is about 62% higher for the black CV compared to the reduction peak of the blue CV during the first potential cycle. Interestingly, no initially varying oxidation peak could be observed in the first potential cycle of the blue CV. The anodic sweeps in the subsequent cycles are identical. Both CVs only differ in their first potential cycle.

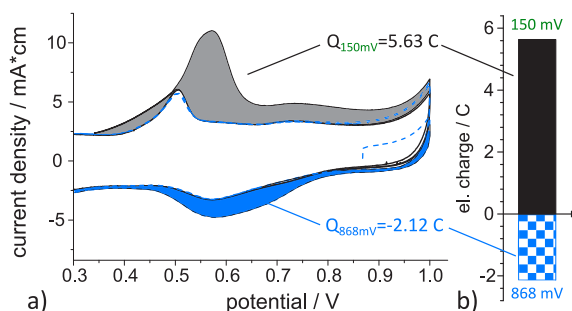


Figure 4. a) Two CVs with different hold potentials at 180°C b) CV peak charges. Measuring conditions: H_2 @ $4.5 L_n h^{-1}$ on anode, N_2 @ $10 L_n h^{-1}$ on cathode, 10 mV/s scan rate.

It is assumed that the origins of this behavior are active carbon surface functionalities (cf. Figure 5). The activity of those functionalities is apparently triggered by temperature and the hold potential. Similar results were reported in [5].

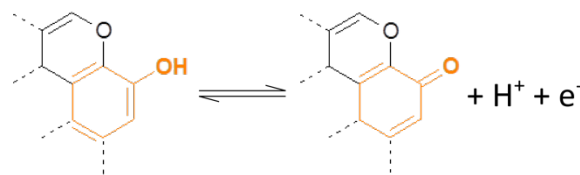
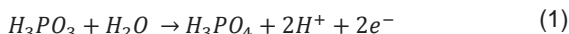


Figure 5. Oxidation/reduction of carbon surface functionalities, e.g. hydroquinone/quinone.

Furthermore, the oxidation of phosphorous acid impurities may also contribute to the initial oxidation peak (cf. Equation (1)) as outlined in ref. [6].



Conclusion

The experiments have clearly shown that with increasing temperature the oxidation peak during the first CV potential cycle increases drastically. Furthermore, the current density during electrode conditioning indicates a similar dependency. Higher temperatures, and flow rates, result in a higher current and therefore a higher total charge (cf. Figure 3).

Those findings are very helpful in order to improve the ability to classify the side reactions that occur during ECSA measurements. It has been shown that it is not accurate to integrate the entire first oxidation peak and assume it is associated with CO electrooxidation ("stripping"). Especially at higher temperatures the main charge contribution is presumably carbon surface or phosphorous acid oxidation. Therefore, the hypotheses put forward in the context of the technique introduced in [4] is supported by these results. However, it is maybe important to reconsider the definition of ECSA. Subtracting the charge value from the reference peak does in fact provide the available active area for adsorbed CO. But oxidizing or reducing surface functionalities also requires an electrochemically active surface area.

Acknowledgment

Financial support from BASF SE is gratefully acknowledged. We thank Christian Marmy and André Meier for technical assistance and our colleges at the PSI for productive discussions.

References

- [1] T.J. Schmidt, J. Baurmeister, ECS Trans. **3**, 861-869 (2006).
- [2] A.D. Modestov, M.R. Tarasevich, et al., Electrochim. Acta **55**, 6073-6080 (2010).
- [3] Elcore GmbH München, **Online**, Available: <http://www.elcore.com/de/home.html>. (Accessed: 19-Jun-2013).
- [4] T. Engl, K. Waltar, ECS Trans. **58**, 819-830 (2013).
- [5] A. Pandey, Z. Yang, et al., J. Electrochem. Soc. **160**, F972-F979 (2013).
- [6] N. Sugishima, J. T. Hinatsu, et al., J. Electrochem. Soc. **141**, 3325-3331 (1994).

Positive effect of CO during start/stop on high-temperature PEFCs

T. Engl, L. Gubler, T.J. Schmidt

phone: +41 56 310 5237, e-mail: tom.engl@psi.ch

One of the most beneficial unique features of a high-temperature polymer electrolyte fuel cell (HT-PEFC) is the capability to tolerate orders of magnitude larger amounts of CO (up to 2% [1]) compared to a LT-PEFC (approx. 10ppm [2]). Therefore, the system can be used to generate electricity from hydrogen-rich reformat gases without complex and energy intensive CO-cleanup.

Nevertheless, the HT-PEFC can suffer from numerous degradation mechanisms in different locations of the membrane electrode assembly (MEA), e.g. pinhole formation in the membrane, acid evaporation and membrane thinning [3], [4]. Electrodes can also represent a major area of degradation. Interestingly, specific degradation mechanisms, such as carbon corrosion, catalyst detachment and catalyst particle growth can be found in the LT-PEFC as well. Additionally, structural changes and acid flooding of the gas diffusion layer of the cell can occur. All degradation effects are complex functions of the specific operation conditions, making it challenging to identify them individually. This in turn is necessary to gain insights into limitations of MEA lifetime and is the key to successful development of mitigation strategies to reach a desired lifetime of more than 40.000 hours [4] for stationary applications.

One of the specific degradation triggers is known as “start/stop”- or “reverse-current decay” mechanism [5,6]. The mechanism is induced during the fuel cell startup or shutdown and is one of the main reasons for carbon corrosion at the cathode. The number of start/stop cycles is closely related to the overall lifetime of the fuel cell. If, for example, a HT-PEFC is used in a CHP system, it is conceivable that several hundred cycles will be accumulated, which lead to a rapid and irreversible damage of the cell. Therefore it is necessary to improve the understandings of the start/stop mechanism in order to deduce appropriate mitigation strategies.

Experimental

Start/stop experiments were carried out using different reformat-like fuel gas mixtures on the anode side. The H₂/CO ratio was gradually varied. Starting from 72 vol.% of H₂ and 0 vol.% of CO the hydrogen content was reduced in steps of 1 vol.% to 62 vol.%, whereas the CO content was increased accordingly (cf. Fig. 1,2). The anode CO₂ concentration was maintained at 28 vol.%. A cycle time of 60 seconds was chosen for switching between the reformat and the oxidant gas on the anode side, simulating start-up and shut-down processes. Pure oxygen and air were used as oxidants in two different experimental runs. The anode flow rate was set to 36 L_nh⁻¹ resulting in a residence time of 0.44 s. On the cathode side the oxidant flow rate was set to 72 L_nh⁻¹ resulting in a residence time of 0.22 s. The cell temperature was held at 160°C. The carbon corrosion was measured via the CO₂ signal in the cathode exhaust gas using a real time infrared CO₂ detector (California Analytical Instruments Model 601). For each mixing ratio two consecutive start and stop events were recorded.

Results

Figures 1 and 2 indicate a very clear dependence on the CO content on the anode side during start and as well during stop events. Using pure oxygen on the cathode side (Figure 1) leads to a higher overall corrosion and to a more pronounced CO₂ signal response compared to when air is used as oxidant (Figure 2) because there is no CO₂ present in the reactant gas itself. This CO₂ in air is also the explanation for the elevated CO₂ baseline in Figure 2. For pure oxygen the CO₂ signal in Figure 1 between 0 and 2 vol.% CO during start reaches the detection limit of the CO₂ sensor. From there on the CO₂ corrosion response declines gradually with increasing CO content for start and stop operations. Especially for air conditions on the cathode side in Figure 2, one can see that higher CO concentrations have a higher influence on stop than they have on start events.

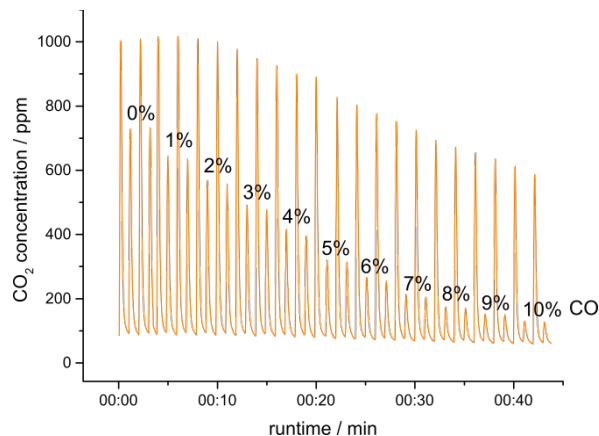


Figure 1. CO₂ signal in the cathodes exhaust gas during start/stop with different CO contents in the anodes fuel gas. Measuring conditions: 160°C, reformat (72-x% H₂, 28% CO₂, x% CO) @ 36 L_nh⁻¹, O₂ @ 72 L_nh⁻¹, 60 seconds cycle time.

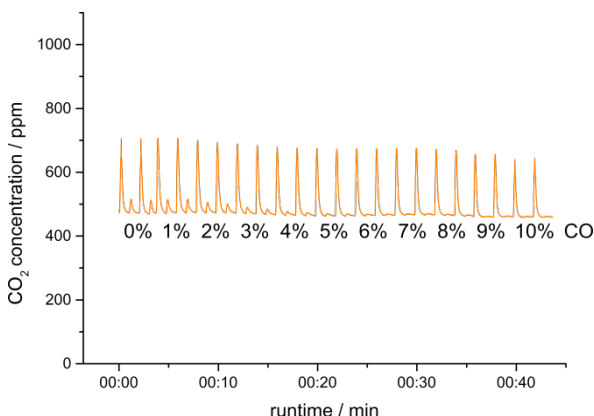


Figure 2. CO₂ signal in the cathodes exhaust gas during start/stop with different CO contents in the anodes fuel gas. Measuring conditions: 160°C, reformat (72-x% H₂, 28% CO₂, x% CO) @ 36 L_nh⁻¹, Air @ 72 L_nh⁻¹, 60 seconds cycle time.

The gradually declining carbon corrosion with higher CO content can be explained conclusively with arguments of CO-coverage, illustrated in Figure 3. In order to oxidize carbon on the cathode side in the passive fuel cell compartment hydrogen needs to be oxidized on the anode side in the active fuel cell compartment (cf. [5,6]). If the CO content increases the available sites for the hydrogen oxidation reaction are diminished because of the strong CO coverage. Therefore, less hydrogen is oxidized, which consequently leads to a smaller amount of oxidized carbon because less protons and electrons are required.

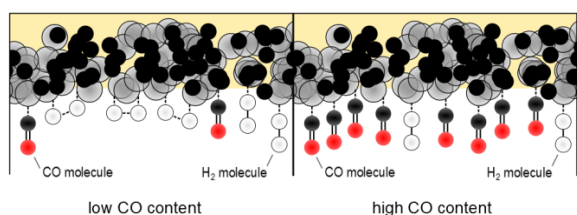


Figure 3. Detailed anode three phase boundary sketches with low and high CO contents in the reformate gas.

The proposed model is furthermore able to explain the different CO₂ response for start and stop events at various CO contents. Subsequent to a shutdown one can assume that after a certain time period only oxygen/air is present at the anode and no active sites are covered with CO. If now a start event is carried out a reformate gas front, containing CO, is introduced to the anode (cf. Figure 4). Whereas the hydrogen oxidation on the left side is now hindered, depending on the CO content, the oxygen reduction reaction on the right side is not subject to this restriction because there are no blocked active sites.

A contrary behavior can be observed during stop events (cf. Figure 5). The entire anode is, depending on the CO content, covered by CO. If now the fuel cell is stopped oxygen/air is introduced to the anode (right side). The difference now compared to the start event is that in both compartments (left and right) CO is blocking active sites. Therefore, not only the hydrogen oxidation is hindered but also the oxygen reduction reaction, which leads to a stronger CO dependence with respect to carbon corrosion during stop events compared to start events. An animation of the described model can be found online (<http://ge.tt/5NDxIzW>).

In future experiments this model could be verified by measuring the CO₂ content during start and stop events in the anode exhaust gas. The lower the CO₂ signal resulting from carbon corrosion on the cathode side, the higher should be the CO₂ signal on the anode side due to CO oxidation.

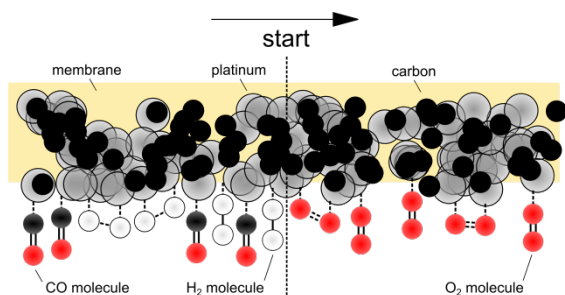


Figure 4. Detailed sketch of the anode three phase boundary during start with CO in the reformate gas.

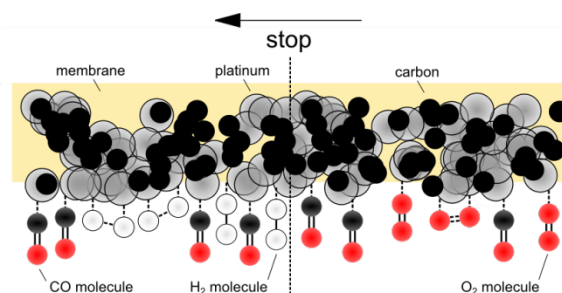


Figure 5. Detailed sketch of the anode three phase boundary during stop with CO in the reformate gas.

Conclusion

The HT-PEFC can be operated with a rather high content of CO [1], but in this manuscript it was furthermore shown that in fact CO acts as a degradation mitigation agent. Increasing the CO content in the reformate gas on the anode side during start/stop results in a reduced CO₂ response on the cathode side, which indicates a reduced amount of oxidized carbon. Therefore, it is not only possible but desirable to use CO containing fuel gases to improve the overall lifetime of the fuel cell. In order to support the aforementioned newly developed model, experiments are going to be carried out in which in addition to the cathode also the anode CO₂ response is going to be measured during start/stop.

Acknowledgment

Financial support from BASF SE is gratefully acknowledged. We thank Christian Marmy and André Meier for technical assistance and our colleagues at the PSI for productive discussions.

References

- [1] T.J. Schmidt, J. Baurmeister, ECS Trans. **3**, 861–869 (2006).
- [2] A.D. Modestov, M.R. Tarasevich, et al., Electrochim. Acta **55**, 6073–6080 (2010).
- [3] A.D. Modestov, M.R. Tarasevich, et al., Electrochim. Acta **54**, 7121–7127 (2009).
- [4] T.J. Schmidt, ECS Trans. **1**, 19–31 (2006).
- [5] W. Gu, R.N. Carter, et al., ECS Trans. **11**, 963–973 (2007).
- [6] C.A. Reiser, L. Bregoli, et al., Electrochem. Solid-State Lett. **8**, A273 (2005).

Composite catalysts made by $\text{Ba}_{0.5}\text{Sr}_{0.5}\text{Co}_{0.8}\text{Fe}_{0.2}\text{O}_{3-\delta}$ perovskite and acetylene black carbon for the oxygen reduction reaction in alkaline media

E. Fabbri, R. Mohamed¹, P. Levecque¹, O. Conrad¹, R. Kötzt, T.J. Schmidt

phone: +41 56 310 2795, e-mail: emiliana.fabbri@psi.ch

Alkaline fuel cells (AFCs) were the first low temperature fuel cell developed in the 1960s, particularly for space program applications. The main drawback of AFCs was related to the electrolyte deterioration in contact with CO_2 . Recently, the development of alkaline conductive membranes showing satisfactory stability has stimulated a renewed interest in AFCs [1]. Alkaline energy conversion systems have the great advantages of using an electrolyte medium less corrosive compared to an acidic environment with respect to a wider range of compounds and also allowing more favourable oxygen electrocatalysis [2]. For the above mentioned reasons the research is very active in exploring novel catalyst materials, particularly for the oxygen electrode. The main goal is to develop a catalyst materials showing adequate stability, high activity towards oxygen reduction reaction (ORR) and being also relatively inexpensive. Recently, great attention has been pointed out towards the perovskite oxide family. The potential of perovskites as oxygen electrocatalysts in alkaline media was known since the early 70's, and recently the advantage of perovskite as oxygen catalysts has been remarked by a growing number of publications. Indeed, as commented by R. F. Savinell [3], since perovskite oxides easily allow tailoring their composition by cation substitutions, promising catalytic properties could be unravelled. In some of the recent publications [4,5] the attention has been pointed out towards a correlation between band structure and perovskite catalytic activity. Particularly it was found out that the highest activity towards oxygen electrocatalysis can be achieved for perovskites presenting e_g orbital occupancy close to unity. $\text{Ba}_{0.5}\text{Sr}_{0.5}\text{Fe}_{0.2}\text{Co}_{0.8}\text{O}_{3-\delta}$ (BSCF), which fulfills the criterion of e_g orbital occupancy close to unity, has shown indeed high catalytic activity towards oxygen evolution reaction [5]. Since the same band descriptor has been reported valid also for designing superior ORR catalysts, the e_g orbital configuration of BSCF would suggest this material as a promising ORR catalyst as well. However we have found that BSCF displays quite high ORR overpotential and that the reaction did not result in an overall 4 electron process, leading to parallel OH^- and HO_2^- production [6]. Given the poor performance of BSCF as ORR catalyst compared to those expected by considering BSCF band structure and the proposed band descriptor in ref. [4] and [5] for superior ORR catalysts, in the present work we have designed composite electrodes made of BSCF and carbon in order to boost BSCF ORR catalytic activity.

Experimental

$\text{Ba}_{0.5}\text{Sr}_{0.5}\text{Co}_{0.8}\text{Fe}_{0.2}\text{O}_{3-\delta}$ (BSCF) powder was synthesized using a modified sol gel process. Stoichiometric quantities of commercial $\text{Ba}(\text{NO}_3)_2$ (Aldrich, 99%), $\text{Sr}(\text{NO}_3)_2$ (Aldrich, 99%), $\text{Co}(\text{NO}_3)_2 \cdot 6\text{H}_2\text{O}$ (Aldrich, 99%), and $\text{Fe}(\text{NO}_3)_3 \cdot 9\text{H}_2\text{O}$ (Aldrich, 98%) nitrate precursors were dissolved in an aqueous solution of 0.2 M nitric acid. Citric acid (Aldrich, 99.5%) was used as a chelating agent in a 2:1 ratio with respect to the total metal cations. After obtaining a transparent solution, the

pH was then adjusted between 6 and 8 by NH_4OH additions. The solution was then heated under stirring to evaporate water until it changed into a viscous gel and finally ignited to flame, resulting in a black ash. To obtain single phase material, the BSCF powder was calcined at 1000 °C for 2 h in air. Single phase material was obtained as revealed by X-ray diffraction analysis [6]. The specific surface area of the powder determined by Brunauer-Emmett-Teller (BET) analysis was about $10 \pm 1 \text{ m}^2 \text{ g}^{-1}$. Acetylene black was purchased from Alfa Aesar and prior the utilization it was treated in concentrated nitric acid overnight at 80 °C, then washed and dried at 100 °C. The BET surface area of the acid treated AB was found to be $90 \pm 4 \text{ m}^2 \text{ g}^{-1}$. For the electrochemical characterization, porous thin films were prepared by drop-coating a cathode ink on a rotating glassy carbon disk. The total loading was kept constant among all the investigated electrodes, being $\sim 460 \mu\text{g cm}^{-2}$ of BSCF and/or AB and $\sim 50 \mu\text{g cm}^{-2}$ Na^+ -exchanged Nafion. The catalyst layer microstructure was observed using a scanning electron microscope (SEM, Gemini Ultra 55). The working electrodes were immersed under potential control (0.8 V vs. RHE) in 0.1 M KOH electrolyte saturated with pure Ar or O_2 at room temperature and the measurements were performed using a hydrogen reference electrode and a gold counter electrode in a three electrode configuration. Rotating ring disk electrode (RRDE) measurements were performed in a home-made Teflon cell by cathodically scanning the disk electrode between 1 and 0.05 V at 5 mV s^{-1} while the Pt ring electrode was held at 1.2 V (RHE). The cathodic scan obtained from RRDE measurements of the disk electrodes were corrected for capacitive currents measured under cathodic scan at 5 mV s^{-1} in Ar-saturated electrolyte [6]. The collection efficiency of the Pt ring was 0.2 ± 0.02 .

Results

The influence of the carbon addition on the BSCF ORR activity and selectivity has been investigated by systematically increasing the Acetylene black (AB) content into the BSCF electrodes, keeping the overall loading constant. Figure 1 shows a typical SEM micrograph of a composite electrode containing BSCF and AB in a 1.25 weight ration. The mixture of BSCF and AB resulted in a homogeneous electrode, where BSCF appeared uniformly encapsulated into the AB layer.

Rotating ring disk electrode (RRDE) measurements of BSCF, AB and all the composite electrodes were recorded in 0.1 M KOH, cathodically sweeping the working electrode at 5 mV s^{-1} and 1600 rpm. The current plateau in the disk currents characteristic for a diffusion-controlled reaction regime was not observed for any of the electrodes. These results indicate that for each electrode the ORR is under a mixed kinetic-diffusion control over the whole potential range. By introducing AB into the BSCF electrode lower overpotentials for the ORR were achieved with an increased current density at higher overpotentials.

¹ HySA/Catalysis, University of Cape Town, South Africa

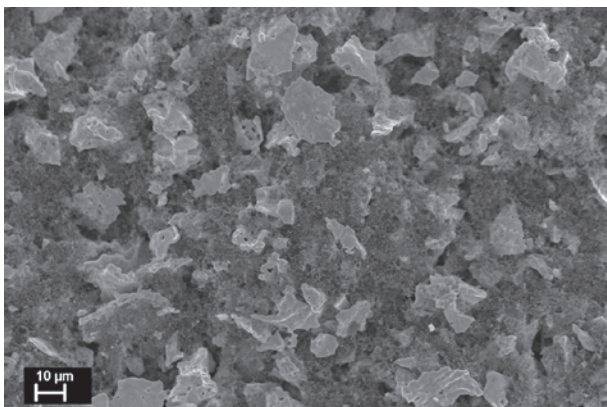


Figure 1. SEM micrograph of a composite electrode made by BSCF and AB in a 1.25 weight ratio.

Figure 2 shows the onset potential for the ORR, arbitrarily defined here as the potential required for an ORR current of $-25 \mu\text{A cm}^{-2}$, as a function of the AB content in the electrodes. An optimal BSCF/AB ratio exists and the ORR onset is described by a volcano plot. By introducing only 10 wt% of AB, a significant increase in the onset potential could be already observed. By further increasing the AB content, the ORR onset potential still increased until a maximum value was obtained. The lowest overpotential for the ORR could be achieved for a BSCF and AB weight ratio of 1.25. Upon further AB content increase, a slight decrease in the ORR onset was observed. Since the overall electrode loading was purposely kept constant, the enhanced performance of the composite electrodes cannot be explained by the simple addition of currents resulting from the ORR occurring on the BSCF and the AB simultaneously.

Apart from the analysis of the ORR onset, a better comprehension of the ORR mechanism can be achieved by the analysis of the Pt ring current. Indeed, the latter allows calculating the hydroperoxide formation at the working electrode during the ORR. Figure 2 also shows the hydroperoxide formation as a function of the electrode compositions at 0.4 V vs. RHE. A volcano type behavior was observed also for the hydroperoxide formation as a function of the electrode composition, with a minimum of $28.5 \% \pm 3.5$ for the electrode having BSCF and AB in a 1.25 weight ratio. Not surprisingly, this electrode composition also showed the lowest ORR onset overpotential.

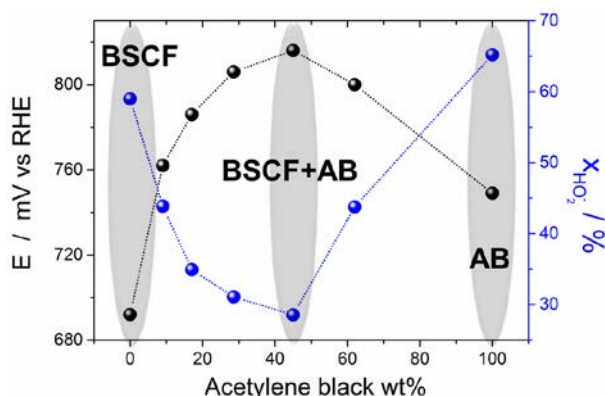


Figure 2. Onset for the ORR (defined as the potential vs. RHE reached at $25 \mu\text{A cm}^{-2}$) and mole fraction (in percent) of produced hydroperoxide as a function of the AB weight percent in the investigated electrode compositions.

Specific kinetic currents (normalized by the BSCF and/or AB surface area) for BSCF, AB and the most performing composite electrode (weight ratio 1.25) are reported in Figure 3. No major difference in the Tafel slope was observed, being 64, 65, and 55 mV dec^{-1} for BSCF, BSCF/AB_1.25, and AB, respectively. Nonetheless, the composite electrode showed much improved ORR activity compared to the single BSCF and AB electrode. For example, at 0.725 V vs. RHE the kinetic current was 0.0053 and 0.0474 mA cm^{-2} for the BSCF and the AB, respectively, while it reached 0.4965 mA cm^{-2} for the BSCF/AB_1.25. The composite electrode showed indeed kinetic currents two and one order of magnitude higher than that of BSCF and AB, respectively.

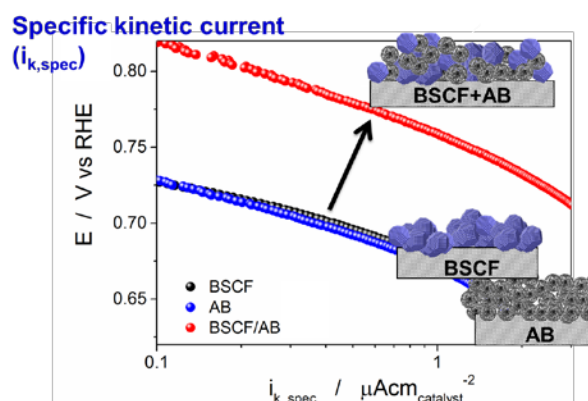


Figure 3. Normalization of the Tafel plots by the catalyst specific surface area. Tafel plots were related to mass-transport and capacitive current corrected ORR currents obtained from a cathodic scan at 5mV s^{-1} and 1600 rpm for BSCF, AB, and the composite electrode BSCF/AB_1.25.

Conclusion and Summary

Herein we report the electrochemical activity and selectivity towards the oxygen reduction reaction (ORR) for composite electrodes made of BSCF perovskite oxide and Acetylene black carbon in alkaline media. The onset potential and the selectivity, i.e. hydroperoxide formation, towards the ORR exhibit a volcano type behaviour as a function of the electrode composition. Therefore, the overall results point toward a beneficial interaction between BSCF and AB. Ligand (electronic) effects between the two materials might be responsible for the enhanced ORR activity of the composite electrodes.

References

- [1] J.R. Varcoe, R.C.T. Slade, *Electrochem. Commun.* **8** (5), 839-843 (2006).
- [2] G. Merle, M. Wessling, K. Nijmeijer, *J. Membr. Sci.* **377**, 1-35 (2011).
- [3] R.F. Savinell, *Nat. Chem.* **3**, 501-502 (2011).
- [4] J. Suntivich, H.A. Gasteiger, N. Yabuuchi, H. Nakanishi, J.B. Goodenough, Y. Shao-Horn, *Nat. Chem.* **3**, 647-647 (2011).
- [5] J. Suntivich, K.J. May, H.A. Gasteiger, J.B. Goodenough, Y. Shao-Horn, *Science* **334**, 1383-1385 (2011).
- [6] E. Fabbri, R. Mohamed, P. Levecque, O. Conrad, R. Kötzt, T.J. Schmidt, *ChemElectroChem* (2013). DOI:10.1002/celec.201300157

Structural investigation on Pt₄₀Pd₆₀ aerogel by using multi-edge extended X-ray absorption fine structure (EXAFS) fit analysis

M. Özaslan, M. Nachtegaal, C. Laugier Bonnaud¹, W. Liu², A.-K. Herrmann², M. Werheid², N. Gaponik², A. Eychmüller², R. Kötz, T.J. Schmidt

phone: +41 56 310 5572, e-mail: mehtap.oezaslan@psi.ch

Unsupported bimetallic Pt-Pd aerogels are a new and promising generation of electrocatalysts for the oxygen reduction reaction (ORR, $O_2 + 4 H^+ + e^- \rightarrow 2 H_2O$) in PEFCs due to their unique long-range particle network structure. Our previous work highlighted the beneficial performance in activity and durability for the ORR.^{1, 2} Knowledge about the relationship between structure and reactivity is important to understand the kinetics and mechanism for the ORR. The spatial distribution of both metals and the homogeneity within the Pt-Pd aerogels, yet, are unclear to date. The critical issues for the utilization of typical characterization techniques like X-ray diffraction and electron microscopy on Pt-Pd aerogels are: (i) the almost similar lattice parameters of Pt and Pd, (ii) the small crystallite sizes and (iii) the large effort to analyse a sufficient number of single nanoparticles by (S)TEM equipped with spectroscopic tools like EDX or EELS. Therefore, the goal in this work is to investigate the structure and the spatially chemical distribution of Pt-Pd aerogel by using X-ray absorption spectroscopy (XAS). XAS is an element-specific technique that provides structural and electronic information (oxidation state) of nanoparticles under reaction conditions. The influence of the applied potential, potential range, electrolyte, pH and temperature on the structure of bimetallic nanoparticles can be probed by in-situ electrochemical XAS measurements. Atomic parameters including identity of nearest neighbor atoms, coordination numbers, atomic distances and degree of disorder of the atoms (pseudo Debye-Waller factor) can be determined up to a distance of 6 Angstrom. In particular, the homogeneity and spatial distribution of two different elements can be determined by the parameter, so-called Cowley short range order parameter α , which is calculated by the coordination numbers.³⁻⁶ The Cowley short range order parameter (α) indicates the degree of alloying or clustering within bimetallic nanoparticles and can be calculated by

$$\alpha = 1 - \frac{N(AB)/N(AM)}{xB}$$

where x_B is the molar concentration of B-type atoms, $N(AB)$ is the coordination number between atom A and atom B, $N(AM)$ is the total coordination number in the sample. In the case of the pristine Pt₄₀Pd₆₀ aerogel, we will show the strong benefits for the utilization of extended X-ray absorption fine structure (EXAFS) to provide the chemical homogeneity and spatial distribution of both elements, Pt and Pd, within the aerogel material.

Experimental

Structural investigation on the pristine Pt₄₀Pd₆₀ aerogel was performed by using X-ray absorption spectroscopy (XAS). XAS spectra for the Pt and Pd edge were acquired on the X10DA (SuperXAS) beamline at the Swiss Light Source (SLS). The storage ring was operated at a beam current of 400 mA. The sample powders were

pressed with cellulose as binder material to form a pellet with a diameter of 0.5 cm. Both edges were measured in transmission mode by using ionization chambers filled with a He/N₂ mixture. Data were collected from 11.46 to 12.48 keV for Pt (Pt L₃-edge 11.565 keV) and 24.25 to 25.50 keV for Pd (Pd K-edge 24.350 keV). The data acquisition time was approx. 15 - 20 min for one complete EXAFS scan. Several scans for each sample were averaged to improve the signal to noise ratio. To process and to analyze the EXAFS spectra, the lfeffit⁷ software package was employed. Data reduction consisted of background subtraction and edge-step normalization. The EXAFS spectra were Fourier transformed and subsequently fitted by a nonlinear least-squares fitting approach. Multi-edge EXAFS fits for Pt and Pd were concurrently performed. The scattering paths for all spectra measured at the Pt edge were calculated using a face centered cubic (fcc) Pt-Pd structure (space group Fm-3m). For all EXAFS spectra, the coordination number (CN), atomic bond distance (R), inner potential shift (E_0) and degree of disorder (σ^2) of each relevant scattering path were determined.

Results

Pt and Pd EXAFS spectra of the pristine Pt₄₀Pd₆₀ aerogel were collected to establish its atomic parameters such as identify of the nearest neighbor, coordination number (N), atomic distance (R), degree of disorder (σ^2) as well as short-range order parameter (α). The disorder parameter can be described as a pseudo Debye-Waller factor. With increasing value of σ^2 , the arrangement of atoms in the structure is more flexible. Furthermore, the chemical composition of the pristine aerogel was established by EDX and was close to the atomic Pt:Pd ratio of 40:60 (not shown).

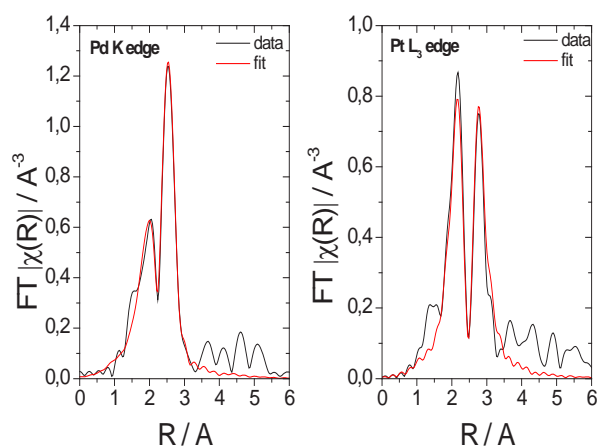


Figure 1. k^2 -weighted Fourier transformed EXAFS spectra (black line) and the best fits (red line) for Pd (left side) and Pt (right side) on pristine Pt₄₀Pd₆₀ aerogel, respectively.

¹ Phelma Grenoble INP, Grenoble, France

² TU Dresden, Dresden, Germany

Figure 1 shows the k^2 -weighted Fourier transformed EXAFS spectra (black lines) collected at the Pd and Pt edge, respectively. Both edges were concurrently fitted by assuming that the degree of disorder and the atomic distance between Pt and Pd atoms were equal. The quality of the corresponding fits (red line) is shown for both spectra in Figure 1. Two intense peaks between 1.5 and 3.0 Å were clearly observed. The first peak at around 1.5 – 2.0 Å was assigned to the coordination shell for the Pt-Pd or Pd-Pt, while the second one at around 2.5 – 3.0 Å was assigned to a (single) coordination shell for Pd-Pd and Pt-Pt, respectively.

Tables 1 – 4 summarize the best fit parameters of the nearest coordination numbers, atomic distances, disorder parameters (σ^2) and short-range order parameters (α) estimated from the multi-edge fits for the pristine Pt₄₀Pd₆₀ aerogel. The coordination numbers (Table 1) for the Pt-Pt as well as Pd-Pd in the first shell were larger than those for Pt-Pd or Pd-Pt. The first nearest atomic distances between Pt-Pt, Pt-Pd and Pd-Pd were very similar, as shown in Table 2. However, these values were smaller compared to those for bulk materials. The decrease of atomic distance is related to the compressive lattice strain which is well-known for nanoparticles.⁸ Table 3 shows the disorder parameters for the pristine Pt₄₀Pd₆₀ aerogel. Only, the Pd-Pd bond exhibited the largest value of disorder (σ^2), indicating a larger disordering for Pd-Pd. The other values for the Pt-Pt and Pt-Pd bonds, however, were similar and small, signifying a well-ordering in the aerogel structure.

$N_{\text{Ptabs-Pt}}$	$N_{\text{Ptabs-Pd}}$	$N_{\text{Pdabs-Pt}}$	$N_{\text{Pdabs-Pd}}$
6.1 ± 0.9	3.7 ± 0.6	4.3 ± 0.8	5.9 ± 0.7

Table 1. Summary of the first nearest neighbor coordination numbers N for the pristine Pt₄₀Pd₆₀ aerogel obtained from the best fit parameters.

$R_{\text{Ptabs-Pt}}[\text{Å}]$	$R_{\text{Ptabs-Pd}}[\text{Å}]$	$R_{\text{Pdabs-Pt}}[\text{Å}]$	$R_{\text{Pdabs-Pd}}[\text{Å}]$
2.73 ± 0.03	2.73 ± 0.03	2.73 ± 0.03	2.76 ± 0.01

Table 2. Summary of the atomic distances (R) for the pristine Pt₄₀Pd₆₀ aerogel obtained from the best fit parameters.

$\sigma^2_{\text{Ptabs-Pt}}$	$\sigma^2_{\text{Ptabs-Pd}}$	$\sigma^2_{\text{Pdabs-Pt}}$	$\sigma^2_{\text{Pdabs-Pd}}$
[*10 ⁴ Å]	[*10 ⁴ Å]	[*10 ⁴ Å]	[*10 ⁴ Å]
73 ± 11	73 ± 11	73 ± 11	81 ± 9

Table 3. Summary of the first nearest disorder parameters (σ^2) for the pristine Pt₄₀Pd₆₀ aerogel obtained from the best fit parameters.

The total coordination numbers and the short-range order parameters (see Table 4) can be used to examine the chemical distribution of both elements inside the pristine Pt₄₀Pd₆₀ aerogel. Based on our best fit results, the total coordination numbers for the Pt-M and Pd-M ($M = \text{Pt}, \text{Pd}$) in the first shell differed clearly from the expected values for macroscopic materials with fcc structure ($N = 12$). Since the total coordination number is smaller than 12, the Pt₄₀Pd₆₀ aerogel exhibited the behavior of nanoparticles despite the long-range network arrangement. Furthermore, the relation between $N(\text{Pt-M})$ and $N(\text{Pd-M})$ values can be used to provide,

if/which metal atoms segregate to the core and to the shell of bimetallic particles. Here, the established total coordination numbers for Pt-M and Pd-M were similar, indicating, that both metals were equally distributed on the surface as well as in the core of the aerogel.

Interestingly, the short-range order parameter revealed a significant difference in the chemical homogeneity and the spatial distribution of these dissimilar elements. The large positive value of α for the first Pt-Pd shell indicated that the platinum atoms formed Pt-rich clusters inside the pristine aerogel material. Unlike the observed strong cluster formation of Pt, the calculated value of α for Pd was slightly positive, signifying that the Pd atoms were homogeneously surrounded by Pt atoms. It is evident, that the pristine Pt₄₀Pd₆₀ aerogel showed heterogeneity of the distribution of Pt atoms.

$N_{\text{Ptabs-M}}$	$N_{\text{Pdabs-M}}$	$\alpha_{\text{Pdabs-Pt}}$	$\alpha_{\text{Ptabs-Pd}}$
9.8	10.2	0.14	0.40

Table 4. Summary of the total coordination numbers ($N_{\text{Ptabs-M}}$ and $N_{\text{Pdabs-M}}$) and short-range order parameter ($\alpha_{\text{Pdabs-Pt}}$ and $\alpha_{\text{Ptabs-Pd}}$) for the pristine Pt₄₀Pd₆₀ aerogel obtained from the best fit parameters.

Conclusions

In this work, the structure and chemical homogeneity of the pristine Pt₄₀Pd₆₀ aerogel were studied by utilizing EXAFS spectroscopy. Atomic parameters like kind of atom neighbors, total and partial coordination numbers, atomic distances, disordering, for the pristine Pt₄₀Pd₆₀ aerogel were determined. Our data showed that Pt and Pd atoms were located on the surface as well as in the core of the pristine bimetallic aerogel. No segregation tendency was observed. In addition, the Pd atoms were homogeneously distributed inside the aerogel. However, the Pt atoms showed a strong cluster behavior. The cluster formation was an indication for heterogeneity of Pt inside the pristine Pt₄₀Pd₆₀ aerogel.

This study provided a better understanding of the structure and chemical distribution for highly complex bimetallic nanoparticle architectures.

References

- [1] W. Liu, A.-K. Herrmann, D. Geiger, L. Borchardt, F. Simon, S. Kaskel, N. Gaponik, A. Eychmüller, *Angew. Chem. Int. Ed.* **51**, 5743-5747 (2012).
- [2] W. Liu, P. Rodriguez, L. Borchardt, A. Foelske, J. Yuan, A.-K. Herrmann, D. Geiger, Z. Zheng, S. Kaskel, N. Gaponik, R. Kötz, T.J. Schmidt, A. Eychmüller, *Angew. Chem. Int. Ed.* **52**, 9849-9852 (2013).
- [3] A.I. Frenkel, Q. Wang, S.I. Sanchez, M.W. Small, R.G. Nuzzo, *JCP* **138**, 064202 (2013).
- [4] J.M. Cowley, *Phys. Rev.* **138**, A1384-A1389 (1965).
- [5] J.M. Cowley, *Phys. Rev.* **120**, 1648-1657 (1960).
- [6] J.M. Cowley, *Phys. Rev.* **77**, 669-675 (1950).
- [7] M. Newville, *J. Synchrot. Radiat.* **8**, 322-324 (2001).
- [8] M. Klimenkov, S. Nepijko, H. Kühlenbeck, M. Bäumer, R. Schlögl, H.J. Freund, *Surf. Sci.* **391**, 27-36 (1997).

Fabrication of membrane electrode assemblies with oxide based catalyst by spray coating

A. Pătru, R. Kötzt, T.J. Schmidt

phone: +41 56 310 2318, e-mail: alexandra.patru@psi.ch

One of the problems closely connected to the durability of PEFC is the utilization of carbon as support for platinum catalysts. Under operation conditions of a PEFC, the carbon can be corroded [1], which calls for alternative, more stable support materials for platinum catalyst. The actual trend is focused on conductive metal oxides, since this class of materials exhibits a high electrochemical stability when used in their highest oxidation state, as well as a high specific surface compatible with the PEFC application.

A crucial step in the utilization of this new type of catalyst in real PEFC systems is the electrode preparation and design. Few data are available in the literature regarding oxide supports for Pt in PEFC catalyst layers (CL). A series of key parameters must be optimized in order to get optimal performances with a maximum utilization of platinum catalyst. We started the development of CLs by preparing oxide-based catalytic inks and applying these onto commercial Nafion® membrane by different spraying techniques.

Experimental

Two commercial oxide catalysts were used as model materials for the development of a generic ink formulation: SnO₂ and Sb₂O₅-SnO₂ (Alfa Aesar, NanoArc®). For the preparation of a standard ink, a given quantity of catalyst was mixed with appropriate amounts of a commercial Nafion® solution (5 %wt in a water-aliphatic alcohol mixture, Sigma Aldrich) and an additional solvent (20 %wt isopropanol solution in deionised water). The Nafion® content was fixed at 30 %wt of the catalyst used. Additionally, the eventual use of 1,2-propanediol as co-solvent was similarly evaluated. Two ink compositions with appropriate physical properties were identified. Their corresponding compositions are given in Table 1. No significant particle agglomeration or sedimentation was observed for these compositions, as characterized by optical microscopy.

	Composition 1	Composition 2
Substance	Quantity	Quantity
SnO ₂ /Sb ₂ O ₅ SnO ₂	500 mg	500 mg
Water	4 ml	4 ml
Isopropanol	1.3 ml	1.3 ml
1,2 – propanediol	0.25 ml	-
Nafion® 5 %wt.	4.9 ml	4.9 ml

Table 1. Ink composition summary.

These ink formulations were applied by spraying at room temperature directly on the pretreated Nafion® XL membrane (acid and dry form). A "classical" air brush and the EcoSpray® technique were used independently for spraying the different inks selected. The total loading of the catalyst on the CL was fixed at 4 mg cm⁻². This loading was chosen in the hypothesis of a future use of a 10 %wt Pt catalyst on oxide and a desired 0.4 mg cm⁻² Pt loading on the electrode.

Results

Depending on the spray technique used, different morphologies are obtained. Using an air brush, an agglomeration of the oxide particles is observed, independently of the oxide nature (Fig.1. A and B). The coatings obtained have thicknesses of 70 µm for SnO₂ and 35 µm for Sb₂O₅-SnO₂ and are mechanically not stable. Using the EcoSpray® spray device, the coating morphologies obtained are drastically different (Fig.1. C and D). In this case, no significant particle agglomeration is observed. The coating thicknesses are 23 µm for SnO₂ and 21 µm for Sb₂O₅SnO₂ for the same final electrode catalyst loading. The difference in thicknesses observed at constant catalyst loading is consistent with the production of a more heterogeneous structure in the case of the air brush technique. This observation is also consistent with the electrode mechanical instability observed in this latter case.

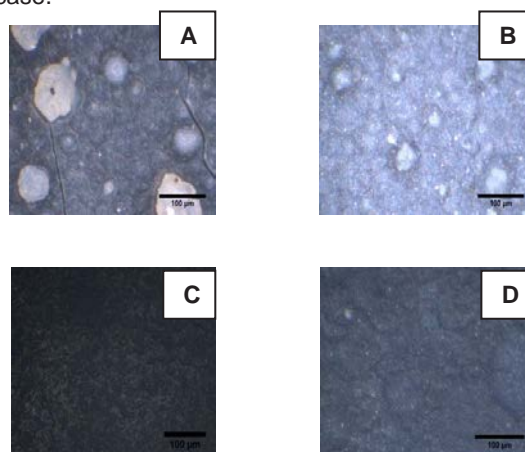


Figure 1. Optical microscopic images of Nafion® membrane coated with SnO₂ (A, C) and Sb₂O₅-SnO₂ (B, D) using an air brush (A, B) and the EcoSpray® technique (C, D). For both oxides, an ink containing 1,2-propanediol was used (composition 1, Table 1).

Conclusions

New types of electrodes for PEFC were fabricated using oxide-based catalyst. The spray technique used (EcoSpray® vs. air brush) plays a crucial role on the electrode morphology obtained, keeping the ink formulation unchanged. Further investigations regarding the process of oxide particles agglomeration during the spray process are in progress.

In the next research phase, the catalyst coated membranes will be characterized in a single cell. The performances of such assemblies will be evaluated *in situ* by polarization curves and impedance spectroscopy. The stability of the oxide-supported catalysts will be studied by performing start stop cycle and accelerated stress tests, respectively Pt/IrTiO_x will be used as a benchmark catalyst and characterized similarly. [2]

Acknowledgement: CCEM and Umicore AG&Co. KG.

References

- [1] F.N. Büchi, M. Inaba, T.J. Schmidt, editors. Polymer Electrolyte Fuel Cell Durability, Springer (2009).
- [2] T. Binninger, E. Fabbri, R. Kötzt, T.J. Schmidt, ECS Trans. 58, 1835-1841 (2013).

Structural and electrochemical investigation of Pt films produced by PLD

S.E. Temmel, D. Pergolesi, E. Fabbri, R. Kötzt, T. Lippert, T.J. Schmidt

phone: +41 56 310 2128, e-mail: sandra.temmel@psi.ch

One of the major limiting factors for the wide-range application of polymer electrolyte fuel cells (PEFCs) is the slow kinetics of the oxygen reduction reaction (ORR) at the cathode, causing overpotentials of about 0.3 V. State-of-the-art catalysts are Pt-based materials. However, due to the limited activity of platinum, great efforts have been put into increasing the ORR kinetics through (i) reducing the interatomic distances and hence modifying the physical structure of Pt [1] or (ii) tailoring the Pt (hkl) surface and hereby manipulating the specific adsorption of species [2].

The influence of Pt interatomic distances and/or surface orientation on its electrocatalytic activity towards the ORR will be examined. Thin films of varying crystalline orientation and strain, produced by pulsed laser deposition, were chosen as model systems to investigate those properties. First results on as-deposited Pt films (5-10 nm) concerning the crystalline orientation, the growth behaviour, the surface morphology, and the surface properties for electrocatalytic reactions are presented.

Experimental

Thin Pt films were grown in an ultra-high vacuum of 3×10^{-7} mbar on (001) oriented STO substrates (CrysTec, thickness of 0.5 mm, one-sided epipolished, miscut angle $< 0.5^\circ$, $5 \times 10 \text{ mm}^2$) by pulsed laser deposition using a KrF excimer laser (248 nm, 9 Hz, 28 kV). The target (positioned at a distance of 5 cm normal to the substrate surface) was rastered by the laser beam (Rectangular spot size = $1.1 \times 10^{-2} \text{ cm}^2$, Fluence $F = 3\text{-}4 \text{ J/cm}^2$) under a 45° angle for a total number of 5200 pulses. The substrate temperature was set to 630°C . The collecting optics of a pyrometer were focused on the substrate surface to double check the set temperature. For a more uniform heating, a silicon platelet of the same dimension as the substrate was inserted at the back of the substrate. A heating rate of 15°C/min was always applied to reach the final deposition temperature and oxygen was introduced as a background gas to reduce the oxygen loss of the substrate. Prior to deposition, the substrates were ultrasonically cleaned in ethanol, acetone and isopropanol for 2 min each. The Pt target surface was preblasted for 5 min to smoothen and clean its surface. All deposition parameters are summarized in Table 1.

Laser repetition rate	9 Hz
No. of pulses	5200
Spot size	$1.1 \times 10^{-2} \text{ cm}^2$
Fluence	3.7 J/cm^2
Substrate-Target-Distance	5 cm
Pressure	3×10^{-7} mbar
Background gas	None
Temperature	630°C

Table 1. Deposition parameters for the fabrication of thin Pt films on (100) STO using pulsed laser deposition.

Reflection high energy electron diffraction (RHEED) was applied to follow film growth *in situ*. In RHEED, a high energetic electron beam strikes the sample surface under a grazing angle (1°) and is reflected onto a phosphorescent screen positioned in the chamber. The recorded pattern gives information about the growth mode, surface morphology and crystallographic orientation. Θ - 2θ x-ray scans were carried out with a D500 diffractometer (Bruker, Germany) using $\text{Cu-K}\alpha$ and $\text{Cu-K}\beta$ radiation to examine the crystal structure. All measurements were realized at room temperature in the Bragg-Brentano diffraction geometry varying 2θ from 30° to 110° . The film thickness was determined via x-ray reflectometry in a Θ - 2θ scan in the range of 1° to 6° using the same diffractometer. The morphology of the film was investigated with scanning electron microscopy (Zeiss Supra). Cyclic voltammograms (CVs) were recorded at room temperature in oxygen-free 0.5 M sulfuric acid at a sweep rate of 50 mV sec^{-1} using a three-electrode setup to test the surface properties of the as-produced Pt-films.

<i>In situ</i>	Growth behaviour	RHEED
<i>Post growth</i>	Film thickness	XRR
	Crystalline orientation	XRD
	Surface morphology	SEM
<i>Electro-chemical</i>	Crystalline orientation and active surface area	CV

Table 2. Measurement techniques applied to characterize as-produced Pt films.

Results

The XRD pattern clearly shows the presence of the (002) Pt peak. In contrast, the (111) Pt peak is absent; which proves the epitaxial growth of the Pt film.

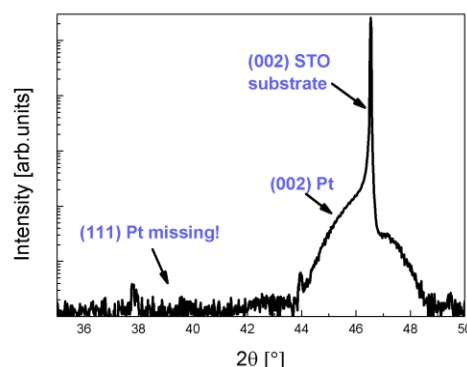


Figure 1. XRD pattern of a Pt film grown in vacuum on (001) STO at 9 Hz, 5200 pulses, 3.7 J cm^{-2} at 630°C .

The recorded RHEED images seem to be a combination of two RHEED patterns originating from two competing growth mechanisms. The transmission-like spotty pattern, pointed out by the green arrows, suggests a 3D Volmer-Weber-growth. In contrast, the emerging streaks on spots and their characteristic position indicate a 2D epitaxial growth, outlined by the blue arrows in Figure 2.

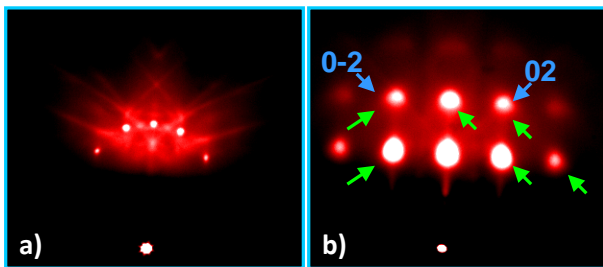


Figure 2. RHEED patterns of a) the initial STO surface before film growth and b) of an as-produced Pt film showing features of a combination of a 3D Volmer-Weber Growth (green arrows) and of a 2D epitaxial growth (blue arrows). 0-2 and 02 refer to the epitaxially grown crystallographic Pt planes.

SEM images show clearly separated Pt crystallites confirming a 3D Volmer-Weber growth. It also becomes obvious that no microdroplets, a common problem for metal ablation, are covering the surface.

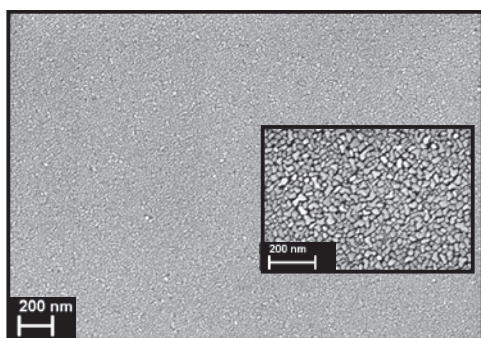


Figure 3. SEM images of an as-produced Pt film showing clearly separated Pt crystallites.

The CV (Figure 4, black line) taken for as-produced Pt films resemble the CV of a (111) single crystal (Figure 4, red line) without the features originating from long-ranged order (111) terraces. The selective adsorption of hydrogen under potential deposition (H_{upd}) and HSO_4^- ions around 0.45 V vs. RHE represents a clear fingerprint of {111} planes. This result is in accordance with a model which will be illustrated in the following, explaining that <111> facets are dominating the electrochemical response. However, it has to be pointed out that those features only emerged after cycling up to 1.2 V. Further investigations are necessary to check whether the Pt surface was initially blocked by contaminants after transfer from the PLD chamber into the electrolyte or whether restructuring occurred upon oxidation/reduction of the Pt surface at high potentials.

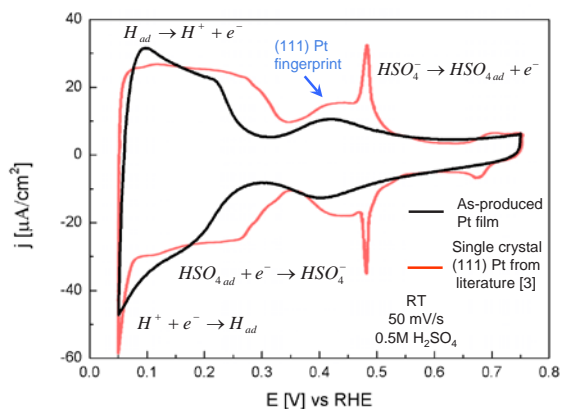


Figure 4. CV taken in 0.5 M H_2SO_4 at 50mV/sec at RT of a Pt film (black line), compared to a (111) Pt single crystal (red line).

Conclusion and Summary

Platinum is a cubic crystal of fcc structure. Like all metals, it forms facets to minimize its surface energy. One possible shape of Pt crystallites is a cubo-octahedron where the surface is built up by two bound low-index planes as shown in Figure 5.

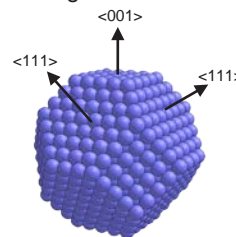


Figure 5. Cubo-octahedral shape of a Pt crystallite, bound by two low-index crystal planes.

Thus, it could be assumed that during Pt deposition, a large number of cubo-octahedrally shaped Pt crystallites grew together on the substrate surface. On this base, a film growth model was developed considering the results from the different measurement techniques. The illustration in Figure 6 shows that the Pt film consists of separated crystallites that are observed in the SEM images. The model further demonstrates that the (001) planes face the out-of-plane direction, which in turn has been confirmed by the XRD patterns. The RHEED pattern originates from the fact that the electrons are partly reflected from the epitaxially grown (001) surfaces and are partly transmitted through the crystallites, explaining the 3D features. The (111) Pt fingerprint observed in the CV's can therefore be explained by the surface which is mainly formed by <111> facets.

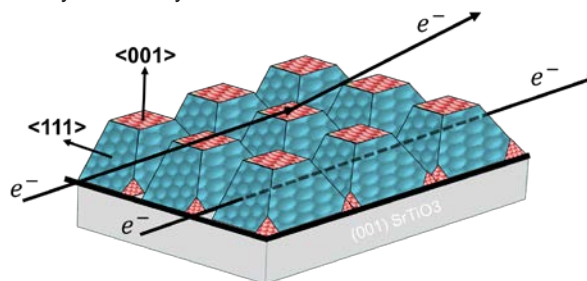


Figure 6. Model for the Pt film growth taking into account all the results from the different measurement techniques. The model assumes that cubo-octahedral Pt crystallites intergrow (see RHEED and SEM) with the (001) planes parallel to the substrate surface (see XRD) and that the <111> facets are dominating the Pt surface (see CV).

To conclude, a model for PLD Pt film growth and surface formation has been developed, where each single physicochemical characterization carried out in the present work supports this Pt growth model. However, further electrochemical measurements are still necessary to prove this concept.

Acknowledgement

Kindly acknowledged is financial support from Kabelwerke Brugg Holding AG, FH Nordwestschweiz und PSI.

References

- [1] V. Jalan, J. Electrochem. Soc. **130**, 2299-2302 (1983).
- [2] N.M. Markovic, T.J. Schmidt, V. Stamenkovic, P.N. Ross, Fuel Cells **2**, 105-115 (2001).
- [3] A.A. El-Shafei, M. Eiswirth, Surf. Science **604**, 862-867 (2010).

Extreme ultraviolet lithography for the fabrication of nanoscale Pt model catalysts

S.A. Tschupp, Y. Ekinci, W. Karim, M. Özaslan, R. Kötz, T.J. Schmidt

phone: +41 56 310 2127, e-mail: simon.tschupp@psi.ch

Well-defined supporting surfaces covered with metallic nanoparticles have attracted increasing interest as catalyst model systems due to the great potential to study their structure-activity relationships and the reaction mechanisms of heterogeneous and (electro-) chemical reactions under controlled, but more realistic conditions than on single crystal surfaces. Using conventional synthesis methods such as precipitation from a soluble metal precursor or by evaporation of metal clusters on a support material, systematic investigations of particle size, coverage and inter-particle distance are hindered by the broad distribution of these values. However, lithography-based processes for the fabrication of model catalysts enable controlling these experimental parameters in a straightforward manner. Pt catalysts used in fuel cells are of high scientific and technological interest to provide the increasing demands of energy conversion in the future [1]. A better understanding of the catalytic properties may help to reduce the content of costly Pt and to penetrate commercial markets in bulk.

Pt nanoparticles with a diameter below 20 nm, ideally in the single-digit nm range, have attracted large attention. This size range lies most closely to the real systems and particle size [2] and proximity [3] play an important role in the determination of the activity of the catalyst. This demand limits the choice of the lithography techniques not only due to the resolution required but also because patterned areas should be sufficiently large in order to study chemical reactions. In this context, electron-beam (e-beam) lithography is of particular interest due to its capabilities of patterning features below 20 nm; the drawback of e-beam lithography being a serial writing method is that patterning large areas (in the range of mm^2) is very time-consuming. Another promising technique which has been shown to reach sub-10 nm feature sizes [4] is extreme ultraviolet (EUV) lithography, a next generation lithography technique extending commonly used optical lithography to photons with a wavelength of 13.5 nm allowing for both high resolution and large area patterning within a reasonable time frame.

Experimental

Due to its advantages of resolution, large area, and throughput, we adopted EUV lithography to manufacture well-defined Pt nanoparticles over large areas. In EUV lithography, the desired pattern on the substrates is generated using diffraction gratings on thin Si_3N_4 membranes, i.e. masks. The critical challenge lies in the fabrication of these masks using e-beam lithography. EUV transmission masks were produced using standard cleanroom techniques according to the process flow, shown in Figure 1, based on work from Wang et al. [5]. Briefly, a Cr/Au/Cr multilayer with a thickness of 2/8/2 nm, respectively, was thermally evaporated on a 100-nm-thick Si_3N_4 membrane and spin-coated with a 300-nm-thick layer of negative tone hydrogen silesquioxane (HSQ) resist (FOX 16, Dow Corning). The resist was exposed by e-beam lithography (Vistec EBPG5000+) and developed in an aqueous solution of Developer 351 (Microposit, Shipley) for 2.5 min. The top

Cr layer was removed by chlorine plasma etching followed by electroplating ~200 nm of Ni between the resist pillars, which were subsequently removed using buffered oxide etcher. A second chlorine dry etching step was performed to obtain the final gratings. The gratings are in fact a 2D grating of hole-arrays with a period of 300 nm and diameter of 150 nm on an area of $480 \times 480 \mu\text{m}^2$.

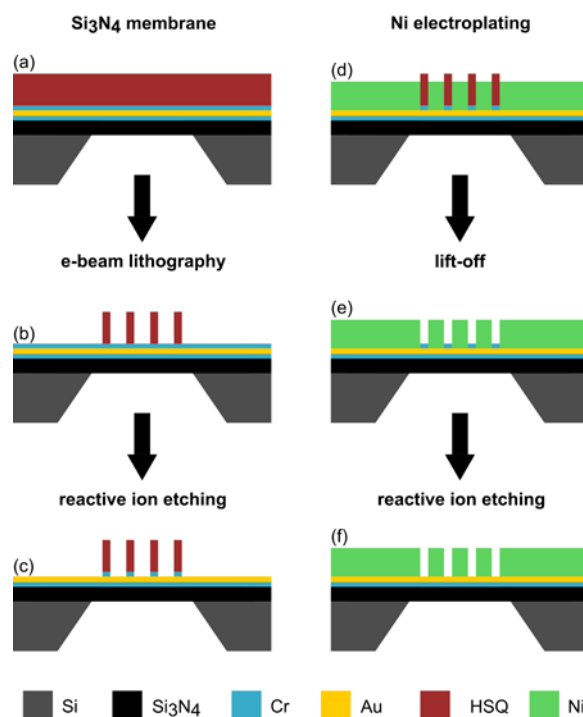


Figure 1. Scheme of the process flow for the fabrication of the EUV transmission mask. (a) Si_3N_4 membrane with thermally evaporated Cr/Au/Cr multilayer and spin-coated HSQ resist; (b) e-beam lithography and development; (c) chlorine plasma etching; (d) Ni electroplating; (e) resist removal; (f) reactive ion etching.

EUV transmission exposures were conducted at the XIL-II beamline of the Swiss Light Source (SLS) on Si wafers by spin-coating HSQ resist (FOX XR1541, Dow Corning) at 5000 rpm for 45 s resulting in a nominally 35 nm thick resist layer. The mask-sample gap was set to 1.5 mm and the dose-on-mask was varied between 50 - 2400 mJ cm^{-2} . After the exposure the samples were developed in a 25% aqueous solution of Developer 351 for 30 s.

For the transfer of the pattern into Pt, Si chips of $14 \times 14 \text{ mm}^2$ were coated with an e-beam evaporated Ti/Pt/ SiO_2 multilayer with a thickness of 50/15/5 nm, respectively, and spin-coated with HSQ resist using the same parameters as mentioned above. The mask-sample gap was set to 1.5 mm and exposure doses ranged from 100 - 800 mJ cm^{-2} (dose-on-mask). The development was performed as described above.

Scanning electron microscopy (SEM) and atomic force microscopy (AFM) were used to study the particle size in lateral and vertical dimensions as well as the surface morphology before exposures. A sufficient flatness of the substrate was necessary for successful exposures.

Results

Figure 2 shows several SEM images of the dot patterns in HSQ resist obtained by EUV exposures using different exposure doses on both a Si wafer and a Ti/Pt/SiO₂ multilayer. For both systems the dot diameters in HSQ resist in the range of 30 – 130 nm were fabricated by varying the exposure dose. The height of the dots was around 30 – 35 nm established by AFM (not shown) as expected from the spin-coating parameters applied. At high doses secondary order effects from the mask patterns start appearing in the form of smaller dots within the dot-array, eventually forming a hole-array in HSQ resist that could be used as a hard-mask for the evaporation of metals in a lift-off process.

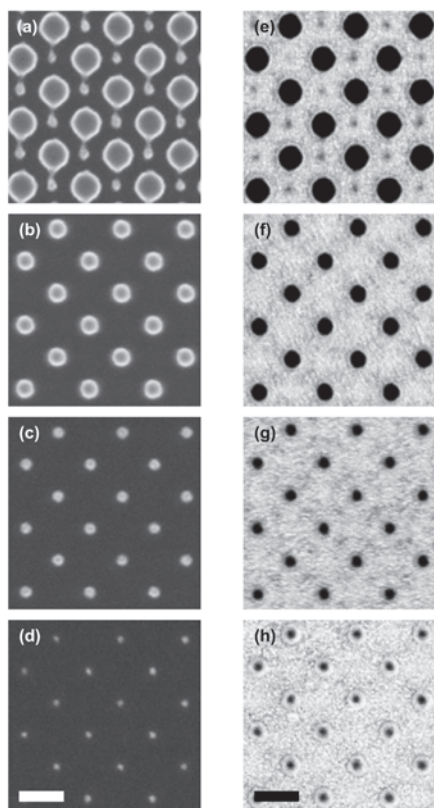


Figure 2. SEM images of a dot-array with a period of 300 nm in HSQ resist on a Si wafer (a) – (d) and on chips coated with a Ti/Pt/SiO₂ multilayer (e) – (h) with decreasing dose-on-mask from top to bottom. Scale bars are 200 nm.

Conclusions

EUV transmission masks with Ni gratings were fabricated successfully by e-beam lithography. With a hole-array grating of 150 nm diameter and period of 300 nm, exposures performed at the XIL-II beamline on Si wafers using HSQ resist showed a regular dot pattern with dot diameters of 30 – 130 nm depending on dose. The pattern was transferred on Si chips coated with a Ti/Pt/SiO₂ multilayer, suitable for electrochemical studies after reactive ion etching of the Pt layer.

In the next steps, masks with smaller hole-array gratings will be fabricated to study smaller and denser nanoparticle-arrays for electrocatalysis. In addition, we will increase the patterned area up to several cm² with a *step-and-repeat* method. We will optimize the dry etching process for Pt based on Ar ion sputtering in order to achieve a reproducible pattern transfer.

Our aim is to establish the structure-activity relationships of different nano-scale Pt model catalysts by performing electrochemical experiments using a flow cell designed and fabricated in-house based on a wall-jet electrode arrangement [6].

Acknowledgement

The authors would like to thank Michaela Vockenhuber for technical support at the XIL-II beamline and acknowledge PSI Research Commission for financial support.

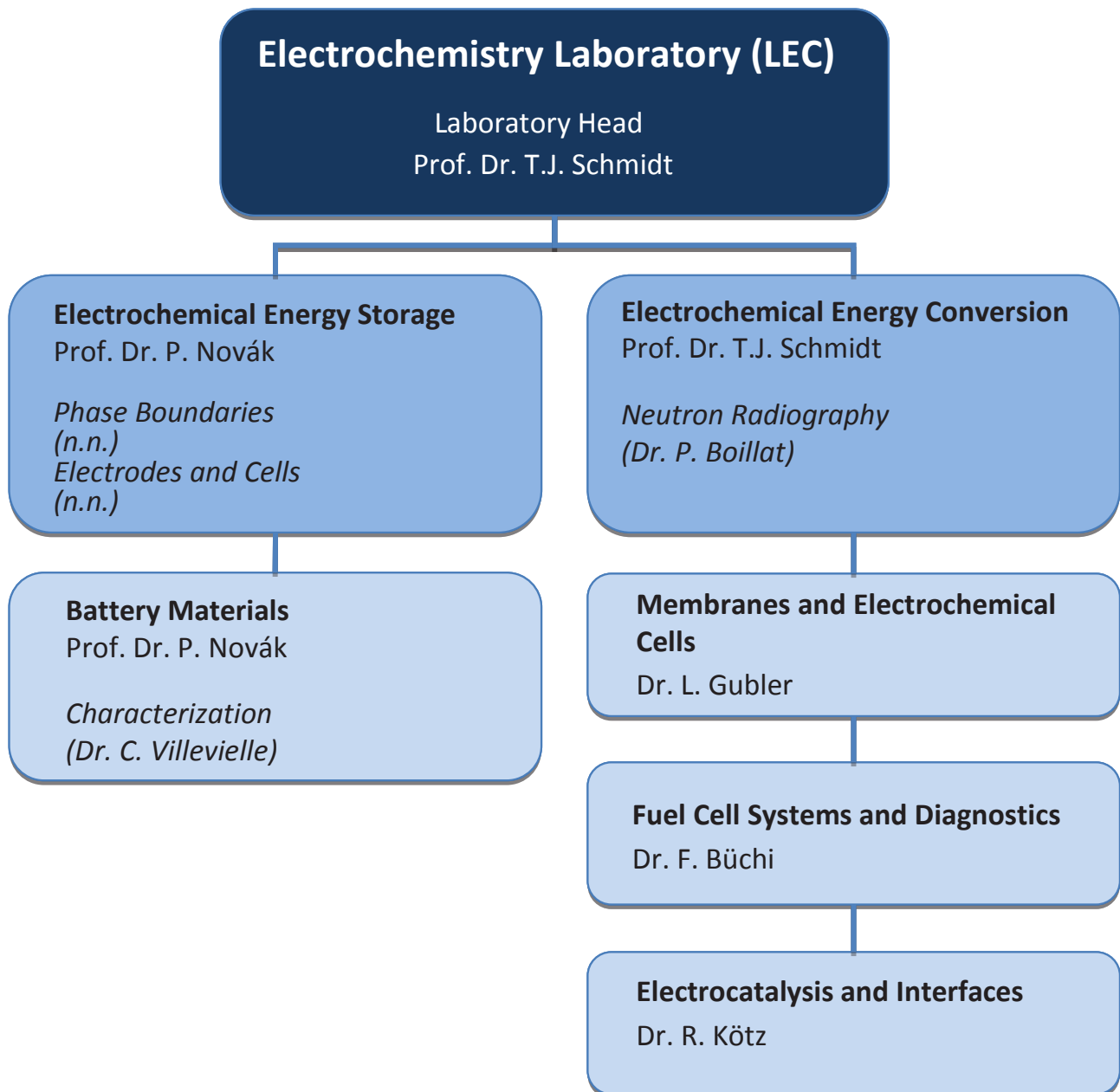
References

- [1] A. Rabis, P. Rodriguez, T.J. Schmidt, *ACS Catal.* **2**, 864 (2012).
- [2] M. Shao, A. Peles, K. Shoemaker, *Nano Lett.* **11**, 3714-3719 (2011).
- [3] M. Nesselberger, M. Roefzaad, R.F. Hamou, P.U. Biedermann, F.F. Schweinberger, S. Kunz, K. Schloegl, G.K.H. Wiberg, S. Ashton, U. Heinz, K.J.J. Mayrhofer, M. Arenz, *Nat. Mater.* **12**, 1-6 (2013).
- [4] B. Päivänranta, A. Langner, E. Kirk, C. David, Y. Ekinci, *Nanotechnology* **22**, 375302 (2011).
- [5] L. Wang, B. Terhalle, M. Hojeij, V.A. Guzenko, Y. Ekinci, *J. Vac. Sci. Technol. B* **30**, 031603 (2012).
- [6] J. Yamada, H. Matsuda, *J. Electroanal. Chem.* **44**, 189-198 (1973).

THE ELECTROCHEMISTRY LABORATORY

FACTS & NUMBERS

STRUCTURE 2013



ECL-PERSONNEL 2013

Staff

Martin AMMANN (Technician)
Felix BERNAUER (Engineer)
Dr. Pierre BOILLAT (Project Leader)
Lukas BONORAND (Engineer)
Dr. Felix BÜCHI (Group Leader)
Dr. Christa BÜNZLI (Post Doctoral Researcher)
Dr. Elias CASTEL (Post Doctoral Researcher)
Dr. Mario EL KAZZI (Scientist)
Dr. Jens ELLER (Post Doctoral Researcher)
Dr. Emiliana FABBRI (Scientist)
Dr. Annette FOELSKE-SCHMITZ (Scientist)
Dr. Maria GEORMEZI (Post Doctoral Researcher)
Cordelia GLOOR (Assistant)
Thomas GLOOR (Technician)
Dr. Juan Luis GÓMEZ-CÁMER (Post Doctoral Researcher)
Dr. Lorenz GUBLER (Group Leader)
Dr. Aurélie GUÉGUÉN (Scientist)
Dr. Moritz HANTEL (Post Doctoral Guest Researcher)
Dr. Marcel HOFER (Engineer)
Dr. Erik JÄMSTORP-BERG (Post Doctoral Researcher)
Christoph JUNKER (Technician)
Hermann KAISER (Technician)
Dr. Rüdiger KÖTZ (Group Leader)
Dr. Adrien LAMBRAC (Post Doctoral Researcher)
Christian MARMY (Technician)
André MEIER (Technician)
George NEOPHYTIDES (Project Engineer)
Prof. Dr. Petr NOVÁK (Section Head)
Dr. Pierre OBERHOLZER (Post Doctoral Researcher)
Dr. Mehtap ÖZASLAN (Scientist)
Dr. Alexandra PĂTRU (Post Doctoral Researcher)
Christian PETER (Engineer)
Pia REICHEL (Technician)
Dr. Rosa ROBERT (Scientist)
Dr. Jörg ROTH (Scientist)
Dr. Sébastien SALLARD (Scientist)
Prof. Dr. Thomas J. SCHMIDT (Laboratory Head)
Dr. Daniel STREICH (Post Doctoral Researcher)
Jürg THUT (Technician)
Dr. Sigita URBONAITE (Scientist)
Dr. Claire VILLEVIELLE (Project Leader)

PhD Students

Albert ALBERT
Tobias BINNINGER
Johannes BIESDORF
Peter BLEITH
Lucien BOULET
Yves BUCHMÜLLER
Joanna CONDER
Sebastian EBERHARDT
Tom ENGL
Jorge FERREIRA DE ARAUJO
Antoni FORNER-CUENCA
Anja HABEREDER
Minglong HE
Michael HEß
Kaewta JETSRISUPARB
Immanuel MAYRHUBER
Stefan KREITMEIER
Patrick LANZ
Hai-Jung PENG
Annett RABIS
Martin REICHARDT
Sebastian SCHMIDT
Véronique SPROLL
Sandra TEMMEL
Simon TSCHUPP
Leonie VOGT
Kay WALTAR
Daniel WEINGARTH
Zhuoxiang ZHANG

DISSERTATIONS 2013

Dr. Stefan Kreitmeier



Local degradation of the membrane and catalyst support in polymer electrolyte fuel cells

Ph.D. Thesis No. 20976, ETH Zürich, Januar 2013.

Examiners: Prof. Dr. A. Wokaun, ETH Zürich
Prof. Dr. T.J. Schmidt, PSI Villigen/ETH Zürich
Dr. F.N. Büchi, PSI Villigen

Dr. Michael Heß



Kinetics and stage transitions of graphite for lithium-ion batteries

Ph.D. Thesis No. 21240, ETH Zürich, Juni 2013.

Examiners: Prof. Dr. P. Novák, PSI Villigen/ETH Zürich
Prof. Dr. R. Nesper, ETH Zürich

Dr. Daniel Weingarth



Ionic liquids for electrochemical double layer capacitors

Ph.D. Thesis No. 21213, ETH Zürich, Mai 2013.

Examiners: Prof. Dr. A. Wokaun, ETH Zürich
Prof. Dr. T.J. Schmidt, PSI Villigen/ETH Zürich
Dr. R. Kötz, PSI Villigen
Dr. A. Foelske-Schmitz, PSI Villigen

Dr. Moritz M. Hantel



Graphite oxide and graphene oxide based electrode Materials for electrochemical double layer capacitors

Ph.D. Thesis No. 21212, ETH Zürich, Mai 2013.

Examiners: Prof. Dr. A. Wokaun, ETH Zürich
Prof. Dr. R. Nesper, ETH Zürich
Dr. R. Kötz, PSI Villigen

**Dr. Kaewta
Jetsrisuparb**



Comonomer effects in radiation grafted membranes for polymer electrolyte fuel cells

Ph.D. Thesis No. 21257, ETH Zürich, Juni 2013.

Examiners: Prof. Dr. A. Wokaun, ETH Zürich
Prof. Dr. T.J. Schmidt, PSI Villigen/ETH Zürich
Dr. L. Gubler, PSI Villigen

EXCHANGE STUDENTS, DIPLOMA THESES, SUMMER STUDENTS, GUEST SCIENTISTS

Vanja Vargek	<i>Onion-like carbon as a novel promising support material for Pt fuel cell catalysts & Mass transport in gas diffusion layers (GLD) for fuel cell application</i> RHTW Aachen, Germany, October 2012 - March 2013 (Fuel Cell Systems & Electrocatalysis and Interfaces).
Simon Tschupp	<i>Pyrolysis of patterned SU-8 photoresist for electrodes in microfluidic redox flow cells</i> ETH Zürich, October 2012 - March 2013 (Electrocatalysis and Interfaces).
Lucien Boulet	<i>Study of full lithium-ion cells using HE-NCM/Graphite system</i> Université de Montpellier II, France, February – June 2013 (Battery Materials).
Peter Benedek	<i>Synthesis and electrochemical properties of organometallic positive electrode materials</i> ETH Zürich, February – May 2013 (Battery Materials).
Dr. Davide de Focatiis	<i>Polymer membranes for fuel cells: failure mechanisms and biaxial orientation</i> University of Nottingham, UK, February – May 2013 (Membranes and Electrochemical Cells).
Kay Waltar	<i>Analysis of spatially resolved currents in high-temperature polymer electrolyte fuel cells under stationary and transient operation</i> ETH Zürich, April – July 2013 (Membranes and Electrochemical Cells).
Sebastian Ohrem	<i>Fundamentals of fuel cells</i> BOGY Berufserkundigungspraktikum, Murg, Germany, April 2013 (Fuel Cell Systems and Diagnostics).
Céline Bonnaud	<i>Activity and durability investigations on high-surface-area Pt-Pd aerogel electrocatalysts</i> Phelma, Grenoble, France, April – August 2013 (Electrocatalysis and Interfaces).
Raphaël Chattot	<i>Investigations on gas diffusivity in fuel cell membranes</i> Phelma, Grenoble, France, April – August 2013 (Membranes and Electrochemical Cells).
Zhuning Wang	<i>Characterization of high temperature polymer electrolyte fuel cells</i> ETH Zürich, June – August 2013 (Fuel Cell Systems and Diagnostics).
Benedicte Nilssen	<i>Transmission FTIR spectroscopy for characterization of discharge products, deposited on positive electrode surface in Lithium-air batteries</i> Norwegian University of Science and Technology, Trondheim, Norway, June – August 2013 (Battery Materials).
Rhiyaad Mohamed	<i>Perovskites as catalysts for alkaline fuel cells and electrolyzers</i> University of Cape Town, South Africa, July – October 2013 (Electrocatalysis and Interfaces).
Eva Cznotka	<i>Identification of formed products on the cathode side of Lithium-air batteries with FTIR spectroscopy</i> Westfälische Wilhelms-Universität Münster, Germany, August - October 2013 (Battery Materials).

Simon Müller

Energiespeicher und –Wandler für unbemannte elektrische Fahrzeuge
ETH Zürich, Juni – Juli 2013 (Fuel Cell Systems and Diagnostics).

Miloš Toulec

Analyzing X-ray tomographic images
Institute of Chemical Technology Prague, Czech Republic, August 2013 – April 2014
(Fuel Cell Systems and Diagnostics).

Ceren Yilmaz

Determination of the electrochemically active surface area (ECSA) of a commercial Ptblack electrocatalyst and CO stripping experiments probed by in situ FT-IR
ETH Zürich, September – November 2013 (Electrocatalysis and Interfaces).

Jörn Käse

Charakterisierung von Hochtemperatur Polymerelektrolyt-Brennstoffzellen
Ostbayrische Technische Hochschule Amberg-Weiden, Germany, October 2013 – March 2014 (Membranes and Electrochemical Cells).

SEMINAR, INVITED SPEAKERS

Dasuke Izuhara,
Toray Industries Inc.,
Japan

Advances in hydrocarbon membranes
January 16, 2013.

Dr. Davide De Focatiis,
The University of
Nottingham, UK

Tailoring solid-state polymer properties: activities and expertise at the Polymer Engineering Laboratory of the University of Nottingham
February 27, 2013.

PD Dr. Julia Kunze-Liebhäuser,
TU München, Germany

Compact and nanotubular TiO_xC_y as catalyst support and anode material in Li-Ion batteries
April 10, 2013.

Dr. Jiazhao Wang,
University of
Wollongong, Australia

Thin film and free-standing electrode materials for flexible bendable batteries
June 26, 2013.

Dr. Dirk Henkensmeier,
Fuel Cell Research
Center, Korea Institute of
Science and Technology
(KIST), Seoul, Korea

Short introduction of KIST, anion conducting membranes based on polybenzimidazole and Nafion membranes with one porous surface
July 01, 2013.

Daniel R. Baker,
General Motors R&D
Center, Chemical
Sciences and Materials
Systems Lab, Warren,
USA

Intercalate diffusion in multiphase electrode materials and application to lithiated graphite
July 03, 2013.

Dr. Günther G. Scherer,
Hägglingen, Switzerland
(formerly ECL PSI)

Der BBC Membrel Prozess - ein Blick zurück in die Jahre 1980 bis 1986
July 17, 2013.

Prof. Dr. Hajime Arai,
Kyoto University, Japan

Non-equilibrium phase transition behavior of electrode materials tracked by in situ X-ray absorption and diffraction analysis
September 17, 2013.

AWARDS

Sandra Temmel

EFCE Student Mobility Award 2013
9th European Congress of Chemical Engineering, The Hague, The Netherlands,
April 24, 2013.

Tobias Binninger

Alumni-Preis 2013 der Fakultät für Mathematik und Physik
University of Freiburg, Freiburg, Germany, Best Master Thesis, July 5, 2013.

Christa Bünzli

Best Poster Award
Experimental Challenges of Electrochemical Impedance Spectroscopy of Practical
Electrodes for Lithium-Ion Batteries
EIS2013, 9th International Symposium on Electrochemical Impedance Spectroscopy,
Okinawa, Japan, June 20, 2013.

Emiliana Fabbri

Best Oral Presentation Award
Advanced cathode materials based on Pt-oxide systems for application in polymer
electrolyte fuel cells (PEFCs)
Fall Meeting of the Swiss Chemical Society 2013, Ecole Polytechnique Fédérale de
Lausanne, September 6, 2013.



Sandra Temmel (1st left)



Tobias Binninger (2nd left)



Christa Bünzli (right)



Emiliana Fabbri

CONFERENCES – SYMPOSIA

**29th One-Day-Symposium
April 24, 2013.**

*Insights from the Inside:
Imaging Electrochemical Systems*

Organizers: Thomas J. Schmidt, Rüdiger Kötz, Cordelia Gloor

Contributions from (in order of appearance):

Robert Kostecki, Lawrence Berkeley National Laboratory, Berkeley, USA

Wolfgang Schuhmann, Ruhr-Universität Bochum, Germany

Pierre Boillat, Paul Scherrer Institut

Olaf Magnussen, Christian-Albrechts-Universität zu Kiel, Germany

Karl J.J. Mayrhofer, Max-Planck-Institut für Eisenforschung, Düsseldorf, Germany

Felix N. Büchi, Paul Scherrer Institut



Standing from left to right:
Wolfgang Schuhmann, Thomas J. Schmidt, Olaf Magnussen, Cordelia Gloor, Rüdiger Kötz, Robert Kostecki, Petr Novák

Front row from left to right:
Pierre Boillat, Karl J.J. Mayrhofer, Lorenz Gubler, Felix N. Büchi

REVIEW ACTIVITIES OF THE LABORATORY

Journals

Accounts of Chemical Research ♦ ACS Applied Materials & Interface ♦ Advanced Materials ♦ Advanced Functional Materials of Wiley ♦ Angewandte Chemie International Edition ♦ Analytical Methods ♦ Applied Catalysis B: Environmental ♦ Applied Energy ♦ Applied Surface Science

Carbon ♦ ChemElectrochem of Wiley ♦ Chemical Communications ♦ Chemical Reviews ♦ Chemistry of Materials of ACS ♦ Crystal Growth & Design

ECS Electrochemistry Letters ♦ Electrochemistry Communications ♦ Electrochimica Acta ♦ Energy & Environmental Science

Fuel Cells

High Performance Polymers

International Journal of Hydrogen Energy

Journal of the American Chemical Society ♦ Journal of Applied Crystallography ♦ Journal of Catalysis ♦ Journal of the Electrochemical Society ♦ Journal of Materials Chemistry A ♦ Journal of Materials Chemistry of RSC ♦ Journal of Membrane Science ♦ Journal of New Materials for Electrochemical Systems ♦ Journal of Physical Chemistry ♦ Journal of Power Sources ♦ Journal of Solid State Electrochemistry ♦ Journal of Synchrotron Radiation

Macromolecular Chemistry and Physics ♦ Materials

Nature Materials ♦ Nature Chemistry ♦ Nature Communications ♦ New Journal of Chemistry

Physical Chemistry Chemical Physics ♦ Polymer

RCS Advances

Science ♦ Solid State Ionics

Organisations

Alexander von Humboldt-Stiftung, Germany

CCEM-CH

ETH Zürich Research Commission

Helmholtz Society, Germany

Research Council of Norway

SNF (Schweizerischer Nationalfond)

External Dissertations: Review activities

Thomas J. Schmidt :

• K. Moskovitz, University of Cape Town

• M. Weiland, TU Berlin

Felix N. Büchi :

• Zhe Peng, Université Montpellier 2

Lorenz Gubler :

• Etienne Labalme, Université Montpellier 2

INDUSTRIAL PARTNERS

The Laboratory had the pleasure to collaborate with the following industrial partners during the year 2013:

BASF SE, Ludwigshafen, Germany

Belenos Clean Power Holding, Biel/Bienne

Heraeus Quarzglas GmbH & Co. KG, Kleinostheim, Germany

IBM Zürich Research Laboratory, Rüschlikon

Saft SA, Bordeaux, France

SolviCore GmbH & Co. KG, Hanau, Germany

TIMCAL SA, Bodio

UMICORE AG & Co. KG, Hanau, Germany

PROJECT COLLABORATIONS WITH EXTERNAL PARTNERS

BFE

P. Boillat Projektleiter	<i>In situ study of water transport processes in polymer electrolyte electrolyzers with neutron imaging</i>
L. Gubler Projektleiter	<i>Lebensdauer Limitierungen von Brennstoffzellen-Membranen: Mechanismen, Methoden und Innovationen</i>
P. Novák Projektleiter	<i>Untersuchung zur Machbarkeit einer Salz-Flow-Batterie with Battery Consult GmbH, Meiringen</i>
J. Roth Projektleiter	<i>S_Chain Fundamentals with ZHAW Winterthur and Belenos Clean Power, Biel/Bienne</i>
T.J. Schmidt Projektleiter	<i>Renewable Energies in Future Energy Supply (RENERG²)</i>

CCEM

T.J. Schmidt Projektleiter	<i>DURACAT (Highly durable oxide-based catalysts for polymer electrolyte fuel cells) with ETH Zürich, CSEM Neuchâtel, University of Southampton UK and Umicore AG & Co KG.</i>
C. Bach, T.J. Schmidt Projektleiter	<i>RENERG² (Renewable Energies in Future Energy Supply) with ETH Zürich, Empa Dübendorf, EPF Lausanne, ZAHW Winterthur</i>

EU

P. Boillat Projektleiter	<i>H2FC (Integrating European infrastructure to support science and development of hydrogen- and fuel cell technologies towards European strategy for sustainable competitive and secure energy)</i>
F.N. Büchi Projektleiter	<i>Auto-Stack CORE (Automotive Fuel Cell Stack Cluster Initiative for Europe)</i>
L. Gubler Projektleiter	<i>NOVEL (Novel materials and system designs for low cost, efficient and durable PEM electrolyzers)</i>
R. Kötz Member of MC	<i>COST Action MP1004 (Hybrid energy storage devices and systems for mobile and stationary applications)</i>
P. Novák Projektleiter	<i>MAHEATT (Materials for high energy accumulators in traction and tools)</i>
J. Roth Projektleiter	<i>IMPALA (Improved PEMFC with advanced water management and gas diffusion layers for automotive application)</i>

SNSF

P. Boillat Projektleiter	<i>Synthesis and characterization of porous materials with patterned wettability for advanced fuel cell water management strategies</i>
L. Gubler Projektleiter	<i>Antioxidant strategies for the stabilization of fuel cell membranes against oxidative stress</i>
L. Gubler Projektleiter (Co-PI)	<i>Connecting the renewable energy to green mobility using hydrogen as energy carrier under the Belenos Clean Power initiative (GreenPower) EPFL, CSEM, PSI, Belenos Clean Power</i>
L. Gubler Projektleiter	<i>Lithium conducting polymer electrolytes with polysulphide barrier properties</i>
R. Kötz Projektleiter	<i>Graphite oxides and graphene for electrochemical energy storage</i> PSI, ETH Zürich
P. Novák Projektleiter	<i>New oxyphosphates as high specific charge electrode materials for lithium-ion batteries</i>
P. Novák Projektleiter	<i>In situ research on new generation of electrochemical capacitors (Polish-Swiss research programme)</i>
S. Sallard Projektleiter	<i>Hybrid organic-inorganic lithium metal diphosphonates and derivatives, new insertion materials for Li-ion batteries</i>
T.J. Schmidt, L. Gubler Projektleiter (Co-PIs)	<i>Redox flow electrochemistry for power delivery and cooling (REPCOOL)</i>

Industry

P. Boillat Projektleiter	<i>Diagnostics of polymer electrolyte fuel cells</i> Automotive Industry
F.N. Büchi Projektleiter	<i>Stack and system development</i> Belenos Clean Power, Biel/Bienne
F.N. Büchi Projektleiter	<i>Study on the application of electrochemical energy storage in unmanned vehicles</i> RUAG Schweiz AG
M. Hofer Projektleiter	<i>System integration H₂/O₂ systems</i> Belenos Clean Power, Biel/Bienne
J.L. Gómez-Cámer Projektleiter	<i>Graphite für Lithiumionen-Batterien</i> TIMCAL SA, Bodio
L. Gubler Projektleiter	<i>Development of components for fuel cells</i> Belenos Clean Power, Biel/Bienne
P. Novák Projektleiter	<i>Forschungsnetzwerk „Elektrochemie und Batterien“</i> BASF SE, Ludwigshafen, Germany
P. Novák Projektleiter	<i>Projekt HE-Lion (Hochenergie-Lithiumionenbatterien für die Zukunft)</i> BASF SE, Ludwigshafen, Germany
T.J. Schmidt Projektleiter	<i>Advanced degradation studies on PBI/H₃PO₄ based MEAs for High Temperature PEFCs</i> BASF SE, Ludwigshafen, Germany

T.J. Schmidt Projektleiter	<i>S_Chain</i> Belenos Clean Power Holding, Biel/Bienne
T.J. Schmidt Projektleiter	<i>Strained Pt/Perovskites as a novel class of oxygen reduction electrocatalysts</i> Dysenos
S. Urbonaite Projektleiterin	<i>Spezialkohlenstoffe</i> Heraeus Quarzglas GmbH & Co. KG, Kleinostheim, Germany
C. Villevieille Projektleiterin	<i>Study of full cell reaction mechanism of lithium-ion batteries using 5V spinel materials</i> Saft SA, Bordeaux, France

TEACHING ACTIVITIES

University Level Teaching

Prof. Dr. P. Novák	<i>Elektrochemie</i> ETH Zürich, HS 2013
Prof. Dr. T.J. Schmidt	<i>Renewable Energy Technologies II, Energy Conversion and Storage</i> ETH Zürich, SS 2013
Prof. Dr. T.J. Schmidt, Prof. Dr. M. Quack	<i>Advanced Kinetics</i> ETH Zürich, SS 2013

Lecture Courses at Other Schools

Dr. P. Boillat	<i>Neutron imaging of liquid water in fuel cells</i> European Technical School on Hydrogen and Fuel Cells 2013.
Dr. P. Boillat	<i>Combining imaging with advanced electrochemical methods</i> European Technical School on Hydrogen and Fuel Cells 2013.

Contributions to Courses at Universities, FHL, and other Institutes

L. Gubler	<i>Renewable Energy Technologies II, Energy Conversion and Storage</i> ETH Zürich, April 9, May 7, May 14, May 21, May 28, 2013.
-----------	---

PUBLICATIONS

Books and Reviewed Book Chapters

F.N. Büchi, P. Boillat	<i>Mass Transport in Polymer Electrolyte Fuel Cells</i> doi: 10.1007/SpringerReference_303651, Encyclopedia of Applied Electrochemistry, R. Savinell, K. Ota, G. Kreysa (Eds.), SpringerReference (www.springerreference.com), Springer-Verlag Berlin Heidelberg (2013).
F.N. Büchi, C. Gloor, R. Kötz, T.J. Schmidt	<i>PSI Electrochemistry Laboratory Annual Report 2012</i> doi: 103929/ethz-a-007047464, ISSN 1661-5379 (2013).
E. Fabbri, T.J. Schmidt	<i>Platinum-Based Cathode Catalysts for Polymer Electrolyte Fuel Cells</i> doi: 10.1007/SpringerReference_303661 Encyclopedia of Applied Electrochemistry, Springer Science + Business Media LLC, New York, R.F. Savinell, K. Ota, G. Krysa (Eds.), (2013).

- M. Inaba, T.J. Schmidt
Section Editors
Fuel Cells, a Section of the Encyclopedia of Applied Electrochemistry
doi: 10.1007/SpringerReference_303660. ISBN 978-1-4419-6996-5,
R.F. Savinell, K. Ota, G. Kreysa (ediors-in-chief), SpringerReference
(www.springerreference.com). Springer-Verlag Berlin Heidelberg,
(2013).
- G. Neophytides, T.J. Schmidt
High-Temperature polymer electrolyte fuel cells
doi: 10.1007/SpringerReference_303646, Encyclopedia of Applied
Electrochemistry, Springer Science + Business Media LLC, New York,
R.F. Savinell, K. Ota, G. Krysa (Eds.), (2013).
- P. Rodriguez, T.J. Schmidt
Platinum-based anode catalysts for polymer electrolyte fuel cells
doi: 10.1007/SpringerReference_303660, Encyclopedia of Applied
Electrochemistry, Springer Science + Business Media LLC, New York,
R.F. Savinell, K. Ota, G. Krysa (Eds.), (2013).

Peer Reviewed Papers

- S. Balog, U. Gasser,
K. Jetsrisuparb, L. Gubler
*Structure of the hydrophilic phase and its impact on the conductivity of
graft copolymer ionomers at low hydration level*
doi: 10.1016/j.polymer.2013.06.015, Polymer **54**, 4266-4275 (2013).
- M.H. Bayer, I.A. Schneider
*Application of the Kramers Kronig relations to locally resolved
impedance data of polymer electrolyte fuel cells*
doi: 10.1016/j.jelechem.2012.11.011, J. Electroanal. Chem. **689**, 42-45,
(2013).
- P. Bleith, P. Novák,
C. Villevieille
*Influence of cut-off potential on the electrochemistry of $M_{0.5}TiOPO_4$
($M=Fe, Cu$) synthesized by a new route*
doi: 10.1149/2.096309jes, J. Electrochem. Soc. **160**, A1534-A1538
(2013).
- Y. Buchmüller, A. Wokaun,
L. Gubler
*Fuel cell membranes based on grafted and post-sulfonated glycidyl
methacrylate (GMA)*
doi: 10.1002/face.201300144, Fuel Cells **13** (6), 1177-1185 (2013).
- D.S.A. De Focatiis, L. Gubler
*Uniaxial deformation and orientation of ethylene-tetrafluoroethylene
films*
doi: 10.1016/j.polymertesting.2013.09.007, Polym. Test. **32**, 1423-1435
(2013).
- S.M. Dockheer, L. Gubler,
W.H. Koppenol
*Reactions of the tetraoxidosulfate and hydroxyl radicals with
poly(sodium α -methylstyrene sulfonate)*
doi: 10.1039/c3cp44341h, Phys. Chem. Chem. Phys. **15**, 4975-4983
(2013).
- A. Foelske-Schmitz,
D. Weingarh, A. Wokaun,
R. Kötzt
*Core level data of ionic liquids: Monitoring charging by in situ
electrochemical X-ray photoelectron spectroscopy*
doi: 10.1149/2.002304eel, ECS Electrochemistry Letters **2** (4), H13-
H15 (2013).
- N. Garcia Araez, P. Novák
Critical aspects in the development of lithium-air batteries
doi: 10.1007/s10008-013-1999-1, J. Solid State Electrochem. **17**, 1793-
1807 (2013).
- V.A. Godbole, C. Villevieille,
P. Novák
*Effect of metal ion and ball milling on the electrochemical properties of
 $M_{0.5}TiOPO_4$ ($M = Ni, Cu, Mg$)*
doi: 10.1016/j.electacta.2013.01.104, Electrochim. Acta **93**, 179-188
(2013).
- V.A. Godbole, M. Heß,
C. Villevieille, H. Kaiser,
J.F. Colin, P. Novák
*Circular in situ neutron powder diffraction cell for study of reaction
mechanism in electrode materials for Li-ion batteries*
doi: 10.1039/C2RA21526H, RSC Adv. **3**, 757-763 (2013).

- J.L. Gómez-Cámer, C. Villevieille, P. Novák *Antimony based negative electrodes for next generation Li-ion batteries*
doi: 10.1039/c3ta12762a, *J. Mater. Chem. A* **1**, 13011-13016 (2013).
- J.L. Gómez-Cámer, P. Novák *Electrochemical impedance spectroscopy: understanding the role of the reference electrode*
doi:10.1016/j.elecom.2013.06.0161, *Electrochem. Commun.* **34**, 208-210 (2013).
- M.M. Hantel, T. Kaspar, R. Nesper, A. Wokaun, R. Kötz *Persistent electrochemical pillaring of graphene ensembles*
doi: 10.1016/j.elecom.2013.06.007, *Electrochem. Commun.* **34**, 189-191 (2013).
- M.M. Hantel, A. Płatek, T. Kaspar, R. Nesper, A. Wokaun, R. Kötz *Investigation of diluted ionic liquid 1-ethyl-3-methyl imidazolium tetrafluoroborate electrolytes for intercalation-like electrodes used in supercapacitors*
doi: 10.1016/j.electacta.2013.04.057, *Electrochim. Acta* **110**, 234-239 (2013).
- M.M. Hantel, T. Kaspar, R. Nesper, A. Wokaun, R. Kötz *Partially reduced graphene oxide paper: A thin film electrode for electrochemical capacitors*
doi: 10.1149/2.019306jes, *J. Electrochem. Soc.* **160** (4), A747-A750 (2013).
- D. Henkensmeier, H. Ben youcef, F. Wallasch, L. Gubler *Radiation grafted ETFE-graft-poly(α -methylstyrenesulfonic acid-co-methacrylonitrile) membranes for fuel cell applications*
doi: 10.1016/j.memsci.2013.07.034, *J. Membr. Sci.* **447**, 228-235 (2013).
- M. Heß, P. Novák *Shrinking annuli mechanism and stage-dependent rate capability of thin layer graphite electrodes for lithium-ion batteries*
doi:10.1016/j.electacta.2013.05.056, *Electrochim. Acta* **106**, 149-158 (2013).
- K. Jetsrisuparb, H. Ben youcef, A. Wokaun, L. Gubler *Radiation grafted membranes for fuel cells containing styrene sulfonic acid and nitrile comonomers*
doi: 10.1016/j.memsci.2013.08.037, *J. Membr. Sci.* **450**, 28-37 (2013).
- F. Kaasik, T. Tamm, M.M. Hantel, E. Perre, A. Aabloo, E. Lust, M.Z. Bazant, V. Presser *Anisometric charge dependent swelling of porous carbon in an ionic liquid*
doi: 10.1016/j.elecom.2013.06.011, *Electrochem. Commun.* **34**, 196-199 (2013).
- S. Kreitmeier, P. Lerch, A. Wokaun, F.N. Büchi *Local degradation at membrane defects in polymer electrolyte fuel cells*
doi: 10.1149/1.023306jes, *J. Electrochem. Soc.* **160**, F456-F463 (2013).
- P. Lanz, C. Villevieille, P. Novák *Electrochemical activation of Li_2MnO_3 at elevated temperature investigated by in situ Raman microscopy*
doi:10.1016/j.electacta.2013.07.130, *Electrochim. Acta* **109**, 426-432 (2013).
- P. Lanz, H. Sommer, M. Schulz-Dobrick, P. Novák *Oxygen release from high energy $x\text{Li}_2\text{MnO}_3(1-x)\text{LiMO}_2$ ($M=\text{Mn},\text{Ni},\text{Co}$): electrochemical, differential electrochemical mass spectrometric, in situ pressure, and in situ temperature characterization*
doi:10.1016/j.electacta.2013.01.105, *Electrochim. Acta* **93**, 114-119 (2013).
- Y. Leterrier, J. Thivolle, F. Oliveira, J.-A. Månson, L. Gubler, H. Ben youcef, L. Bonorand *Viscoelastic phase diagram of fluorinated and grafted polymer films and proton exchange membranes for fuel cell applications*
doi: 10.1002/polb.23309, *J. Polym. Sci. Part B: Polym. Phys.* **51**, 1139-1148 (2013).

- W. Liu, P. Rodriguez, L. Borchardt, A. Foelske-Schmitz, J. Yuan, A.-K. Herrmann, D. Geiger, Z. Zheng, S. Kaskel, N. Gaponik, R. Kötz, T.J. Schmidt, A. Eychmüller
Bimetallic aerogels: High-Performance electrocatalysts for the oxygen reduction reaction
doi: 10.1002/anie.201303109, Angew. Chem. Int. Ed. **52**, 9849-9852 (2013).
- J.E. Low, A. Foelske-Schmitz, F. Krumeich, M. Würle, D. Baudouin, F. Rascón, Ch. Copéret
Narrowly dispersed silica supported osmium nanoparticles prepared by an organometallic approach: H₂ and CO adsorption stoichiometry and hydrogenolysis catalytic activity
doi: 10.1039/c3dt50980j, Dalton Trans. **42**, 12620-12625 (2013).
- G. Neophytides, L. Quaroni, F.N. Büchi, A. Orfanidi, S.G. Neophytides, T.J. Schmidt
A new in situ spectroelectrochemical setup for FTIR measurements in operating high temperature polymer electrolyte fuel cells
doi: 10.1016/j.elecom.2013.06.012, Electrochem. Commun. **34**, 200-203 (2013).
- P. Oberholzer, P. Boillat, A. Kaestner, E.H. Lehmann, G.G. Scherer, T.J. Schmidt, A. Wokaun
Characterizing local O₂ diffusive losses in GDLs of PEFCs using simplified flow field patterns ("2D", "1D", "0D")
doi:10.1149/2.119306jes, J. Electrochem. Soc. **160**, F659-F669 (2013).
- P. Oberholzer, P. Boillat
In situ diffusimetry of porous media in polymer electrolyte fuel cells using transient ²H labeling and neutron imaging
doi:10.1021/jp4045435, J. Phys. Chem. C **117** (39), 19945-19954 (2013).
- N.I. Prasianakis, T. Rosen, J. Kang, J. Eller, J. Mantzaras, F.N. Büchi
Simulation of 3D porous media flows with application to polymer electrolyte fuel cells
doi:10.4208/cicp.341011.310112s, Commun. Comput. Phys. **13**, 851-866 (2013).
- S. Pérez-Villar, P. Lanz, H. Schneider, P. Novák
Characterization of a model solid electrolyte interphase/carbon interface by combined in situ Raman/Fourier transform infrared microscopy
doi:10.1016/j.electacta.2013.05.124, Electrochim. Acta **106**, 506-515 (2013).
- T. Sasaki, Y. Ukyo, P. Novák
Memory effect in a lithium-ion battery
doi:10.1038/NMAT3623, Nature Mater. **12**, 569-775 (2013).
- J. Schmid, K.R. Bickel, P. Novák, R. Schuster
Microcalorimetric measurements of the solvent contribution to the entropy changes upon electrochemical lithium bulk deposition
doi:10.1002/anie.201305508, 10.1002/ange.201305508, Angew. Chem. Int. Ed. **125**, 13475-13479 (2013).
- C. Villevieille, P. Novák
A metastable β-sulfur phase stabilized at room temperature during cycling of high efficiency carbon fibre-sulfur composites for Li-S batteries
doi:10.1039/c3ta13072j, J. Mater. Chem. A **1**, 13089-13092 (2013).
- X.J. Wang, R. Nesper, C. Villevieille, P. Novák
Ammonolyzed MoO₃ nanobelts as novel cathode material of rechargeable Li-ion batteries
doi:10.1002/aenm.201200692, Adv. Energy Mater. **3**, 606-614 (2013).
- O. Waser, M. Heß, A. Güntner, P. Novák, S.E. Pratsinis
Size controlled CuO nanoparticles for Li-ion batteries
doi:10.1016/j.jpowsour.2013.04.147, J. Power Sources **241**, 415-422 (2013).
- M. Weiland, P. Boillat, P. Oberholzer, A. Kaestner, E.H. Lehmann, T.J. Schmidt, G.G. Scherer, H. Reichl¹
High resolution neutron imaging for pulsed and constant load operation of passive self-breathing polymer electrolyte fuel cells
doi:10.1016/j.electacta.2012.09.091, Electrochim. Acta **87**, 567-574 (2013).

- D. Weingarh, H. Noh,
A. Foelske-Schmitz,
A. Wokaun, R. Kötzt
- A reliable determination method of stability limits for electrochemical double layer capacitors*
doi: 10.1016/j.electacta.2013.04.057, *Electrochim. Acta* **103**, 119-124 (2013).
- D. Weingarh, A. Foelske-Schmitz, R. Kötzt
- Cycle versus voltage hold - Which is the better stability test for electrochemical double layer capacitors?*
doi: 10.1016/j.jpowsour.2012.10.019, *J. Power Sources* **225**, 84-88 (2013).
- Z. Zhang, K. Jetsrisuparb,
A. Wokaun, L. Gubler
- Study of nitrile-containing proton exchange membranes prepared by radiation grafting: performance and degradation in the polymer electrolyte fuel cell*
doi: 10.1016/j.jpowsour.2013.06.009, *J. Power Sources* **243**, 306-316 (2013).
- Z. Zhang, Y. Buchmüller,
A. Wokaun, L. Gubler
- Degradation study of radiation grafted membranes under low humidity conditions in the PEFC*
doi: 10.1149/2.002310eel, *ECS Electrochem. Lett.* **2**, F69-F72 (2013).

Conference Proceedings / Other Papers

- J. Biesdorf, P. Oberholzer,
F. Bernauer, A. Kaestner,
P. Vontobel, E. Lehmann,
T.J. Schmidt, P. Boillat
- Distinction of liquid water and ice based on dual spectrum neutron imaging*
doi: 10.1149/05801.0309ecst, *ECS Trans.* **58** (1), 309-314 (2013).
- T. Binninger, E. Fabbri,
R. Kötzt, T.J. Schmidt
- Iridium-Titanium oxide as support for Pt catalyst in PEFC cathodes*
doi: 10.1149/05801.1835ecst, *ECS Trans.* **58** (1), 1835-1841 (2013).
- P. Boillat, P. Oberholzer,
E.H. Lehmann, G.G. Scherer,
A. Wokaun
- The role of the micro-porous layer (MPL) in fuel cells: neutron imaging and advanced electrochemical analysis study*
doi:10.1557/opl.2013.424, *Mater. Res. Soc. Symp. Proc.* **1528** (2013).
- S. H. Eberhardt, F. N. Büchi,
T.J. Schmidt
- Localization of phosphoric acid in HT-PEFCs by X-ray tomographic microscopy*
Proceedings of the 4th European PEFC & H₂ Forum, Lucerne, July 2-5 (2013).
- T. Engl, K. Waltar, L. Gubler,
T.J. Schmidt
- Advanced studies of start/stop induced MEA degradation in high temperature PEFC*
B1203, 4th European PEFC & H₂ Forum, Lucerne, July 2-5 (2013).
- T. Engl, K. Waltar, L. Gubler,
T.J. Schmidt
- CV or not CV: development of electrode diagnostics for high-temperature polymer electrolyte fuel cells*
doi: 10.1149/05801.0819ecst, *ECS Trans.* **58** (1), 819-830 (2013).
- J. Eller, J. Roth, R. Gaudenzi,
S. Irvine, F. Marone,
M. Stapanoni, A. Wokaun,
F.N. Büchi
- Water distribution in GDL near optimal humidification*
doi: 10.1149/05002.0477ecst, *ECS Trans.* **50** (2), 477-486 (2013).
- L. Gubler, L. Bonorand
- Radiation grafted membranes for fuel cells: Strategies to compete with PFSA membranes*
doi: 10.1149/05801.0149ecst, *ECS Trans.* **58** (1), 149-162 (2013).
- A. Iranzo, P. Boillat,
P. Oberholzer
- Integrated neutron imaging data and model development for the analysis of the impact of water on fuel cell performance*
Proc. IV Iberian Symposium on Hydrogen, Fuel Cells and Advanced Batteries, Estoril, Portugal, June 26–28, 2013, Rangel, C., Ed.; ISBN 978-989-98482-0-7
- S. Kreitmeier, A. Wokaun,
F.N. Büchi
- Polymer electrolyte membrane durability - local degradation at pinholes*
doi: 10.1149/05002.0927ecst, *ECS Trans.* **50**, 927-933 (2013).

- A. Rabis, E. Fabbri, A. Foelske-Schmitz, M. Horisberger, R. Kötzt, T.J. Schmidt *Durable oxide-based catalysts for application as cathode materials in polymer electrolyte fuel cells (PEFCs)*
doi: 10.1149/05036.0009ecst, ECS Trans. **50** (36), 9-17 (2013).
- J. Roth, M.R. Zurbrügg, S. Irvine, F. Marone, M. Stampanoni, F.N. Büchi *Investigation of PEFC freeze start by X-Ray tomographic microscopy*
doi: 10.1149/05801.0453ecst, ECS Trans. **58**,453-462 (2013).
- T.J. Schmidt, A. Rabis, B. Schwanitz, G.G. Scherer *Electrocatalysis for PEFCs: Oxygen reduction on nanoparticles and extended surfaces*
doi: 10.1557/opl.2012.1738, Mater. Res. Soc. Symp. Proc. **1491** (2013).
- T.J. Schmidt *Dezentrale Brennstoffzellen-Heizgeräte: Auf dem Weg in die tägliche Anwendung*
Aqua & Gas Nr. 12 (2013).
- D. Weingarth, A. Foelske-Schmitz, A. Wokaun, R. Kötzt *PTFE bound activated carbon – a quasi reference electrode for ionic liquids and its application*
doi: 10.1149/05011.0111ecst, ECS Trans. **50** (11), 111-117 (2013).
- Z. Zhang, K. Jetsrisuparb, A. Wokaun, L. Gubler *Degradation study of advanced radiation grafted membranes in the fuel cell*
Proc. 5th International Conference on Fundamentals & Development of Fuel Cells (FDFC), extended abstract No. S0705, Karlsruhe, Germany, April 16-18, 2013.
- Z. Zhang, Y. Buchmüller, T.J. Schmidt, A. Wokaun, L. Gubler *The effect of relative humidity on chemical degradation of styrene based radiation grafted membranes in the PEFC*
doi: 10.1149/05801.0955ecst, ECS Trans. **58** (1), 955-968 (2013).

TALKS

Invited Talks

- P. Boillat *Neutron imaging of fuel cells: combining visualization with advanced diagnostics*
29th One-Day-Symposium of the PSI Electrochemistry Laboratory, Villigen, April 24, 2013.
- P. Boillat *Neutron imaging and advanced electrochemical analysis of operating fuel cells*
ESS Symposium "Neutrons for Future Energy Strategies", Villigen, May 27-29, 2013.
- F.N. Büchi *Brennstoffzellen – Grundlagen*
Schweizerischer Verein des Gas- und Wasserfaches SVGW, Schwerzenbach, February 28, 2013.
- F.N. Büchi *Brennstoffzellen – Technologie und Anwendungen*
AMI-Kolloquium, Villigen PSI, March 1, 2013.
- F.N. Büchi *X-ray tomographic microscopy of low temperature polymer electrolyte fuel cells*
29th One-Day-Symposium of the PSI Electrochemistry Laboratory, Villigen, April 24, 2013.
- F.N. Büchi *Transport properties of gas diffusion layers in polymer electrolyte fuel cells*
Industrial Workshop on Thin Porous Media, Prague, Czech Republic, May 21, 2013.
- F.N. Büchi *Drive trains based on electrochemical systems*
European Campus of Excellence, Energy perspectives: present and future technologies, Villigen PSI, July 11, 2013.

- F.N. Büchi *Imaging liquid water in polymer electrolyte fuel cells by XTM*
JUM@P '13: Joint Users' Meeting at PSI 2013, Villigen PSI, September 19, 2013.
- F.N. Büchi *Bottleneck: Water management in PEFC – Results from X-ray imaging*
H2FC: European annual research progress review meeting 2013, Rome, Italy, October 17, 2013.
- L. Gubler *Radiation grafted membranes: strategies to outperform and outlast state-of-the-art PFSA materials*
Asilomar Conference on Advances in Materials for Proton Exchange Membrane Fuel Cells Systems, Pacific Grove CA, USA, February 17-20, 2013.
- L. Gubler *Die Brennstoffzelle: Was ist der Stand der Technologie, wo drückt der Schuh?*
Hochrhein-Seminar für Mathematik und Naturwissenschaften, Waldshut, Germany, October 11, 2013.
- L. Gubler *Radiation grafted membranes for fuel cells: Strategies to compete with PFSA membranes*
224th ECS Meeting, San Francisco CA, USA, October 26-November 1, 2013.
- L. Gubler *Radiation grafting: tailoring of ion-conducting membranes for electrochemical applications*
Physical Chemistry Colloquium, ETH Zürich, December 3, 2013.
- E. Jämstorp Berg *In situ interface analysis - the key to performance and safety of battery materials*
7th International Conference on Materials for Advanced Technologies (ICMAT), Singapore, June 30-July 5, 2013.
- R. Kötz *EC Capacitor Fundamentals and Technology*
AABC13 Europe, Strasbourg, June 2013.
- R. Kötz *Ionic liquids for supercapacitors: potential window and stability considerations*
The 2013 International Conference on Advanced Capacitors (ICAC2013), Osaka, Japan, May 27-30, 2013.
- P. Novák *The battery materials' challenges: bulk or surface?*
CIC Energigune, Vitoria-Gasteiz, Spain, March 7, 2013.
- P. Novák *In situ characterization of materials and electrodes: the key to future batteries*
Keynote presentation at the IBA 2013 - International Battery Association Meeting, Barcelona, Spain, March 14, 2013.
- P. Novák *How to understand batteries: in situ look into their reactions*
Keynote presentation at the PBFC 2013 - 6th International Conference on Polymer Batteries and Fuel Cells, Ulm, Germany, June 4, 2013.
- P. Novák *Advanced characterization of materials and electrodes for batteries*
Keynote presentation at the International Conference "Next Generation Batteries - Materials, Technology, and Applications", Delmenhorst, Germany, June 15, 2013.
- P. Novák *Bulk with surface - the primary challenge of battery materials*
Helmholtz-Institut Ulm, Ulm, Germany, July 9, 2013.
- P. Novák *What structural methods can tell us about battery materials*
Keynote presentation at the 1st Graz Battery Days, Graz, Austria, October 1, 2013.
- M. Özaslan *Platinarme Elektrokatalysatoren für die Sauerstoffreduktion*
Materialinnovationen in der Wasserstoff- und Brennstoffzellentechnologie Workshop, Hanau, Germany, March 20, 2013.

- T.J. Schmidt *Fundamental materials science for electrochemical energy conversion*
Materials Research Center ETH Zürich, Zürich, January 15, 2013.
- T.J. Schmidt *Materials and electrocatalysts for future polymer electrolyte fuel cells*
University of Liverpool, Stephenson Institute for Renewable Energy,
Liverpool, Great Britain, January 30, 2013.
- T.J. Schmidt *New electrocatalyst systems and old questions: Can we overcome
current PEFC catalysis limits?*
International Exploratory Workshop: Soft x-Rays, Electrochemistry,
Energy Materials, Dübendorf, June 3-5, 2013.
- T.J. Schmidt *Swiss Competence Center for Energy Research – Heat and electricity
storage*
Hydropole Annual Symposium, St. Gallen, May 23, 2013.
- T.J. Schmidt *The Electrochemistry Laboratory@PSI – Activity Overview*
Technical University of Denmark, Lyngby, Denmark, July 31, 2013.
- T.J. Schmidt *Electrocatalyst development and diagnostics for PEFCs*
Technical University of Denmark, Lyngby, Denmark, August 7, 2013.
- T.J. Schmidt *Insights into polymer electrolyte fuel cells – Catalysts, components,
cells*
GDCh Wissenschaftsforum, Darmstadt, Germany, September 1-4,
2013.
- T.J. Schmidt *Regenerative fuel cells: A future energy storage option?*
Alstom Future Technology Day, Baden, September 19, 2013.
- T.J. Schmidt *Challenges and solutions for renewable and transitional energies
(Panel Discussion Talk)*
10th Science and Technology in Society (STS) Forum, Kyoto, Japan,
October 6-8, 2013.
- T.J. Schmidt *Beyond the Limits of PEFC materials and diagnostics*
17th International Symposium on Batteries, Fuel Cells and
Supercapacitors, Osaka, Japan, October 7-9, 2013.
- T.J. Schmidt, H.A. Gasteiger *ECS Short Course Polymer Electrolyte Fuel Cells*
San Francisco, USA, October 27, 2013.
- T.J. Schmidt *Sauber Unterwegs – Wie aus neuen Materialien effizientere
Katalysatoren und Brennstoffzellen entstehen*
Treffpunkt Science City, Zürich, November 17, 2013.
- T.J. Schmidt *Electrocatalytic specific surface areas: The key to understand catalytic
activities*
Workshop Towards an Optimal Electrode Structure for Polymer
Electrolyte Fuel Cells, Cape Town, South Africa, November 21, 2013.
- C. Villevieille *Designing, synthesizing, and understanding of host materials for
battery electrodes*
CIC Energigune, Vitoria-Gasteiz, Spain, July 23, 2013.

Contributed Talks

- S. Balog, K. Jetsrisuparb,
U. Gasser, L. Gubler *Nanostructure of the aqueous phase and impact on proton transport in
radiation-grafted fuel cell membranes*
ESS Symposium - Neutrons for Future Energy Strategies, Paul
Scherrer Institut, May 27-29, 2013.
- J. Biesdorf, P. Boillat,
P. Oberholzer, F. Bernauer,
A. Kaestner, P. Vontobel,
E. Lehmann, T.J. Schmidt *Distinction between liquid water and ice based on dual spectrum
neutron imaging*
10th Symposium for Fuel Cell and Battery Modelling and Experimental
Validation, ECS Meeting, Bad Boll, Germany, March 19-20, 2013.

- J. Biesdorf, P. Oberholzer, F. Bernauer, A. Kaestner, P. Vontobel, E. Lehmann, T.J. Schmidt, P. Boillat *Distinction of liquid water and ice based on dual spectrum neutron imaging*
224th ECS Meeting, San Francisco, CA, USA, October 27-November 1, 2013.
- T. Binninger, E. Fabbri, R. Kötz, T.J. Schmidt *Iridium-Titanium oxide as support for Pt catalyst in PEFC cathodes*
Symposium on Polymer Electrolyte Fuel Cells 13, 224th ECS Meeting, San Francisco, CA, USA, October 27-November 1, 2013.
- P. Bleith, P. Novák, C. Villevieille *Dual reaction mechanism - combining insertion and conversion*
224th ECS Meeting, San Francisco, CA, USA, October 31, 2013.
- P. Bleith, C. Villevieille, P. Novák *Reaction mechanism of $M_{0.5}TiOPO_4$ upon lithiation and delithiation*
International Conference "Next Generation Batteries - Materials, Technology, and Applications", Delmenhorst, Germany, June 15, 2013.
- L. Bonorand, P. Reichel, J. Thut, L. Gubler *Radiation grafted membranes providing low cost, high performance and durability*
4th European PEFC and H₂ Forum, Lucerne, July 2-5, 2013.
- F.N. Büchi S. Kreitmeier, A. Wokaun *Validation of membrane degradation mechanisms at defects by synchrotron based methods*
10th Symposium for Fuel Cell and Battery Modelling and Experimental Validation (ModVal 10), Bad Boll/Stuttgart, Germany, March 19, 2013.
- F.N. Büchi, S.H. Eberhardt, F. Marone¹, M. Stampanoni¹, T.J. Schmidt *Imaging phosphoric acid in HT-PEFC by X-ray tomographic microscopy*
224th ECS Meeting, San Francisco, CA, USA, October 29, 2013.
¹Swiss Light Source, Paul Scherrer Institut
- Y. Buchmüller, A. Wokaun, L. Gubler *Fuel cell membranes based on grafted and post-sulfonated GMA*
XI^{ème} Colloque de l'Association PolyRay, Rouen, France, April 11-12, 2013.
- E. Castel, E. J. Berg, P. Lanz, C. Villevieille, P. Novák *Advanced investigation of oxygen release during cycling of HE-NCM*
LiBD 6 - 6th Lithium Battery Discussion - Electrode Materials, Arcachon, France, June 16-21, 2013.
- E. Castel, E. Jämstorp Berg, C. Villevieille, P. Novák *Reactions of HE-NCM at high potentials: a DEMS study*
SSI 19 - The 19th International Conference on Solid State Ionics, Kyoto, Japan, June 2-7, 2013.
- S. H. Eberhardt, F.N. Büchi, T.J. Schmidt *Localization of phosphoric acid in HT-PEFCs by X-ray tomographic microscopy*
4th European PEFC and H₂ Forum, Lucerne, Switzerland, July 4 (2013).
- J. Eller, J. Roth, R. Gaudenzi, S. Irvine, F. Marone, M. Stampanoni, A. Wokaun, F.N. Büchi *Influence of feed gas humidity and current density on the 3D water distribution in PEFC*
10th Symposium for Fuel Cell and Battery Modelling and Experimental Validation (ModVal 10), Bad Boll, Germany, March 19, 2013.
- J. Eller, F. Marone, M. Stampanoni, F.N. Büchi *On the effects of irradiation during X-Ray imaging of PEFC*
224th ECS Meeting, San Francisco, CA, USA, October 29, 2013.
- T. Engl, L. Gubler, T.J. Schmidt *Advanced studies of start/stop induced MEA degradation in high temperature PEFC*
4th European PEFC and H₂ Forum, Lucerne, July 2-5, 2013.
- T. Engl, K. Waltar, L. Gubler, T.J. Schmidt *CV or not CV: Development of electrode diagnostics for high-temperature polymer electrolyte fuel cells*
224th ECS Meeting, San Francisco, CA, USA, October 26-November 1, 2013.
- E. Fabbri, R. Kötz, T.J. Schmidt *Advanced cathode materials based on Pt-oxide systems for application in polymer electrolyte fuel cells (PEFCs)*
SCS Fall Meeting, Lausanne, September 6, 2013.

- E. Fabbri, R. Mohamed, P. Levecque, O. Conrad, R. Kötz, T.J. Schmidt *Unraveling the Oxygen Reduction Reaction Mechanism and Activity of Composite Ba_{0.5}Sr_{0.5}Co_{0.8}Fe_{0.52}O_{3-d}/Carbon Electrodes in Alkaline Media by Thin Film Rotating Ring Disk Electrode (RRDE) Measurements*
224th ECS Meeting, San Francisco, CA, USA, October 27–November 1, 2013.
- E. Fabbri, R. Mohamed, P. Levecque, S. Blair, O. Conrad, R. Kötz, T.J. Schmidt *Electrochemical characterization of oxide catalysts by thin film rotating ring disk electrode (RRDE) measurements for application in alkaline energy conversion devices*
223th ECS Meeting, Toronto, Ontario, Canada, May 12–16, 2013.
- E. Fabbri, S. Taylor, A. Rabis, P. Levecque, S. Blair, O. Conrad, R. Kötz, T.J. Schmidt *Electrochemical investigation of Pt model electrodes for application in polymer electrolyte fuel cells (PEFCs)*
223th ECS Meeting, Toronto, Ontario, Canada, May 12–16, 2013.
- M.M. Hantel, T. Kaspar, R. Nesper, A. Wokaun, R. Kötz *Stacked graphene structures for supercapacitor electrodes produced by electrochemical activation of partially reduced graphite oxide*
The 2013 International Conference on Advanced Capacitors (ICAC2013), Osaka, Japan, May 27-30, 2013.
- P. Lanz, C. Villevieille, P. Novák *In situ et ex situ spectroscopies Raman et infrarouge appliquées à la caractérisation de NCM surlithié et des matériaux références*
Annual Meeting of the 'Groupe Français d'Étude des Composés d'Insertion' GFECI 2013, Chambon-sur-Lac, France, March 18-21, 2013.
- M. Maalouf, T. Nauser, L. Gubler, W.H. Koppenol *Chemical degradation of poly(styrenesulfonic acid) model compound of PSSA-based membranes by the attack of hydrogen radicals (H•) in fuel cell application*
European Young Investigator Conference (EYIC), Słubice, Poland, June 26-30, 2013.
- P. Oberholzer, P. Boillat, A. Kaestner, E.H. Lehmann, T.J. Schmidt, A. Wokaun *Characterization of O₂ diffusive losses in the gas diffusion layer (GDL) of the PEFC by means of simplified flow field patterns*
10th Symposium on Fuel Cell and Battery Modeling and Experimental Validation (ModVal 1), Bad Boll, Germany, March 19-20, 2013.
- M. Özaslan, C. Bonnaud, P. Rodriguez, W. Liu, A. Herrmann, N. Gaponik, A. Eychmüller, R. Kötz, T.J. Schmidt *Enhanced activity and durability for the oxygen reduction reaction on high surface area multimetallic aerogels*
224th ECS Meeting, San Francisco, CA, USA, October 27–November 1, 2013.
- M. Özaslan, M. Heggen, P. Strasser *Formation and analysis of core-shell fine structures in Pt bimetallic nanoparticle fuel cell electrocatalysts*
Prof. Shechtman's Master Class, 63rd Nobel Laureate Meeting, Lindau, Germany, July 1-5, 2013.
- A. Rabis, E. Fabbri, R. Kötz, T.J. Schmidt *Application of tin oxide-based support materials for durable cathode catalysts in PEFCs*
224th ECS Meeting, San Francisco, CA, USA, October 27–November 1, 2013.
- J. Roth, M.R. Zurbrügg, S. Irvine, F. Marone, M. Stambanoni, F.N. Büchi *Investigation of PEFC freeze start by X-ray tomographic microscopy*
224th ECS Meeting, San Francisco, CA, USA, October 29, 2013.
- C. Villevieille *Designing, synthesizing, and understanding of host materials for battery electrodes*
ETH Zürich, January 29, 2013.
- C. Villevieille, S. Urbonaite, P. Novák *New composites for lithium-sulfur batteries*
LiBD 6 - 6th Lithium Battery Discussion - Electrode Materials, Arcachon, France, June 16-21, 2013.

Z. Zhang, K. Jetsrisuparb,
A. Wokaun, L. Gubler

Degradation study of advanced radiation grafted membranes in the fuel cell
5th International Conference on Fundamentals & Development of Fuel Cells (FDFC), Karlsruhe, Germany, April 16-18, 2013.

Z. Zhang, Y. Buchmüller,
T.J. Schmidt, A. Wokaun,
L. Gubler

The effect of relative humidity on chemical degradation of styrene based radiation grafted membranes in the PEFC
224th ECS Meeting, San Francisco, CA, USA, October 26-November 1, 2013.

PATENT APPLICATIONS

S. Sallard, P. Novák,
A. Garsuch, F. Chesneau

Process for producing an active cathode material comprising a mixture of a metal oxide and a metal sulfide and use of the active cathode material in rechargeable electrochemical cells
Patent Application No. EP 13176518.2, 2013.

E. Fabbri, A. Rabis, R. Kötz,
T.J. Schmidt

Thermodynamically stable binary oxide doped with lower valence element, its synthesis and application in electrochemical devices
Patent Application No. EP 13150645.3, 2013.

POSTERS

J.V.F. Araújo, M. Özasan,
P. Rodriguez, R. Kötz,
T.J. Schmidt

Electrochemical reduction of CO₂ and its products analysis,
Zing Electrochemistry Conference, Lanzarote, Spain, February 25-28, 2013.

T. Binninger, E. Fabbri,
R. Kötz, T.J. Schmidt

Ir_xTi_{1-x}O₂ support for Pt in PEFC cathodes
Zing Electrochemistry Conference, Lanzarote, Spain, February 25-28, 2013.

T. Binninger, E. Fabbri,
R. Kötz, T.J. Schmidt

Ir_xTi_{1-x}O₂ support for Pt in PEFC cathodes
SCS Fall Meeting, Lausanne, September 6, 2013.

C. Bünzli, J.L. Gómez-Cámer,
P. Novák

Experimental challenges of electrochemical impedance spectroscopy of practical electrodes for lithium-ion batteries
9th International Symposium on Electrochemical Impedance Spectroscopy, Okinawa, Japan, June 16-21, 2013.

Y. Buchmüller, A. Wokaun,
L. Gubler

In situ degradation studies of radiation grafted membranes doped with antioxidants
5th International Conference on Fundamentals & Development of Fuel Cells (FDFC), Karlsruhe, Germany, April 16-18, 2013.

J. Conder, S. Urbonaite,
P. Novák, L. Gubler

Grafting of styrene onto plasma-activated polypropylene
6th International Conference on Polymer Batteries and Fuel Cells, Ulm, Germany, June 3-7, 2013.

A. Forner Cuenca, L. Gubler,
T.J. Schmidt, P. Boillat

Gas diffusion layers with patterned wettability
European Technical School on Hydrogen and Fuel Cells 2013, Heraklion, Greece, September 23-27, 2013.

J.L. Gómez-Cámer, P. Novák

Electrochemical impedance spectroscopy: understanding the role of the reference electrode
LiBD 6 - 6th Lithium Battery Discussion - Electrode Materials, Arcachon, France, June 16-21, 2013

- M. Maalouf, T. Nausser,
L. Gubler, W.H. Koppenol
Study of H• radical attack on poly(styrenesulfonic acid)-based membranes in fuel cell application
Fall Meeting of the Swiss Chemical Society, EPF Lausanne, September 6, 2013.
- R. Robert, P. Lanz,
C. Villevieille, P. Novák
New insights into the (de)lithiation of Li(NiCoAlMg)O₂ cathode materials
LiBD 6 - 6th Lithium Battery Discussion - Electrode Materials, Arcachon, France, June 16-21, 2013.
- S. Temmel, E. Fabbri, R. Kötz,
D. Pergolesi, T. Lippert,
T.J. Schmidt
Structural and electrochemical investigation of thin platinum films fabricated by pulsed laser deposition
SCS Fall Meeting, Lausanne, September 6, 2013.
- S. Temmel, E. Fabbri, R. Kötz,
D. Pergolesi, T. Lippert,
T.J. Schmidt
Development of thin platinum films by pulsed laser deposition
E-MRS (European Materials Research Society), Strasbourg, France, May 27-31, 2013.
- S. Urbonaite, C. Neumann,
J. Becker, M. Otter, S. Pihan,
P. Novák
Characterization of porocarb-Si composite materials for negative Li-ion battery electrodes
LiBD 6 - 6th Lithium Battery Discussion - Electrode Materials, Arcachon, France, June 16-21, 2013.
- C. Villevieille, P. Lanz,
P. Novák
Ageing of overlithiated NCM positive electrode material upon exposure to water vapor
IBA 2013 - International Battery Association Meeting, Barcelona, Spain, March 10-15, 2013.
- C. Villevieille, M. El Kazzi,
S. Pérez-Villar, P. Novák
Understanding the SEI properties due to conversion reactions on Sn electrodes used in Na-ion batteries
1st Sodium symposium, Vitoria-Gasteiz, Spain, October 16-17, 2013.

CONFERENCES & WORKSHOPS ORGANIZATIONS

- F.N. Büchi, T.J. Schmidt
13th Symposium on Polymer Electrolyte Fuel Cells PEFC 13
224th ECS Meeting, San Francisco, CA, USA, October 27-November 1, 2013.
Members of Organizing committee
- E. Fabbri
Symposium Hydrogen Production, Conversion, and Storage 4
223rd ECS Meeting, Toronto, Canada, May 12–16, 2013.
Member of Organizing committee
- E. Fabbri
New nano-materials in energy technology
Annual meeting, European academy of Science (EURASC), Karlsruhe, Germany, May 13-15, 2013.
Member of Organizing committee (Winning team of the Kepler award)
- M. Özaslan
46. Jahrestreffen Deutscher Katalytiker
Weimar, Germany, March 13-15, 2013.
Member of Scientific committee

MEMBERS IN EXTERNAL COMMITTEES

- R. Kötz
Electrochimica Acta
Associate Editor
- P. Novák
Int. Meetings on Lithium Batteries LLC
Director

P. Novák	<i>CIC Energigune, Vitoria, Spain</i> Member of Scientific Committee
P. Novák	<i>Danish Council for Strategic Research</i> Member of the Peer Review Panel
P. Novák	<i>The Northeastern Center for Chemical Energy Storage (NECCES)</i> Member of Scientific Advisory Board
T.J. Schmidt	<i>Journal of the Electrochemical Society/ECS Electrochemistry Letters</i> Associate Editor
T.J. Schmidt	<i>HySA/Catalysis, University of Cape Town</i> Member Technical Steering Committee
T.J. Schmidt	<i>4M Centre - Mechanisms, Materials, Manufacturing and Management – Interdisciplinary Fundamental Research to Promote commercialization of HT-PEMFC, Technical University of Denmark</i> Member Technical Steering Committee
T.J. Schmidt	<i>Belenos Clean Power Holding, Biel/Bienne</i> Member Advisory Board
T.J. Schmidt	<i>Competence Center Energy and Mobility Switzerland, CCEM</i> Member Steering Committee
S. Urbonaite	<i>The Research Council of Norway</i> Expert Evaluator

